Patient-Specific Simulation Models of the Abdominal Aorta With and Without Aneurysms

Enevoldsen, Marie Sand

Publication date:
2012

Document Version
Publisher's PDF, also known as Version of record

Technical University of Denmark

Marie Sand Enevoldsen

Patient-Specific Models of the Abdominal Aorta with and without Aneurysms

PhD thesis, November 2011

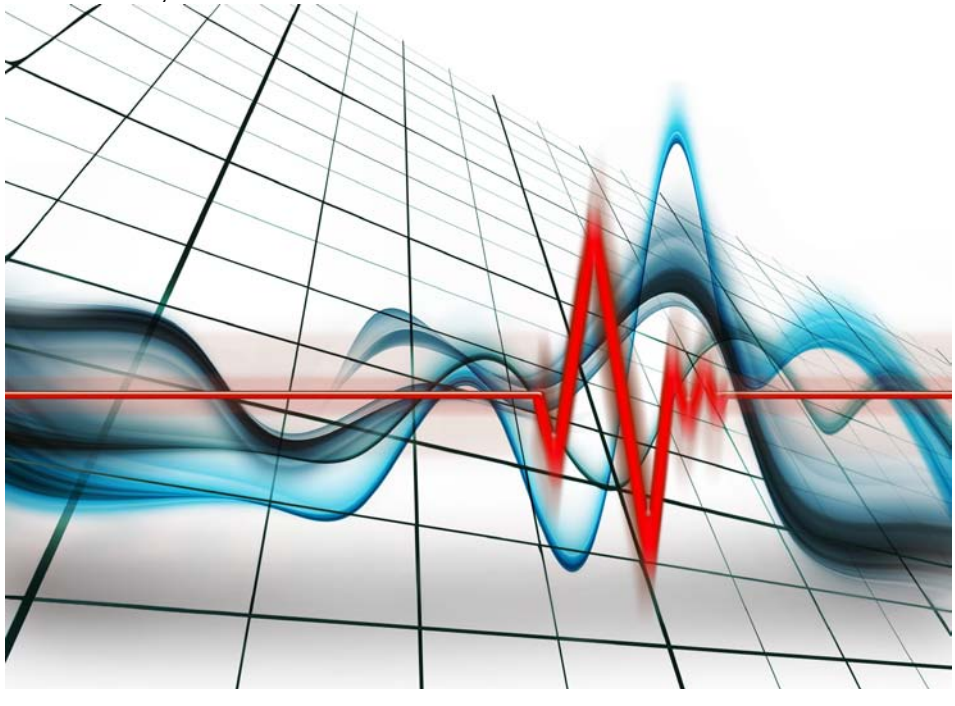

DTU Electrical Engineering
Department of Electrical Engineering

Patient-Specific Simulation Models of the Abdominal Aorta With and Without Aneurysms, 2nd Edition, January 2012.

Technical University of Denmark
Department of Electical Engineering
DK-2800 Kgs. Lyngby
Denmark

Submitted in fulfillment of the requirements for the degree of Doctor of Philosophy at Technical University of Denmark.

ASSESSMENT COMMITTEE

Chairman:

Associate Professor, PhD Lars G. Hansson,

Department of Electrical Engineering,
Technical University of Denmark, Denmark

External examinator:

Associate Professor, PhD Jonas Stålhand,

Division of Mechanics/IEI,
Linköping University, Sweden

External examinator:

Associate Professor, PhD Per Axel Magnus Cinthio,

Faculty of Engineering, LTH,
Lund University, Sweden

PREFACE

This PhD dissertation is submitted to DTU Electrical Engineering, Technical University of Denmark, in partial fulfillment of the requirements for the degree of Doctor of Philosophy. The work has been supervised by Associate Professor Kaj-Åge Henneberg, Professor Dr. Techn. Jørgen Arendt Jensen, and Professor PhD MD Lars Lönn.
This dissertation consists of a recapitulation of the research work carried out from September 2008 to November 2011 at the section of Biomedical Engineering, Department of Electrical Engineering, Technical University of Denmark. This work includes two journal papers and three conference contributions, as well as three co-authored publications.

The preparation for this PhD dissertation has been achieved in three years of research. The work has provided me with the opportunity to explore the field of cardiovascular biomechanics. The work has challenged my engineering skills, and taken my skills within mathematical modeling and medical imaging to a whole new level. I have had the opportunity to work with Professor Jay D. Humphrey for six months which gave me an extra dimension in my research work.

During my work I have had the possibility to travel both in Europe and USA in order to present my work at various conferences. These provided me with an invaluable professional network, many fruitful discussions about my work, and not least many new friends. I have enjoyed working with engineers and physicians who continuously provide me with increased understanding and new challenges with cardiovascular engineering. Furthermore, I have had the opportunity to teach students in fundamental biomechanics, physiological transport phenomina, and tissue biomechanics through my time as a PhD student. It has been a pleasure to share my knowledge within cardiovascular biomechanics and to work with professors, colleagues, and students at the Section of Biomedical Engineering.

Marie Sand Enevoldsen
Lyngby, November 2011

ACKNOWLEDGEMENTS

First of all I would like to thank my supervisors, Lars Lönn from the Department of Radiology at Rigshospitalet, Jørgen Arendt Jensen and Kaj-Åge Henneberg from the Technical University of Denmark for giving me the opportunity to develop both my understanding for clinical challenges in the management of AAAs as well as extend my skills within biomechanics and image processing to the high scientific level expected. You have all shown great enthusiasm in driving my research forward. A special thanks goes to Kaj-Åge Henneberg for thinking of me as the best suited candidate for this research project. You have been a source of inspiration and my primary mentor for the past three years.

Professor Jay D. Humphrey, now at Yale University, deserves much gratitude. Thank you for letting me come to Texas A& M University and being part of your research group. It has been an honor working with you. I genuinely hope that we can maintain our collaboration for many years to come. In this regard, I must also express my deepest gratitude to my fellow PhD students during my stay in College Station; Heather Hayenga, John Wilson, and Jacopo Ferruzzi. You all gave me a once in a life time experience, and I hope we will continue our friendship for many years.

The staff at the Department of Radiology at Rigshspitalet deserves a thankful mentioning for welcoming me at the department and involving me in the clinical challenges related to AAA. I have to thank Professor Carsten Thomsen for showing interest in my project and teaching me how to maneuver the MRI scanner.

Furthermore, I have thank all my current and former colleagues. Especially, Mads Møller Pedersen and Martin Christian Hemmsen deserves much appreciation in making the combination of medical imaging and biomechanics possible. Also my fellow ”Medtekkere” deserves much gratitude for numerous discussions, inputs, and good spirit; Michael Johannes Pihl, Joachim Hee Rasmussen, Isa Conradsen, and of course my office mate throughout three years Sara Matteoli. In addtion, Elna Sørensen and Henrik Laursen for their always kind help.

Last, but definitely not least, I would like to thank my best friend and life partner Andreas Traberg for always being there for me when I needed it the most.

Thanks to you all!

ABSTRACT

This research study presents computational simulation models for analysis of parameters which are in evidence of development and clinical management of abdominal aortic aneurysms (AAA). The research covers three main areas: interpretation of material parameters, implementation of the constitutive relations for computational analysis, and evaluation of the material model predictability. The constitutive framework applied is the four fiber family (4FF) model. This model assumes that the wall is a constrained mixture of an amorphous isotropic elastin dominated matrix reinforced by collagen fibers. The collagen fibers are grouped in four directions of orientation. The purpose of the first study was to investigate whether significant risk factors related to AAA development can be identified from a specific pattern in the material parameters of the 4FF model. Smoking is a leading self-inflicted risk factor for cardiovascular diseases in general, and AAA in particular. Results suggests that arterial stiffening caused by smoking is reflected by consistent increase in an elastin-associated material parameter, and moreover by marked increase in the collagen-associated material parameters. The arterial stiffening appears to be isotropic, which may allow simpler phenomenological models to capture these effects. There is a pressing need, however, for more detailed histological information coupled with more complete experimental data for the systemic arteries. The second study was aimed at developing computational simulation models incorporating subject-specific geometry of the abdominal aorta (AA) as well as subject-specific blood flow conditions. The geometry was acquired from magnetic resonance imaging, and the blood flow characteristics were acquired from ultrasound. The solid AA wall was modeled as a thick-walled cylinder allowing for inspection of the stress distributions inside the wall. The 4FF model characterizes the mechanical behavior. The blood is assumed to be an incompressible Newtonian fluid. The fluid and solid models were implemented in a commercially available finite element software. The goal of third study was to evaluate the predictability of the 4FF model. This was achieved by combining subject-specific blood flow and age-matched material parameters of the 4FF model in a fluid-structure interaction (FSI) model. The predicted wall dynamics were compared to *in vivo* wall dynamics obtained with ultrasound. Simulation results indicate that the 4FF model overestimates the displacement of the AA wall in a realistic simulation setup. This is believed to be the first study to evaluate the predictability of the 4FF model using a FSI model environment.

NOMENCLATURE

$\bar{\bar{\mathrm{F}}}$	Deformation gradient tensor
$\bar{\bar{\mathrm{C}}}$	Right Cauchy-Green tensor
$\bar{\bar{\sigma}}$	Cauchy stress tensor
$\bar{\bar{\mathrm{P}}}$	First Piola-Kirchhoff stress tensor
$\bar{\bar{\mathrm{S}}}$	Second Piola-Kirchhoff stress tensor
J	Determinant of $\bar{\bar{\mathrm{F}}}$
ρ_0, ρ	Mass density in the reference and deformed configuration respectively
ψ	Strain-energy function
c, $c_1^{(k)}$, $c_2^{(k)}$	Material parameters for the 4FF model
I_1, $I_4^{(k)}$	Invariants of the Cauchy-Green tensor

ABBREVIATIONS

2FF	Two fiber family
4FF	Four fiber family
AA	Abdominal aorta
AAA	Abdominal aortic aneurysm
CT	Computed tomography
ED	End diastole
FSI	Fluid-structure interaction
ILT	Intraluminal thrombus
MRI	Magnetic resonance imaging
PS	Peak systole
RBCs	Red blood cells
vSMCs	Vascular smooth muscle cells

CONTENTS

CHAPTER

ONE

INTRODUCTION

The overall purpose of this research study has been to develop new finite element (FE) based simulation models for analysis of parameters which are in evidence of development and clinical management of abdominal aortic aneurysms (AAA). This PhD project covers three main areas: interpretation of material parameters in the 4FF model, development of FE models for analysis of mechanical behavior and blood flow patterns in the AA, and, finally, evaluation of the 4FF model predictability in a realistic computational simulation setup. In order to develop new FE models for AAA it is necessary to obtain an in depth knowledge about the mechanobiology of the normal healthy abdominal aorta (AA) as well as the AAA, and use this knowledge in development of constitutive frameworks applied for prediction of AAA rupture risk. The mortality in case of AAA rupture in more than 85% [116]. If the AAA is identified prior to rupture, the time of intervention is based on empirical data such as diameter and growth rate of the AAA. However, research within the mechanical behavior of AAA indicate that physical principles such as the ratio of wall stress to wall strength provides a better indication of the rupture risk [115]. But the use of these principles remains to be implemented in the clinical settings.

General FE methods for solution of nonlinear elastic problems has long been available, and the evolution of the constitutive framework for the AA as well as the AAA is well described in the literature. Several studies on the wall stress distribution are based on the isotropic hyperelastic material model proposed by Raghavan and Vorp [85]. Recently, however, structurally motivated phenomenological material models have been presented [3, 42] which consider the wall tissue as a composite material composed of an amorphous isotropic elastin-dominated matrix reinforced by collagen fibers.

A major part of this PhD project has been concerned with implementation of the four fiber family (4FF) model proposed by Baek et al. [3] and fitted to experimental data obtained from AA tissue samples from a broad population as well as AAA patients [110, 111] by Ferruzzi et al. [28]. The 4FF model has been implemented in the commercially available FE software COMSOL Multiphysics (COMSOL AB, Stockholm, Sweden) and the predictability of the model was evaluated using human *in vivo* data. An overview of the FE model development in this research project is shown in Fig. 1.1.

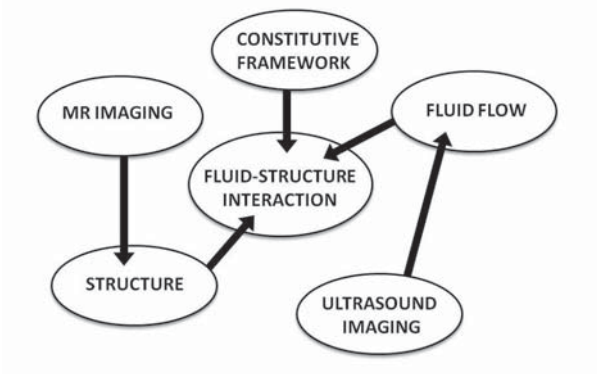

Figure 1.1: Overview of the approach to the FE model development in this research project. Magnetic resonance (MR) imaging provide the realistic anatomy, i.e. structure, of the abdominal aorta. Ultrasound imaging of the flowing blood and tracking of the wall dynamics are applied both as input to the fluid domain in the fluid-structure interaction model, and as validation of the applied material model in the structural domain.

This thesis is structured in three parts to illustrate the progress of the research performed. The first part sets the scene with respect to the anatomical, the pathophysiological, the clinical, and the engineering challenges related to the development of a simulation scheme for patient-specific models. The second part of the thesis describes the theoretical foundation of the simulation models developed in this work. The third part summarize the results and conclusions from the publications produced during this research project. The accepted and submitted publications can be found in the appendix.

Chapter 2 presents an overview of the structure and function of the human AA, as well as a description of the incidence, pathogenesis, and treatment of AAA. Much of this knowledge and understanding of the challenges originates from the close collaboration with Lars Lönn at the Departments of Radiology and Vascular Surgery at Rigshospitalet.

Chapter 3 and **Chapter 4** provides the theoretical framework for the mathematical models applied in COMSOL Multiphysics. The solid model relies on the theory of continuum biomechanics. This theory has been studied in the course ”Vascular Mechanics” at Texas A&M University with Jay D. Humphrey as supervisor, as well as by literature studies in collaboration with Kaj-Åge Henneberg.

Chapter 5 presents the methods for the acquisition and the processing of the medical imaging data collected for development of subject-specific models. The data acquisition was carried out at the Center for Fast Ultrasound Imaging and at the Department of Radiology at Rigshospitalet. The data acquisition was performed in collaboration with Mads Møller Pedersen, Martin Christian Hemmsen, and Carsten Thomsen.

Chapter 6 presents the results of Paper I which has the purpose of investigating whether significant risk factors related to AAA development can be identified from specific patterns in the material parameters of the 4FF model. The paper focus on the relation between AAA

development and smoking. This study was performed in collaboration with Jay D. Humphrey and Jacopo Ferruzzi at Texas A&M University.

Chapter 7 contains a description of the model implementation process which resulted in Paper IV and Paper VI, as well as contributions to Paper III and Paper V. Paper IV presents implementation of subject-specific fluid flow models based on anatomically correct geometries and subject-specific flow boundary conditions. This work was performed in collaboration with Mads Møller Pedersen and Martin Christian Hemmsen. Paper VI presents the implementation of the 4FF model in three dimensions in the FE software.

Chapter 8 summarize the framework for establishment of a fluid-structure interaction (FSI) model for evaluation of the predictability of the 4FF model within a group of healthy volunteers by combining subject-specific blood flow and age-matched material parameters in the 4FF model. This work is presented in Paper II.

Contributions

The contribution to the field of vascular biomechanics developed during my PhD project covers one published journal article, one submitted journal article, one published conference paper, one published conference abstract, and one accepted extended conference abstract, as well as one co-authored journal paper accepted for publication, one co-authored extended conference abstract, and one co-authored conference paper. These are listed as follows:

Journal Papers

- M.S. Enevoldsen, K.-A. Henneberg, J.A. Jensen, L. Lönn, and J.D. Humphrey, "*New Interpretation of Arterial Stiffening due to Cigarette Smoking Using a Structurally Motivated Constitutive Model*", Journal of Biomechanics, 44:1209–1211, 2011
- M.S. Enevoldsen, M.M. Pedersen, M.C. Hemmsen, L. Lönn, J.A. Jensen, and K.-A. Henneberg, *Comparison of In Vivo and Simulated Abdominal Aortic Deformation*, submitted to Journal of Biomechanics, October 2011

Conference Paper and Abstracts

- M.S. Enevoldsen, M.M. Pedersen, M.C. Hemmsen, L. Lönn, K.-A. Henneberg, and J.A. Jensen, *Age and Gender Related Differences in Aortic Blood Flow*, accepted for presentation at *SPIE Medical Imaging*, 2012, San Diego, CA, USA
- M.S. Enevoldsen, K.-A. Henneberg, L. Lönn, and J.A. Jensen, *Finite Element Implementation of a Structurally Motivated Constitutive Relation for Abdominal Aortas and Aneurysms*, presented at *Nordic-Baltic Conference on Biomedical Engineering and Physics*, 2011, Aalborg, Denmark

- M.S. Enevoldsen, J.D. Humphrey, L. Lönn, J.A. Jensen, and K.-A. Henneberg, *Effect of Cigarette Smoking on Arterial Stiffness Re-Interpreted Using a Structurally-Based Model*, presented at *Biomedical Engineering Society 2010 Annual Meeting*, Austin, TX, USA

Co-authored Paper and Abstracts

- M.C. Hemmsen, S.I. Nikolov, M.M. Pedersen, M.J. Pihl, M.S. Enevoldsen, J.M. Hansen, J.A. Jensen, *Implementation of a Versatile Research Interface Data Acquisition System Using a Commercially Available Medical Ultrasound Scanner*, accepted for publication in *IEEE Transactions on Ultrasonics, Ferroelectrics and Frequency Control: Special issue on Novel Embedded Systems for Ultrasonic Imaging and Signal Processing*, 2011
- J. Ferruzzi, M.S. Enevoldsen, J.D. Humphrey, *On the Machanical Behavior of Healthy and Aneurysmal Aorta*, presented at *ASME Summer Bioengineering Conference 2011*, Farmington, PA, USA
- J. Rasmussen, J. Thyregod, M.S. Enevoldsen, and K.-A. Henneberg, *Using COMSOL Multiphysics for Biomechanical Analysis of Stent Technology in Cerebral Aneurysms*, presented at *COMSOL Conference 2009*, Milan, Italy

CHAPTER

TWO

STRUCTURE AND FUNCTION OF THE ABDOMINAL AORTA AND ANEURYSMS

Objective *The aorta serves two purposes; conduit pipe distributing oxygenated blood to the entire body, and elastic pressure reservoir ensuring continuous blood supply to the organs. Normal aortic function relies on the elasticity and strength of the vascular wall. The abdominal aorta consists of three distinct layers; the intima, the media, and the adventitia with the media and the adventitia being the load-bearing structures. Aneurysms can develop in all parts of the aorta, but nearly 90% are found in the abdominal region below the renal arteries. An abdominal aortic aneurysms (AAA) is a focal chronical (localized) degenerative dilatation of the aorta. Slow progressive weakening of the wall cause enlargement of the aorta and eventually rupture if left untreated. The degradation of elastic fibers and improper collagen turnover, damage, and crosslinking are structural hallmarks of the developing and ruptured AAA. Rupture represents an immediate emergency with high mortality. Treatment of a ruptured AAA is associated with high perioperative mortality and morbidity. If the AAA is detected at an early stage a rupture-preventive elective operation can be conducted if the risk of rupture surpasses the risk of surgery. Clinical assessment of rupture risk is still based on empirical data, such as size and growth rate, instead of physical principles such as the wall stress to wall strength ratio. The challenge is to determine wall stress and strength accurately. Prediction of aortic and aneurysmal wall stress and strength is a combination of experimental testing, empirical data, and mathematical modeling.*

2.1 Abdominal aorta structure

Arteries can be classified into elastic arteries and muscular arteries. The elastic arteries are large proximal vessels including the aorta, the iliac, and the common carotid arteries. The muscular arteries are smaller distal vessels including the coronary, femoral, and cerebral arteries [45]. The aorta is the largest blood vessel in the human body and serves both as a

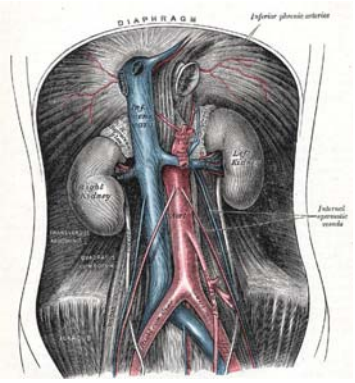

Figure 2.1: The anatomy of the human aorta, adapted from Gray [34].

conduit vessel distributing oxygenated blood from the left ventricle of the heart to the entire arterial system, and as an elastic pressure reservoir for the ejected blood volume ensuring prolonged driving force between heart contractions, see Fig. 2.1. The aorta is divided into two segments; the thoracic aorta (TA) and the abdominal aorta (AA) separated by the diaphragm. The length and diameter of the AA depend on age, gender, and body surface area. The diameter of the aorta decreases gradually from the aortic arch to the aortic bifurcation in the pelvis [92].

The AA consists of three layers; the intima, the media, and the adventitia, see Fig. 2.2. The elastic arteries are characterized by a thick media (90% of the wall thickness) as opposed to the muscular arteries in which the media comprises 50% of the total wall thickness. The aortic wall is capable of remodeling in response to hemodynamic, mechanical, and various biochemical stimuli [46, 104].

Intima The intima consists of a linning of endothelial cells supported by the internal elastic membrane, while the medial and adventitial layers are thicker, hence considered important from a structurally perspective since they are the load-bearing part. The intima plays a significant role in vascular mechanics and pathology. The endothelium possesses several important functions such as maintenance of vascular tone (i.e. release of nitric oxide), formation of growth regulatory molecules, and maintenance of connective tissue matrix [106]. Damage to the endothelial cells initiates a chain of pathological processes with atherosclerosis and aneurysm formation as final outcomes.

Media The media provides the artery with elasticity and strength. The primary structural constituents of the media are elastic fibers, collagen fibers, and vascular smooth muscle cells (vSMCs). These constituents are organized in a specific pattern with the vSMCs oriented circumferentially in concentric layers surrounded by collagen fibers and separated by sheets of an amorphous matrix dominated by elastic fibers (elastic lamina), see Fig. 2.2. A unit of

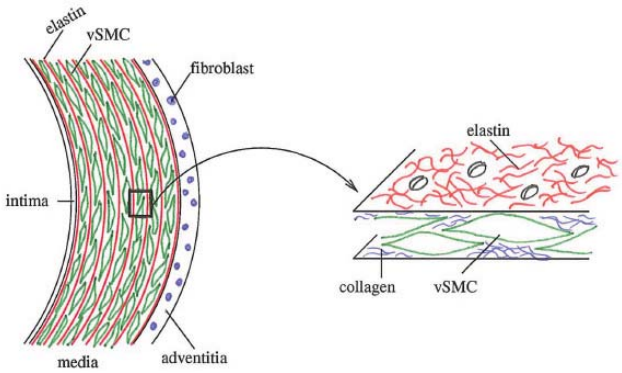

Figure 2.2: Structure of a healthy elastic artery. The intima consists of a layer of endothelial cells supported by a basal membrane. The media consists primarily of vascular smooth muscle cells (green spindle shapes) sandwiched between concentric elastic sheets (red solid lines) and collagen fibers (blue lines). The adventitia is mostly composed of collagen fibers (not shown) and fibroblasts (blue circles).

two adjacent elastic laminae is called a musculo-elastic fascicle (MEF) [10] and can be considered as a discrete structural and functional unit. In the human AA there are approximately 28-30 of these units [49].

Adventitia The adventitia provides the AA with strength to prevent over-dilatation during an abrupt increase in physiological loads. The adventitia consists of a dense network of collagen fibers mixed with nerves, few elastic fibers, fibroblasts, and the vasa vasorum (blood supply to the aortic tissue). The collagen in this region tends to be oriented axially and slightly undulated.

In this work, focus is on the passive response of the AA and AAA, hence two structural components are of particular interest when formulating the constitutive relation between stress and strain (see Sec. 3.2); the elastic fibers and the collagen fibers.

Elastic fibers Elastic fibers consists of 90% elastin, a protein, and 10% elastin associated micro-fibrils which are glucoproteins. Often elastic fibers are referred to as elastin, hence elastin will be used throughout this text. The most important property of elastin is that it is highly elastic over extreme extensions providing the AA with extensibility, elastic recoil, and resilience [109]. Elastin is primarily produced during the perinatal period and has a long half-life in humans ($\geq$ 40 years). Elastin is thought to be the origin of the residual stress and axial pre-stress in the arteries, which are important for maintenance of arterial homeostasis. Finally, elastin provides important biological cues to the vSMCs which ensure that these cells sustain a mature phenotype.

Collagen fibers The dominating collagen types in the AA are type I and III, both of which are fibrillar collagens. They consist of a triple helix with peptide end-groups. The end-groups have to be cleaved for the molecule to become active and form collagen fibrils. The fibrils are combined to form the collagen fibers. The half-life of collagen is around 70 days in humans and there is a constant turnover of fibrillar collagen throughout life [45]. Collagen is distributed throughout all three AA wall layers, less in the intima and most in the adventitia. Collagen is responsible for the overall strength of the AA due to its high stiffness and low extension which protects the vSMCs from damage during periods of overloading [21, 109].

2.2 Mechanical behavior of the abdominal aorta

Knowledge of the relationship between structure of the AA and the mechanical behavior is essential in the search of a mathematical description for prediction of biomechanical properties. This relationship is deduced mainly from experiments mimicking the mechanical behavior *in vivo*. The basis for identification of the characteristic behavior originates primarily from the *in vitro* tests conducted by R.H. Cox [11, 12] and P.B. Dobrin [20, 21] on canines, rabbits, and rats. From these studies the non-linear mechanical behavior of arteries is demonstrated. Elastin dominates the response at lower pressure levels, and collagen gradually starts contributing as the loading increases due to gradual stretching of the undulated collagen fibers [56].

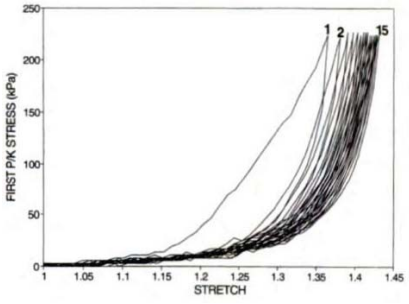

Figure 2.3: Pre-conditioning of the arterial tissue before performing the mechanical test. Reproduced from [45] with kind permission of Springer Science+Business Media.

Purely elastic behavior is characterized by coinciding stress-strain curves in loading and unloading, i.e. there is no energy dissipation (hysteresis) in the tissue during the deformation cycle. Arteries *in vitro* under cyclic loading show repeatable response after approximately ten deformation cycles, see Fig. 2.3. Hence, arterial tissue is considered to be pseudo-elastic [33] due to the hysteresis in the initial deformation cycles.
The relationship between circumferential loading and stretch is nonlinear, and has shown to depend on the present level of axial stretch, see Fig. 2.4a. The relationship between axial load and stretch is nonlinear but independent of the present level of circumferential stretch as

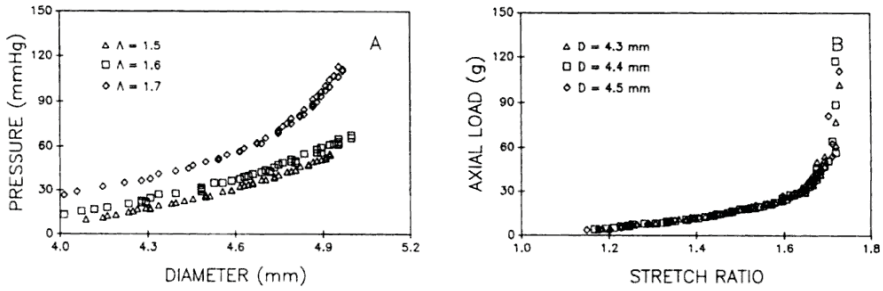

Figure 2.4: The left figure shows the pressure-diameter relation at different axial stretch ratios (Λ) illustrating the circumferential stiffening introduced by increased axial stretch above the *in vivo* level. The right figure shows the stretch ratio as a function of axial loading at different constant diameters illustrating that the axial force needed to obtain a certain axial stretch depend little on the diameter of the artery. Reproduced from [45] with kind permission of Springer Science+Business Media.

illustrated in Fig. 2.4b. Overall, these experimental observations indicate a complex coupling between the axial and circumferential stress-strain responses. Thus, the mechanical properties of elasticity and strength are best considered as anisotropic, i.e. directional dependent properties.

2.2.1 Evaluation of mechanical behavior

Evaluation of the mechanical response of arteries and can be done either *in vivo* or *in vitro*. *In vivo* evaluation is challenging because stress and strain in the undeformed, but not stress-free, configuration of the AA *in vivo* cannot be measured. However, it is possible to quantify the dynamics of the arterial wall using ultrasound or magnetic resonance imaging [2, 70]. *In vitro* tests present several techniques to evaluate the mechanical response under well-controlled conditions. Sumner et al. [103] were among the first to determine a correlation between the stiffness of a tissue sample and its content of elastin and collagen. There are four common *in vitro* tests; the ring test, the uniaxial test, the biaxial test, and the inflation-extension test [45]. The material parameters used for simulation in this work originates from biaxial tests, as described in the following. For further reading on the experimental testing methods the reader is referred to the book by Humphrey [45].

He and Roach [38] performed uniaxial tests on aneurysmal tissue as well as non-aneurysmal controls. They found that the aneurysmal tissue was stiffer compared to the controls. This study is very important since it was one of the first methods to demonstrate direct measurement of mechanical properties. Raghavan et al. [86] extended the uniaxial testing to include samples cut along the axial direction as well as the circumferential direction comparing the mechanical behavior in the two directions. They found no significant difference in the mechanical response of axial and circumferential cut tissue samples, and concluded that aneurysmal tissue is isotropic with respect to certain mechanical properties such as yield

stress, ultimate strength and stiffness. An important drawback in using uniaxial tests is that the aortic tissue *in vivo* is loaded in multiple directions and considered anisotropic. These properties are not captured by the uniaxial test.

The biaxial test has been developed and used extensively to determine mechanical behavior due to its capability to capture anisotropy. Vande Geest et al. [110, 111] provide population-wide mechanical behavior of human AA and AAA tissue using the well-validated biaxial tensile testing system introduced by Sacks [91]. Both tissue types were shown to express anisotropic behavior. The most significant drawback of biaxial testing is that tissue samples are stretched in the plane the experiment therefore does not account for the natural curvature of the artery or the third (radial) direction of stress.

Factors affecting the mechanical response Factors influencing the mechanical response are divided in two groups, inevitable factors such as gender, aging and genetics, and environmental factors like smoking, hypertension, and increased serum cholesterol levels.
In general cardiovascular disease is more common in men than women, regarding AAA, the ratio is 4:1 in favor of male patients [94]. Aging has a significant impact on the mechanical behavior of the AA by increasing the stiffness of the tissue. The stiffness of the arterial tissue can be deduced from the relationship between stress and stretch ratio as the tangent of the curves seen in Fig. 2.5. The tissue stiffens when the slope of the tangent becomes steeper. Furthermore, from Fig. 2.5 it is seen that the age dependent stiffness increase in both the circumferential and axial direction. The increased stiffness and, hence, a decreased distensibility render the AA more vulnerable to damage. These macroscopic observations are manifested structurally in the AA media, where an increased elastin fragmentation and an increased collagen deposition found in tissue samples from elderly individuals has been observed [35, 82]. Smoking is known to increase the wall stiffness, i.e. the natural aging process is increased, but the precise mechanisms and influence on AAA development remain unknown [25].

2.3 Abdominal aortic aneurysms

An aneurysm is a focal dilatation of an artery. The term aneurysm originates from Greek ”aneurysma” meaning a widening. In the aorta, aneurysms occur most often in the abdomen [56, 77], see Fig. 2.6. An aneurysm is defined as a ”permanent localized dilatation of an artery having at least a 50% increase in diameter compared with the expected normal diameter of the artery in question” by the Ad Hoc Committee on Reporting Standards [51]. An AAA encompasses all three layers of the vessel wall but originates in the media. Aneurysms enlarge and rupture if they are left untreated. But not at a constant rate and not all of them rupture.

Incidence AAA is often diagnosed after rupture resulting in a high mortality of up to 85% [116]. Studies on rupture incidence are either retrospective or prospective studies on small aneurysms. The best way to avoid death as a result of a ruptured AAA is a timely intervention

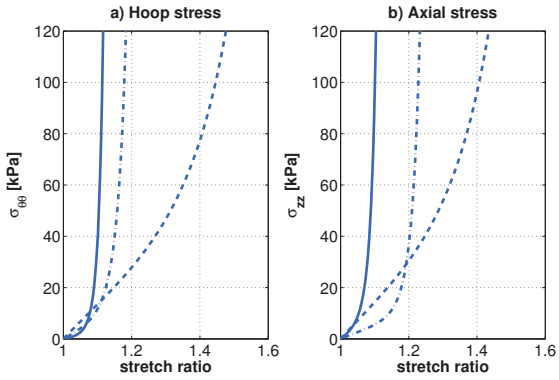

Figure 2.5: Stress-stretch plot comparing different age groups and AAA patients. (a) shows the circumferential Cauchy stress ($\sigma_{\theta\theta}$) as a function of circumferential (hoop) stretch ratio. (b) shows the axial Cauchy stress (σ_{zz}) as a function of axial stretch ratio. The solid lines are subjects above 60 years, the dash-dot lines are subjects between 30 and 60 years, and the dashed lines are subjects below 30 years.

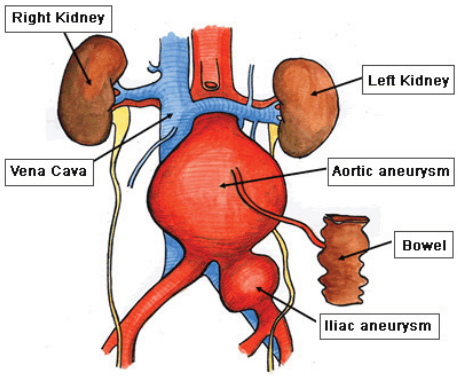

Figure 2.6: Example of an abdominal aortic aneurysm, `http://www.thevascularsurgeon.com/abdominal.htm`

in an asymptomatic period. But, most AAAs are undiagnosed and a majority of patients with a rupture die before they reach the emergency room. Screening might help identify patients with aneurysms, and then offer preventive interventions in due time [97]. Hence, it is of therapeutic value to obtain a better assessment of rupture risk.

The morphology of established AAAs is very well described, but little is known about the initiating etiological factors. Reed et al. [87] performed a large epidemiological study on AAAs among more than 8000 men with a 20-year follow-up, and found that AAA increase constantly with age in men above 60 years of age. Also a positive correlation to risk factors such as increased systolic blood pressure, serum cholesterol, cigarette smoking and height was reported. The prevalence of AAA is around 3% in the population above 50 years, and the

incidence increases with aging [1]. Despite the relatively high prevalence and a vast amount of literature and clinical experience, the pathogenesis of AAA is still not well understood.

Pathogenesis The initiation of AAA is still debated, but two structural hallmarks are common; elastin degradation in the media, and incomplete and unbalanced collagen fiber turnover, damage, and crosslinking. The degradation of elastin is a key factor for AAA development, and collagen fracture is a key factor in AAA rupture. He and Roach [38] found that the fractions (by dry weight) of elastin, collagen and vSMC in the AA are 22.7($\pm$ 5.7)%, 54.8($\pm$ 4.5)%, and 22.6($\pm$ 5.5)% respectively. Contrary, in AAA tissue the fractions are 2.4($\pm$ 2.2)%, 95.6($\pm$ 2.5)%, and 2.2($\pm$ 2.0)%.
The morphology of the developed AAA is well defined. The aneurysmal wall is very thin and fibrotic with minimal amounts of elastin and vSMCs which are poorly organized compared to the AA. Next to the wall a thin lining of atherosclerotic plaque material is often seen including calcifications. 75% of AAAs also contain an intraluminal thrombus (ILT) located between the atherosclerotic plaque lining and the lumen. This ILT is a complex structure with major inter-patient differences. Its role in the AAA pathogenesis remains controversial. Some clinicians consider damage to the ILT a hallmark for pending rupture since fissures in the ILT expose a small area of the weak wall to a high pressure load creating a critical peak stress point.
From the morphology, there seems to be a connection between atherosclerosis and AAA development, and two theories dominate. One theory is that rupture of a vulnerable atherosclerotic plaque leads to thrombus formation and neovascularization of the vasa vasorum [1]. The second theory is that early degradation and fragmentation of elastin due to inflammation lead to atherosclerosis and thrombus formation [92]. Even if risk factor association suggests that AAA is caused by atherosclerosis, the pathobiology of the diseases differ as well as the theories behind. Still, the initiating cause of AAA remains unknown.

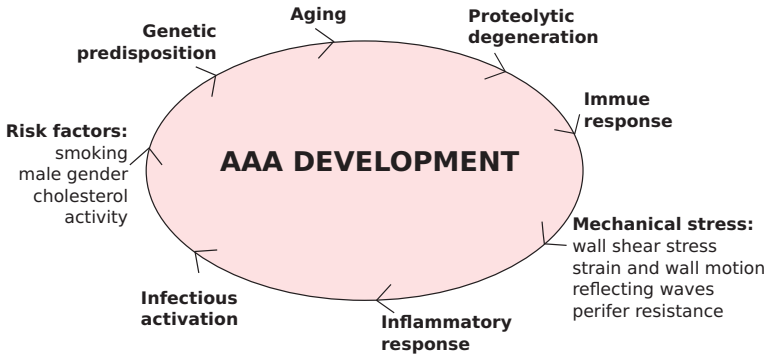

Figure 2.7: The contributors to development of AAA. Reproduced from Fig. 3 in the Doctoral Thesis of D. Flondell-Cité [30] with permission.

Contributing risk factors to the pathogenesis, besides advancing age, male gender, and atherosclerosis, include cigarette smoking, positive family history, inflammation, and hypertension, see Fig. 2.7. The largest environmental risk factor is smoking. Up to 80% of

AAA patients are smokers at the time of diagnosis indicating a relation between smoking and AAA development. Cigarette smoking contains more than 4,000 known components of which only a few has been studied in detail in relation to cardiovascular disease in general. Production of nitric oxide by the endothelium, which mediates vasodilatation in response to altered hemodynamics, is reduced in both active and passive smokers [5]. Thus, endothelial dysfunction caused by smoking can diminish the dilatory capacity of arteries, which yields a stiffer wall. In addition, smokers have shown to have a higher risk of rupture as well as expansion rate.
Research into genetic factors have demonstrated that 15-20% of AAA patients report a family history, and life time risk for siblings (i.e. first degree relatives) is three to seven times that of the general population [39]. Approximately 10% of AAAs are termed inflammatory AAAs due to a high level of immune response activity degrading the elastin of the AA media. Lastly, hypertension favors higher prevalence and rupture risk. This could be due to an increased pulse pressure in the AA due to wave reflection from the iliac bifurcation leading to a higher lateral pressure in the AA increasing with age.

2.4 Treatment of AAA

The treatment of AAAs is based on the balance between risk of rupture and risk of intervention. In the clinical setting the risk of rupture is primarily determined from empirical data such as diameter and growth rate, i.e. the larger the diameter the higher the risk of rupture [6], and AAAs expand slowly initially and increase in growth rate with increasing diameter. At Copenhagen University Hospital females are considered for intervention from +5.0 cm and males from +5.5 cm, if no collagen disease exist, or signs of rapid growth are absent. In the latter conditions one might intervene at an earlier stage.

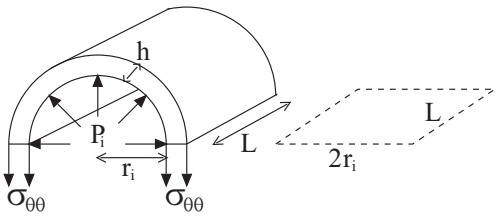

Figure 2.8: Free body diagram for a pressurized vessel. The luminal pressure is P_i, the vessel has a length L, and an inner radius of r_i with a wall thickness of h.

The size criteria is based on the Law of Laplace, which relates the inner radius, r_i, luminal pressure, P_i, and tensile wall stress, $\sigma_{\theta\theta}$, see Fig. 2.8. The Law of Laplace is deduced from equilibrium by considering the free body diagram of a pressurized vessel, where the hemodynamic force exerted by the pressure must equal the elastic force exerted by the tensile stress in the wall, i.e.

$$P_i\, 2r_i L - 2\sigma_{\theta\theta}\, hL = 0 \;\Leftrightarrow\; \sigma_{\theta\theta} = \frac{P_i r_i}{h}\ . \tag{2.1}$$

The hemodynamic force is found by projecting the pressure on the fictive plane cutting the cylinder in half, see Fig. 2.8. The elastic force in the wall is found by multiplying the tensile stress and the cross-sectional area of the wall. The stress increase is proportional with radius, hence, the larger the radius, the higher the stress, and the higher the risk of rupture [60]. The law of Laplace is derived independently of material properties, thus it is considered a universal solution. The key assumption in using (2.1) is that $\sigma_{\theta\theta}$ is uniform, not that the wall is thin. The pressure is assumed to be uniform, but the tensile stress does not necessarily increase linearly with the increase in pressure [48], hence the radius at a given loading pressure depends on the material properties of the wall, which is not captured by (2.1). Therefore (2.1) cannot capture the wall stress adequately as shown in several works [29, 112, 117]. In addition, the large population study by Darling et al. [14] has shown both that small AAAs (3-4 cm) rupture, and large AAAs (7-10 cm) remain stable without bursting. Thus, it is necessary to increase the knowledge of the mechanical behavior and stress/strength analysis techniques to provide the clinicians with an improved diagnostic tool.
The risk of rupture should be considered as a mechanical problem constituted, for example, by a risk of rupture index. Vorp et al. [115] suggested the risk of rupture index defined as the ratio of wall strength to wall stress. Kleinstreuer and Li [55], on the other hand, suggested rupture potential determined from a severity parameter including eight biomechanical factors with associated weighting. The factors include neck-to-maximum AAA diameter ratio, expansion rate, stress ratio, and asymmetry index. But none of these are yet part of the clinical management of AAA patients.

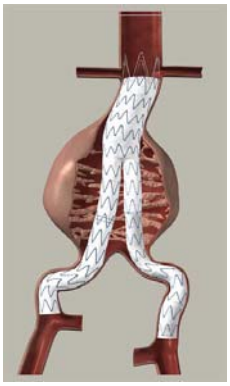

Figure 2.9: Illustration of the principle of the stent-graft positioned inside the AAA. Image taken from the Endurant Stent Graft System Deployment OR Poster.

Open surgery In open surgery the AAA is accessed through an incision in the abdomen of the patient. Upon exposure of the aorta the surgeon cuts the aorta close to the aneurysm and insert a synthetic tube graft made from a polymer material after the thrombus material has

been removed, see Fig. 2.9. The artificial aorta forms a new blood vessel inside the aneurysm sac. After surgery the patient typically remains hospitalized four to seven days.

Endovascular aortic aneurysm repair EVAR was developed in the late 1980s by Volodos [113, 114] and Parodi [83] independently. In the EVAR procedure the AAA is accessed by introducing the artificial aorta through one of the femoral arteries of the patient via a long catheter. Using x-ray flouroscopy the operating physician guides the enclosed stent-graft to the correct position inside the AAA. Typically, the endovascular module system consists of three parts, the main body and two extensions, one for each iliac artery. Extensions are delivered in a similar mode from the ipsi-lateral and the contra-lateral side, respectively. Two part modules does also exist, then the main body and ipsi-lateral leg is made in one-piece merged together.

Once positioned, the sleeve containing the constricted stent-graft is withdrawn and the stent-graft resume the natural configuration either by ballooning or due to a self-expandable construction material. The stent-graft then carries the hemodynamic load and prevents rupture. Patients undergoing EVAR remain hospitalized for approximately two to three days.

CHAPTER

THREE

MODELING OF THE AORTIC AND ANEURYSMAL WALL

Objective *In order to analyze the mechanical behavior of the aortic wall a theoretical base is needed. Nonlinear continuum mechanics describes physical phenomena such as the deformation and the motion of a soft biological tissue. Application of continuum mechanics requires consideration of three main concepts; kinematics (description of motion), the concept of stress, and balance of forces and moments. The mechanical behavior is analyzed using the relationship between stress and strain, which is described by nonlinear constitutive theory, i.e. finite elasticity. Finite elasticity applies to aortic tissue as it is considered a hyper-elastic material, and provides the relation between stress and strain given a suitable form of the strain energy function. The strain energy function can be interpreted as the elastic energy which is stored in the tissue during deformation. Many different formulations of the strain energy function exists. The model types range from isotropic models such as the Ogden model and the Fung model, to anisotropic models such as the two and four fiber family models. In this work the structurally motivated four fiber family model is applied to describe the mechanical behavior of aortic and aneurysmal tissue.*

3.1 Continuum biomechanics

The AA wall as well as the AAA wall are assemblies of many different structural components. However, when studying the mechanical behavior it is inconvenient to describe each structural component individually. Instead it is considered as one continuum. The continuum hypothesis is valid when the characteristic length of the microstructure, δ, is much smaller than the characteristic length of the problem of interest, l, i.e. $\frac{\delta}{l} \ll 1$. For the AA wall, the characteristic length of the structural components (elastin, collagen, vSMCs) is 10^{-6}m, while the characteristic length of the problem of interest (the wall thickness) is 10^{-3}m, hence $\frac{\delta}{l} \ll 1$.

In general, application of continuum mechanics requires consideration of three main concepts; kinematics, stress, and balance principles. These concepts are described in the follow-

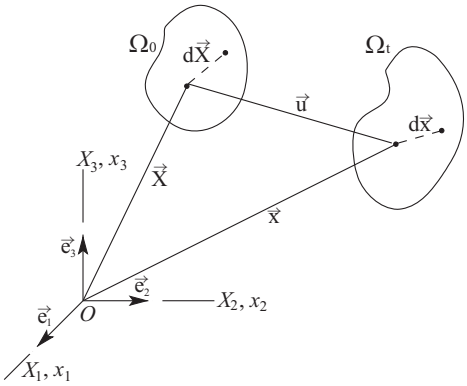

Figure 3.1: The motion despription is based on the reference approach where displacement of a material point is defined as the vector $\vec{u}$. The material point is described by the position vector $\vec{X}$ in the reference configuration (Ω_0) and $\vec{x}$ in the current configuration (Ω_t).

ing. The description is based on the text books by Holzapfel [41] and Humphrey [45].

3.1.1 Kinematics

When quantifying motion, there are two preferred descriptions; the referential description (alternatively material or Lagrangian description) and the spatial description (alternatively Eulerian description). In solid mechanics both approaches are used, but the constitutive relationship quantifying the motion is often defined with respect to the referential coordinate system. Thus, throughout this work, motion is quantified with respect to the referential configuration. Motion of a particle is found by tracking the particle from the reference configuration to a deformed configuration, see Fig. 3.1,

$$\vec{u}\left(\vec{X},t\right) = \vec{x}\left(\vec{X},t\right) - \vec{X} \tag{3.1}$$

where $\vec{u}$ is the displacement field relating the particle position $\vec{X} = X_a\vec{e}_a$ in the reference configuration Ω_0 to the particle position $\vec{x} = x_a\vec{e}_a$ in a deformed configuration Ω_t assuming that the reference frame, i.e. coordinate system, of the deformed and the reference configurations coincide. Capital letters are assigned to the reference configuration, and lower case letters are assigned to the deformed configuration. This applies to both scalars, vectors, and tensors. Furthermore, the summation convention is enforced for repeated indices, i.e.,

$$\vec{x} = \sum_{a=1}^{3} x_a\vec{e}_a = x_a\vec{e}_a \quad . \tag{3.2}$$

Deformation is caused by loads giving rise to tractions, which is a force acting on the surface of the object. Traction can be quantified by tracking the changes in direction and magnitude during deformation of a vector connecting two points on the body surface, see Fig. 3.1. A measure of the motion from the reference configuration to a current configuration can be established by defining the changes in traction. Since $\vec{x}$ is a function of $\vec{X}$ at every fixed time, the chain rule applies,

$$\mathrm{d}\vec{x} = \frac{\partial \vec{x}}{\partial \vec{X}}\,\mathrm{d}\vec{X}\ ,\ \mathrm{d}x_i = \frac{\partial x_i}{\partial X_A}\,\mathrm{d}X_A\ . \tag{3.3}$$

Mapping a traction vector from the reference configuration to a current configuration requires a linear transformation which must be a 2[nd] order tensor. Thus, using (3.3) the *deformation gradient tensor* $\bar{\bar{\mathrm{F}}}$ can be written as,

$$\bar{\bar{\mathrm{F}}} = \frac{\partial \vec{x}}{\partial \vec{X}} = F_{iA}\,\vec{e}_i \otimes \vec{e}_A\ ,\ \text{where } F_{iA} = \frac{\partial x_i}{\partial X_A}\ , \tag{3.4}$$

where $\otimes$ is the outer product of two vectors resulting in a tensor (a dyad). The deformation gradient $\bar{\bar{\mathrm{F}}}$ is a fundamental measure of motion in nonlinear continuum biomechanics, since it provides information on both deformation and rigid body motions. However, $\bar{\bar{\mathrm{F}}}$ is inconvenient to handle mathematically as it is a two-point asymmetric tensor with nine components at each time. A more suitable deformation measures such as the *right Cauchy-Green tensor* $\bar{\bar{\mathrm{C}}}$, is derived from polar decomposition of $\bar{\bar{\mathrm{F}}}$. The polar decomposition theorem split the motion into a rigid rotation followed by a stretch or vise versa,

$$\bar{\bar{\mathrm{F}}} = \bar{\bar{\mathrm{R}}}\bar{\bar{\mathrm{U}}} = \bar{\bar{\mathrm{V}}}\bar{\bar{\mathrm{R}}} \quad , \tag{3.5}$$

where $\bar{\bar{\mathrm{R}}}$ is rigid body motion in form of a rotation which is a proper orthogonal tensor ($\bar{\bar{\mathrm{R}}}^{-1} = \bar{\bar{\mathrm{R}}}^{\mathrm{T}}$, $\det \bar{\bar{\mathrm{R}}} = 1$). While $\bar{\bar{\mathrm{U}}}$ is the right stretch tensor, and $\bar{\bar{\mathrm{V}}}$ is the left stretch tensor. The tensors $\bar{\bar{\mathrm{U}}}$ and $\bar{\bar{\mathrm{V}}}$ are both positive definite symmetric one-point tensors and complete the deformation. The tensor $\bar{\bar{\mathrm{C}}}$ is then derived from the right stretch tensor, i.e.

$$\bar{\bar{\mathrm{C}}} = \bar{\bar{\mathrm{F}}}^{\mathrm{T}}\bar{\bar{\mathrm{F}}} = \bar{\bar{\mathrm{U}}}^2 \quad , \tag{3.6}$$

where $\bar{\bar{\mathrm{C}}}$ is defined in the reference configuration Ω_0. To identify the principal directions and principal stretches consider the eigenvectors and eigenvalues of $\bar{\bar{\mathrm{U}}}$,

$$\bar{\bar{\mathrm{U}}}\hat{\vec{\mathrm{N}}}_a = \lambda_a \hat{\vec{\mathrm{N}}}_a \text{ where } |\hat{\vec{\mathrm{N}}}_a| = 1 \tag{3.7}$$

$$\Rightarrow \bar{\bar{\mathrm{C}}}\hat{\vec{\mathrm{N}}}_a = \bar{\bar{\mathrm{U}}}\bar{\bar{\mathrm{U}}}\hat{\vec{\mathrm{N}}}_a = \lambda_a^2 \hat{\vec{\mathrm{N}}}_a \quad , \tag{3.8}$$

using (3.6) it is seen that $\bar{\bar{\mathrm{U}}}$ and $\bar{\bar{\mathrm{C}}}$ share the same orthonormal vectors, $\hat{\vec{\mathrm{N}}}_a$, corresponding to the principal directions in the reference configuration, and λ_a are the principal stretches. The sum of diagonal elements of $\bar{\bar{\mathrm{C}}}$ are equal to the sum of the squared principal stretches, i.e., $\mathrm{tr}\,\bar{\bar{\mathrm{C}}} = \lambda_1^2 + \lambda_2^2 + \lambda_3^2$.

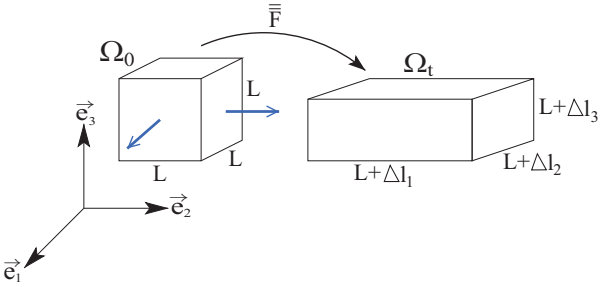

Figure 3.2: Homogeneous (uniform) deformation of a cube undergoing biaxial stretch without rotation. The applied stretch to the cube is indicated by the blue arrows.

As an example of calculation of the two stress tensors, $\bar{\bar{\mathrm{F}}}$ and $\bar{\bar{\mathrm{C}}}$, consider biaxial deformation without rotation of an incompressible cube with unit side length, see Fig. 3.2. Since no rigid body rotation occurs, $\bar{\bar{\mathrm{R}}} = \bar{\bar{\mathrm{I}}}$, the deformation is pure stretch, and $\bar{\bar{\mathrm{F}}} = \bar{\bar{\mathrm{U}}} = \bar{\bar{\mathrm{V}}}$. The biaxial stretch will also result in a thinning in the third direction due to incompressibility. Assuming that the deformation in the center of the cube is homogeneous, and shear stress is negligible,

$$\begin{aligned} x_1 &= (1+\Lambda_1)X_1 = \lambda_1 X_1 \,, \\ x_2 &= (1+\Lambda_2)X_2 = \lambda_2 X_2 \,, \\ x_3 &= (1+\Lambda_3)X_3 = \lambda_3 X_3 \,, \end{aligned}$$

where Λ_i is the stretch due to the applied deformation, i.e. $\Lambda_i = \frac{\triangle l_i}{L}$ with $L = 1$ and $\triangle l_i = \Lambda_i$, and λ_i is the stretch ratio. If two stretch ratios, λ_1 and λ_2, are chosen arbitrarily the third stretch ratio λ_3 can be determined since constant volume is ensured using incompressibility as kinematic constriction (see Sec. 3.1.3). From (3.4) the deformation gradient tensor takes the form,

$$\bar{\bar{\mathrm{F}}} = \begin{bmatrix} \frac{\partial x_1}{\partial X_1} & \frac{\partial x_1}{\partial X_2} & \frac{\partial x_1}{\partial X_3} \\ \frac{\partial x_2}{\partial X_1} & \frac{\partial x_2}{\partial X_2} & \frac{\partial x_2}{\partial X_3} \\ \frac{\partial x_3}{\partial X_1} & \frac{\partial x_3}{\partial X_2} & \frac{\partial x_3}{\partial X_3} \end{bmatrix} = \begin{bmatrix} \lambda_1 & 0 & 0 \\ 0 & \lambda_2 & 0 \\ 0 & 0 & \lambda_3 \end{bmatrix} .$$

Knowing the components of $\bar{\bar{\mathrm{F}}}$ makes it easy to compute the components of $\bar{\bar{\mathrm{C}}}$ using (3.6) where $C_{AB} = C_{BA}$,

$$\bar{\bar{\mathrm{C}}} = \bar{\bar{\mathrm{F}}}^{\mathrm{T}}\,\bar{\bar{\mathrm{F}}} = \begin{bmatrix} \lambda_1^2 & 0 & 0 \\ 0 & \lambda_2^2 & 0 \\ 0 & 0 & \lambda_3^2 \end{bmatrix} \quad .$$

3.1.2 Concept of stress

Stress is a measure of the force acting over an oriented area. To identify stress it is useful to consider surface tractions which are defined as a unique stress tensor acting on a normal unit vector to a surface plane, see Fig. 3.3. Cauchy's stress theorem claims that unique second-order tensor fields (stress tensors) exists such that

$$\vec{\mathrm{t}} = \frac{\mathrm{d}\vec{\mathrm{f}}}{\mathrm{d}a}\,, \quad \vec{\mathrm{t}} = \bar{\bar{\sigma}}\vec{\mathrm{n}}\,, \quad t_a = \sigma_{ab} n_b \quad , \tag{3.9}$$

$$\vec{\mathrm{T}} = \frac{\mathrm{d}\vec{\mathrm{f}}}{\mathrm{d}A}\,, \quad \vec{\mathrm{T}} = \bar{\bar{\mathrm{P}}}\vec{\mathrm{N}}\,, \quad T_A = P_{aA} N_A \quad , \tag{3.10}$$

where $\vec{\mathrm{t}}$ is the traction vector in Ω_t, $\bar{\bar{\sigma}}$ is the *Cauchy stress tensor*, and $\vec{\mathrm{n}}$ is the unit normal vector to the surface area $\mathrm{d}a$. The vector $\vec{\mathrm{t}}$ is often referred as the true traction vector, since it is defined by the force acting on surface areas in the current configuration. Cauchy stress is difficult to relate experimentally given that the configuration of the body after deformation is rarely known in advance.

In Ω_0 the traction vector is $\vec{\mathrm{T}}$, $\bar{\bar{\mathrm{P}}}$ is the *1st Piola-Kirchhoff stress tensor* acting on the normal unit vector $\vec{\mathrm{N}}$. The tensor $\bar{\bar{\mathrm{P}}}$ is, on the other hand, a convenient measure of stress in experiments because it relates forces measured in Ω_t to surface areas in Ω_0.

The tensor $\bar{\bar{\mathrm{P}}}$ is a two-point asymmetric tensor with nine independent components, thus, making it difficult to handle mathematically. A symmetric one-point tensor is more suitable as it is easier to handle computationally as well as experimentally. The *2nd Piola-Kirchhoff stress tensor* $\bar{\bar{\mathrm{S}}}$ is a symmetric one-point tensor defined in terms of Ω_0. However, $\bar{\bar{\mathrm{S}}}$ does not have a direct physical interpretation as it is defined from "fictive" forces $\mathrm{d}\vec{\underset{\sim}{\mathrm{f}}}$ in Ω_0. Here $\mathrm{d}\vec{\underset{\sim}{\mathrm{f}}}$ is determined by mapping $\mathrm{d}\vec{\mathrm{f}}$ in Ω_t back to Ω_0 using the inverse of $\bar{\bar{\mathrm{F}}}$, see Fig. 3.3,

$$\vec{\underset{\sim}{\mathrm{T}}} = \frac{\mathrm{d}\vec{\underset{\sim}{\mathrm{f}}}}{\mathrm{d}A}\,, \quad \vec{\underset{\sim}{\mathrm{T}}} = \vec{\mathrm{N}}\bar{\bar{\mathrm{S}}}\,, \quad \underset{\sim}{T}_A = N_B S_{BA}\,. \tag{3.11}$$

Where $\vec{\underset{\sim}{\mathrm{T}}}$ is the "fictive" traction vector defined by the "fictive" force $\mathrm{d}\vec{\underset{\sim}{\mathrm{f}}}$ per area $\mathrm{d}A$ in the reference configuration. The 2nd Piola-Kirchhoff stress, $\bar{\bar{\mathrm{S}}}$, is convenient in constitutive formulations because it provides a simple description of hyperelastic behavior, see Humphrey [45] for details.

To complete this section the mathematical relationship between $\bar{\bar{\sigma}}$, $\bar{\bar{\mathrm{P}}}$, and $\bar{\bar{\mathrm{S}}}$ is shown utilizing

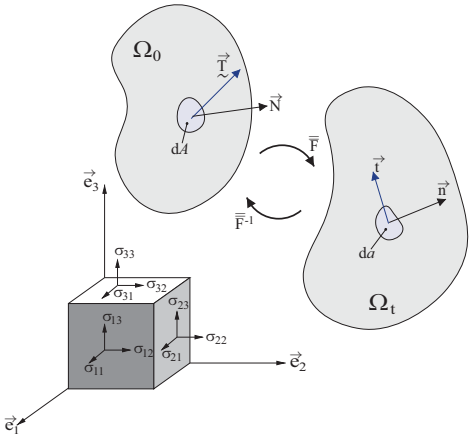

Figure 3.3: Illustration of traction vector $\vec{\underset{\sim}{T}}$ in Ω_0 and $\vec{t}$ in Ω_t respectively. The cube show the index notation for the nine components of the Cauchy stress tensor.

Nanson's formula for mapping of surface areas between configurations [41],

$$\vec{n}\mathrm{d}a = J\bar{\bar{F}}^{-\mathrm{T}} \cdot \vec{N}\mathrm{d}A = J\vec{N}\mathrm{d}A \cdot \bar{\bar{F}}^{-1} \;\Leftrightarrow\; \vec{N}\mathrm{d}A = \frac{1}{J}\vec{n}\mathrm{d}a \cdot \bar{\bar{F}} \,. \tag{3.12}$$

where $J = \det \bar{\bar{F}}$ maps the volume in Ω_0 to the volume in Ω_t, thus J is considered a volume ratio. The derivation of (3.12) is omitted, but the interested reader is referred to Holzapfel [41] and Humphrey [45] for details. The equation (3.12) is used to map $\vec{N}$ associated with $\mathrm{d}A$ in Ω_0 to $\vec{n}$ associated with $\mathrm{d}a$ in Ω_t.

The relation between $\bar{\sigma}$ and $\bar{\bar{P}}$ is deduced by rewriting (3.10) and replacing $\vec{N}\mathrm{d}A$ with the right-hand-side in (3.12)b,

$$\mathrm{d}\vec{f} = \bar{\bar{P}}\vec{N}\mathrm{d}A = \bar{\bar{\sigma}}\vec{n}\mathrm{d}a = \bar{\bar{\sigma}}J\bar{\bar{F}}^{-\mathrm{T}} \cdot \vec{N}\mathrm{d}A \;\Leftrightarrow\; \bar{\bar{P}} = J\bar{\bar{\sigma}}\bar{\bar{F}}^{-T} \,,\; P_{iA} = J\sigma_{ij}F^{-1}_{Aj} \tag{3.13}$$

This relationship shows that $\bar{\bar{P}}$ transforms the stress state in the current configuration back to the reference configuration by pullback of $\bar{\sigma}$ through $\bar{\bar{F}}$ so that the forces in Ω_t are related to areas in Ω_0. The transformation scales with the volume ratio J.

Using (3.9), (3.11), and Nanson's formula the relation between $\bar{\sigma}$ and $\bar{\bar{S}}$ is derived,

$$\mathrm{d}\vec{\underset{\sim}{f}} = \bar{\bar{S}}\vec{N}\mathrm{d}A = \frac{1}{J}\bar{\bar{S}}\vec{n}\mathrm{d}a\bar{\bar{F}} = \mathrm{d}\vec{f}\bar{\bar{F}}^{-1} = (\bar{\bar{\sigma}}\vec{n}\mathrm{d}a)\,\bar{\bar{F}}^{-1} \Leftrightarrow\; \bar{\bar{S}} = J\bar{\bar{F}}^{-1}\bar{\bar{\sigma}}\bar{\bar{F}}^{-\mathrm{T}} \,,\; S_{AB} = JF^{-1}_{Ai}F^{-1}_{Bj}\sigma_{ij} \,. \tag{3.14}$$

Thus, $\bar{\bar{\mathrm{S}}}$ defines the transformation of the forces in Ω_t back to the reference configuration by pullback of $\bar{\sigma}$ through $\bar{\bar{\mathrm{F}}}$ and scaling with the volume ratio J.

Table 3.1: Table showing the relation between the components of the components of the Cauchy stress, the 1st Piola-Kirchhoff stress, and the 2nd Piola-Kirchhoff stress.

	σ_{ij}	P_{iA}	S_{AB}
σ_{ij}	1	$J^{-1}F_{jA}$	$J^{-1}F_{iA}F_{jB}$
P_{iA}	JF_{Aj}^{-1}	1	F_{iB}
S_{AB}	$JF_{Ai}^{-1}F_{Bj}^{-1}$	F_{Ai}^{-1}	1

In conclusion the three measures of stress described in this section are all related through the deformation gradient tensor $\bar{\bar{\mathrm{F}}}$ and its determinant J as summarized in Table 3.1. In this work, the stress state in the AA wall is quantified as Cauchy stress.

3.1.3 Balance principles

There are five general postulates about balance: conservation of mass, conservation of linear momentum, conservation of angular momentum, and the 1st and 2nd laws of thermodynamics. These basic balance principles are used for computation of the wall stress and must be respected at all times.

Conservation of mass Balance of mass is a powerful relation in continuum mechanics because it is used as a kinematic constrictor simplifying the problem of interest. Conservation of mass requires that the mass of a body, m, does not change with time,

$$\mathrm{d}m = \rho_0(\vec{\mathrm{X}})\mathrm{d}V = \mathrm{d}m(\vec{\mathrm{x}}, t) = \rho(\vec{\mathrm{x}}, t)\mathrm{d}v \quad , \tag{3.15}$$

where ρ_0, ρ are the mass densities in Ω_0 and Ω_t, respectively. Integration over the entire volume produce the well-known mass balance relation,

$$m = \int_{\Omega_0} \rho_0 \mathrm{d}V = \int_{\Omega_t} \rho \mathrm{d}v = \text{constant} > 0 \quad . \tag{3.16}$$

Incompressibility is a widely used assumption in vascular solid mechanics. Incompressibility requires the motion to be isochoric, and the fluid is homogeneous. These two assumptions imply that $\frac{\partial \rho}{\partial t} = 0$, which is evident from the conservation of mass. Thus, incompressibility is a kinematic restriction on the mechanical problem. Comparing to (3.13) and (3.14),

incompressibility is incorporated in the volume ratio as $J = \frac{\rho_0}{\rho} = 1$. In fluid dynamics conservation of mass is often referred to as continuity, see Sec. 4.1.

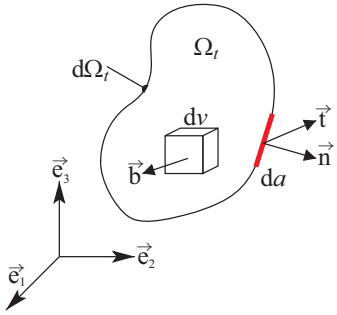

Figure 3.4: Illustration of surface and volume elements in the current configuration Ω_t where $\vec{b}$ is the body forces acting within the volume and dv is an infinitesimal volume element in the continuum body.

Conservation of linear momentum Balance of linear momentum is a generalization of Newton's second law of motion, $\sum \vec{f} = m\vec{a}$, where $\vec{a}$ is the acceleration of the body. Consider the body in Fig. 3.4, then the linear momentum balance can be written as,

$$\int_{d\Omega_t} \vec{t} da + \int_{\Omega_t} \vec{b} dv = \frac{d}{dt} \int_{\Omega_t} \rho \vec{v} dv \ . \tag{3.17}$$

Assuming conservation of mass and applying (3.9) together with Gauss' theorem, (3.17) reduces to

$$\int_{\Omega_t} \nabla \cdot \bar{\sigma} dv + \int_{\Omega_t} \vec{b} dv = \frac{d}{dt} \int_{\Omega_t} \rho \vec{v} dv = \int_{\Omega_t} \rho \frac{\partial \vec{v}}{\partial t} + \rho \vec{v} \cdot \nabla \vec{v} dv = \int_{\Omega_t} \rho \dot{\vec{v}} \quad , \tag{3.18}$$

where $\vec{v}$ is the velocity of the motion, ∇ is the del operator, and $\dot{\vec{v}}$ total change of velocity per time. The linear momentum balance is most often defined in the spatial configuration since the forces acting on the continuum body are defined in this configuration.

Angular momentum balance The angular momentum balance requires that the rate of change in the total moment of momentum equals the applied moments on the body at all times, i.e. in the reference configuration

$$\frac{\mathrm{d}}{\mathrm{d}t}\int\limits_{\Omega_0}\vec{\mathrm{r}}\times\rho_0(\vec{\mathrm{X}})\vec{\mathrm{U}}(\vec{\mathrm{X}},t)\mathrm{d}V=\int\limits_{\Omega_0}\vec{\mathrm{r}}\times\rho_0(\vec{\mathrm{X}})\vec{\mathrm{b}}(\vec{\mathrm{X}},t)\mathrm{d}V+\int\limits_{\partial\Omega_0}\vec{\mathrm{r}}\times\rho_0(\vec{\mathrm{X}})\vec{\mathrm{T}}(\vec{\mathrm{N}})\mathrm{d}A \quad . \tag{3.19}$$

Where $\vec{\mathrm{r}}(\vec{\mathrm{x}})=\vec{\mathrm{x}}-\vec{\mathrm{x}}_0$ is the the moment arm, and $\vec{\mathrm{U}}(\vec{\mathrm{X}},t)$ is the velocity field in the reference configuration. The force acting on the moment arm originates from the body force $\vec{\mathrm{b}}(\vec{\mathrm{X}},t)$ and the traction $\vec{\mathrm{T}}(\vec{\mathrm{N}})$ at the surface of the body. The angular momentum balance provides restrictions on constitutive relations formulated with $\bar{\bar{\sigma}}$, $\bar{\bar{\mathrm{P}}}$, and $\bar{\bar{\mathrm{S}}}$ by requiring specific symmetries in the stress-strain relations to be fulfilled.

First and second law of thermodynamics When an solid body deforms due to increase in the applied external loads, the work *W* is performed during the deformation. The first law of thermodynamics (conservation of energy), demands that the time rate of total energy change of a body must equal the time rate of work exerted on the body due to applied loads, and the time rate at which heat is added to the body,

$$\rho_0\frac{\mathrm{d}\varepsilon}{\mathrm{d}t}=\bar{\bar{\mathrm{P}}}^{\mathrm{T}}:\frac{\mathrm{d}\bar{\bar{\mathrm{F}}}}{\mathrm{d}t}-\nabla_0\cdot\vec{q}_0+\rho_0 g \quad , \tag{3.20}$$

where ε is the internal energy density, ∇_0 is the referential del operator, $\vec{q}_0$ is the referential heat flux vector, and g is addition of heat (per unit mass). Any heat exchange is negligible because the temperature of the AA is the same as the surrounding tissue. Therefore, there is no temperature difference to drive the heat flow and the process becomes adiabatic. Hence, the work done on the body is stored in the body as elastic strain energy. Application of energy considerations are useful in derivation of stress-strain relations for both small and large elastic deformation, and failure analysis.
The second law of thermodynamics (entropy inequality) is essential in formulation of constitutive relations for all hyperelastic materials [41]. It is used to establish the relationship between stress and strain (or stretch) through the Clausius-Duhem equation, which reduces to the Clausius-Planck inequality upon using the experimental finding that heat flows from hot to cold regions, i.e., $\vec{Q}\cdot\nabla\vartheta\leq 0$, where $\vec{Q}$ is the heat flux and $\vartheta>0$ is the temperature [41], i.e.,

$$-\rho_0\frac{\mathrm{d}\xi}{\mathrm{d}t}+\bar{\bar{\mathrm{P}}}^{\mathrm{T}}:\frac{\mathrm{d}\bar{\bar{\mathrm{F}}}}{\mathrm{d}t}\geq 0 \quad . \tag{3.21}$$

Here $\frac{\mathrm{d}\xi}{\mathrm{d}t}$ is the Helmholtz potential corresponding to the derivative of the Helmholtz free energy function (free energy), and the mathematical operator : is the double contraction of two tensors. In solid mechanics the free energy is most often expressed as a strain-energy function per unit volume in the reference configuration,

$$\Pi_{int} = \int_{\Omega_0} \psi \mathrm{d}V \ , \tag{3.22}$$

where Π_{int} is the total internal potential energy in the body, and $\psi = \rho_0 \xi$ denotes the strain-energy function defined per unit reference volume. The local deformation of the AA wall is characterized by $\bar{\bar{\mathrm{F}}}$, and the strain energy function ψ characterize the elastic properties of the wall. For homogeneous materials ψ is only a function of $\bar{\bar{\mathrm{F}}}$, and for heterogeneous materials ψ also depends on the position in the media.

3.1.4 Finite elasticity

The AA tissue behaves as a nonlinear pseudo-elastic material, see Sec. 2.2, thus nonlinear constitutive theory is needed for the description of the mechanical behavior during the cardiac cycle. The behavior is characterized by large strains, i.e. finite strains, and the theory describing this physical phenomena is called finite elasticity. The stress measure of most interest here is the Cauchy stress tensor, $\bar{\bar{\sigma}}$, as the it is true stress, see Sec. 3.1.2. Stress measures must be independent of the observer position and orientation, i.e. the AA tissue should behave the same independently of the observer. The independence is imposed by considering the objectivity, or material-indifference, of the strain energy function.

Objectivity As an example of how objectivity applies to the strain energy function, consider a stretched rubber band with a certain amount of elastic energy stored in the material. If the stretched rubber band undergoes a rotation and a translation in space, then $\psi(\bar{\bar{\mathrm{F}}})$ is objective if the energy stored in the rubber band remains the same. Thus, to obey objectivity, the strain energy function must fulfill the restriction,

$$\psi(\bar{\bar{\mathrm{F}}}) = \psi(\bar{\bar{\mathrm{F}}}^*) = \psi(\bar{\bar{\mathrm{Q}}}\bar{\bar{\mathrm{F}}}) \quad . \tag{3.23}$$

Here $\bar{\bar{\mathrm{F}}}^*$ characterize the rotation and the translation of the stretched rubber band, and $\bar{\bar{\mathrm{Q}}}$ is an orthogonal tensor. Moreover, $\psi(\bar{\bar{\mathrm{F}}})$ needs to be objective during superimposed rigid body motions to ensure that the Cauchy stress tensor is independent of the observer. This demands that the rotation part of $\bar{\bar{\mathrm{F}}}$ is eliminated from $\psi(\bar{\bar{\mathrm{F}}})$. This is done by choosing $\bar{\bar{\mathrm{Q}}} = \bar{\bar{\mathrm{R}}}^{\mathrm{T}}$ and applying the right side of the polar decomposition, see (3.5), hence from (3.23),

$$\psi(\bar{\bar{\mathrm{Q}}}\bar{\bar{\mathrm{F}}}) = \psi(\bar{\bar{\mathrm{R}}}^{\mathrm{T}}\bar{\bar{\mathrm{F}}}) = \psi(\bar{\bar{\mathrm{R}}}^{\mathrm{T}}\bar{\bar{\mathrm{R}}}\bar{\bar{\mathrm{U}}}) = \psi(\bar{\bar{\mathrm{U}}}) \quad . \tag{3.24}$$

Recalling, that the right Cauchy-Green tensor, $\bar{\bar{\mathrm{C}}}$, is equal to $\bar{\bar{\mathrm{U}}}^2$, the strain energy function can equally be expressed as a function of $\bar{\bar{\mathrm{C}}}$, i.e. $\psi(\bar{\bar{\mathrm{F}}}) = \psi(\bar{\bar{\mathrm{C}}})$.

Definition of stress measures The Cauchy stress, $\bar{\bar{\sigma}}$, can be derived by considering the 2nd law of thermodynamics. The time derivative of $\psi(\bar{\bar{\mathrm{F}}})$ is defined as [45]

$$\frac{\mathrm{d}\psi}{\mathrm{d}t} = \frac{\partial \psi}{\partial \bar{\bar{\mathrm{F}}}} : \frac{\mathrm{d}\bar{\bar{\mathrm{F}}}}{\mathrm{d}t} \quad , \quad \text{with} \quad \frac{\mathrm{d}\bar{\bar{\mathrm{F}}}}{\mathrm{d}t} = \bar{\bar{\mathrm{L}}}\bar{\bar{\mathrm{F}}} \quad . \tag{3.25}$$

Here, $\bar{\bar{\mathrm{L}}}$ is the velocity gradient tensor transforming the vector $\mathrm{d}\vec{x}$ (see Fig. 3.3) into the velocity vector $\mathrm{d}\vec{v}$. Substituting the time derivative of $\psi(\bar{\bar{\mathrm{F}}})$ in (3.25) and replacing the inequality with an equal sign, because elastic responses are reversible by definition, the 2nd law of thermodynamics reads,

$$\left(-\frac{\partial \psi}{\partial \bar{\bar{\mathrm{F}}}} + \bar{\bar{\mathrm{P}}}^{\mathrm{T}} \right) : \frac{\mathrm{d}\bar{\bar{\mathrm{F}}}}{\mathrm{d}t} = 0 \quad \forall\, \bar{\bar{\mathrm{F}}} \quad . \tag{3.26}$$

For (3.26) to be true for all formulations of $\bar{\bar{\mathrm{F}}}$ the expression inside the parenthesis must equal zero. Hence, the 1st Piola-Kirchhoff stress tensor can be derived from ψ,

$$\bar{\bar{\mathrm{P}}} = \frac{\partial \psi}{\partial \bar{\bar{\mathrm{F}}}^{\mathrm{T}}} \quad . \tag{3.27}$$

This equation is only valid for compressible materials. In order to derive the analytical expressions for Cauchy stress components in Chap. 6 it is necessary to add an arbitrary multiplier $p\bar{\bar{\mathrm{F}}}^{-1}$. Based on the objectivity of the strain energy function, it can be shown that [41],

$$\frac{\partial \psi(\bar{\bar{\mathrm{F}}})}{\partial \bar{\bar{\mathrm{F}}}^{\mathrm{T}}} = 2 \frac{\partial \psi(\bar{\bar{\mathrm{C}}})}{\partial \bar{\bar{\mathrm{C}}}} \bar{\bar{\mathrm{F}}}^{\mathrm{T}} \quad . \tag{3.28}$$

Substituting $\bar{\bar{\mathrm{P}}}$ in the relationship between the Cauchy stress tensor, and the 1st Piola-Kirchhoff stress tensor with the right side of (3.28), the general form of the Cauchy stress tensor appears,

$$\bar{\bar{\sigma}} = 2J^{-1} \bar{\bar{\mathrm{F}}} \frac{\partial \psi(\bar{\bar{\mathrm{C}}})}{\partial \bar{\bar{\mathrm{C}}}} \bar{\bar{\mathrm{F}}}^{\mathrm{T}} \quad , \quad \sigma_{ab} = 2J^{-1} F_{aA} F_{bB} \frac{\partial \psi}{\partial C_{AB}} \quad . \tag{3.29}$$

Important assumptions about material properties such as isotropy, anisotropy, incompressibility, compressibility, and composite structure impose restrictions on the general Cauchy stress formulation. In this work, the AA wall is assumed to be a constrained mixture of isotropic elastin-dominated ground matrix reinforced by collagen fibers, thus a composite material. The collagen fibers are grouped according to direction of orientation, see Fig. 3.5.

The semi-inverse approach is one method to determine the stress field in the aorta using Eq. (3.29). The semi-inverse approach was introduced by R.S. Rivlin in the late 1940's and early

1950's to solve nonlinear elasticity problems of rubber materials [89]. Depending on assumptions about the stress state, the stress field is either determined analytically or numerically. The methodology is based on first guessing a motion to determine the components of $\bar{\bar{\mathrm{F}}}$. Then determine the loads that caused this motion ensuring that the loads satisfy equilibrium. The loads are determined from the stress field, for example as stated in (3.29). Specific forms of the strain energy function characterize the elastic behavior of the AA.

3.2 Constitutive Formulation

In this section a brief review of the milestones in formulation of suitable constitutive relations describing the hyper-elastic anisotropic properties of the aortic and aneurysmal mechanical behavior is presented. The review is only brief, but an effort is made to include the most significant developments. For deeper insight into the different models the reader is referred to the detailed reviews by Humphrey [45], Holzapfel and Ogden [43], and Holzapfel et al. [42]. This work only considers phenomenological models based on the argument stated by Vorp [115]:

"Micro-structure-based models are motivated by the known fibrous nature of the tissue, and the material parameters/constitutive parameters are associated with the state of the elastin and collagen within the aortic wall. But micro-structure-based models are difficult to utilize for estimation of wall stresses in 3D vessels. Thus, it is more appropriate to use continuum-based constitutive models which describe the gross mechanical behavior"

The Ogden model The Ogden model is fundamental in the prediction of mechanical behavior of aortic tissue because the strain energy is a function of the principal stretches [79, 80],

$$\psi\left(\lambda_1, \lambda_2, \lambda_3\right) = \sum_{p=1}^{N} \frac{\mu_p}{\alpha_p} \left(\lambda_1^{\alpha_p} + \lambda_2^{\alpha_p} + \lambda_3^{\alpha_p} - 3\right), \tag{3.30}$$

where μ_p are constant shear moduli, N is the number of terms in ψ, and α_p are dimensionless constants. The model is isotropic as well as computationally simple and is based on the state-of-the-art work by Ogden on rubber-like materials [79]. Valanis and Landel [108] proposed that ψ can be written as the sum of three separate functions which depend on each of the principal stretches, known as the Valanis-Landel hypothesis. Using this hypothesis the Ogden model can be formulated as [43],

$$\psi\left(\lambda_1, \lambda_2, \lambda_3\right) = \omega(\lambda_1)+\omega(\lambda_2)+\omega(\lambda_3) = \sum_{a=1}^{3} \omega(\lambda_a), \quad \text{where} \quad \omega(\lambda_a) = \sum_{p=1}^{N} \frac{\mu_p}{\alpha_p} \left(\lambda_a^{\alpha_p} - 1\right) \quad . \tag{3.31}$$

The Neo-Hookean model is the simplest form of ψ and it is a special case of the Ogden model derived from Eq. (3.30) by setting $N = 1$ and $\alpha_1 = 2$ using the first invariant of the right Cauchy-Green tensor, $I_1 = \mathrm{tr}\,\bar{\bar{\mathrm{C}}}$,

$$\psi\left(I_1\right) = c\left(I_1 - 3\right) \quad . \tag{3.32}$$

This equation includes only a single material parameter c and describe the nonlinear elastic behavior of rubber-like materials.

The Fung model In Fig. 2.4 it is seen that the mechanical behavior of the AA is nonlinear; at lower loads the tissue is compliant and as loading increases the AA wall stiffens rapidly. Fung [32] quantified this stiffening behavior by plotting the stress-stretch curve of uniaxial elongation tests on the mesentery artery. Stiffness of the arterial tissue can be deduced from the relationship between stress and stretch ratio as the tangent of the curves seen in Fig. 2.5. Fung expressed the stress-stretch curve in terms of the measured stress (1st Piola-Kirchhoff stress) and the measured stretch (λ_1). The stiffness of the tissue can then be expressed as the gradient of the stress with respect to the stretch. Fung showed that this gradient is linear [32], i.e.

$$\frac{\mathrm{d}P_{11}}{\mathrm{d}\lambda_1} = c_1 P_{11} + c_2 \; . \tag{3.33}$$

This equation, (3.33), is a first order ordinary differential equation with constant coefficients c_1 and c_2 with a solution of the form

$$P_{11} = c\exp\left(a\lambda_1\right) + b \Rightarrow P_{11} = \frac{c_2}{c_1}\left[\exp\left(c_1(\lambda_1 - 1)\right) - 1\right] \quad . \tag{3.34}$$

This equation is important because it is based on experimental data and can be applied to a wide range of soft tissues. Based on Eq. (3.34) Fung proposed that the three dimensional stress-strain behavior can be described by a strain energy function, which is exponential in terms of the Green strain $\bar{\bar{\mathrm{E}}} = \frac{1}{2}(\bar{\bar{\mathrm{C}}} - \bar{\bar{\mathrm{I}}})$ [33],

$$\psi(\bar{\bar{\mathrm{E}}}) = c\left[\exp\left(Q(\bar{\bar{\mathrm{E}}})\right) - 1\right] \quad , \tag{3.35}$$

where $Q(\bar{\bar{\mathrm{E}}})$ is assumed to be a polynomial function of $\bar{\bar{\mathrm{E}}}$, i.e.

$$Q(\bar{\bar{\mathrm{E}}}) = \frac{1}{2}\left(\mathbb{C} : \bar{\bar{\mathrm{E}}}\right) : \bar{\bar{\mathrm{E}}} \quad , \quad Q = \frac{C_{ABCD}}{2} E_{AB} E_{CD} \quad , \tag{3.36}$$

where $\mathbb{C}$ is a fourth order tensor defined by (3.36). The Fung model has been used in multiple studies in the pursue of a strain energy function describing the anisotropic and hyperelastic

behavior of the AA and AAA. Vande Geest et al. [110] used the general anisotropic Fung model to describe experimental data obtained from human AA. Demiray and Vito [16] suggested a layered cylindrical shell model of the aorta including two Fung models with different material parameters for the media and the adventitia respectively.

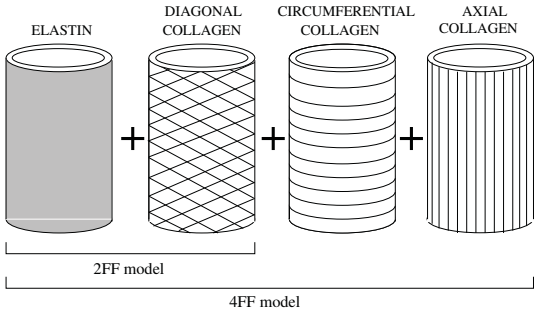

Figure 3.5: Sketch of the principle of the 2FF and 4FF model, where a homogeneous elastin dominated isotropic material (the left-most cylinder) is re-enforced by four families of collagen fibers; circumferential oriented (middle left cylinder), axial oriented (middle right cylinder), and two oblique families oriented symmetrically around the axial direction (right-most cylinder). The 2FF model only comprise the elastin and the diagonal collagen fiber composition.

The two fiber family model Holzapfel and Weizsacker [44] were the first to propose a strain energy function decomposed into an isotropic part, ψ_{iso} and an anisotropic part ψ_{aniso} in the description of arterial tissue. Here, ψ_{iso} accounts for the elastin-dominated ground matrix represented by a Neo-Hookean model, and ψ_{aniso} accounts for the collagen represented by the Fung model, i.e.

$$\psi(\bar{\bar{\mathrm{C}}}) = \psi_{iso} + \psi_{aniso} = c_1\,(I_1 - 3) + c_2\left[\exp\left(Q(\bar{\bar{\mathrm{E}}})\right) - 1\right] \quad , \tag{3.37}$$

where $I_1 = \operatorname{tr}\bar{\bar{\mathrm{C}}} = 2\operatorname{tr}\bar{\bar{\mathrm{E}}} + 3$ is the first invariant of $\bar{\bar{\mathrm{C}}}$, while c_1 and c_2 are material parameters. The decomposition lead to the development of structurally motivated strain energy functions where the AA wall is considered as a fiber reinforced composite material. Holzapfel et al. [42] presented the original two fiber family (2FF) model, see Fig. 3.5,

$$\psi\left(\bar{\bar{\mathrm{C}}}, \vec{\mathrm{M}}_k\right) = \frac{c}{2}\,(I_1 - 3) + \sum_{k=4,6} \frac{c_1^{(k)}}{2c_2^{(k)}}\left(\exp\left[c_2^{(k)}(I_k - 1)^2\right] - 1\right), \tag{3.38}$$

where $\vec{\mathrm{M}}_k$ is the unit vector for the direction of the collagen fiber family, and I_k are the fourth and sixth invariant of $\bar{\bar{\mathrm{C}}}$, respectively. The collagen fibers are assumed have the same mechanical properties, i.e. for the material parameters $c_1^{(4)} = c_1^{(6)}$ and $c_2^{(4)} = c_2^{(6)}$ [42, 43].

The material parameter $c_1^{(k)}$ is a stress-like parameter having a unit of Pascal. The material parameter $c_2^{(k)}$ is dimensionless.

The fiber orientation is defined in a reference frame such that the direction of the fibers are given by the angle, α_0, between the direction of the fiber reinforcement and the axial direction of the vessel. The invariants are given as,

$$I_4 = \vec{\mathrm{M}}_4 \cdot (\bar{\bar{\mathrm{C}}}\,\vec{\mathrm{M}}_4) \;, \quad I_6 = \vec{\mathrm{M}}_6 \cdot (\bar{\bar{\mathrm{C}}}\,\vec{\mathrm{M}}_6) \;, \tag{3.39}$$

with the unit vectors $\vec{\mathrm{M}}_i$ defined as,

$$\vec{\mathrm{M}}_4 = \{0, \cos(\alpha_0), \sin(\alpha_0)\} \;, \quad \vec{\mathrm{M}}_6 = \{0, \cos(\alpha_0), -\sin(\alpha_0)\} \;. \tag{3.40}$$

From (3.39) and (3.40) it is seen that the invariants correspond to the square of the stretch in the given fiber direction.

The model has been applied in several studies on the mechanical behavior of AAAs. Among others, Rodriguez et al. [90] used this model to explore the influence from model geometry and material anisotropy on the magnitude and distribution of peak wall stress in AAAs. Watton et al. [118] used the 2FF model to simulate the growth of AAAs.

The four fiber family model The four fiber family (4FF) model is an extension of the 2FF model in (3.38) based on the histological observations on arterial collagen structure by Wicker et al. [120] and formulated mathematically by Baek et al. [3], see Fig. 3.5. In addition to the two collagen fiber families that are symmetrical around the axial direction, families of axial oriented fibers and families of circumferential oriented fibers are added to the strain energy function,

$$\psi\left(\bar{\bar{\mathrm{C}}}, \vec{\mathrm{M}}_k\right) = \frac{c}{2}\,(I_C - 3) + \sum_{k=1}^{4} \frac{c_1^{(k)}}{4c_2^{(k)}} \left(\exp\left[c_2^{(k)}(I_4^{(k)} - 1)^2\right] - 1\right) . \tag{3.41}$$

Here, c is a material parameter describing the elastin, while $c_1^{(k)}$ and $c_2^{(k)}$ are material parameters describing the each of the four collagen fiber families. Equivalent to the 2FF model, the diagonal collagen fiber families are assumed to have the same mechanical properties, i.e. $c_1^{(3)} = c_1^{(4)}$ and $c_2^{(3)} = c_2^{(4)}$. The angle α_0 for the axial and circumferential fiber families is fixed at 0° and 90°, respectively. For the two diagonal fiber families, it is assumed that $\alpha_0^{(3)} = -\alpha_0^{(4)} = \alpha_0$. Thus, the fourth invariant, $I_4^{(3,4)}$, is [28]

$$I_4^{(3,4)} = I_4^{(d)} = \lambda_z^2 \cos^2(\alpha_0) + \lambda_\varphi^2 \sin^2(\alpha_0) \tag{3.42}$$

assuming that the reference frame is defined in cylindrical coordinates.

Eberth et al. [23] fitted experimental biaxial stress-stretch data from mice carotids to the 4FF model in the pursue of a mouse model of Marfan Syndrome (insufficient elastin synthesis) to gain insight into the vascular abnormalities related to the condition. Cardamone et al. [9] used the 4FF to obtain new knowledge about the origin of residual stress in arteries. Ferruzzi et al. [28] used the 4FF model to fit biaxial data from normal AA as well as AAA, and concluded that the model captures the loss of structural integrity of elastin due to aging. Moreover, Valentin et al. [109] used the 4FF to construct a multi-layered growth and remodeling model of the aging aorta incorporating both elastin degradation and collagen-mediated stiffening.

CHAPTER

FOUR

NUMERICAL SIMULATION OF BLOOD FLOW AND STRUCTURE INTERACTION

Objective *The blood flow in the abdominal aorta is characterized by complex flow patterns due to curves, bends, and flow dividers such as the celiac trunk, the renal arteries, and the iliac bifurcation. As the blood flow is pulsatile, vortices and flow reversal arise in the abdominal aorta during the cardiac cycle. The blood flow is expected to play an important role in the development and rupture of abdominal aortic aneurysms. Fluid-structure interaction models are therefore a natural increase in model complexity from the solid mechanics models described in Chapter 3. An introduction to fluid flow physics in the abdominal aorta and aneurysms is needed for proper characterization of the fluid domain in the fluid-structure interaction model. Knowing the velocity field and pressure enables calculation of forces and stresses exerted by the blood on the vascular wall. The fluid-structure interaction is thus controlled through the boundary condition between the blood flow domain and the solid wall domain.*

4.1 Navier-Stokes Equations

The following section presents the basic postulates which must be satisfied in order to determine velocity field and the pressure conditions in the human AA in a computational simulation model. This is necessary to determine the forces and stress exerted by the blood on the AA wall. For a sufficient description of the blood flow in the AA, balance in mass and momentum must to be satified.
The following section is based on the textbooks by Truskey et al. [107] and Bird et al. [7].

Conservation of mass Considering the control volume in Fig. 4.1 through which the fluid passes the conservation of mass can be formulated in words as,

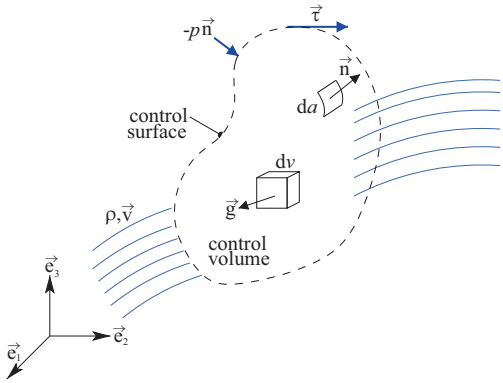

Figure 4.1: Control volume in a fluid flow. The flow is indicated by the blue solid stream lines.

$$\left\{\begin{array}{c}\text{accumulation rate of}\\ \text{mass in control volume}\end{array}\right\} = \left\{\begin{array}{c}\text{mass flow rate of}\\ \text{into control volume}\end{array}\right\} - \left\{\begin{array}{c}\text{mass flow rate out}\\ \text{of control volume}\end{array}\right\}$$

In fluid mechanics the conservation of mass is often referred to as continuity. The general form of the mass conservation is formulated with a moving reference frame opposite of the situation for solid mechanics, where the reference frame is fixed, see Sec. 3.1.3. The accumulation of mass in a control volume can be divided in two parts; one occurring within the control volume and one occurring at the surface of the control volume. Accumulation or loss of mass inside the control volume is a time dependent process expressed as a temporal change in mass density ρ. The change is mass on the surface of the control volume is present when ρ varies with fluid space, i.e there will be a mass flow across the surface of the control volume. In general, the continuity equation can be formulated as,

$$\frac{\partial \rho}{\partial t} + \vec{v} \cdot \nabla \rho = -\rho \nabla \cdot \vec{v} \quad , \tag{4.1}$$

where $\vec{v}$ is the flow velocity vector field. Under the assumption that the blood is an incompressible fluid the continuity equation reduces to,

$$\nabla \cdot \vec{v} = 0 \quad . \tag{4.2}$$

Conservation of linear momentum The general form of the equation of motion in fluid mechanics is the Navier-Stokes equation. Actually, Navier-Stokes equations refer to both the equation of motion and the continuity equation, as both need to be obeyed when solving fluid mechanical problems. The derivation of the Navier-Stokes is omitted from this text, but the interested reader is referred to Truskey et al. [107] and Bird et al. [7] for examples of the

derivation. In words, the linear momentum balance for fluid flow can be expressed as,

$$\left\{\begin{matrix}\text{accumulation rate of}\\ \text{momentum}\end{matrix}\right\} = \left\{\begin{matrix}\text{rate of momentum}\\ \text{flow in}\end{matrix}\right\} - \left\{\begin{matrix}\text{rate of momentum}\\ \text{flow out}\end{matrix}\right\} + \sum \text{forces}$$

The external forces separates into body forces such as gravity and electromagnetic forces, and surface forces characterized by normal and shear stresses, see Fig. 4.1. The linear momentum balance can be expressed per unit volume as,

$$\rho\left(\frac{\partial \vec{\mathrm{v}}}{\partial t} + (\vec{\mathrm{v}}\cdot\nabla)\vec{\mathrm{v}}\right) = -\nabla p + \nabla\cdot\bar{\bar{\tau}} + \rho\vec{\mathrm{g}} \quad , \tag{4.3}$$

where the right hand side represents the sum of the external forces and the body forces. The normal force acting on the surface appears due to pressure gradients, ∇p, and the shear stress, $\bar{\bar{\tau}}$, are present due to velocity gradients along the control surface. The body forces are represented by gravity, $\vec{\mathrm{g}}$. The forms listed in (4.2) and (4.3) are valid for any choice of moving reference frame and coordinate system. The components of the Navier-Stokes equations for various coordinate systems are listed in Truskey et al. [107] and Bird et al. [7] among others.

As blood is assumed to be an incompressible fluid, the shear stress in the blood can be defined as [107],

$$\bar{\bar{\tau}} = \eta\left(\nabla\vec{\mathrm{v}} + (\nabla\vec{\mathrm{v}})^{\mathrm{T}}\right) = \eta\dot{\bar{\bar{\gamma}}} \quad , \quad \tau_{ji} = \eta\left(\frac{\mathrm{d}v_j}{\mathrm{d}x_i} + \frac{\mathrm{d}v_i}{\mathrm{d}x_j}\right) \quad , \tag{4.4}$$

where η is the viscosity of an incompressible generalized Newtonian fluid. The viscosity, η, is a function of the shear rate, $\dot{\bar{\bar{\gamma}}}$, in the fluid. This dependency is utilized in formulation of constitutive relations for fluids, just as the strain energy function is utilized in formulation of the constitutive frame work for hyper-elastic solids, see Sec. 3.2.

4.2 Constitutive formulation

This section presents a short summary of constitutive relations that have been employed to solve fluid flow problems in the human cardiovascular system. Blood is a suspension of red blood cells (RBCs) in plasma, i.e. it cannot be considered as a Newtonian fluid at all times. A fluid is considered non-Newtonian when the viscosity varies with the shear rate. In general, there are two ways that blood deviates from being a Newtonian fluid [76]:

1. A significant increase in viscosity is seen at low shear rates, and

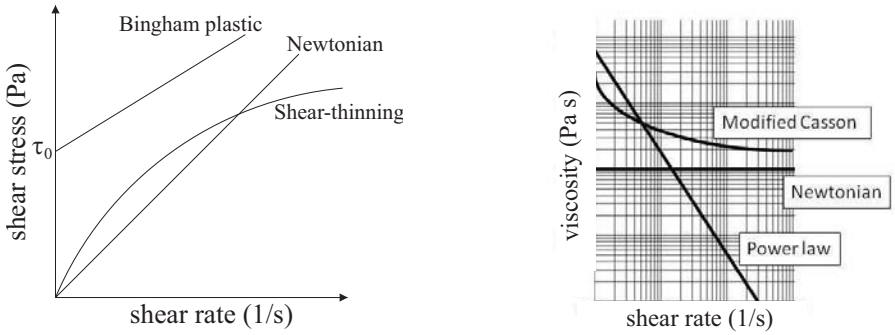

Figure 4.2: Illustration of the mechanical properties when utilizing various constitutive relationships. The left panel show the shear stress as a function of shear rate for a Bingham plastic, a Newtonian fluid, and a shear-thinning fluid respectively. The right panel show the relationship between the viscosity and the shear rate for the three constitutive relations; Newtonian fluid model, power law model, and the modified Casson model.

2. The viscosity in small vessels is higher compared to the viscosity in larger vessels.

The viscosity of blood differs with the amount of suspended RBCs, i.e the hematocrit H_n of the blood. The normal level of RBCs in adults is approximately 42% for females and 47% for males [107]. The plasma is considered a Newtonian fluid [76]. The viscosity of blood increase with increasing hematocrit. However a non-Newtonian is not observed until the hematocrit is at least 10%, see figure 2.3 in Nichols and O'Rourke [76]. The viscosity varies linearly with hematocrit up to $H_n \approx 45\%$.

Newtonian fluid For a Newtonian fluid the shear stress is linear proportional to the viscosity, and the viscosity is constant at any shear rate, see Fig. 4.2. Thus the constitutive relation for an incompressible Newtonian fluid is,

$$\eta(\dot{\bar{\gamma}}) = \mu \quad , \tag{4.5}$$

where μ is constant for a given temperature, pressure, and composition of the fluid. Hence, for incompressible Newtonian fluids (4.3) can be written as,

$$\rho\left(\frac{\partial \vec{\mathrm{v}}}{\partial t} + (\vec{\mathrm{v}} \cdot \nabla)\vec{\mathrm{v}}\right) = -\nabla p + \mu \nabla^2 \vec{\mathrm{v}} + \rho \vec{\mathrm{g}} \quad . \tag{4.6}$$

This is the form of the Navier-Stokes equation which is solved in the fluid-structure interaction simulation model described in Sec. 4.3.

Power law model The power law model applies to a wide variety of shear-thinning as well as shear-thickening aqueous solutions. The constitutive relation is a simple power function [7],

$$\eta(\dot{\bar{\bar{\gamma}}}) = m\dot{\bar{\bar{\gamma}}}^{\,n-1} \quad , \tag{4.7}$$

with m and n representing the material parameters, m has the unit of Pa·s, and n is dimensionless. Whether the fluid is shear-thinning or shear-thickening depends on the magnitude of n. When $n > 1$ fluid is shear-thickening, and when $n < 1$ the fluid is shear-thinning. Blood can be considered as a shear-thinning fluid since the viscosity decrease as the shear rate increase.

Modified Casson model Kleinstreuer et al. [54] applied a modified Casson model to study the hemodynamics in branching vessels of humans. The Casson model is the nonlinear extension of the constitutive relation for a Bingham plastic. The Bingham plastic applies to fluids such as ketchup which resist motion until a certain yield stress, τ_0, see Fig. 4.2. Upon exceeding the yield stress the Bingham plastic display a linear relationship between the viscosity and shear rate just as the Newtonian fluid [55].
The modified Casson model relates the viscosity to the shear rate through the second invariant I_{2D} of the rate-of-strain tensor $\bar{\bar{\mathrm{D}}} = \frac{1}{2}\dot{\bar{\bar{\gamma}}}$ [33, 53],

$$\eta(I_{2D}) = \frac{1}{2\sqrt{I_{2D}}}\left(a + b\sqrt{2\sqrt{I_{2D}}}\right) \quad , \tag{4.8}$$

with

$$I_{2D} = \frac{1}{2}\left[\left(\mathrm{tr}\bar{\bar{\mathrm{D}}}\right)^2 + \left(\mathrm{tr}\bar{\bar{\mathrm{D}}}^2\right)\right] \quad ,$$

and a, b being material parameters which depend on the hematocrit.

Even though blood cannot be represented as a Newtonian fluid in general, this simplification has been commonly used in the simulation of fluid-structure interactions in the AA with and without aneurysms, see Table 4.1. However, Wolters et al. [122] applied the Carreau-Yasuda model which is an extension of the Power Law model. The reason they chose this particular model was to capture the shear-thinning behavior of blood. Newtonian behavior of blood, on the other hand, can be assumed when the shear rate exceed 100 s^{-1} [107]. Due to the geometry and high velocities in the AA, this is done in several studies [19, 88, 96] as well as in this work.

Table 4.1: Overview of suggested FSI models for the human abdominal aorta.

Reference	Fluid	Solid	Geometry
Di Martino et al. [19]	Newtonian	Linear elastic	patient-specific
Wolters et al. [122]	Carreau-Yasuda	Linear elastic Neo-Hookean	patient-specific
Scotti et al. [96]	Newtonian	Isotropic hyper-elastic	idealized
Rissland et al. [88]	Newtonian	Isotropic and 2FF hyper-elastic	patient-specific

4.3 Fluid-Structure Interaction

Fluid-structure interaction (FSI) models have received increasing attention as they provide a coupling between the advanced structural models and the flowing blood in the AA. The fluid flow affects the displacement field of the solid, but the solid also influence the flow field. Table 4.1 lists a few of the proposed FSI-models, which are either based on realistic patient-specific geometries [19, 61, 88, 122], or idealized aneurymal geometries [96].

For solving the FSI problem commercially available code for fluid and solid problems has been applied in this work. It is stressed that the purpose of this work was not to develop new finite element (FE) algorithms, but to implement advanced material models in existing commercially available FE solvers. The disadvantage of using commercial FE solvers are the limited access to the source code, i.e. the applied solvers are partly ”black box” routines. On the other hand, by using commercial FE solvers, highly specialized algorithms optimized for complex fluid and solid problems can be applied. The commercial FE solvers used in this work are provided in COMSOL Multiphysics (COMSOL AB, Stockholm, Sweden). This software contains solution modules for both computational fluid dynamics, solid mechanics, and FSI applications [73, 75]. The following sections provides a summary of the implementation and solver setup in COMSOL Multiphysics utilized in this work. The solution techniques used in COMSOL Multiphysics are described in more details in the COMSOL Multiphysics Reference Guide [74].

A short summary of the finite element method is provided in the following paragraph. For a more detailed presentation of the FE method the interested reader is referred to the works by Zienkiewicz and Taylor [125], and Oden [78].

Finite element method The FE method is a discretization of the original mathematical problem. In order to apply the FE method, the mathematical problem needs to be solved within a spatial geometry which can be either one, two, or three dimensional. The given geometry is meshed so that it consists of a discrete number of elements. Inside each element

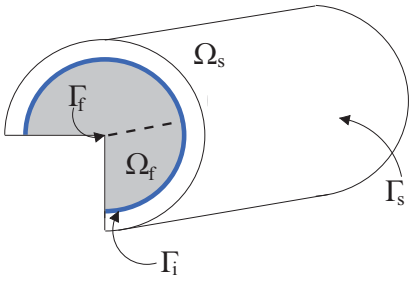

Figure 4.3: The solid and fluid domains of the FSI model with indication of the different boundaries. The Γ_f is the fluid boundary in the center of the vessel, here it corresponds to the symmetry axis of the AA model presented in Paper II. The Γ_i is the boundary condition for the interaction describing the mutual effect between the two materials. The Γ_s is the outer lateral boundary condition for the solid, usually left to move freely. Finally, Ω_f and Ω_s are the fluid and solid volumes respectively.

the solution for the specified physical problem is determined by approximation of the dependent variables using shape functions. For example, the solution to Navier-Stokes equations in an two dimensional axis-symmetric geometry has three dependent variables; the velocity components for the radial and axial direction, and the pressure. In the FE method applied in this work Lagrange elements defines the type of shape functions. Inside each Lagrange element the approximation to the dependent variables is a piecewise polynomial of degree k. Consider the dependent variable "q", then the approximation can be formulated as,

$$q = \sum_i Q_i \zeta_i \quad , \tag{4.9}$$

where $Q_i = q(p_i)$ represents the degrees of freedom for the problem, and ζ_i is the shape function with the restriction $\zeta_i = 1$ for the element node p_i and zero for all other nodes in the element. The approximation of the dependent variables are then inserted in the mathematical weak formulation of the physical problem, which results in a system of equations for the number of degrees of freedom. COMSOL Multiphysics then solves the system of equations with respect to the assigned partial differential equations, material parameters, and boundary conditions using numerical techniques.

Fluid domain solver The Navier-Stokes equations and associated boundary conditions constitute the mathematical description of the fluid domain. In this work the blood is assumed to be an incompressible homogeneous Newtonian fluid with a mass density, ρ_{blood}, of 1,060 kg/m^3 and a dynamic viscosity, μ_{blood} of 3.5 mPa·s. The blood flow is assumed to be laminar as this simplification is commonly assumed in the literature [19, 96, 122]. The solver applied for the fluid domain was in all research studies, i.e. Paper II and IV was a linear direct solver in which linear shape functions are applied to approximate the velocity components and the pressure in the fluid domain. The linear shape functions approximate the dependent

value q within a mesh interval using linear continuous functions between the element nodes. The direct solvers provides numerical robustness in fluid flow problems [73].

Solid domain solver The solver applied to the solid domain with the highly nonlinear material model is a direct linear solver called MUMPS (MUltifrontal Massively Parallel sparse direct Solver) [74]. In the application of the FE method for the hyper-elastic solid, the shape functions are quadratic contrary to the linear shape functions applied for the fluid mechanics. The quadratic elements introduces a midpoint on the mesh element edge between two element nodes, and approximate the dependent variables with continuous second order polynomials. The use of quadratic shape functions provides higher accuracy in the solution but also introduces longer computation time.

Details on the solver settings are provided in Appendix A.

CHAPTER

FIVE

MEDICAL IMAGING APPLICATIONS FOR FE MODEL CONSTRUCTION

Objective *Often abdominal aortic aneurysms are found incidentally as a consequence medical examination for other pathologies that are not related to aneurysmal disease. Medical imaging techniques like ultrasound imaging and flow velocity estimation, computed tomography (CT), and magnetic resonance imaging (MRI), are important clinical evaluation techniques in diagnosis of cardiovascular diseases such as AAA. Upon identification of the AAA, the patient is CT scanned to identify the size and location of the dilatation. The images have a high resolution and are suitable for segmentation of the macroscopic geometry. The segmented geometry can be used in finite element simulation models to identify wall stress distribution, as well as flow patterns in an anatomically realistic setup. Similarity in MR and CT images exist when the images have been post processed, but the details of the intraluminal thrombus are better visualized using MRI. Hence, MRI can be used for identification of structure of the intraluminal thrombus, which is found in 75% of the patients. Ultrasound is a dynamic real-time imaging technique applicable for visualization of both structure and function of the aorta and aneurysms. In conclusion, these medical imaging systems are key to proper clinical management of AAA patients as they are used for monitoring aneurysm development, as well as input to patient-specific models for prediction of wall stress and strength.*

5.1 Imaging for AAA diagnosis

The field of medical imaging systems evolve continuously, and provides medical doctors with important diagnostic information. In the field of AAA, medical imaging plays a significant role in the diagnosis, treatment planning, and follow-up after surgical intervention. As stated in Chap. 2 most AAAs are discovered by coincidence during medical examinations in relation to other health issues. The most frequent methods for discovery of an AAA are either ultrasound scanning or computational tomography (CT) of the abdomen. Ultrasound is a convenient imaging technique for diagnosis of pathologies in the abdomen because it is dynamic, real-time, and without ionizing radiation. The application of ultrasound for quantification of

the geometry and flow in the AA is presented in Sec. 5.3.1.

Death due to a ruptured AAA is a frequent cause of death among men. In Denmark approximately four to five percent of the male population above 65 years harbor an AAA, and a ruptured AAA is assumed to be the cause of death in five to ten percent of 80 year-old males [97]. Thus, screening programs for individuals within a high risk group of developing AAAs have been suggested [71, 95, 97]. The high risk group covers male smokers over 65 years of age. The large population study performed by Lindholt et al. [63] in Viborg County showed that ultrasound screening of the male population between 65 and 75 years reduce the mortality from a ruptured AAA by 67 %. Furthermore, the number of emergency operations due to a ruptured AAA was reduced by 75 % within the screening group compared to the control group.

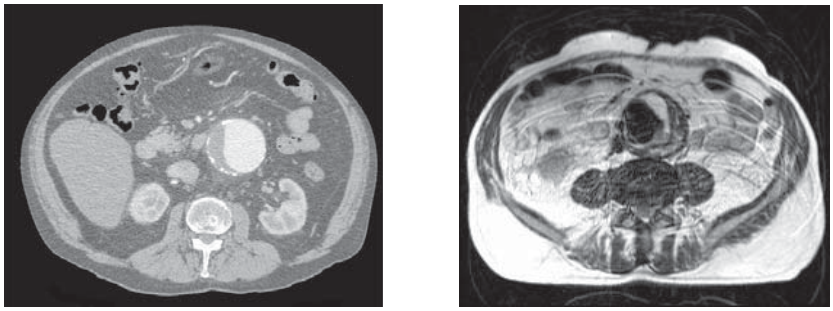

(a) (b)

Figure 5.1: Examples of clinical imaging techniques to visualize AAA. a) show the CT image slice from the abdomen of an AAA patient, the aneurysm is seen to the right of the center in the image. b) show the MR image slice from the abdomen of another AAA patient, the aneurysm is seen in the center of the image with visualisation of the structure of the intraluminal thrombus in contrast to the CT image in a).

CT is based on ionizing radiation, which are electromagnetic waves with short wavelength and high energy, see Fig. 5.2. The advantage in CT is that anatomical structures are visualized in detail due to a high performance in detection of small contrast differences. Modern CT scanners rotate at a speed of approximately 0.4 seconds per rotation, producing multiple image slices in a single rotation. CT is fast and is performed on all AAA patients due to the high image quality and fast processing time. An example of a CT scan of an AAA is shown in Fig. 5.1a. In the CT image the AAA is clearly visible. The high contrast in the lumen is produced as a result of intravenous contrast. This is used for most AAA patients to separate the lumen from the possible ILT. Additionally, the calcifications between the aneurysmal wall and the ILT is clearly marked in the image slice. Unfortunately, the aneurysmal wall can not be descriminated from CT images.

For comparison an image from a magnetic resonance imaging (MRI) sequence is displayed in Fig. 5.1b. While CT provide fast scan time, MRI provides more details on the AAA structure. MRI is primarily used for research when evaluating AAA patients. In this work MRI has been used in the research protocol (H-3-2009-102, 2009/09/01) for studying flow patterns and wall

stresses in the normal AA. The reason for application of MRI instead of CT was to obtain permission from the Danish National Committee on Biomedical Research Ethics, as MRI does not involve ionizing radiation and is able to produce equally good images suitable for segmentation of the geometry of the AA.

5.2 Magnetic resonance imaging

In the following section a short introduction to the theory behind magnetic resonance imaging (MRI) is provided. The section is primarily based on the lecture notes by Hanson [37] and the book by Bushong [8]. Note, that it was out of the scope of this PhD project to obtain an in-depth knowledge of constructing MRI sequences for imaging of the human AA. The assistance by Professor, dr.med. Carsten Thomsen in choosing suitable imaging sequences is gratefully acknowledged.

5.2.1 Basic imaging principle in magnetic resonance

Magnetic resonance imaging (MRI) is a convenient medical imaging technique for visualization of soft tissues and functional imaging of for example blood flow. Magnetic resonance used for imaging is within a frequency range between ten and 200 MHz, i.e. in the radio frequency (RF) domain. The RF waves used for MRI have a wavelength between one and 100 meters. For comparison, diagnostic x-rays have wavelengths between 10^{-12} and 10^{-9} m and ultrasound pulses for imaging result in a wavelength of 10^{-4} m in blood. A general electromagnetic spectrum is shown in Fig. 5.2.

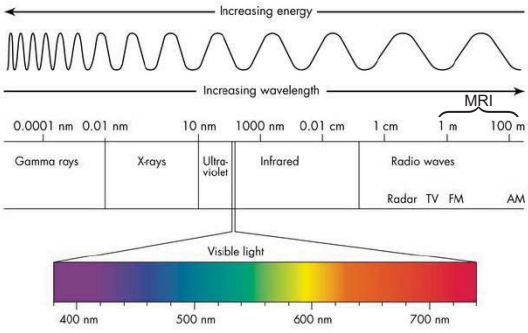

Figure 5.2: The electromagnetic spectrum illustrating the area of wavelengths used in MRI. Adapted from `http://www.antonine-education.co.uk/physics_gcse/Unit_1/Topic_5/topic_5_what_are_the_uses_and_ha.htm` with permission.

The primary source of the MRI signal used in medical imaging originate from protons. Most of the protons in the human body are present in the form of water since the human body is

approximately 70% water. The protons are magnetic and they rotate around their own axis, a motion referred to as spin. Because the protons are magnetic they act as tiny compass needles with the axis of rotation being the direction of magnetization.

The scanner magnet produce a strong magnetic field in the longitudinal direction which align the spins according to the applied field. The magnetic field strength is given in tesla (T). Due to the huge number of protons (10^{27}) the effect of the spin alignment becomes measurable. To produce RF waves for imaging in MRI the spins are pushed out of the equilibrium state. As the spins returns towards equilibrium, i.e. the alignment induced by the scanner, they transmit RF waves at a specific frequency determined by the Larmor equation. This equation relates the frequency of the precessing spins, $f_{\text{resonance}}$ to the applied field of the scanner, B_0, [8]:

$$f_{\text{resonance}} = \gamma B_0 \quad , \tag{5.1}$$

where $\gamma = 42$ MHz/T is the gyro-magnetic ratio for protons. Thus, the RF wave emitted during relaxation of the magnetization back to equilibrium have a frequency of 126 MHz in this case, as the field strength of the MRI scanner is three tesla. The emitted RF waves are recorded and analyzed, and can be used for both stationary as well as dynamic imaging of various anatomical and physiological situations. Note that the protons do not change position, it is the direction of magnetization that changes.

The origin of contrast in MRI are the differences in texture, and presence of large molecules which affect the free motion of water. This gives rise to differences in the relaxation of spins, which happens on two time scales,

- T_1 is the longitudinal relaxation time constant, and
- T_2 is the transverse relaxation time constant.

T_1 is typically longer than T_2. The contrast in the images are controlled by choices of sequences and sequence parameters. Stanisz et al. [101] presents an overview of the relaxation time constants for a variety of tissue types including blood. They compare the relaxation time constants between magnetic field strengths of 1.5T and 3T. In conclusion, T_2 in blood does not vary significantly with field strength; T_2 = 275 $\pm$ 50 ms for 3T and T_2 = 290 $\pm$ 30 ms for 1.5T. However, the longitudinal relaxation time constant varies with field strength; T_1 = 1932 $\pm$ 85 ms for 3T and T_1 = 1441 $\pm$ 120 ms for 1.5T. All scans were performed *in vitro* at 37°, but the relaxation time constants are also dependent on the hematocrit level, as T_1 decreases when the hematocrit level increases [67].

Magnetic resonance angiography Visualization of the circulatory system, with and without contrast agents, using MRI is called magnetic resonance angiography (MRA). The sequence used for production of the maximum contrast in the AA lumen is called *Native True-FISP*. FISP is short for ”Fast Imaging with Steady state Precession” and covers a specific

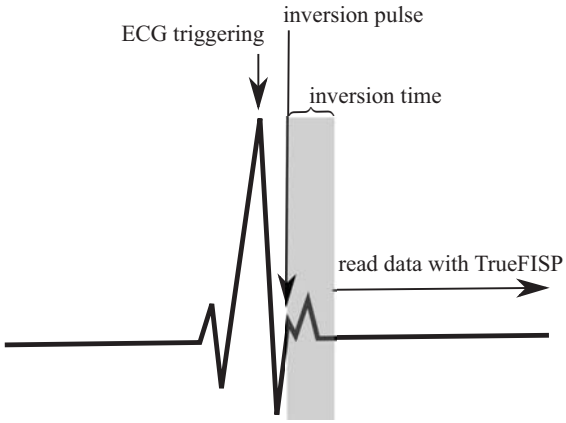

Figure 5.3: Illustration of the imaging sequence when applying the Native TrueFISP. First the imaging sequence is initiated by the R-spike (trigger) in the ECG, then the inversion-recovery pulse is applied. During the inversion time the blood in the probed vascular region is replaced with non-inverted blood. After the inversion time, data is read out using the TrueFISP sequence.

group of imaging pulse sequences where the aim is to establish a steady state in both the longitudinal as well as the transverse magnetization. The Native TrueFISP sequence produces high contrast in the artery of interest without the use of contrast agents such as Gadovist®.

In the TrueFISP sequence it is the ratio $\frac{T_2^*}{T_1}$ which determine the image contrast, which is here changed by in-flow effects. The recorded RF waves are proportional to the transverse magnetization, where the spins initially show overall alignment. But due to inhomogeneities in the field strength, within the region of interest, the spins dephase over time, and this results in loss of signal. This dephasing is characterized by the time relaxation constant T_2^*.
The Native TrueFISP sequence contains several elements necessary to obtain images with high contrast between the vascular lumen and the surrounding tissue. A general inversion-recovery module, which consists of an inversion pulse and the waiting time (inversion time) is shown in Fig. 5.3. The R-spike (the trigger) in the ECG initiates the sequence, which starts by application of an inversion pulse probing the vascular region of interest chosen by the operator, in this case the AA. The inversion pulse is followed by an inversion time period in which the blood in the probed volume is replaced by non-inverted blood. This produces a high contrast between the probed arterial lumen and stationary tissue due to a difference in relaxation time [119]. At the end of the TI period the image data is acquired using the TrueFISP sequence.

The image quality obtained with Native TrueFISP is dependent on the inversion time since this time window must be large enough for all the blood in the probed volume to be replaced with non-inverted blood to produce high contrast as illustrated in Fig. 5.4. Simultaneously, it should be limited in maximum length determined by the recovery of the magnetization in the probed volume, i.e. the relaxation of the excitation back to equilibrium. An inversion time, which is too long, will result in loss of signal, and, hence, lower contrast between the

AA lumen and the surrounding tissue. The inversion time was kept constant during all the MRI scans performed in this work, yet, it did not affect the image quality with regard to the segmentation procedure, see Sec. 5.2.2. However, when dealing with elderly patients (most AAA patients are above 65 years old) it is necessary to carefully plan the TI to obtain the highest image quality.

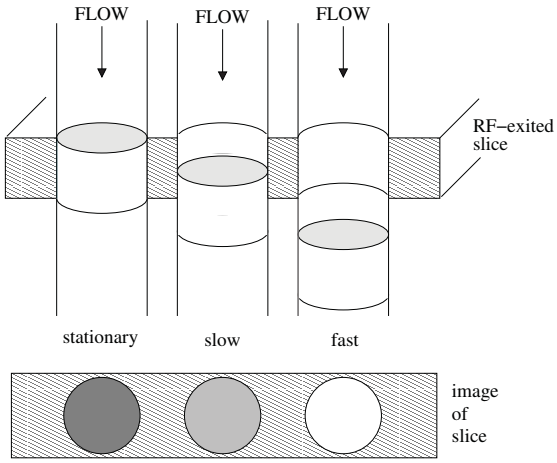

Figure 5.4: Sketch of the origin of contrast in Native TrueFISP sequence. Inspired by Buchong [8].

5.2.2 Segmentation of MRI data

To evaluate flow and structural properties of the AA anatomically correct geometries are preferred for mimicking the *in vivo* situation. In this project the geometries are achieved from MRI scans of 14 healthy volunteers. The demography of the group of volunteers cover differences in age, gender, and smoking habits. An overview of the group is given in Table 5.1.

The segmentation of the MRI data was performed using the commercial segmentation software ScanIP (Simpleware ldt., Exeter, United Kingdom). The geometry included the iliac bifurcation, and was cut just below the branching of the renal arteries. The segmentation procedure is semi-automatic and can be divided into three overall steps; initial automatic coarse segmentation, manual editing of the initial segmentation volume, and finally smoothing and reconstruction of the AA wall. Examples of different AA geometries are shown in Fig. 5.5. Details on the segmentation algorithms can be found in the tutorials and reference guide of ScanIP [58, 59].

Table 5.1: Demographic data for the volunteers included in the research protocol. BMI is body mass index, BMI = [weight (kg)]/[(height (m))^2].

Volunteer	Gender	Age (years)	BMI (kg/m^2)	Smoking
1	Female	26	20.2	No
2	Female	28	23.8	No
3	Female	31	19.0	No
4	Female	28	20.3	No
5	Female	57	29.1	No
6	Female	50	24.0	No
7	Male	27	25.6	No
8	Male	25	21.2	No
9	Male	23	19.9	No
10	Male	34	21.3	No
11	Male	76	22.8	No
12	Male	51	24.2	No
13	Male	53	22.7	Yes
14	Male	57	26.8	No

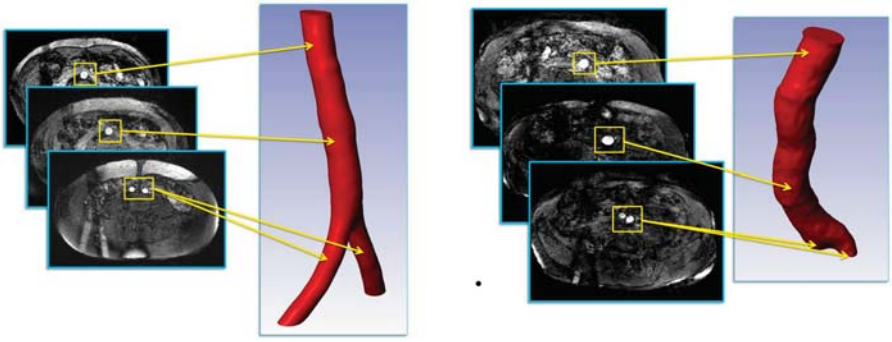

(a) (b)

Figure 5.5: Examples of MRI images used for segmentation. The two examples also illustrate the geometric diversity among the volunteers. (a) 28 years old female, (b) 76 years old male.

Initial automatic segmentation The MRI scan sequences are loaded into ScanIP as a stack of dicom images. During the loading process of the dicom images, complete information on the scan sequence can be reviewed, see Fig. 5.6. In Table 5.2 an overview of selected scan sequence information is provided. The table contains information on image size, specific setup

in the MRI scanner, name of the scan sequence, and information about the volunteer such as name, and date of birth (not included in Table 5.2 due to protection personal information required by the research protocol). Initial cropping and re-sampling of the images, and adjustment of the window width (dynamic range in the image) can be performed prior to import to ScanIP. In this work only the window width was adjusted prior to import to enhance the contrast difference between the AA and surroundings.

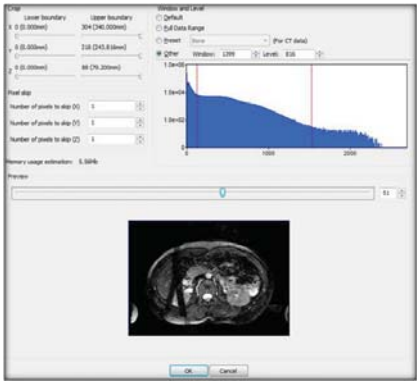

Figure 5.6: Window for adjusting image parameters prior to import to the segmentation software.

The initial automatic segmentation consists of two tasks. First a threshold segmentation is performed which segment the images according to the gray scale values of the pixels in the image. The window of gray scale values are adjusted for each individual set of dicom images, see Fig. 5.7. Second, the ”flood fill” algorithm is applied to fill gaps in the coarse segmented volume (mask). This algorithm is a region grow algorithm applied to the mask by clicking on a pixel in the segmented volume which then acts as input to the algorithm.

Manual editing In the manual editing, two different segmentation algorithms are applied. The algorithm ”confidence connected region growing” is based on the seed point approach of image segmentation. A seed point (pixel) is chosen in the region of interest and the mean and standard deviation of the gray scale pixel values within the initial neighborhood radius defined in the GUI is calculated, see Fig. 5.8. For each iteration the pixels connected to the region are added to the region if the gray scale value of the pixel falls within the confidence interval determined from the mean and the standard deviation of the pixel value for the seed point. For each iteration in the algorithm a new set of mean gray scale value, standard deviation, and confidence interval is calculated. The confidence interval is controlled through the ”multiplier” in the GUI. The second segmentation tool used in the manual editing is called ”paint”, and can be used either with or without restriction on which the pixel gray scale values that can be ”painted” on, see Fig. 5.8. ”Paint” provides editing of segmented masks by hand in order to tidy up the segmentation or disconnect unwanted regions. By adjustment of

Table 5.2: Selected Dicom image information.

Parameter	Value
slice thickness	0.899 mm
repetition time (TR)	700 ms
echo time (TE)	1.7 ms
sequence	NATIVE_TrueFISP_nav_ECG_tra
transmit coil	body
flip angle	72°
pixel spacing	1.118 mm/1.118 mm
window center	580 mm
window width	1195 mm
requested procedure	angiography abdomen
image size	340 mm × 218 mm × 79.2 mm (x y z) 304 px × 218 px × 88 px

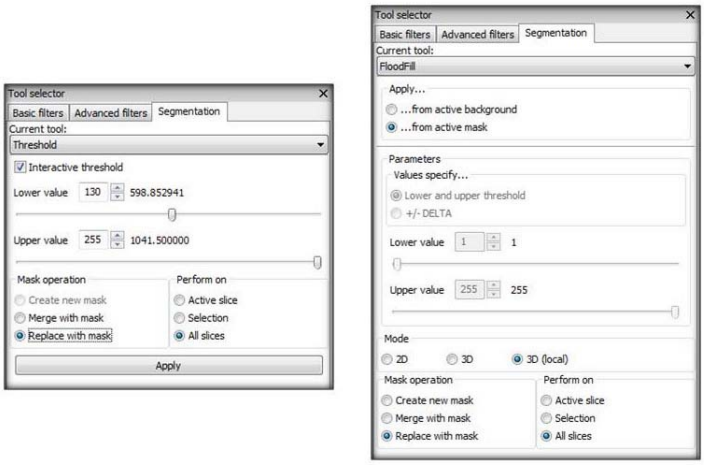

Figure 5.7: The left panel show the GUI for adjusting the threshold algorithm. The right panel show the GUI for adjusting the settings of the ”flood fill” algorithm.

the paint brush size individual pixels can be added or removed from the mask.

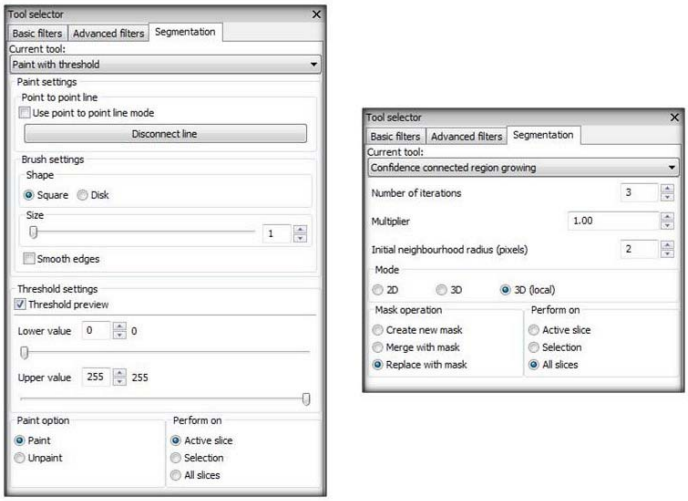

Figure 5.8: The left panel show the GUI of the ”paint” segmentation tool. The right panel show the GUI in which the settings for the ”confidence connected region growing” can be controlled.

Smoothing A smoothing algorithm is applied to the segmented volume to eliminate sharp edges, as these will result in false peak stress points in the simulation model. There are several smoothing algorithms in the ScanIP software. In this work, the smoothing filter called ”recursive Gaussian filter” was applied for all segmented volumes. The visual effect is smooth blurring of the image resulting in an effect compared to looking through a translucent screen. Mathematically, application of this filter corresponds to a convolution of the image with a Gaussian, i.e. a low pass filtering of the image to reduce the noise. The settings of the Gaussian is controlled from the GUI by defining the size of the Gaussian kernel in each direction of the segmented volume, see Fig. 5.9. The size of the kernel determines the number of surrounding pixels included in the smoothing operation.

AA wall reconstruction The AA wall is not visible in the obtained MRI scans, thus the wall geometry was obtained by dilating the lumen mask uniformly and subtract the AA lumen geometry. The dilation of the segmented volume is performed by first producing a copy of the segmented AA lumen. Then a morphological filter is applied to the replica. The morphological filters in ScanIP are a collection of filters based on mathematical morphology which applies to digital image processing. Application of a morphological filter requires definition of a the structure element which characterize the neighborhood of pixels used by the filter, i.e. the larger the structure element the larger the impact of the morphological filter. For reconstruction of the AA wall the ”dilation” option was selected among the morphological filters, see Fig. 5.9.

The final segmented volume of the AA is shown in Fig. 5.10. The final geometry consists

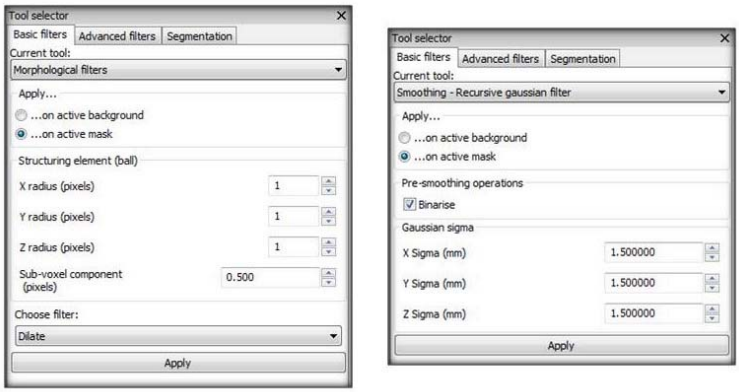

Figure 5.9: The left panel shows the GUI for the morphological filters with the flexibility of choosing size of the structure element and type of filter. The right panel shows the GUI for adjusting the smoothing operation applied on all segmented volumes.

of a lumen part and a wall part which can be exported for FE analysis either as two separate volumes or as a volume consisting of two different domains.

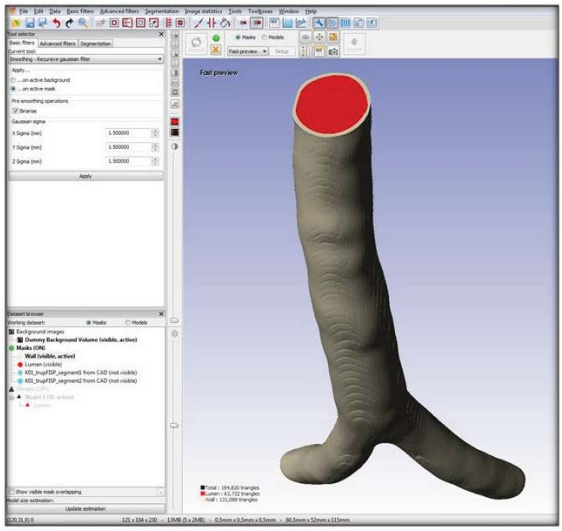

Figure 5.10: Example of a segmented volume consisting of the lumen and the wall of the AA. The example is from a 28 years old female volunteer.

5.3 Ultrasound imaging

In this section the basic principles of ultrasound imaging will be described. First the physics behind ultrasound wave propagation is presented, then the fundamental imaging principles for soft tissue and blood flow are described. This section is based on the book by Jensen [50].

5.3.1 Physical principles

Ultrasonic waves are sound waves with frequencies above the audible range (>20 kHz). Ultrasonic waves propagate in tissue as a disturbance of particles. The pressure impact from the sound wave make the particles oscillate around their mean position. Assuming that the pressure impact of the ultrasound wave is much smaller compared to the equilibrium pressure, the wave propagation is linear. In soft tissue ultrasound propagate as longitudinal waves as shear waves attenuate very quickly. Based on these assumptions the propagation speed of ultrasound in soft tissue is defined as,

$$c_{\text{speed}} = \sqrt{\frac{\kappa}{\rho_0}}\,, \tag{5.2}$$

where c_{speed} is the speed of sound in the media, κ is the bulk modulus of the tissue, and ρ_0 is the mass density of the isonified tissue. c_{speed} increase with bulk modulus, hence low compressibility leads to fast wave propagation. The speed of sound in blood is approximately 1540 m/s, and 1446-1626 m/s in soft tissue (low in fat, high in muscle tissue) [50].

The acoustic pressure exerted by the ultrasonic waves is the basis for imaging with ultrasound. It can be calculated by assuming a harmonic solution to the one dimensional wave equation. Assuming that the spherical wave propagate radially from a central point and characterize the ultrasonic field, the acoustic pressure $p(\vec{\mathrm{r}}, t)$ is

$$p(\vec{\mathrm{r}}, t) = \frac{p_0}{|\vec{\mathrm{r}}|} \sin\left(2\pi f_0 \left(t - \frac{|\vec{\mathrm{r}}|}{c_{\text{speed}}}\right)\right) \quad , \tag{5.3}$$

where $|\vec{\mathrm{r}}|$ is the radial position in the tissue, p_0 is the acoustic pressure amplitude, and f_0 is the center frequency of the transducer transmitting the ultrasonic waves into the tissue. The acoustic pressure described by (5.3) links the spatial position and time through c_{speed}. The ultrasound data acquired for this work was obtained using a convex array transducer (BK8803, BK-Medical, Herlev, Denmark).

The primary physical properties characterizing ultrasound imaging are attenuation and scattering of the transmitted sound waves.

Attenuation The ultrasonic waves attenuate as a function of depth and frequency. The attenuation is caused by scattering and absorption in the tissue. Attenuation of different

tissues is given as dB/[MHz·cm] and depends on the attenuation coefficient (β_n), the center frequency f_0, and the depth in the tissue z. The transfer function expressed in the frequency domain for the amplitude attenuation of a propagating plane wave in tissue is [50],

$$|H(f,z)| = \exp(\beta_0 z + \beta_1 f_0 z) \quad . \tag{5.4}$$

The exponential function in (5.4) contains two attenuation terms. The first term is the frequency independent attenuation, and the second term is the frequency dependent term. The attenuation is dominated by the frequency dependent term, thus the frequency independent term in the exponential function is often left out.

Scattering As the waves propagate through the tissue, scattering occurs due to changes in tissue density and absorption. The backscattering signals propagate in all directions and are received by the transducer. The amplitude, phase, and frequency content of the backscattered signals are used for imaging.

Backscattering from blood originates primarily from the RBCs. The red blood cells constitute approximately 45% of the blood volume whereas the white blood cells constitute 0.8%, and the platelets 0.2%. The cellular component of the blood is suspended in the plasma fluid. The power of the scattered signals varies with flow conditions, as well as vessel type and constituents in the blood. Therefore, ultrasound imaging is widely used in characterization and screening protocols for various cardiovascular diseases.

5.3.2 Data acquisition

Conventional ultrasound scanners use the pulse-echo technique to generate images. A pulsed pressure field is generated by piezoelectric crystals (elements) in the transducer, which propagate through the tissue while undergoing scattering and attenuation. The backscattered (echo) signals are received by the same transducer. The received backscattered signals are in the RF-domain of the electromagnetic spectrum, see Fig. 5.2, hence the acquired data is termed RF-data.

The ultrasound data in this work were acquired using a UA2227 Research Interface (BK-Medical, Herlev, Denmark) implemented on a 2202 ProFocus ultrasound scanner (BK-Medical, Herlev, Denmark), see Hemmsen et al. [40] (Paper III) for details. The ultrasound scans were performed in a duplex mode including B-mode imaging and velocity distribution inside the region of interest as a function of time, i.e. the spectrogram, see Fig. 5.11a. The raw ultrasound data were acquired from the scanner using the research interface equipped with a customized grabber GUI CFU Data Grabber, see Fig. 5.11b. The CFU Data Grabber enables loading of a specific scanner set-up on the scanner, data acquisition from the scanner, fast review of the acquired data, and download of the acquired data to a hard drive.
To obtain usable data, the pulsing strategy for acquiring both B-mode image lines and spectral data is interleaved, i.e. alternating shots of ultrasound pulses for B-mode and spectral

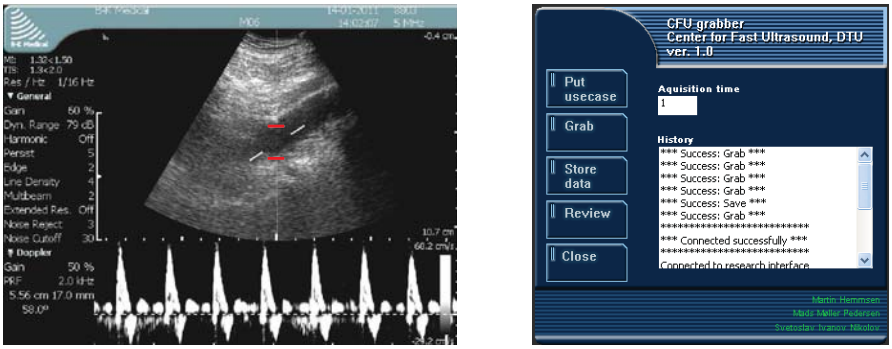

a) b)

Figure 5.11: Illustration of the screen display on a) the ProFocus scanner and b) the CFU Data Grabber GUI, adapted from Hemmsen et al. [40] with permision. In a) the upper window in the console show the B-mode image, and the lower window show the spectrogram for the blood flow variation over time. The spectrogram display the velocity within the range gate placed inside the vessel of interest marked by the range gate, i.e. the red solid lines. The GUI for the research interface facilitates load of specific scan parameters, data acquisition from the scanner, review of the acquired data, and storage on hard drive.

Doppler data acquisition. Each line in the data set is identified by a header, and the data are sorted and processed off line using customized programs written in MATLAB (Mathworks, Natick, MA, USA).

B-mode imaging In dynamic B-mode imaging a multi-element transducer sweeps the ultrasound beam over the region of interest collecting image lines, and displaying consecutive lines as an image. The image lines are formed from the RF-data. The signal processing for reconstruction of B-mode images consists of four overall elements, see Fig. 5.12. First the envelope of the RF-signals is detected utilizing the Hilbert transform. The envelope data are then compressed to a suitable dynamic range to achieve good contrast in the image. Soft tissue encompass large variations in the dynamic range, thus to obtain good quality images this needs to be adjusted for. The final step before image display is application of scan conversion. The scan conversion maps the image lines from rectangular coordinates to polar coordinates, as a convex array transducer is used for imaging in this work.

Spectral estimation The second part of the data is the spectral data, or Doppler data, used for estimation of the blood flow velocity. The Doppler effect is considered as the frequency shift in the ultrasound wave due to motion on the insonified scatters, i.e. the RBCs. The shift in frequency, f_d, is given as [50]

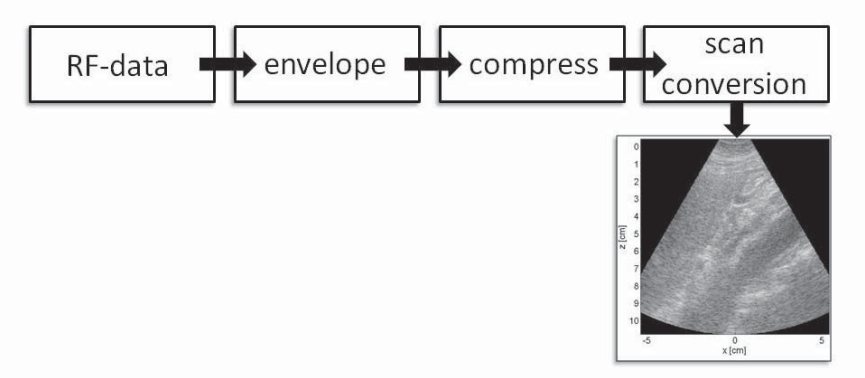

Figure 5.12: The steps in the data processing of B-mode image using data acquired from the research interface.

$$f_d = f_r - f_t = 2f_0 \frac{v\cos(\theta)}{c_{speed}} \quad . \tag{5.5}$$

The transmitted frequency, f_t, corresponds to the center frequency of the transducer, f_0, f_r is the frequency of the received signals, and v is the speed of the insonified scatters, i.e. the RBCs. The Doppler effect is used for velocity estimation in continuous wave ultrasound systems. Satumora [93] was among the first to suggest a continuous wave system for blood flow velocity estimation. The most significant limitation of continuous wave systems is the inability to discriminating tissue depth. A pulsed wave system, on the other hand, is able to discriminate received (echo) signals according to depth. Hereby, it is possible to investigate the blood velocity properties in individual blood vessels at different depths. Among others, Baker [4] suggested such a system.

Pulsed wave systems are based on transmission of short series of ultrasound pulses in well-defined time intervals. The received signals are upon reception sampled according to these time intervals. The echo signal from a single scatter is thus shifted in time due to motion as illustrated in Fig. 5.13a. To trace the displacement of the scatter, the RF-data are sampled in a certain depth indicated by the dashed line in Fig. 5.13a. The resulting sampled signal is seen in the right panel of Fig. 5.13a. The spectrum of the sampled signal is the same as that of the transmitted pulse only shifted in frequency. It can be shown that the frequency scales with the mean velocity of the scatter,

$$\bar{f} = \frac{2v_z\cos(\theta)}{c_{\text{speed}}} f_0 \quad . \tag{5.6}$$

Blood is an assembly of many scatters which results in a complex scatter waveform as illustrated in Fig. 5.13b. Fortunately, (5.6) still applies for velocity estimation based on the spec-

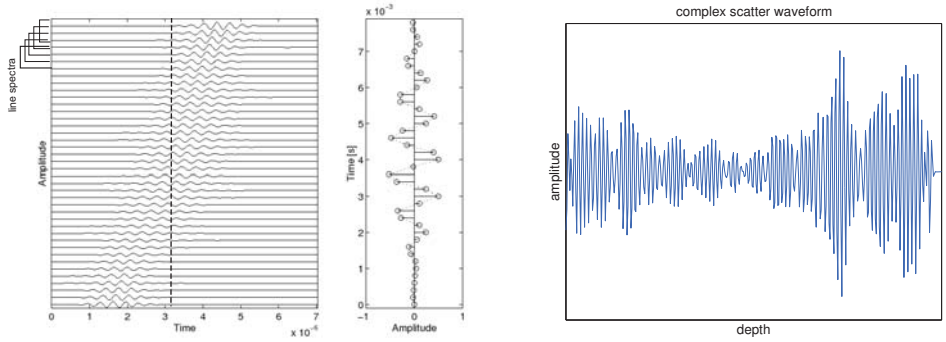

(a) (b)

Figure 5.13: Illustration of the principle behind detection of motion of a single scatter and the sampling of the RF-signals to obtain a better velocity estimate [66]. (a) the left panel show the structure of the data set used for velocity estimation. The first dimension is the RF-signal as a function of depth in the tissue. The second dimension is the number of RF-signal acquired for the scan sequence determined by the time interval of emission. (b) show the complex wave form of the RF-signal from the AA of a healthy volunteer.

trum. The Doppler effect is significantly reduced in pulsed wave systems as the down-shift in frequency, due to attenuation, overshadow the Doppler effect. Hence, the flow dynamics detected with pulsed wave system are based on the scatter displacement rather than the Doppler effect.

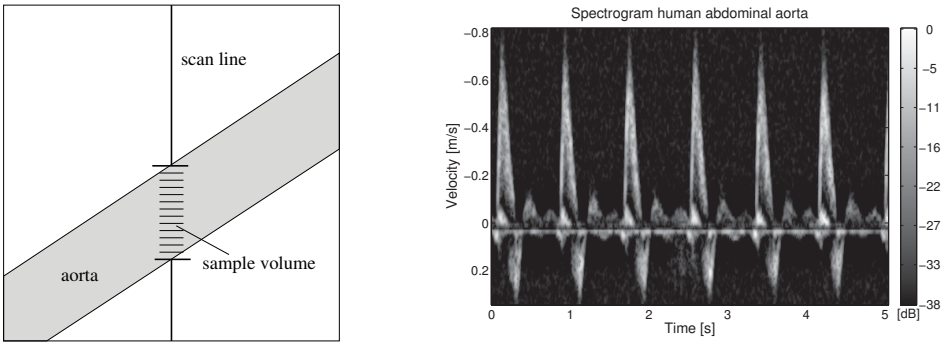

(a) (b)

Figure 5.14: (a) show the principle of the dividing the region of interest into sample volumes for averaging of the RF-signal spectrum over a certain depth. (b) The resulting power density spectrum in the center of the abdominal aorta after 2D spectral estimation. The sonogram is sampled approximately in the center of the abdominal aorta.

To obtain a better estimate of the mean frequency $\bar{f}$ the RF-data are averaged over time and depth following the method suggested by Loupas et al. [66]. Time averaging is performed

by dividing the RF-data into line spectra consisting of 128 echo signals each, see Fig. 5.13a. Averaging is accomplished by applying a window function (Hanning window) on each line spectrum. Depth averaging accomplished similarly to time averaging accept that it is applied to the second dimension of the data set. Hence, the arterial cross-section is divided into smaller volumes (sample volumes) consisting of a number of samples as demonstrated in Fig. 5.14a. The power density spectrum is determined for each sample volume by averaging over the number of samples in the volume. The power density spectrum of each line spectra is calculated as,

$$P(f) = |G(f)|^2 \quad , \tag{5.7}$$

where $G(f)$ is the Fourier transform of the demodulated echo signal. The mean frequency can then be calculated as,

$$\bar{f} = \frac{\int_{-\infty}^{\infty} fP(f)\mathrm{d}f}{\int_{-\infty}^{\infty} P(f)\mathrm{d}f} \quad , \tag{5.8}$$

which is then combined with (5.6) to calculate v_z. In Fig. 5.14b the spectrogram of the velocity variation in the center of the AA of a 53 years old healthy male is seen. The spectrogram is formed by displaying $P(f)$ for each line spectrum side-by-side with time along the x-axis and velocity along the y-axis. The pixel value in the spectrogram indicate the amplitude of the spectrum, which is proportional to the number of scatters moving at that particular velocity. An overview of the signal processing for reconstruction of the power density spectrum is presented in Fig. 5.15.

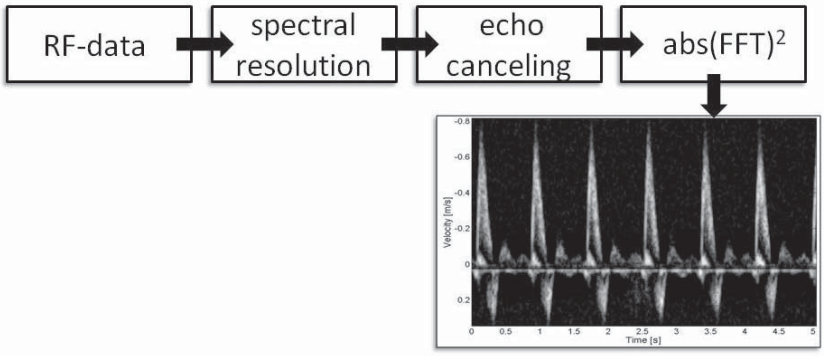

Figure 5.15: The steps in the data processing of spectrogram using data acquired from the research interface. The spectral resolution indicate the process of applying window functions on the acquired spectral data.

5.3.3 AA blood flow profile

To account for the fact that the flow in the AA is pulsating and never fully-developed, complexity to the flow profile is introduced by reformulation of Poiseuille's law for flow in rigid tubes. Mathematically, periodic velocity waveforms can be decomposed into Fourier series when linearity is assumed [107], and then added to the parabolic profile characterizing steady fully-developed flow. In practice, this is done by combining the principles of relating flow rate and pressure developed by Womersley [123], and the determination of the velocity profile when the flow rate is known, as presented by Evans [26]. In this work, the velocity is estimated using (5.6) and (5.8), and the Fourier series is characterized as,

$$V_m = \frac{1}{T}\int_0^T \bar{v}(t)\exp(-jm\omega t)dt\ , \tag{5.9}$$

where T is the duration of one cardiac cycle, $\omega = 2\pi f$ is angular frequency, and m is an index for the harmonics. The relationship between the pressure and volume flow for a single sinusoid was presented by Womersley [123]. Assuming that the blood is a Newtonian fluid, the average spatial velocity over time for a steady pulsatile flow can be found as by superimposing the sinusoidal components for each harmonic frequency [50], i.e.

$$v_{\text{blood}}(t,r) = 2v_0\left(1-\left(\frac{r}{R}\right)^2\right) + \sum_{m=1}^{\infty}|V_m|\,|\psi_m(r,\tau_m)|\cos(m\omega t - \phi_m + \chi_m) \quad , \tag{5.10}$$

where the first term describes steady fully-developed flow in a rigid tube, and the last term is the superposition of the sinusoidal components of the average spatial velocity multiplied by the function ψ_m. In (5.10) ϕ_m is the phase of the sinusoids resulting from the Fourier decomposition, and χ_m is the phase angle of ψ_m. The function ψ_m describes how the velocity changes with time and position over one period for each of the sinusoidal components (harmonics), and is dependent on the radial position in the AA, the angular frequency ω, and the properties of the blood [50],

$$\psi_m(\tau_m, r) = \frac{\tau_m J_0(\tau_m) - \tau_m J_0(\tau_m \frac{r}{R})}{\tau_m J_0(\tau_m) - 2J_1(\tau_m)} \quad , \tag{5.11}$$

where J_n are n'th order Bessel functions of first kind, $\tau_m = j^{3/2}\alpha_m$ and α_m is the Womersley number,

$$\alpha_m = R\sqrt{\frac{\rho_{\text{blood}}}{\mu_{\text{blood}}}\omega_m}\ , \tag{5.12}$$

where ρ_{blood} = 1,060 kg/m^3 is the mass density of the blood, and μ_{blood} = 3.5 mPa·s is the dynamic viscosity of blood.

Complex flow has been observed in the AA by several groups in the 1990s [31, 84, 105]. These observations are partly reflected in the flow patterns obtained in a simple flow simulation in a straight pipe, see Fig. 5.17, using the profiles portrayed in Fig. 5.16.

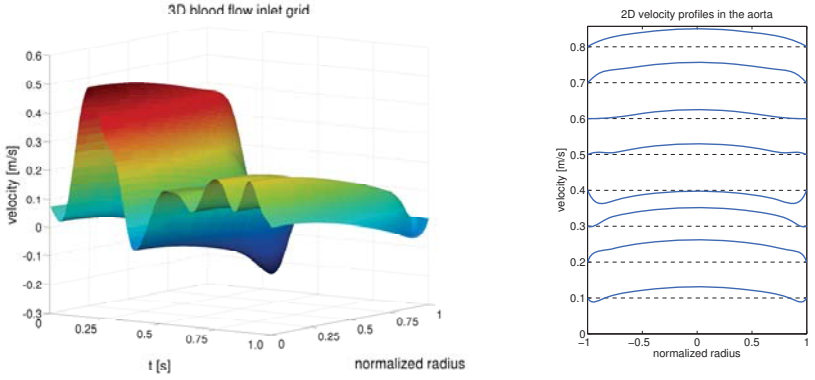

(a) (b)

Figure 5.16: Profiles in the abdominal aorta. a) show an example of the grid applied as inlet condition for the fluid domain in the computational model. The grid consists of a time axis and an axis for the radial position. For each point in the grid there is an associated velocity. b) show the development of the blood flow profile over one cardiac cycle as a function of radial position and time.

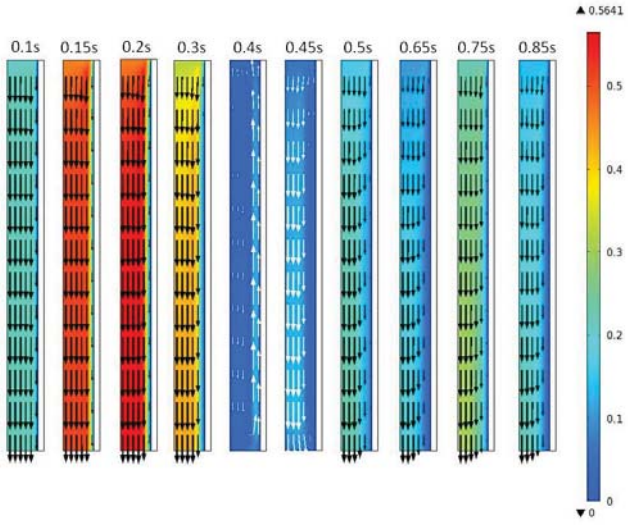

Figure 5.17: Examples of flow patterns in simulation using the subject-specific profiles illustrated in Fig. 5.16. The included time steps were chosen in order to illustrate the complex flow in the human AA. All times are within one cardiac cycle.

CHAPTER

SIX

STUDY I: MATERIAL PARAMETERS

Objective *In order to characterize the mechanical behavior of AA as well as AAA tissue it is necessary to apply appropriate material parameters to the structurally motivated constitutive relation. Material parameters are mostly determined from ex vivo experimental testing of tissue samples, where the measured behavior is fitted to a constitutive relation. The motivation for this study is to investigate whether significant risk factors in relation to AAA development can be identified through a specific pattern in the material parameters. Results suggest that arterial stiffening caused by cigarette smoking is reflected by consistent increase in an elastin-associated parameter, and, moreover by a marked increase in the collagen-associated parameter. In conclusion, it is suggested that arterial stiffening due to smoking appears to be isotropic, which may allow for simpler phenomenological models to capture these effects. There is, however, a pressing need for more detailed histological information coupled with more complete experimental data for the systemic arteries.*

Background

A majority of the published experimental data used for estimation of material parameters in arterial tissue models have been obtained from *ex vivo* uniaxial tests [38, 116], *ex vivo* biaxial tests [110, 111], and *ex vivo* inflation-extension test methods [47, 65]. These tests are valuable for development of general constitutive relations which can be used for quantification and prediction of biomechanical behavior in the AA and AAA. Structurally motivated phenomenological material models such as the 2FF and 4FF models capture the gross mechanical behavior of arteries, and further refinements of these models focus on estimation of material parameters using various statistical techniques [28, 102, 111, 124]. The material parameters have been derived by fitting of experimental data from healthy volunteers and AAA patients. The deduced material parameters reflect the aging process of the AA, as well as the structural features of AAAs, i.e. the degradation of elastin and changes in collagen turn-over and synthesis [28]. Åstrand et al. [2] recently presented a detailed study on the effect of age and gender on the mechanical behavior of the AA with investigation on how this is reflected in the material parameters of the 2FF model. The *in vivo* experimental data were obtained with invasive pressure measurement and non-invasive imaging of the change in diameter during the cardiac cycle with ultrasound, see Stålhand [102] and Sonesson et al. [99] for details. In

the study by Åstrand et al. [2] it was found that the effect of aging, i.e. stiffening of the AA, was much less in women compared to men. Still, it remains to be investigated how significant environmental risk factors affect the mechanical behavior.
Cigarette smoking is the leading self-inflicted risk factor in cardiovascular disease in general, and in AAA development particularly. Approximately 80% of the AAA patients are smokers at the time of diagnosis. The detailed mechanisms behind the vascular damage in systemic arteries induced by smoking remains unclear. However, production of nitric oxide by the endothelium, which mediates vasodilatation in response to altered hemodynamics, is reduced in both active and passive smokers [5]. This endothelial dysfunction can diminish the dilatory capacity of arteries yielding a stiffer wall and promotion of thrombus formation. These detrimental consequences of smoking have long been recognized, but detailed experimental data on associated histo-mechanical changes to arteries are sparse.

Study aims

The goal of Paper I was to gain a better understanding of consequences of smoking on arterial properties and extracellular matrix constituents based on changes in material parameters in the 4FF model.

Methods

Experimental data Inflation-extension data were adapted from Liu and Fung [65]; see the original paper for details. Briefly, 28 initially three-month old Sprague–Dawley rats were exposed to either room air or cigarette smoke for two or three months. Thus yielding four groups of seven rats each, see Table 6.1.

Table 6.1: Overview of the grouping of rats included in the experimental setup.

Group	Age	Smoking
1	2 months	No
2	2 months	Yes
3	3 months	No
4	3 months	Yes

The main pulmonary artery was excised for inflation-extension testing and data were analyzed in terms of the second Piola-Kirchhoff stress and Green strain. To permit use of the 4FF model, the experimental data were regenerated in terms of Cauchy stress components. Note that the constitutive relation in [65] contained reference Green strains, values of which were not given. These reference strains were assumed to be $E^*_{\theta\theta} = 0.182$ and $E^*_{zz} = 0.274$ based on similar data by Debes and Fung [15].

It was not possible to find published experimental data illustrating the effect of smoking on the AA which could be used for estimation of material parameters in the 4FF model. However, Cox et al. [13] performed a study on the longterm effect of smoking on the carotid and femoral arteries in canines. Unfortunately the published stress-strain data could not be utilized in material parameter estimation for the 4FF model as the number of data points was insufficient for reliable estimation.

Constitutive formulation The 4FF model was adopted for the constitutive relation describing the mechanical behavior of the rat pulmonary arteries. By assuming incompressibility for the tissue and a state of plane stress, the analytical forms of the axial and the circumferential Cauchy stress components were determined as,

$$\begin{aligned}\sigma_{zz} = \quad & c\left(\lambda_z^2 - \tfrac{1}{\lambda_\theta^2\lambda_z^2}\right) + c_1^{(1)}(\lambda_z^2-1)\exp\left[c_2^{(1)}(\lambda_z^2-1)^2\right]\lambda_z^2 \\ & +2c_1^{(d)}(I_4^d-1)\exp\left[c_2^{(d)}(I_4^{(d)}-1)^2\right]\lambda_z^2\cos^2(\alpha_0) \quad ,\end{aligned} \tag{6.1}$$

$$\begin{aligned}\sigma_{\theta\theta} = \quad & c\left(\lambda_\theta^2 - \tfrac{1}{\lambda_\theta^2\lambda_z^2}\right) + c_1^{(2)}(\lambda_\theta^2-1)\exp\left[c_2^{(2)}(\lambda_\theta^2-1)^2\right]\lambda_\theta^2 \\ & +2c_1^{(d)}(I_4^d-1)\exp\left[c_2^{(d)}(I_4^{(d)}-1)^2\right]\lambda_\theta^2\sin^2(\alpha_0) \quad ,\end{aligned} \tag{6.2}$$

where the superscripts 1, 2, and d denote axial, circumferential, and diagonal collagen fiber families, respectively, see Fig. 3.5.

Parameter estimation Best-fit values of the eight material parameters were determined via nonlinear regression by minimizing differences between the theoretically predicted and experimentally measured Cauchy stresses in circumferential and axial directions. The objective function to be minimized was,

$$e(\vec{\beta}) = \sum_{i=1}^{n}\left(\left[\sigma_{zz}^{\text{th}}(\lambda_z,\lambda_\theta,\vec{\beta})_i - (\sigma_{zz}^{\text{exp}})_i\right]^2 + \left[\sigma_{\theta\theta}^{\text{th}}(\lambda_z,\lambda_\theta,\vec{\beta})_i - (\sigma_{\theta\theta}^{\text{exp}})_i\right]^2\right) \quad , \tag{6.3}$$

where $\vec{\beta}$ is the vector containing the eight material parameters, and n is the number of data points needed for proper estimation. In case of the 4FF it is required that $n \gg 8$. The minimization routine was carried out using the Optimization toolbox in MATLAB with build-in function *lsqnonlin*. Every time the regression routine was executed a vector containing the uniformly distributed pseudo-random initial guesses was generated. To restrict the parameter space to physically meaningful values, i.e. that all material parameters are non-negative, the

initial guesses of the unknown parameters were confined by lower and upper boundaries. The regression routine was terminated when the tolerance of the regression function was less than 10^{-10}, or when the tolerance on the estimated parameters was less than 10^{-8}. The most representative set of best-fit parameters was chosen as the mean of each parameter based on 100 consecutive estimations.

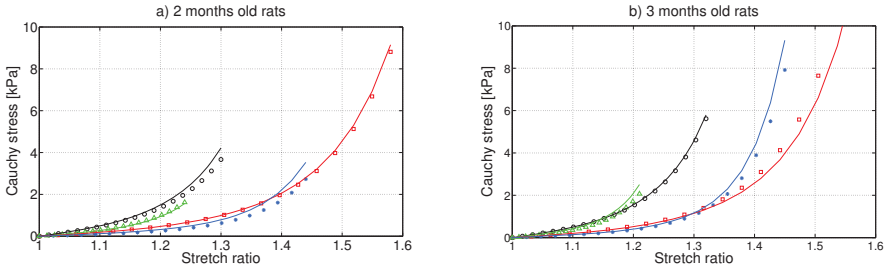

Figure 6.1: Illustrative fit (solid lines) of experimental data (symbols). a) show the result of the fit from rats exposed to smoke for two months and the associated controls. The red open squares are the circumferential stress component for Group 1. The black open circles are the circumferential stress component for Group 2. The blue asterics are the axial stress component for Group 1. The green open triangles are the axial stress component for Group 2. b) show the result of the fit from rats exposed to smoke for three months and the associated controls. The red open squares are the circumferential stress component for Group 3. The black open circles are the circumferential stress component for Group 4. The blue asterics are the axial stress component for Group 3. The green open triangles are the axial stress component for Group 4.

Results

An illustrative fit to data shows that the 4FF model captures well the experimental data from [65], see Fig. 6.1. In general, the Cauchy stress was higher in the circumferential direction compared to the axial direction, and slightly higher in the older rats. More importantly, smoking caused significant stiffening in both age groups. Stresses were generally three times greater in smokers compared to controls when evaluated at a common, upper-level deformation. The effect of smoking on the best-fit values of material parameters in the 4FF model was a marked increase in the value of all parameters, but particularly those associated with collagen, see Table 6.2.

Discussion and Conclusions

The re-interpretation of existing data on effects of smoking on arterial stiffness confirms that smoking accelerates stiffening of pulmonary arteries (cf. [22]), and provides increased insight into this process. Liu and Fung [64] showed that cigarette smoking stimulates an increase in

Table 6.2: Median values of the best-fit model parameters based on data from all 28 animals. Group 1 is the two-month controls, Group 2 denotes the rats exposed to smoke for two months, Group 3 is the three-month controls, and Group 4 denotes rats exposed to smoke for three months. Values in the parentheses show percent increase for smokers relative to controls.

Material parameter	**Group 1**	**Group 2**	**Group 3**	**Group 4**
c (kPa)	0.067	0.115 (+71.6%)	0.076	0.123 (+61.8%)
$c_1^{(1)}$ (kPa)	0.169	0.435 (+168%)	0.103	0.504 (+389%)
$c_2^{(1)}$	1.38	2.83 (+105%)	2.02	5.33 (+164%)
$c_1^{(2)}$ (kPa)	0.482	0.996 (+106%)	0.593	1.36 (+129%)
$c_2^{(2)}$	0.631	1.47 (+133%)	0.809	1.78 (+120%)
$c_1^{(d)}$ (kPa)	0.108	0.44 (+307%)	0.132	0.392 (+197%)
$c_2^{(d)}$	1	2.18 (+118%)	1.844	3.57 (+93.6%)
α_0 (deg)	42.8	57.9 (+35.2%)	17.1	37.7 (+120%)

the volume fractions of both elastin and collagen, together with a decrease in smooth muscle cells in pulmonary rat arteries. The 4FF model similar suggests an increased stiffness due to increases in both the elastin related (parameter c) and collagen related (parameters $c_1^{(k)}$, $c_2^{(k)}$) terms. The elastin related parameter increased by approximately 85%, whereas parameters associated with collagen in general increased at least twofold, thus suggesting an overall nearly isotropic stiffening dominated by collagen.

The material symmetry associated with stiffening due to smoking has not received prior attention in the literature, but increased research on this aspect of stiffening may help increase the understanding of associations between smoking and cardiovascular disease. This could simplify the phenomenological modeling that continues to dominate vascular mechanics. One possibility is to use a concept similar to that in isotropic damage mechanics to model progressive changes in arterial stiffening due to the duration or intensity of smoking.

It should, however, be mentioned that there is a pressing need for more data. Particularly on the time course of longterm effects of smoking. The reason for focusing on pulmonary arteries was simply because the associated data were the most complete. Consequently, there is a need for similar data on systemic arteries, especially for the carotid, the cerebral, and the coronary arteries, as well as the AA, which are susceptible to smoking related diseases. In this regard, it is important to mention that a similar analysis of data from Cox et al. [13] was attempted without success. The associated parameter estimation was deemed unreliable, however, due to their focus on pressure-diameter data alone and too few data points within the systemic pressure range.

In summary, the increased stiffening of arteries due to smoking appears to result from concomitant changes to elastin and collagen, though effects on collagen are more pronounced perhaps because of its intrinsically higher stiffness. These effects appeared to occur nearly isotropically, which could simplify future analysis of the more complete data that are needed.

CHAPTER

SEVEN

STUDY II: MODEL IMPLEMENTATION

Objective *Application of the anisotropic hyper-elastic material model and the fluid mechanical model in a computational simulation requires careful choices of constitutive relation, material parameters, and boundary conditions. Successful model implementation in COMSOL Multiphysics, or any other finite element based modeling software, however, depends on the choice of mesh element geometry and size, numerical solver, and, of cause, the choice of model formulation, the initial conditions, and the boundary conditions. This study is aimed at developing computational models for quantification of the AA biomechanical behavior. The 4FF model characterizes the mechanical behavior. The blood is assumed to be an incompressible Newtonian fluid. The suggested models incorporates subject-specific geometry of the abdominal aorta (AA), subject-specific blood flow conditions, and age-matched material parameters of the 4FF model. The AA geometry is acquired from MRI scans, and the blood flow characteristics are acquired from ultrasound as described in Chap. 5. The AA wall is modeled as a thick-walled cylinder allowing for inspection of the stress distributions within the wall.*

Background

The wall of the human AA is a layered structure consisting of three layers; the intima, the media and the adventitia. The primary structural components of the AA wall are the elastin, collagen fibers and vascular smooth muscle cells. With age the structure of the AA wall changes, it becomes stiffer, and more vulnerable to damage leading to diseases like atherosclerosis and aneurysms, see Chap. 2. So, it is of clinical relevance to provide a computational simulation model to capture these structural changes and gain more insight into the pathology of these diseases from a biomechanical view point. Modeling of both healthy AA and AAA have been the subject in a vast amount of literature over the past 15 to 20 years where the models are becoming more and more sophisticated as knowledge about the vascular wall structure as well as the computational power increase. An introduction to some of the most important developments in computational simulation of both solid and fluid mechanics of the AA and the AAA are presented in Chap. 3 and Chap. 4. Implementation of the 4FF model in three dimensions assuming that it is a thick-walled cylindrical structure allows for inspection of the stresses inside the vascular wall contrary to thin-walled cylindrical structures.

Study aims

The aim of Paper IV was to investigate blood flow patterns in the AA to identify changes and differences related to age and gender, as it is expected that these changes can increase the knowledge of the role of blood flow patterns in AAA development.
The aim of Paper VI was to present the implementation of the 4FF model in a thick-walled axis-symmetric cylinder to mimic the mechanical behavior of the human AA with and without aneurysms.

Methods

Fluid flow model The subject-specific AA geometries were acquired by segmentation of 3D MRI scans, see Sec. 5.2.2 and paper VI for details.

Segmentation of each AA lumen required custom settings in the segmentation algorithms described in Sec. 5.2.2, but in all cases the same customized algorithms were applied in the same order as described in Sec. 5.2.2.

The topic of Paper IV was subject-specific blood flow simulations in the AA, hence only the lumen geometry was included in the FE model simulation. Examples of 3D AA geometries are presented in Fig. 7.1.

Figure 7.1: Example of the geometric diversity among the volunteers. (a) 28 years old female, (b) 51 years old female, (c) 76 years old male, and (d) 51 years old male.

ScanIP provides smoothing and meshing of the segmented AA geometry. The option of meshing and direct export to COMSOL Multiphysics was tried initially, however, it did not provide the desirable flexibility of mesh adjustments performed directly in COMSOL Multiphysics during the computational simulations. This flexibility is necessary to obtain faster convergence of the solution as well as reduction in computation time. Hence, the segmented smooth 3D geometry was imported in COMSOL Multiphysics and meshed in this software environment instead. The segmented geometry included the iliac bifurcation in all cases

accept for two volunteers, and was cut just below the branching of the renal arteries. The reason for the cropping of the geometries was because the image quality was too poor for proper segmentation.

The boundary conditions for the flow model were acquired by reconstruction of the temporal-spatial velocity profile from raw ultrasound data, see Sec. 5.3 as well as Paper III and Paper VI for details. In summary, 11 healthy volunteers were included in the study of age and gender related differences on AA blood flow presented in Paper IV. The mean spatial velocity $\bar{v}$ in the AA was estimated using the power spectrum of the recorded spectral data. The data was acquired real-time and processed off line using MATLAB. From Fourier decomposition of $\bar{v}$ the temporal and spatial evolution can be calculated using the Womersley-Evans method [26, 123]. Neglecting entrance effects the spatial-temporal velocity profile for each subject was calculated as:

$$v(t,r) = 2v_0\left(1-\left(\frac{r}{R}\right)^2\right) + \sum_{m=1}^{\infty}|V_m||\psi_m|\cos\left(m\omega t - \phi_m + \chi_m\right) \quad . \tag{7.1}$$

It was not possible to reconstruct the velocity profiles for all included volunteers due to aliasing in the flow data.

The subject-specific velocity was applied as inlet boundary condition with a corresponding physiological outlet pressure applied as a normal stress to simulate the vascular impedance. No-slip condition was applied to the wall. The blood was assumed to be a Newtonian fluid with $\rho = 1,060$ kg/m^3 and $\mu = 3.5$ mPa·s. The setting in COMSOL Multiphysics for the simulations presented in Paper IV is listed in Table A.1 in Appendix A.

4FF model implementation As a first step in Paper VI, a two dimensional FE model implementation was presented and used as a benchmark to numerically reproduce the stress-stretch relations obtained in the biaxial tension experiments performed by Vande Geest et al. [110, 111]. Next, the 4FF model was implemented in a three dimensional circular axis-symmetric thick-walled cylinder. To implement the 4FF model in COMSOL Multiphysics the general form of the Cauchy stress was used to quantify the wall stress distribution, i.e.

$$\bar{\bar{\sigma}} = \underbrace{-p\bar{\bar{\mathrm{I}}}}_{\text{reaction stress}} + \underbrace{2\bar{\bar{\mathrm{F}}}\frac{\partial\psi}{\partial\bar{\bar{\mathrm{C}}}}\bar{\bar{\mathrm{F}}}^{\mathrm{T}}}_{\text{passive stress}} \quad , \tag{7.2}$$

where p is the Lagrange multiplier, and $\bar{\bar{\mathrm{I}}}$ is the identity tensor. Through out the work only the passive stress state was considered. The AA wall tissue was assumed to be nearly incompressible. A nearly incompressible material is characterized by requiring a much higher exterior work to dilate compared to the amount of work required for a volume-preserving deformation [41]. This assumption requires multiplicative decomposition of the deformation gradient tensor $\bar{\bar{\mathrm{F}}}$ into a volume-changing part and a volume-preserving part [41, 42],

$$\bar{\bar{\mathrm{F}}} = (J^{1/3}\bar{\bar{\mathrm{I}}})\bar{\bar{\mathrm{F}}}_{\dagger} = (J^{1/3})\bar{\bar{\mathrm{F}}}_{\dagger} \quad , \tag{7.3}$$

where $\bar{\bar{\mathrm{F}}}_\dagger$ is the modified deformation gradient, and following this, the right Cauchy-Green tensor can be written as,

$$\bar{\bar{\mathrm{C}}} = (J^{2/3}\bar{\bar{\mathrm{I}}})\bar{\bar{\mathrm{C}}}_\dagger = (J^{2/3})\bar{\bar{\mathrm{C}}}_\dagger \quad . \tag{7.4}$$

The terms $J^{1/3}\bar{\bar{\mathrm{I}}}$ and $J^{2/3}\bar{\bar{\mathrm{I}}}$ in (7.3) and (7.4) refer to the deformation due to volume changes, and $\bar{\bar{\mathrm{F}}}_\dagger$ and $\bar{\bar{\mathrm{C}}}_\dagger$ refer to isochoric deformation. This division of the deformation is also reflected in the formulation of the strain energy function, ψ, which is equally divided in a purely volumetric deformation response, ψ_{vol}, and a purely isochoric deformation response, ψ_{iso},

$$\psi(\bar{\bar{\mathrm{C}}}_\dagger, \vec{\mathrm{M}}^{(k)}) = \psi_{vol}(J) + \psi_{iso}(\bar{\bar{\mathrm{C}}}_\dagger, \vec{\mathrm{M}}^{(k)}) \quad . \tag{7.5}$$

The following form of the volumetric strain energy function [41] was assumed,

$$\psi_{vol} = \frac{\kappa}{2}(1-J)^2 \quad , \tag{7.6}$$

where $\kappa = 10^9$ Pa is the bulk modulus of the tissue. The isochoric strain energy function corresponds to the 4FF model in (3.41) but formulated with modified invariants instead, i.e.

$$\psi_{iso}(\bar{\bar{\mathrm{C}}}_\dagger, \vec{\mathrm{M}}^{(k)}) = \frac{c}{2}(I_{1\dagger} - 3) + \sum_{k=1}^{4} \frac{c_1^{(k)}}{4c_2^{(k)}} \left(\exp\left[c_2^{(k)} (I_{4\dagger}^{(k)} - 1)^2 \right] - 1 \right) \quad , \tag{7.7}$$

where,

$$\begin{aligned} I_{1\dagger} &= J^{-2/3} I_1 \quad , \quad I_{4\dagger}^{(1)} = C_{zz,\dagger} \quad , \quad I_{4\dagger}^{(2)} = C_{\theta\theta,\dagger} \\ I_{4\dagger}^{(3,4)} &= C_{zz,\dagger} \cos^2(\alpha_0) + C_{\theta\theta,\dagger} \sin^2(\alpha_0) \quad , \end{aligned}$$

are the modified invariants used in the implementation of the 4FF model in COMSOL Multiphysics.

Benchmarking of implementation Biaxial tension test of arteries is a well-known method for deducing the biomechanical properties of arteries [91]. To replicate the biaxial test in numerical simulation a tension load of $T_1 = T_2 = 120$ N/m was applied on the edges of the tissue sample geometry, see Fig. 7.2. This tension corresponds to the circumferential tension per unit axial length in a thin-walled cylindrical tube with dimensions corresponding to the AA pressurized to 113 mmHg [110]. The mechanical response was estimated and compared to the analytical solution to evaluate the accuracy of the numerical solver and use this as a benchmark for the model implementation. The result is shown in Fig. 7.3. There was good agreement between the analytical and numerical solutions for the biaxial mechanical behav-

ior. The maximum standard deviation was under 0.5% for both the hoop and axial stress; ± 0.224 kPa and ± 0.283 kPa respectively for the AAA patient group, which has the highest standard deviation compared to the other groups. In general the AA tissue becomes less compliant with age, and AAA tissue is significantly stiffer than normal AA tissue. However, using the mean values of the material parameters indicate that the biomechanical properties of the normal AA for the groups 30-60 years and >60 years are similar. The tissue from the group >60 years is less compliant in the axial direction compared to the group of 30-60 years old healthy subjects. But in the circumferential direction the difference is minimal. This clearly shows that the anisotropy of the AA tissue is captured by the constitutive relation, since the stretch ratios in the two directions are different from each other for all four groups.

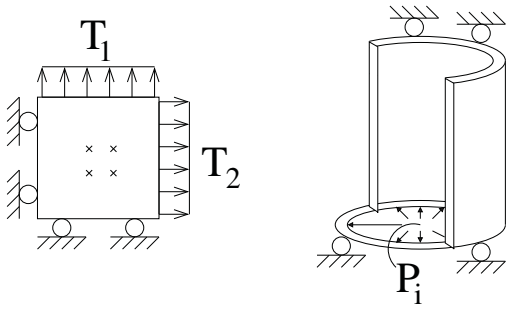

Figure 7.2: Illustration of the simulated biaxial test (to the right) and the inflation-extension test (to the left) setup in COMSOL Multiphysics. The cylindrical vessel is only allowed to moved in the radial direction at the top and bottom, but allowed to move freely at the outer radial edges.

After performing the benchmarking of the implementation, the 4FF model was applied in a three dimensional axis-symmetric cylinder illustrated with the associated boundary conditions in left panel of Fig. 7.2. This implementation was inspired by the inflation-extension test, which is a commonly used experiment for determination of arterial properties, as the healthy geometrical configuration of the artery is preserved [45]. The cylinder was modeled as a thick-walled cylinder which allows for inspection of the wall stress distribution inside the cylindrical wall.
The model settings are listed in Table A.2 and Table A.3.

Results

Influence of geometry on flow patterns In the investigation of the influence of age and gender four parameters were chosen for comparison; age, AA diameter, velocity in the peak systole (PS), and velocity at the end diastole (ED). It was not possible to reproduce the spectrogram for all volunteers due to aliasing, hence the velocities at PS and ED was read of the video sequences obtained simultaneously. The results are summarized in Table 7.1.

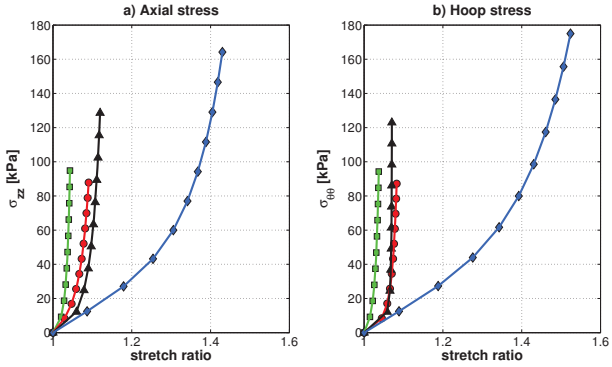

Figure 7.3: (a) The axial Cauchy stress components. (b) The circumferential (hoop) Cauchy stress components. The symbols are the analytical solution, and the solid lines are the numerical simulation of the biaxial test. The blue color represents the youngest group of AA tissue aged 19-29 years. The black color denotes the middle-aged group aged 30-60 years. The red color denotes the oldest AA group aged 61-79 years, and the green color represents the AAA patients.

Table 7.1: Blood flow velocity parameters for the 11 volunteers.

Parameter	**Males**		**Females**	
Age	$<$ 35 years	$\geq$ 35 years	$<$ 35 years	$\geq$ 35 years
AA diameter (mm)	17.5 ($\pm$ 1.60)	19.7 ($\pm$ 1.33)	12.4 ($\pm$ 0.605)	17.0 ($\pm$ 0.113)
PS velocity (m/s)	0.978 ($\pm$ 0.145)	0.836 ($\pm$ 0.127)	1.02 ($\pm$ 0.336)	0.891 ($\pm$ 0.027)
ED velocity (m/s)	-0.075 ($\pm$ 0.016)	-0.059 ($\pm$ 0.018)	-0.069 ($\pm$ 0.004)	-0.072 ($\pm$ 0.009)

The AA diameter increases with age for both genders. The average diameter among males is larger compared to the female group. Comparing the velocity at PS and ED the highest positive velocity (forward flow towards the iliac bifurcation) is in the young group of both genders. The velocity at ED is more even in magnitude among the volunteers, except in the group of elderly males where the velocity is lower. The marked influence of the geometry on the velocity field is seen in Fig. 7.4 where a young female and an elderly male are compared.

3D implementation The material parameters used for the 4FF model was the median value of the parameters presented by Ferruzzi et al. [28]. This is because the mean provides a more conservative measure of the arterial stiffness compared to the median [27]. In addition, using the median of each material parameter within each age group decreases the influence from outliers, and, thus, provides better reflection of the general mechanical behavior within each

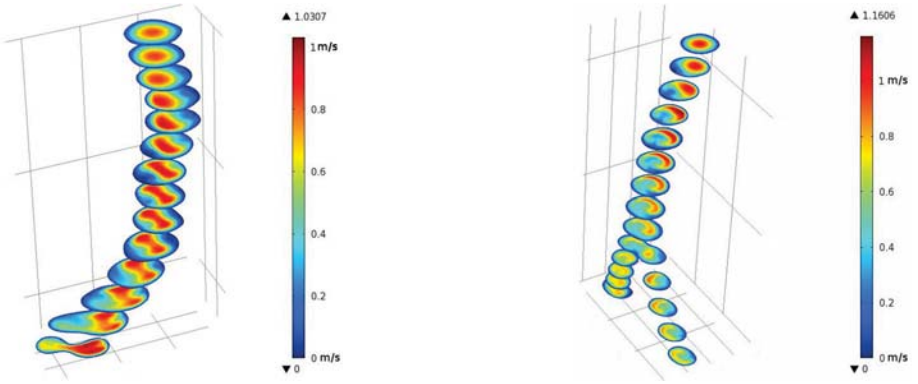

Figure 7.4: Example of the blood flow velocity pattern at PS in the AA. The distribution of velocity in the AA of a 76 years old male is shown to the left. To the right the velocity distribution in the AA of a 28 years old female is shown. Geometries are not to scale.

group. This is illustrated in Fig. 7.5.

In Fig. 7.6 the principal stress components within the vessel wall is shown for the elderly group of healthy subjects and the AAA patients. The applied inner pressure is 80 mmHg (red lines) and 120 mmHg (black lines) respectively. With the 3D model it is possible to investigate the stress distribution within the AA wall, see Fig. 7.6. The circumferential stress component is the largest through out the wall. The axial stress is almost constant varying around 10 kPa, and the radial stress increase from the applied inner pressure at the luminal face of the wall to zero at the external part of the wall. Comparing these results to the work by Di Achille et al. [18] the circumferential stress components show similar distribution. They used data for a specific AAA patient, and in Paper VI the median values for the material parameters were used. Residual stress was not accounted for.

Discussion and Conclusions

The implementation of the fluid flow presents unique flow patterns for each individual. Combination of ultrasound flow data and subject-specific geometry provides a unique tool for development a patient-specific model for characterization of the wall stress distribution as AAA development is influenced by the hemodynamics. The results in Paper IV revealed a close relation between the flow patterns and the lumen geometry as the geometry showed to have the highest impact on the flow patterns. This motivates for the use of patient-specific geometries to gain knowledge on how flow patterns change with age, and how this might initiate AAA development.

The 4FF was successfully implemented in both two and three dimensions using the mean values of material parameters for three different age groups as well as AAA patients. In the search of a proper description of the mechanical behavior of both AA and AAA it is common

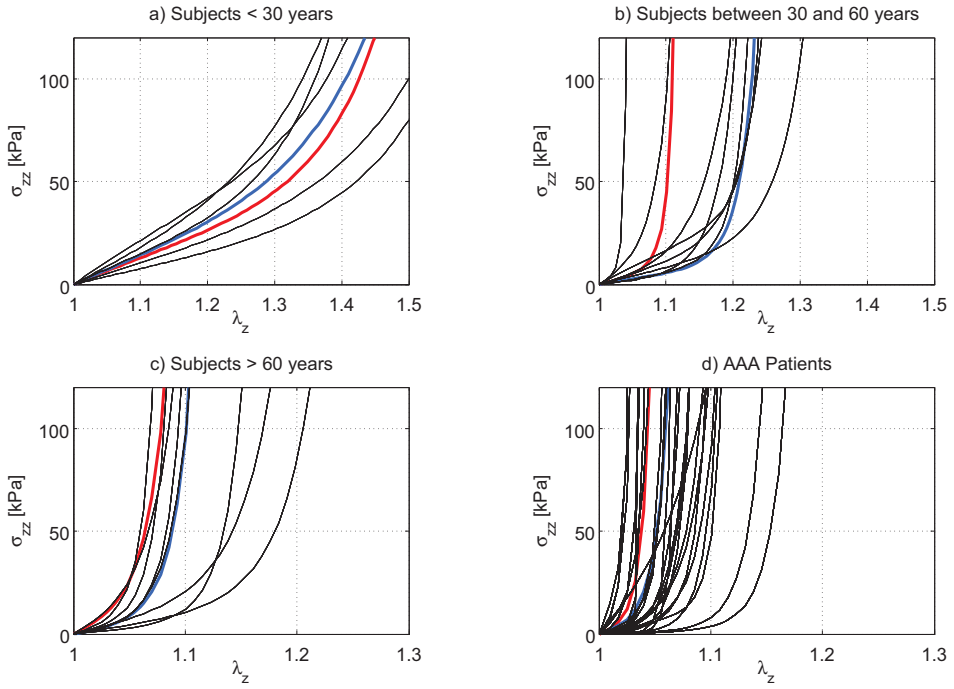

Figure 7.5: Illustration of the mechanical behavior of AA tissue within the three age groups and AAA patients. The behavior is determined using the 4FF model and the material parameters listed in Ferruzzi et al. [28]. a) the axial stress-stretch relation for the youngest group of healthy subjects. b) the axial stress-stretch relation for the middle-aged group of healthy subjects. c) the axial stress-stretch relation for the elderly group of healthy subjects. d) the axial stress-stretch relation for the AAA patients. The mean of material parameters is marked by the solid red line, and the median of the the material parameters is marked by the blue solid line. Note the reduced stretch ratio magnitude in c) and d).

in the literature (cf. the review by Vorp [115]) to apply the mean values of the material parameters. But as Fig. 7.5 shows, the mechanical behavior within a general population is better reflected by the median of the material parameters compared to the mean. However, the implementation of the 4FF model in three dimensions by using the material parameters based on biaxial testing provides new insights into the mechanical behavior of both AA and AAAs.

Recently, the isotropic representation of elastin in structurally motivated phenomenological material models such as the 4FF and the 2FF model has been questioned [62, 98, 126]. Specifically, elastin is speculated to induce circumferential stiffening [126]. Hence, Paper V presents a comparison of two different anisotropic models for elastin; the model proposed by Gundiah et al. [36] which accounts for multiple preferred elastic fiber directions, and a reduced version of the Gundiah model that only accounts for one preferred elastic fiber direction [27]. Comparing the two suggested anisotropic models of elastin to the isotropic Neo-Hookean model the improvements of the fit was not significant. However, the anisotropic

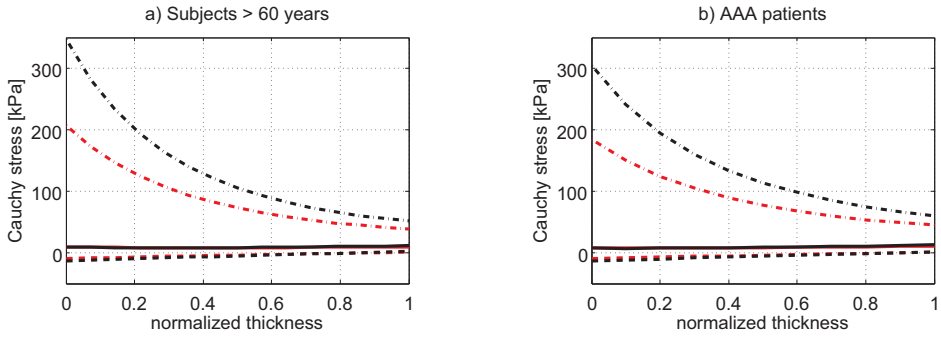

Figure 7.6: Comparison of the intramural stress distribution in a) healthy subjects above 60 years of age and b) AAA patients. The three principal stress components are plotted at 80 mmHg (red lines) and 120 mmHg (black lines) respectively. The solid line is the axial component, the dashed line is the radial stress component, and the dash-dot line is the circumferential stress component.

model accounting only for one preferred direction of orientation provided a better fit to the AA data at high stretch levels. This contradicts the common assumption that the stress in higher stretch regions is mainly produced by collagen. Overall, the inclusion of extra parameters in the 4FF model due to the anisotropy of elastin did not improve the descriptability of the 4FF model regarding AAAs. Thus, the Neo-Hookean representation of elastin in the 4FF model captures the mechanical response of the AA as well as the AAA.

CHAPTER

EIGHT

STUDY III: MODEL PREDICTABILITY

Objective *Experimental data for parameter estimation has been obtained both in vivo and ex vivo. The experimental data are applied in estimation of material parameters for the structurally motivated constitutive models, such as the 4FF model. The purpose of this study is to compare the mechanical behavior predicted by the 4FF model to in vivo mechanical behavior obtained from ultrasound scannings. The method involves signal processing and construction of a FSI model environment. The predictability of the 4FF model is evaluated within a group of three healthy volunteers aged 53 to 76 years including one female and two males, as well as one smoker, thus capturing three of the major risk factors related to AAA development. The material parameters of the 4FF model are based on averaged human data from a wide population study. In the FSI simulation age-matched material parameters are applied for each volunteer. The simulation results indicate that the 4FF model overestimates the displacement of the AA wall in this FSI simulation setup. The volunteers included in this study cover differences in age, gender, and smoking habits which capture the three most common risk factors in AAA development.*

Background

The mechanical behavior of the AA wall influence the mechanobiology which controls the overall vascular homeostasis [46]. Imbalances in the vascular adaptation to various biological stimuli can lead to vascular pathologies such as atherosclerosis and AAA development [45, 76, 109]. Therefore, it is interesting to study the AA wall in a computational simulation environment to gain more knowledge about the onset of mechanical events which might lead to these pathologies. In order to do this, both the constitutive framework and the associated material parameters should be chosen carefully.

Experimental data have been obtained both *ex vivo* and *in vivo*. The majority of the *ex vivo* data are obtained from either uniaxial tests, biaxial tests or inflation-extension tests [17, 38, 47, 110, 111, 116]. On the other hand, the *in vivo* data are primarily achieved using medical imaging techniques such as ultrasound imaging [57, 100, 102] or MRI [70]. The material parameters for the 4FF model published by Ferruzzi et al. [28] are considered the most complete, as they cover three different age groups of normal AA tissue samples, as well as a large group of AAA patients. The experimental data used for the fitting was originally

obtained by Vande Geest et al. [110, 111]. Still, however, it remains to be investigated how well these averaged material parameters fit the general population in order to evaluate the predictability of the 4FF model.

Study aims

The aim of this study is to compare the wall dynamics predicted by the 4FF model and *in vivo* wall dynamics obtained with ultrasound. The predictability of the 4FF model is evaluated in three healthy volunteers. The three volunteers cover differences in age, gender, and smoking habits, thus capturing the three most common risk factors in AAA development, i.e. increasing age, male gender, and smoking [87, 94], see Sec. 2.3.

Methods

In vivo data Previously, ultrasound has been used for characterization of human AA mechanical behavior by estimation of the elastic pressure-strain modulus, E_p, [57, 68, 100],

$$E_p = \frac{d_d(p_s - p_d)}{d_s - d_d} \quad , \tag{8.1}$$

where d_s, d_d are the AA diameter in systole and diastole, and p_s, p_d are the luminal pressures in systole and diastole. This method of wall characterization presents a few challenges. The method relies on the macroscopic relation between pressure and diameter, while AAA development is related to structural changes at the microscopic level, i.e. elastin degradation and altered collagen cross-linking [109]. The measurement of the luminal pressure in the AA is another challenge as the conventional brachial measurement results in an overestimation of the stiffness [121], and the alternative is invasive pressure measurement [99]. Non-invasive measurements are preferred due to minimized health risks for the patients.

The acquired *in vivo* data sets contain two types of data; data for reconstruction of B-mode images, and data for estimation of blood flow velocities and wall dynamics. The data was acquired using a convex array transducer connected to a 2202 ProFocus scanner implemented with a UA2227 research interface, see Sec. 5.3.2 for the detailed description. The velocity estimation and reconstruction of the flow profile in the AA were performed according to the theory described in Sec. 5.3.2 and Sec. 5.3.3.

The wall motion of the AA was estimated from the same data set used in the velocity estimation. The acquired data set provide full flexibility of extracting the RF-data at a specified depth. The sampling of the spectral data for motion estimation starts at the top of the range gate, see Fig. 5.11a, and stops slightly below the range gate. The range gate is positioned by the operating physician. An example of the acquired spectral data after envelope detection is displayed in Fig. 8.1. In all cases, the position of the range gate was inspected on the video sequences to determine whether the wall was positioned in the top or the bottom of the range

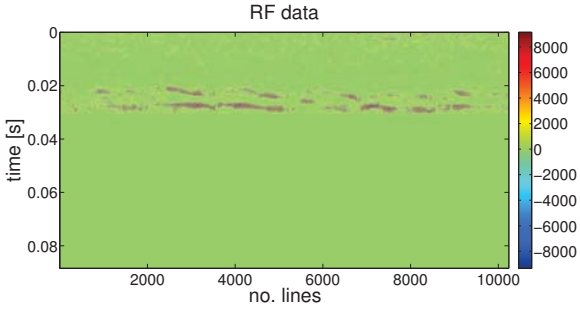

Figure 8.1: Example of the RF data after envelope detection.

gate so that the sample volume could be determined properly.

Measurements of the motion along the scan line exclude detection of the axial motion. The autocorrelation technique was applied on the received RF data, thus the velocity component along the scan line was determined as [50, 52, 66],

$$v_{\text{wall}} = -\frac{c_{\text{speed}} f_{prf} \sin(\theta)}{4\pi f_0} \arctan\left(\frac{\mathcal{I}\{R(1)\}}{\mathcal{R}\{R(1)\}}\right) \quad , \tag{8.2}$$

where f_{prf} is the pulse repetition time, $\mathcal{I}\{R(1)\}$ is the imaginary part of the autocorrelation function, $R(\tau)$ at lag one, and $\mathcal{R}\{R(1)\}$ is the real part of $R(1)$. The autocorrelation technique is widely used in medical ultrasound scanners for visualization of the blood flow. The autocorrelation technique was proposed by Kasai et al. [52], however, to obtain a better velocity estimate the 2D autocorrelation technique proposed by Loupas et al. [66] was applied in this study. This technique incorporates both estimates of the mean Doppler frequency and the mean RF frequency for each position inside the defined sample volume, see Sec. 5.3.2.

The displacement field, $\vec{\mathrm{u}}(\vec{\mathrm{x}}, t)$, for the AA wall is defined as,

$$\vec{\mathrm{u}}(\vec{\mathrm{x}}, t) = \vec{\mathrm{x}} - \vec{\mathrm{X}}(\vec{\mathrm{x}}, t) \quad , \tag{8.3}$$

where $\vec{\mathrm{x}}$ is the position vector of a point in the AA wall in a deformed configuration, see Sec. 3.1.1. The vector $\vec{\mathrm{X}}$ denotes the reference position of the same point in the AA wall. The reference configuration was assumed to be the geometry at the end diastole of the cardiac cycle defined as the last local minimum in the time-velocity spectrogram before peak velocity, see Fig. 8.2. The displacement over time can be determined by integration of the velocity field over time,

$$\vec{\mathrm{u}}(\vec{\mathrm{x}}, t) = \int_0^{T_{\text{pulse}}} \vec{\mathrm{v}}(\vec{\mathrm{x}}, t) dt \ , \tag{8.4}$$

where T_{pulse} is the length of the cardiac cycle in seconds.

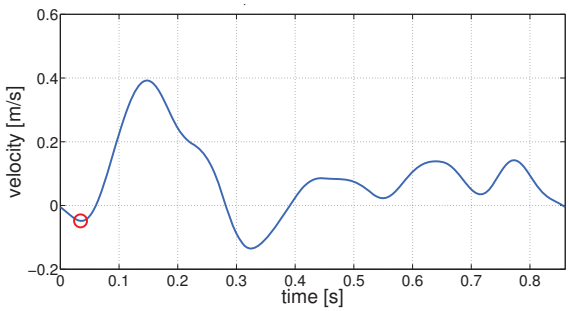

Figure 8.2: Plot of the average velocity variation over the cardiac cycle. The position of the end diastole is indicated by the red circle. The velocity variation is based on spectral data acquired from the AA of a 53 years old healthy male.

Constitutive framework The AA wall material is assumed to be nearly incompressible resulting in a decomposition of the strain energy function (4FF model) into a volumetric and isochoric deformation as described in Paper VI and Chap. 7. The material parameters were adopted from Ferruzzi et al. [28] as the median of the listed parameters. The parameters for the individual age groups are listed in Table 8.1.

Table 8.1: Material parameters applied in Paper II.

Parameter	Middle-age	Elderly
c [kPa]	8.05	$3.02\times\ 1^{-10}$
$c_1^{(1)}$ [kPa]	1.85	28.975
$c_2^{(1)}$	12.720	19.940
$c_1^{(2)}$ [kPa]	0.580	2.850
$c_2^{(2)}$	15.860	30.140
$c_1^{(d)}$ [kPa]	7.190	16.340
$c_2^{(d)}$	16.660	59.140
α_0 [deg]	48.9	47.7

FE modeling As described in Chap. 7 the 4FF model was implemented in the commercial FE code COMSOL Multiphysics. The geometry of the AA was simplified as a 10 cm long cylindrical vessel having a lumen radius corresponding to the measured lumen radius for each volunteer. The wall thickness was assumed to be uniform, i.e. 1.5 mm in the reference

configuration before application of luminal flow, see Table 8.2. The AA wall was modeled as a thick-walled cylindrical structure. The fluid and the solid domains were coupled during the simulations by letting the total stress induced by the pulsating blood control the displacement of the AA wall.

Table 8.2: Anatomical and physiological AA data for the volunteers included in Paper II.

Volunteer	Diameter	Wall thickness	Peak velocity
5	13.2 mm	1.5 mm	0.40 m/s
11	13.9 mm	1.5 mm	0.45 m/s
13	15.6 mm	1.5 mm	0.39 m/s

The AA wall was fixed at the upper and lower boundary to simulate the tethering of the AA. On the external lateral wall boundary a pressure of 0.87 kPa was applied to simulate the abdominal pressure under normal conditions. In this work the reference configuration was assumed to be the geometry at the end-diastole pressurized to 80 mmHg (10.7 kPa) resulting in a radial residual displacement. These model settings are summarized in Table A.4.

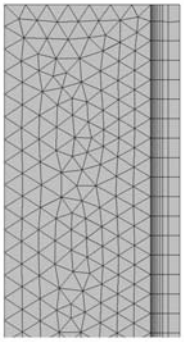

Figure 8.3: Mesh of the fluid and solid domains in the fluid-structure interaction model. The figure is a zoomed example of the complete geometry to obtain a better visualization of the mesh details.

The model is axis-symmetric, hence it was only necessary to mesh a rectangular model consisting of a fluid domain and a solid domain, see Fig. 8.3. The fluid domain was meshed using a user-controlled mesh algorithm in COMSOL Multiphysics calibrated for fluid dynamics. A mesh convergence test was performed and the solution was considered stable when further refinement of the mesh resulted in changes less than 1% in the peak velocity in the center of the AA lumen. A stable solution was achieved with 1680 tetrahedral elements, see Table A.4.

The solid domain was meshed with a fixed number of rectangular elements in the axial direction. The number of elements in the radial direction was determined from a mesh convergence test comparing the magnitude of the circumferential Cauchy stress, $\sigma_{\theta\theta}$, at positions inside the AA wall in two consecutive refinement steps. The solution was considered stable when further refinement of the mesh resulted in changes less than 10 Pa in the magnitude of $\sigma_{\theta\theta}$. A stable solution was achieved with 8 rectangular elements in the radial direction. The rectangular elements increase in width trough the wall, i.e. the elements are more slender at the inner wall boundary compared to the outer wall boundary, see Fig. 8.3. The reason for this was to ensure fast convergence as the 4FF model is highly nonlinear and resulted in large stress gradients at the inner wall when applying a constant luminal pressure of 80 mmHg as described in Paper II. See for example Fig. 7.6.

Results

Blood flow Due to aliasing in the acquired ultrasound data it was only possible to produce realistic blood flow profiles for three of the 14 volunteers included in this study. Fig. 8.4 show the velocity averages over the radial position at several instances during the cardiac cycle. Fig. 8.4a show the blood flow profiles for a 57 years old female. For comparison Fig. 8.4b and Fig. 8.4c show the blood flow profiles in the AA of two males aged 53 and 76. The maximum velocity during the cardiac cycle occurs within the first third of the cardiac cycle with a magnitude of 0.39 m/s to 0.45 m/s, see Table 8.2.

These differences in blood flow are illustrated as a function of lumen radius in the three volunteers in Fig. 8.5. As it can be seen, a parabolic flow profile is never obtained. This was also expected, as the flow in the AA is affected by curves and bends, as well as flow dividers such as the branching of the celiac trunk, the renal arteries, and the iliac bifurcation. The flow profile shifts from a blunt forward flow profile at peak systole through a complex profile with both forward and backward flow, and recurrence to the blunt profile at the end diastole of the cardiac cycle. These observations are similar to the observations of complex flow in the AA [31, 84, 105]. The reconstructed blood flow profiles were defined on a grid in order to apply them as inlet conditions in the FSI model, see Fig. 8.6.

Wall behavior The estimation of the wall displacement was performed by locating either the lower or upper boundary of the AA using the information from the ultrasound scanning videos. To obtain a good measure of the displacement, the motion detection was performed by averaging over a window of 2.5 wavelengths of the transmitted ultrasound pulse, $\lambda_{\text{wavelength}}$, centered around the chosen wall boundary. The resulting displacements of the AA wall for each of the three volunteers are depicted in Fig. 8.7. The displacement was tracked during the first complete cardiac cycle (first peak systole to second peak systole) in the data sequence.

Looking at the wall displacement curves in Fig. 8.7, the displacement for the female volunteer was calculated from a sample volume centered around the upper AA wall boundary. For the

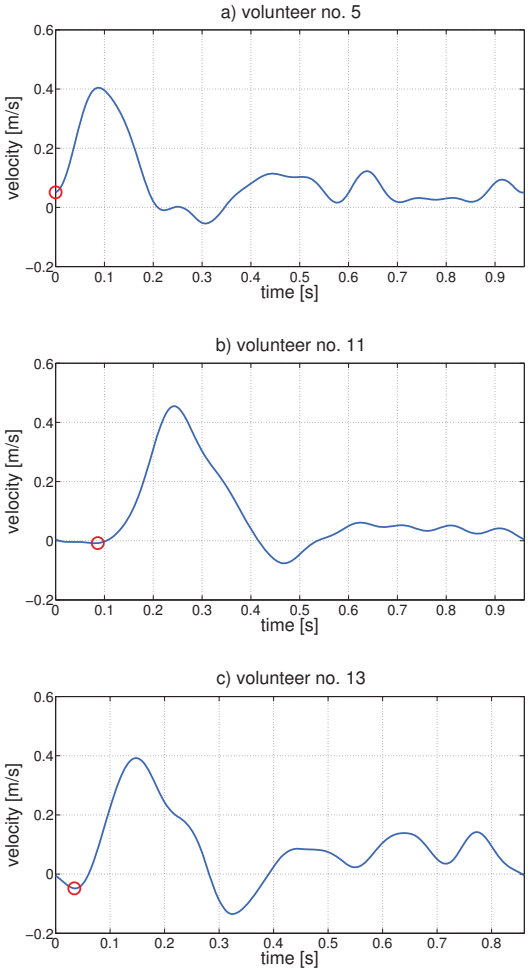

Figure 8.4: Plot of the velocity evolution during the cardiac cycle for three volunteers; a) a 57 years old healthy female (volunteer no. 5), b) a 76 years old healthy male (volunteer no. 11), and c) a 53 years old healthy male (volunteer no. 13). The velocity is averaged over the radial position. The red circle indicate the position of the end diastole during the cardiac cycle.

two male volunteers the displacement was tracked at the lower AA wall boundary. Table 8.3 summarize the estimated total displacement from the ultrasound data, and the calculated stretch ratio for each of the three volunteers. The total displacement is highest for the female volunteer (0.59 mm) compared to the male volunteers, where the 76 years old male show a 7.1% higher displacement compared to the 53 years old male volunteer.

For the female volunteer the AA wall constrict slightly (0.2 mm) at the beginning of the cardiac cycle, and then dilates, only to return to the reference configuration at the end of the

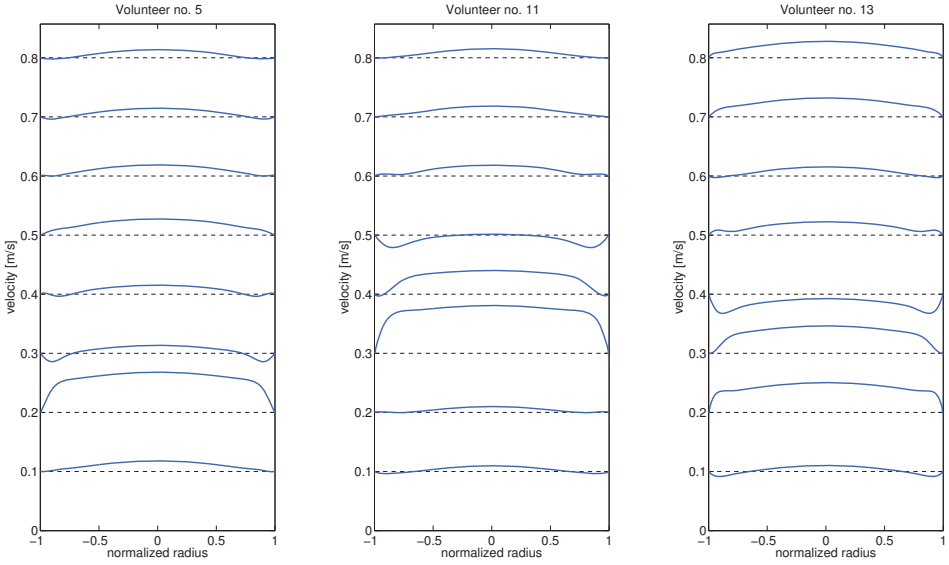

Figure 8.5: Plot of the blood flow profile for three volunteers; a) a 57 years old healthy female (volunteer no. 5), b) a 76 years old healthy male (volunteer no. 11), and c) a 53 years old healthy male (volunteer no. 13). The plot show the difference in evolution of the flow profile. The profiles are reconstructed from acquired *in vivo* data using (5.10).

Table 8.3: Experimentally acquired measures of the total displacement u_{total}, and the resulting stretch ratio, λ, for each volunteer.

Volunteer	$\mathbf{u}_{\text{total}}$ **[mm]**	λ
5	0.59	1.09
11	0.45	1.076
13	0.42	1.068

cardiac cycle, see Fig. 8.7. Comparing the displacement, relative to the diameter at the ED, over the cardiac cycle for each male volunteer, a slight constriction (0.15 mm) of the AA in volunteer no. 11 is observed towards the end of the cardiac cycle, where the motion observed for volunteer no. 13 is only dilatation.

Simulation results The FSI model runs over an entire cardiac cycle for each of the three volunteers presented here as examples. To compare the simulation results, the circumferential stretch ratio and the radial displacement are presented in Fig. 8.8.

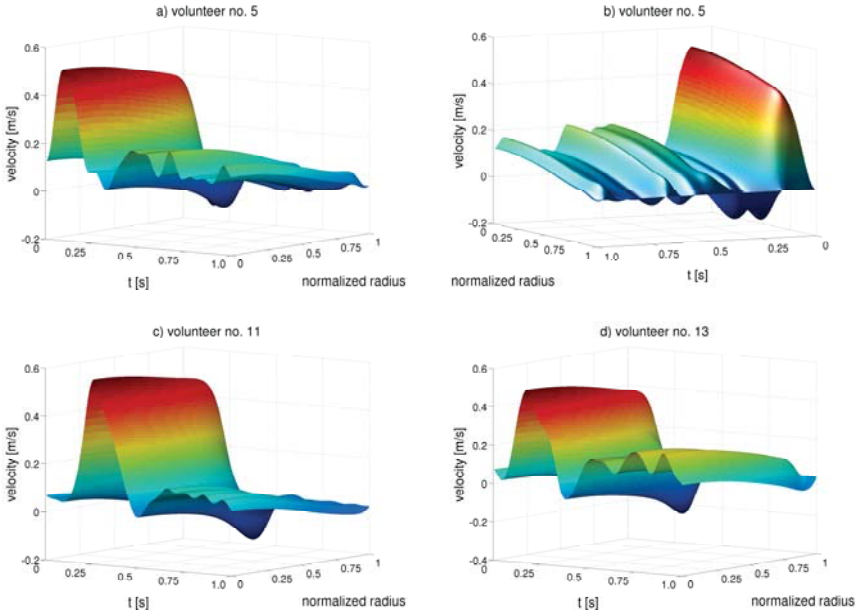

Figure 8.6: Three dimensional grid implemented as boundary condition in the FSI model for three volunteers; a) a 57 years old healthy female (volunteer no. 5), b) the velocity grid for volunteer no. 5 seen from the back, c) a 76 years old healthy male (volunteer no. 11), and d) a 53 years old healthy male (volunteer no. 13).

The radial displacement and the circumferential stretch ratio is extracted from four positions in the AA wall. The positions are defined as percentage of total wall thickness, i.e. position inside the AA wall along the radial direction, with 0% at the luminal wall boundary, and 100% at the external lateral boundary of the AA wall. The displacement is highest at 0% wall thickness in all three cases, and decreases through out the wall, see Fig. 8.8. The simulation model predict a significantly higher displacement of the AA wall compared to the experimentally measured. The displacement of the AA wall of volunteer no. 13 is more than four times higher compared to the *in vivo* measurement, i.e 1.9 mm (average) in simulation versus 0.44 mm *in vivo*. The same pattern is observed for the female volunteer (1.6 mm in simulation vs. 0.59 mm *in vivo*). For the 76 years old male (volunteer no. 11) the difference between simulation and measurement is smaller; 0.72 mm in simulation vs. 0.42 mm *in vivo*.

The implementation of subject-specific blood flow profiles do affect the displacement as illustrated in Fig. 8.8. A smaller displacement is observed for the female volunteer (1.6 mm) compared to the male volunteer (1.9 mm) who are within the same age group, and thus the same set of material parameters are applied in the 4FF model. Compared to the 76 years old male, the displacement within the subjects in the middle-aged group is significantly higher, where the displacement is 0.7 mm on average in the wall for the elderly male, and 1.9 mm for the two middle-aged volunteers.

The average stretch ratio estimated in the FSI model is also significantly larger compared

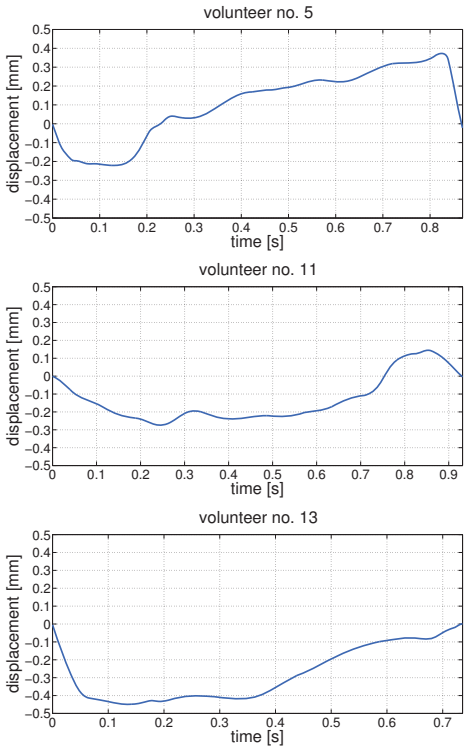

Figure 8.7: Movement and displacement experienced by the abdominal aortic wall during one heart cycle from peak systole to peak systole. The top figure is the displacement for volunteer no. 5. The figure in the center is the wall displacement of volunteer no. 11. The lower figure is the displacement of the wall for volunteer no. 13.

to the stretch ratio calculated from the *in vivo* measurements, see Fig. 8.8 and Table 8.3 for comparison. The two volunteers in the middle-aged group (volunteer no. 5 and 11) experience approximately the same stretch over the cardiac cycle, i.e. $\lambda = 1.22$ on average in both cases. In contrast, the volunteer from the elderly age group show less stretch, $\lambda = 1.09$. Comparing the stretch ratios obtained by simulation and the stretch ratio obtained from the experimental data, the 4FF model appears to underestimate the stiffness of the AA wall using the material parameters from Ferruzzi et al. [28].

Examples from the FSI simulation are shown in Fig. 8.9 and Fig. 8.10. The implementation of the 4FF model in a thick-walled cylinder allows inspection of the intramural stress components, and, hence, provides a detailed reflection of the mechanical behavior compared to thin-walled cylinders.

Fig. 8.9 show example of the three dimensional cylindrical structure applied to imitate the human AA in Paper II. However, to provide a better description of the simulation results, it is more convenient to inspect the Cauchy stress components inside the AA wall as illustrated in Fig. 8.10.

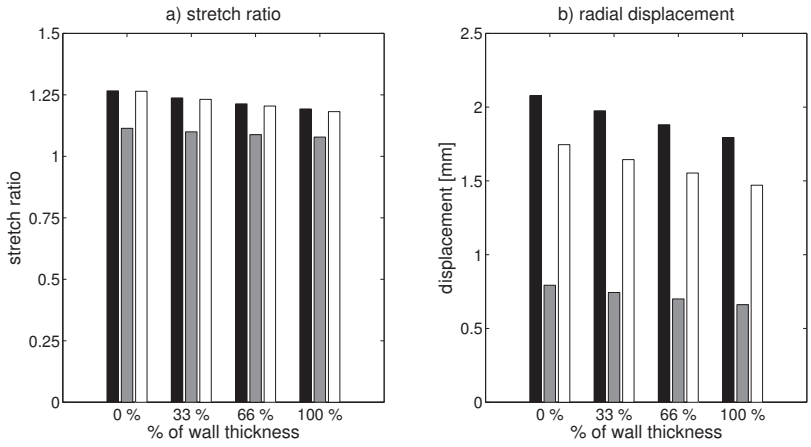

Figure 8.8: Bar graph of the simulation results using the 4FF model. a) show the stretch ratio obtained in the circumferential direction as a function of percentage of the wall thickness. b) show the displacement as a result of the applied fluid flow as a function of percentage of the wall thickness. The black bars are volunteer no. 13, the gray bars are volunteer no. 11, and the white bars are volunteer no. 5.

The radial Cauchy stress decrease from 8 kPa to zero for the two middle-aged volunteers, and decrease from 10 kPa to zero for the elderly volunteer. Regarding the circumferential Cauchy stress, the stress magnitude is higher in the middle-aged volunteers, i.e. approximate 200 kPa, compared to the elderly volunteer where the maximum circumferential stress is 130 kPa at the luminal surface of the AA wall. All three circumferential stress components decrease exponentially towards 20 kPa.
Finally, the axial Cauchy stress components display a smaller variation in magnitude through the AA wall compared to the other principal stress components. However, the axial stress of the elderly volunteer appears more constant, varying only slightly around 7 kPa, compared to the other volunteers. The axial stress components of the middle-aged volunteers decrease by 5 kPa from 10 and 11 kPa to 5 and 6 kPa, respectively, with the highest stress magnitude observed for the male volunteer. The general pattern of stress distribution for each of the three principal Cauchy stresses has been observed in several studies [18, 24, 42].
The stress components are plotted at the end of each cardiac cycle, and obtained at a position 50% below the inlet of the FSI model. Residual stress was not included in this study.

Discussion and Conclusions

This third study presents a FSI model for prediction of the biomechanical behavior of the human AA using the 4FF model with age-matched material parameters and subject-specific blood flow profiles. Based on the simulations the 4FF model appears to overestimates the displacement, and hence the stretch of the AA tissue. The application of subject-specific blood

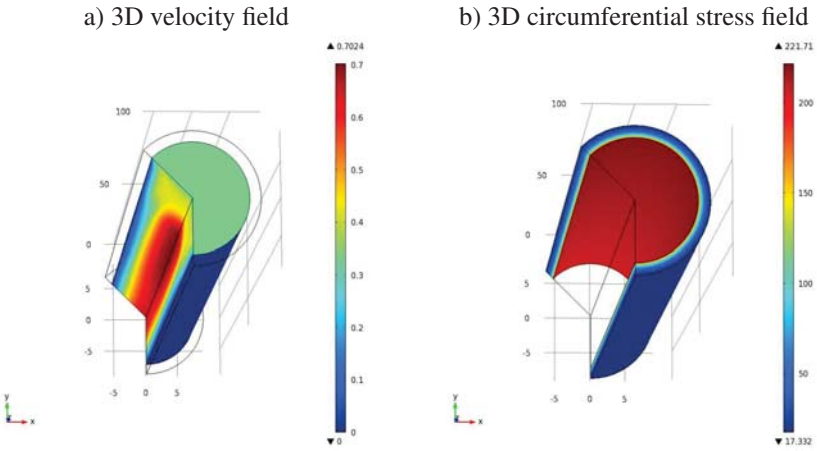

Figure 8.9: a) 3D velocity in the aorta at t = 0.2 s. b) the corresponding 3D circumferential stress field in the aortic wall.

flow profiles introduce a difference in displacement even though the same set of material parameters are applied.

Determination of material parameters is a vital part of predicting the wall stress under both the healthy and the pathological conditions in the human AA. The biaxial data published by Vande Geest et al. [110, 111] is probably the most widely used for determination of material parameters, as it comprise data on both normal AA and AAA. Fit of a material model should preferably be based on individual data, but this is difficult to obtain. Ultrasound techniques has been applied in several studies to obtain model fits based on *in vivo* data. Masson et al. [69] demonstrated the viability of estimation of material parameters for the 4FF model based on non-invasive *in vivo* dynamics of the human carotid artery. Furthermore, Stålhand et al. [102] used pressure-radius measurements obtained with ultrasound by Sonesson et al. [99] to obtain material parameters fitted to the 2FF model proposed by Holzapfel et al. [42]. The proposed method for fit of human *in vivo* data was applied in three male volunteers. The human AA was modeled as a hyper-elastic incompressible thin-walled cylinder.

Several FSI models for simulation of the wall stress in AAAs have been proposed [19, 88, 96, 122]. Scotti et al. [96] compared FSI modeling and finite element analysis in an idealized three dimensional geometry in order to investigate the effect of assuming a uniform arbitrary determined pressure inside the AAA sac compared to application of a non-uniform pressure resulting from FSI modeling in the same geometry. They found that the coupled FSI analysis produced a higher wall stress in the AAA compared to application of a stationary luminal pressure. The fluid domain properties originated from Mills et al. [72] assuming a parabolic time varying velocity profile in the inlet, and a time varying pressure in at the outlet. The material model for the solid domain was the isotropic hyper-elastic model proposed by Raghavan and Vorp [85]. Rissland et al. [88] and Di Martino et al. [19] applied FSI models to realistic AAA geometries. Di Martino et al. used average blood flow velocity from the aorta obtained with Doppler ultrasound. The inlet profile was assumed to be fully-developed at

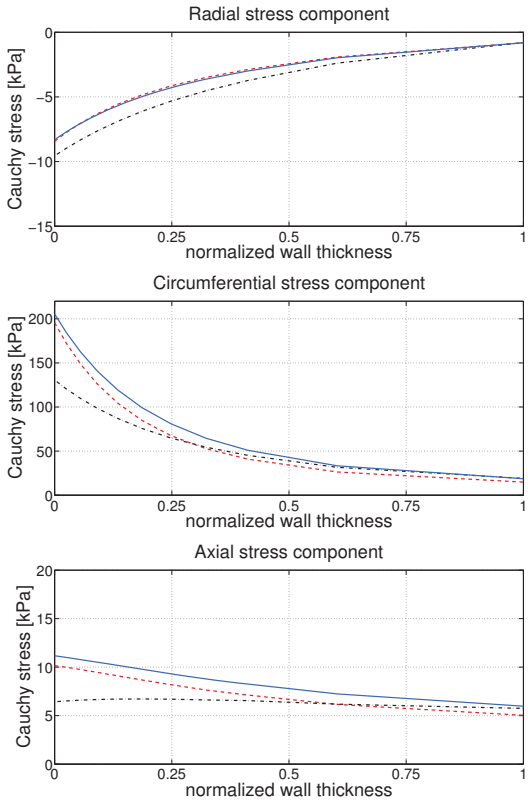

Figure 8.10: The three principal stress components within the AA wall as a function of the normalized wall thickness. The solid blue line ascribe to volunteer no. 13, the black dash-dot line ascribe to volunteer no. 11, and the red dashed line ascribe to volunteer no. 5. The top panel shows the radial stress components. The center panel shows the circumferential stress components, and the bottom panel displays the axial stress components for each volunteer. All stress components are deduces from the AA wall 50 % below the inlet of the FSI model.

the inlet of the aneurysm. Rissland et al. produced inlet and outlet conditions using the data provided by Olufsen et al. [81], and applied the two fiber family model in the aneurysmal tissue. Because the analysis of the FSI models were performed in realistic AAA models, it is not possible to perform a direct comparison to the predicted stress levels. Both studies do not account for the residual stress in arteries, which is also the case for the present work as the aortic geometry is assumed to be stress free initially.

This study presents the initial evaluation of the predictability of the 4FF model in a FSI model environment using published material parameters describing the mechanical behavior of a broad population. There are limitations to the presented work. The application of the Womersley-Evans method for reconstruction of blood flow profiles assumes that the flow is Newtonian, and that the pulsation is steady. In addition, the inlet geometry is assumed to

be rotational symmetric. The experimental *in vivo* data were gathered from 14 volunteers, however aliasing in the ultrasound flow data limited the use of data from all volunteers. Thus, the predictability could only be evaluated in three volunteers as the FSI model setup requires subject-specific blood flow conditions in the inlet. The three volunteers cover differences in age, gender, and smoking habits, thus capturing the three most common risk factors in AAA development, i.e. increasing age, male gender, and smoking. To investigate the effect of smoking, which is the largest environmental risk factor for aneurysmal disease, more smokers needs to be included in the study. This was also stressed in Paper I in order to gain more knowledge on how smoking is related to AAA disease.

In conclusion, to be able to obtain better validation of the predictability of the 4FF model, the FSI modeling environment needs to account for residual stresses. Furthermore, anatomically correct geometries should be applied as the next step in the evaluation process.

CHAPTER

NINE

PROJECT CONCLUSION

The overall purpose of this research work has been to develop FE based simulation models for analysis of parameters which are in evidence of development and clinical management of AAA. This PhD project covers three main areas: interpretation of material parameters in the 4FF model, development of FE models for analysis of mechanical behavior and blood flow patterns in the AA, and, finally, evaluation of the 4FF model predictability in a realistic computational simulation setup.

Within the first research area, the goal was to gain a better understanding of the consequences of smoking on arterial properties and extracellular matrix constituents of the arterial wall based on changes in material parameters of the 4FF model. Smoking is a leading self-inflicted risk factor for cardiovascular diseases in general, and AAA in particular. This goal was achieved by re-interpreting experimental data from main pulmonary arteries in rats. The results show that smoking caused a significant arterial stiffening independent of the age of the rats. This result is reflected by a consistent increase in the elastin-associated material parameter (85% on average), together with a marked increase in the collagen-associated parameter (160% on average). In summary, the increased stiffening appears to result from concomitant changes to elastin and collagen, though effects on collagen are more pronounced. This might be due to the intrinsically higher stiffness of collagen. The effects appeared to occur nearly isotropically, which could simplify future analysis. However, there is a pressing need for more detailed histological information coupled with more complete experimental data for a broader range of systemic arteries.

The second research area concerns implementation of subject-specific AA lumen geometries and blood flow profiles, as well as the 4FF model in the commercially available FE software COMSOL Multiphysics (COMSOL AB, Stockholm, Sweden).
The subject-specific blood flow model of the human AA illustrate the demographic differences within a group of healthy volunteers aged 23 to 76 years. The AA undergo changes with age in the geometrical configuration. This strongly influence the blood flow patterns, and with the direct access to both geometrical information and blood flow data a powerful tool for further research on the role of blood flow patterns in the development of AAA is accessible. The 4FF model was implemented in both 2D and 3D. The 2D implementation served the purpose of benchmarking the implementation by comparing the numerical solution to the analytical solution which is derived under the assumption of plane stress. In 3D

the wall stress components cannot be determined analytically, hence the 2D implementation served as benchmarking of the implementation. The 4FF model was successfully implemented using the mean values of published material parameters which captures the loss of structural integrity constituted by elastin degradation and increased collagen turnover. The use of mean values of material parameters is widely used, but in this implementation of the 4FF model this approach indicate that there is not a significant difference between the groups of 30-60 years and $>$60 years in the biomechanical properties. However, it should mentioned that the median of each material parameter provides a more representative reflection of the average response of the provided data. This is an important observation when dealing with human data, as it is not possible to acquire knowledge of the natural history of each individual. In addition complex genetic and environmental factors, which are not always known either, might influence the mechanical response and, hence, the disease progression.

The final research area concerned evaluation of the predictability of the 4FF model. The suggested method encompasses construction of a FSI model where subject-specific blood flow properties determine the boundary conditions for the fluid domain, and age-matched material parameters are applied in the 4FF model describing the solid mechanics of the AA wall. The predicted wall dynamics were compared to *in vivo* wall dynamics obtained with ultrasound. Simulation results indicate that the 4FF model underestimates the AA wall stiffness in a realistic simulation setup. This is believed to be one of the first studies to evaluate the predictability of the 4FF model using a FSI model environment.

BIBLIOGRAPHY

[1] J. Jeffrey Alexander. The pathobiology of aortic aneurysms. *The Journal of Surgical Research*, 117(1):163–175, 2004.

[2] H. Åstrand, J. Stålhand, J. Karlsson, M. Karlsson, B. Sonesson, and T. Länne. In vivo estimation of the contribution of elastin and collagen to the mechanical properties in the human abdominal aorta: effect of age and sex. *Journal of Applied Physiology*, 110(1):176–187, 2011.

[3] S. Baek, R.L. Gleason, K.R. Rajagopal, and J.D. Humphrey. Theory of small on large: Potential utility in computations of fluid-solid interactions in arteries. *Computer Methods in Applied Mechanics and Engineering*, 196:3070–3078, 2007.

[4] D.W. Baker. Pulsed ultrasonic Doppler blood-flow sensing. *IEEE Transactions on Sonics and Ultrasonics*, 17:170–185, 1970.

[5] R.S. Barua, J.A. Ambrose, L.J. Eales-Reynolds, M.C. DeVoe, J.G. Zervas, and D.C. Saha. Dysfunctional endothelial nitric oxide biosynthesis in healthy smokers with impaired endothelium-dependent vasodilatation. *Circulation*, 104(16):1905–1910, 2001.

[6] H. Bengtsson, P. Nilsson, and D. Bergqvist. Natural history of abdominal aortic aneurysm detected by screening. *British Journal of Surgery*, 80(6):718–720, 1993.

[7] R.B. Bird, R.C. Armstrong, and O. Hassager. *Dynamics of Polymeric Liquids. Volume 1: Fluid Mechanics*. A Wiley-Interscience Publication, John Wiley & Sons, 1987.

[8] S.C. Bushong. *Magnetic resonance imaging*. St. Louis, MO (USA); CV Mosby Co., 1988.

[9] L. Cardamone, A. Valentín, J.F. Eberth, and J.D. Humphrey. Origin of axial prestretch and residual stress in arteries. *Biomechanics and Modeling in Mechanobiology*, 8(6):431–446, 2009.

[10] J.M. Clark and S. Glagov. Transmural organization of the arterial media. The lamellar unit revisited. *Arteriosclerosis, Thrombosis, and Vascular Biology*, 5(1):19–34, 1985.

[11] R.H. Cox. Passive mechanics and connective tissue composition of canine arteries. *American Journal of Physiology-Heart and Circulatory Physiology*, 234(5):H533–541, 1978.

[12] R.H. Cox. Regional, species, and age related variations in the mechanical properties of arteries. *Biorheology*, 16(1-2):85–94, 1979.

[13] R.H. Cox, T. Tulenko, and W.P. Santamore. Effects of chronic cigarette smoking on canine arteries. *American Journal of Physiology - Heart and Circulatory Physiology*, 15(1):H97–H103, 1984.

[14] R.C. Darling, C.R. Messina, D.C. Brewster, and L.W. Ottinger. Autopsy study of unoperated abdominal aortic aneurysms. The case for early resection. *Circulation*, 56(3 Suppl II):161–164, 1977.

[15] J.C. Debes and Y.C. Fung. Biaxial mechanics of excised canine pulmonary arteries. *American Journal of Physiology - Heart and Circulatory Physiology*, 269(2 38-2):H433–H442, 1995.

[16] H. Demiray and R.P. Vito. A layered cylindrical shell model for and aorta. *International Journal of Engineering Science*, 29(1):47–54, 1991.

[17] S.X. Deng, J. Tomioka, J.C. Debes, and Y.C. Fung. New experiments on shear modulus of elasticity of arteries. *American Journal of Physiology-Heart and Circulatory Physiology*, 266(1):H1–H10, 1994.

[18] P. Di Achille, S. Celi, F. Di Puccio, and P. Forte. Anisotropic AAA: Computational comparison between four and two fiber family material models. *Journal of Biomechanics*, 44:2418–2426, 2011.

[19] E.S. Di Martino, G. Guadagni, A. Fumero, G. Ballerini, R. Spirito, P. Biglioli, and A. Redaelli. Fluid-structure interaction within realistic three-dimensional models of the aneurysmatic aorta as a guidance to assess the risk of rupture of the aneurysm. *Medical Engineering & Physics*, 23(9):647–655, 2001.

[20] P.B. Dobrin. Influence of initial length on length-tension relationship of vascular smooth muscle. *American Journal of Physiology–Legacy Content*, 225(3):664–670, 1973.

[21] P.B. Dobrin. Mechanical properties of arterises. *Physiological Reviews*, 58(2):397–460, 1978.

[22] R.J. Doonan, A. Hausvater, C. Scallan, D.P. Mikhailidis, L. Pilote, and S.S. Daskalopoulou. The effect of smoking on arterial stiffness. *Hypertension Research: Official Journal of the Japanese Society of Hypertension*, 33(5):1–13, 2010.

[23] J.F. Eberth, A.I. Taucer, E. Wilson, and J.D. Humphrey. Mechanics of carotid arteries in a mouse model of marfan syndrome. *Annals of Biomedical Engineering*, 37(6):1093–1104, 2009.

[24] M.S. Enevoldsen, K.-A. Henneberg, L. Lönn, and J.A. Jensen. Finite element implementation of a structurally-motivated constitutive relation for the human abdominal aortic wall with and without aneurysms. In *15th Nordic-Baltic Conference on Biomedical Engineering and Medical Physics (NBC 2011)*, pages 13–16. Springer, 2011.

[25] M.S. Enevoldsen, K.A. Henneberg, J.A. Jensen, L. Lönn, and JD Humphrey. New interpretation of arterial stiffening due to cigarette smoking using a structurally motivated constitutive model. *Journal of Biomechanics*, 44(6):1209–1211, 2011.

[26] D.H. Evans. Some aspects of the relationship between instantaneous volumetric blood flow and continuous wave Doppler ultrasound recordings. iii. the calculation of doppler power spectra from mean velocity waveforms, and the results of processing these spectra with maximum, mean, and rms frequency processors. *Ultrasound in Medicine and Biology*, 8(6):617–623, 1982.

[27] J. Ferruzzi, M.S. Enevoldsen, and J.D. Humphrey. On the mechanical behavior of healthy and aneurysmal abdominal aorta. In *Proceeding of the ASME 2011 Summer Bioengineering Conference*, Farmington, Pennsylvania, USA, June 2011.

[28] J. Ferruzzi, D.A. Vorp, and J.D. Humphrey. On constitutive descriptors of the biaxial mechanical behaviour of human abdominal aorta and aneurysms. *Journal of The Royal Society Interface*, 8(56):435–450, 2011.

[29] M.F. Fillinger, S.P. Marra, M.L. Raghavan, and F.E. Kennedy. Prediction of rupture risk in abdominal aortic aneurysm during observation: wall stress versus diameter. *Journal of Vascular Surgery*, 37(4):724–732, 2003.

[30] D. Flondell-Sité. *Circulating biomarkers in patients with abdominal aortic aneurysm*. Skåne University Hospital, Lund University, 2010.

[31] L.J. Frazin, G. Lanza, M. Vonesh, F. Khasho, C. Spitzzeri, S. McGee, D. Mehlman, K.B. Chandran, J. Talano, and D. McPherson. Functional chiral asymmetry in descending thoracic aorta. *Circulation*, 82(6):1985–1994, 1990.

[32] Y.C. Fung. Elasticity of soft tissues in simple elongation. *American Journal of Physiology–Legacy Content*, 213(6):1532–44, 1967.

[33] Y.C. Fung. *Biomechanics: mechanical properties of living tissues*, volume 12. Springer, 1993.

[34] H. Gray. *Anatomy of the human body*. Philadelphia: Lea & Febiger; Bartleby.com, 2000, 1918.

[35] S.E. Greenwald. Ageing of the conduit arteries. *Journal of Pathology*, 211(2):157–172, 2007.

[36] N. Gundiah, M.B. Ratcliffe, and L.A. Pruitt. The biomechanics of arterial elastin. *Journal of the Mechanical Behavior of Biomedical Materials*, 2(3):288–296, 2009.

[37] L.G. Hanson. Introduction to magnetic resonance imaging techniques. Teaching resource, 2009.

[38] C.M. He and M.R. Roach. The composition and mechanical properties of abdominal aortic aneurysms. *Journal of Vascular Surgery*, 20(1):6–13, 1994.

[39] K. Hemminki, X. Li, S.E. Johansson, K. Sundquist, and J. Sundquist. Familial risks of aortic aneurysms among siblings in a nationwide swedish study. *Genetics in Medicine*, 8(1):43–49, 2006.

[40] M. C. Hemmsen, , S. I. Nikolov, M. M. Pedersen, M. J. Pihl, M. S. Enevoldsen, J. M. Hansen, and J. A. Jensen. Implementation of a versatile research data acquisition system using a commercially available medical ultrasound scanner. *IEEE Transactions on Ultrasonics, Ferroelectrics, and Frequency Control*, 2011. accepted for publication.

[41] G.A. Holzapfel. *Nonlinear solid mechanics: a continuum approach for engineering*. John Wiley & Sons Ltd., 2000.

[42] G.A. Holzapfel, T.C. Gasser, and R.W. Ogden. A new constitutive framework for arterial wall mechanics and a comparative study of material models. *Journal of Elasticity*, 61(1):1–48, 2000.

[43] G.A. Holzapfel and R.W. Ogden. Constitutive modelling of arteries. *Proceedings of the Royal Society A: Mathematical, Physical and Engineering Sciences*, 466(2118):1551–1597, 2010.

[44] G.A. Holzapfel and H.W. Weizsäcker. Biomechanical behavior of the arterial wall and its numerical characterization. *Computers in Biology and Medicine*, 28(4):377–392, 1998.

[45] J.D. Humphrey. *Cardiovascular solid mechanics: cells, tissues, and organs*. Springer Verlag, 2002.

[46] J.D. Humphrey. Vascular adaptation and mechanical homeostasis at tissue, cellular, and sub-cellular levels. *Cell Biochemistry and Biophysics*, 50(2):53–78, 2008.

[47] J.D. Humphrey, T. Kang, P. Sakarda, and M. Anjanappa. Computer-aided vascular experimentation: a new electromechanical test system. *Annals of Biomedical Engineering*, 21(1):33–43, 1993.

[48] J.D. Humphrey and S.K. Kyriacou. The use of Laplace's equation in aneurysm mechanics. *Neurological Research*, 18(3):204, 1996.

[49] J.D. Humphrey and C.A. Taylor. Intracranial and abdominal aortic aneurysms: similarities, differences, and need for a new class of computational models. *Annual Review of Biomedical Engineering*, 10:221–246, 2008.

[50] J.A. Jensen. *Estimation of blood velocities using ultrasound: a signal processing approach*. Cambridge Univ Pr, 1996.

[51] K.W. Johnston, R.B. Rutherford, and M.D. Tilson. Suggested standards for reporting on arterial aneurysms. *Journal of Vascular Surgery*, 1991.

[52] C. Kasai, K. Namekawa, A. Koyano, and R. Omoto. Real-time two-dimensional blood flow imaging using an autocorrelation technique. *IEEE Transactions on Ultrasonics, Ferroelectrics, and Frequency Control*, 32(3):458–464, 1985.

[53] C. Kleinstreuer. *Biofluid dynamics: principles and selected applications*. CRC, 2006.

[54] C. Kleinstreuer, S. Hyun, J.R. Buchanan, P.W. Longest, J.P. Archie, and G.A. Truskey. Hemodynamic parameters and early intimal thickening in branching blood vessels. *Critical Reviews in Biomedical Engineering*, 29(1):1–64, 2001.

[55] C. Kleinstreuer and Z. Li. Analysis and computer program for rupture-risk prediction of abdominal aortic aneurysms. *Biomedical Engineering Online*, 5(19), 2006.

[56] C. Kleinstreuer, Z. Li, and M.A. Farber. Fluid-structure interaction analyses of stented abdominal aortic aneurysms. *Annual Review of Biomedical Engineering*, 9:169–204, 2007.

[57] T. Lanne, B. Sonesson, D. Bergqvist, H. Bengtsson, and D. Gustafsson. Diameter and compliance in the male human abdominal aorta: Influence of age and aortic aneurysm. *European Journal of Vascular Surgery*, 6(2):178–184, 1992.

[58] © Simpleware LDT. ScanIP, ScanFE, and ScanCAD Reference Guide, 2010.

[59] © Simpleware LDT. ScanIP, ScanFE, and ScanCAD Tutorial Guide, 2010.

[60] F.A. Lederle, G.R. Johnson, S.E. Wilson, D.J. Ballard, W.D. Jordan, J. Blebea, F.N. Littooy, J.A. Freischlag, D. Bandyk, J.H. Rapp, et al. Rupture rate of large abdominal aortic aneurysms in patients refusing or unfit for elective repair. *The Journal of the American Medical Association*, 287(22):2968–72, 2002.

[61] J. Leung, A. Wright, N. Cheshire, J. Crane, S. Thom, A. Hughes, and Y. Xu. Fluid structure interaction of patient specific abdominal aortic aneurysms: a comparison with solid stress models. *BioMedical Engineering OnLine*, 5(1):33, 2006.

[62] M.A. Lillie, R.E. Shadwick, and J.M. Gosline. Mechanical anisotropy of inflated elastic tissue from the pig aorta. *Journal of Biomechanics*, 43(11):2070–2078, 2010.

[63] J.S. Lindholt, S. Juul, H. Fasting, and E.W. Henneberg. Screening for abdominal aortic aneurysms: single centre randomised controlled trial. *British Medical Journal*, 330(7494):750–755, 2005.

[64] S.Q. Liu and Y.C. Fung. Changes in the structure and mechanical properties of pulmonary arteries of rats exposed to cigarette smoke. *American Journal of Respiratory and Critical Care Medicine*, 148(3):768–777, 1993.

[65] S.Q. Liu and Y.C. Fung. Material coefficients of the strain energy function of pulmonary arteries in normal and cigarette smoke-exposed rats. *Journal of Biomechanics*, 26(11):1261–1269, 1993.

[66] T. Loupas, J.T. Powers, and R.W. Gill. An axial velocity estimator for ultrasound blood flow imaging, based on a full evaluation of the doppler equation by means of a two-dimensional autocorrelation approach. *IEEE Transactions on Ultrasonics, Ferroelectrics and Frequency Control*, 42(4):672 –688, july 1995.

[67] H. Lu, C. Clingman, X. Golay, and P. van Zijl. Determining the longitudinal relaxation time (T1) of blood at 3.0 Tesla. *Magnetic Resonance in Medicine*, 52(3):679–682, 2004.

[68] S.T.R. MacSweeney, G. Young, R.M. Greenhalgh, and J.T. Powell. Mechanical properties of the aneurysmal aorta. *British Journal of Surgery*, 79(12):1281–1284, 1992.

[69] I. Masson, P. Boutouyrie, S. Laurent, Jay D. Humphrey, and M. Zidi. Characterization of arterial wall mechanical behavior and stresses from human clinical data. *Journal of Biomechanics*, 41(12):2618–2627, 2008.

[70] M.A.G. Merkx, M. van't Veer, L. Speelman, M. Breeuwer, J. Buth, and F.N. van de Vosse. Importance of initial stress for abdominal aortic aneurysm wall motion: Dynamic mri validated finite element analysis. *Journal of Biomechanics*, 42(14):2369–2373, 2009.

[71] D. Metcalfe, P.J.E. Holt, and M.M. Thompson. The management of abdominal aortic aneurysms. *British Medical Journal*, 342, 2011.

[72] CJ Mills, IT Gabe, JH Gault, DT Mason, J. Ross Jr, E. Braunwald, and JP Shillingford. Pressure-flow relationships and vascular impedance in man. *Cardiovascular Research*, 4(4):405–417, 1970.

[73] COMSOL Multiphysics v4.2. CFD Module, Users Guide, 2011.

[74] COMSOL Multiphysics v4.2. Comsol Multiphysics, Reference Guide, 2011.

[75] COMSOL Multiphysics v4.2. Structural Mechanics Module, Users Guide, 2011.

[76] W.W. Nichols and M.F. O'Rourke. *McDonald's blood flow in arteries: theoretic, experimental and clinical principles*. Lea & Febiger Philadelphia, 1990.

[77] T.J. Nowak and A.G. Handford. *Pathophysiology: concepts and applications for health care professionals*. McGraw-Hill Higher Education, 2004.

[78] J.T. Oden. *Finite elements of nonlinear continua*, volume 45. McGraw-Hill New York, 1972.

[79] R.W. Ogden. *Non-linear elastic deformations*. Dover Pubns, 1997.

[80] R.W. Ogden and P. Chadwick. On the deformation of solid and tubular cylinders of incompressible isotropic elastic material. *Journal of the Mechanics and Physics of Solids*, 20(2):77–90, 1972.

[81] Mette S. Olufsen, C.S. Peskin, W.Y. Kim, Erik M. Pedersen, A. Nadim, and J. Larsen. Numerical simulation and experimental validation of blood flow in arteries with structured-tree outflow conditions. *Annals of Biomedical Engineering*, 28(11):1281–1299, 2000.

[82] M.F. O'Rourke and J. Hashimoto. Mechanical factors in arterial aging. a clinical perspective. *Journal of the American College of Cardiology*, 50(1):1–13, 2007.

[83] J.C. Parodi, J.C. Palmaz, and H.D. Barone. Transfemoral intraluminal graft implantation for abdominal aortic aneurysms. *Annals of Vascular Surgery*, 5(6):491–499, 1991.

[84] E.M. Pedersen, H.W. Sung, A.C. Burlson, and A.P. Yoganathan. Two-dimensional velocity measurements in a pulsatile flow model of the normal abdominal aorta simulating different hemodynamic conditions. *Journal of Biomechanics*, 26(10):1237–1247, 1993.

[85] M.L. Raghavan and D.A. Vorp. Toward a biomechanical tool to evaluate rupture potential of abdominal aortic aneurysm: identification of a finite strain constitutive model and evaluation of its applicability. *Journal of Biomechanics*, 33(4):475–482, 2000.

[86] M.L. Raghavan, M.W. Webster, and D.A. Vorp. Ex vivo biomechanical behavior of abdominal aortic aneurysm: assessment using a new mathematical model. *Annals of Biomedical Engineering*, 24(5):573–582, 1996.

[87] D. Reed, C. Reed, G. Stemmermann, and T. Hayashi. Are aortic aneurysms caused by atherosclerosis? *Circulation*, 85(1):205–211, 1992.

[88] P. Rissland, Y. Alemu, S. Einav, J. Ricotta, and D. Bluestein. Abdominal aortic aneurysm risk of rupture: patient-specific fsi simulations using anisotropic model. *Journal of Biomechanical Engineering*, 131:031001–1–013001–10, 2009.

[89] R.S. Rivlin and DW Saunders. Large elastic deformations of isotropic materials. vii. experiments on the deformation of rubber. *Philosophical Transactions of the Royal Society of London. Series A, Mathematical and Physical Sciences*, 243(865):251–288, 1951.

[90] J.F. Rodríguez, G. Martufi, M. Doblaré, and E.A. Finol. The effect of material model formulation in the stress analysis of abdominal aortic aneurysms. *Annals of Biomedical Engineering*, 37(11):2218–2221, 2009.

[91] M.S. Sacks. Biaxial mechanical evaluation of planar biological materials. *Journal of Elasticity*, 61(1):199–246, 2000.

[92] N. Sakalihasan, R. Limet, and O.D. Defawe. Abdominal aortic aneurysm. *The Lancet*, 365(9470):1577–1589, 2005.

[93] S. Satomura. Ultrasonic Doppler method for the inspection of cardiac functions. *Journal of the Acoustical Society of America*, 29:1181–1185, 1957.

[94] M.L. Schermerhorn and J.L. Cronenwett. Abdominal aortic and iliac aneurysms. *Vascular Surgery*, pages 1408–1452, 2005.

[95] R.A.P. Scott and The Multicentre Aneurysm Screening Study Group. The multicentre aneurysm screening study (mass) into the effect of abdominal aortic aneurysm screening on mortality in men: a randomised controlled trial. *The Lancet*, 360(9345):1531–1539, 2002.

[96] C.M. Scotti, J. Jimenez, S.C. Muluk, and E.A. Finol. Wall stress and flow dynamics in abdominal aortic aneurysms: finite element analysis vs. fluid–structure interaction. *Computer Methods in Biomechanics and Biomedical Engineering*, 11(3):301–322, 2008.

[97] H.O.L. Sillesen and T.V. Schroeder. Dødeligheden ved abdominale aortaaneurismer nedsættes ved screening. *Ugeskrift for Læger*, 167(15):1621, 2005.

[98] D.P. Sokolis. A passive strain-energy function for elastic and muscular arteries: correlation of material parameters with histological data. *Medical and Biological Engineering and Computing*, 48(6):507–518, 2010.

[99] B. Sonesson, T. Länne, E. Vernersson, and F. Hansen. Sex difference in the mechanical properties of the abdominal aorta in human beings. *Journal of Vascular Surgery*, 20(6):959–969, 1994.

[100] B. Sonesson, T. Sandgren, and T. Länne. Abdominal aortic aneurysm wall mechanics and their relation to risk of rupture. *European Journal of Vascular and Endovascular Surgery*, 18(6):487–493, 1999.

[101] G.J. Stanisz, E.E. Odrobina, J. Pun, M. Escaravage, S.J. Graham, M.J. Bronskill, and R.M. Henkelman. T1, T2 relaxation and magnetization transfer in tissue at 3T. *Magnetic Resonance in Medicine*, 54(3):507–512, 2005.

[102] J. Stålhand. Determination of human arterial wall parameters from clinical data. *Biomechanics and Modeling in Mechanobiology*, 8(2):141–148, 2009.

[103] D.S. Sumner, D.E. Hokanson, and D.E. Strandness Jr. Stress-strain characteristics and collagen-elastin content of abdominal aortic aneurysms. *Surgery, Gynecology & Obstetrics*, 130(3):459–466, 1970.

[104] L.A. Taber. Biomechanics of cardiovascular development. *Annual Review of Biomedical Engineering*, 3(1):1–25, 2001.

[105] J.D. Thomas. Flow in the descending aorta. A turn of the screw or a sideways glance? *Circulation*, 82(6):2263–2265, 1990.

[106] M. Thubrikar. *Vascular mechanics and pathology*. Springer, 2007.

[107] G.A. Truskey, F. Yuan, and D.F. Katz. *Transport phenomena in biological systems*. Pearson Prentice Hall Upper Saddle River, NJ, 2004.

[108] K.C. Valanis and R.F. Landel. The strain-energy function of a hyperelastic material in terms of the extension ratios. *Journal of Applied Physics*, 38(7):2997–3002, 1967.

[109] A. Valentín, J.D. Humphrey, and G.A. Holzapfel. A multi-layered computational model of coupled elastin degradation, vasoactive dysfunction, and collagenous stiffening in aortic aging. *Annals of Biomedical Engineering*, pages 1–19, 2011.

[110] J.P. Vande Geest, M.S. Sacks, and D.A. Vorp. Age dependency of the biaxial biomechanical behavior of human abdominal aorta. *Journal of Biomechanical Engineering*, 126:815–822, 2004.

[111] J.P. Vande Geest, M.S. Sacks, and D.A. Vorp. The effects of aneurysm on the biaxial mechanical behavior of human abdominal aorta. *Journal of Biomechanics*, 39(7):1324–1334, 2006.

[112] A.K. Venkatasubramaniam, M.J. Fagan, T. Mehta, K.J. Mylankal, B. Ray, G. Kuhan, I.C. Chetter, and P.T. McCollum. A comparative study of aortic wall stress using finite element analysis for ruptured and non-ruptured abdominal aortic aneurysms. *European Journal of Vascular and Endovascular Surgery*, 28(2):168–176, 2004.

[113] N.L. Volodos, I.P. Karpovich, V.I. Troyan, Y.V. Kalashnikova, V.E. Shekhanin, N.E. Ternyuk, A.S. Neoneta, N.I. Ustinov, and L.F. Yakovenko. Clinical experience of the use of self-fixing synthetic prostheses for remote endoprosthetics of the thoracic and the abdominal aorta and iliac arteries through the femoral artery and as intraoperative endoprosthesis for aorta reconstruction. *VASA. Supplementum*, 33:93, 1991.

[114] N.L. Volodos, V.E. Shekhanin, I.P. Karpovich, V.I. Troyan, and Y.A. Guriev. Self-fixing synthetic prosthesis for endoprosthetics of the vessels (in russian). *Vestn Khir Im*, 137:123–125, 1986.

[115] D.A. Vorp. Biomechanics of abdominal aortic aneurysm. *Journal of Biomechanics*, 40(9):1887–1902, 2007.

[116] D.A. Vorp, M.L. Raghavan, S.C. Muluk, M.S. Makaroun, D.L. Steed, R. Shapiro, and M.W. Webster. Wall strength and stiffness of aneurysmal and nonaneurysmal abdominal aorta. *Annals of the New York Academy of Sciences*, 800(1):274–276, 1996.

[117] D.A. Vorp, M.L. Raghavan, and M.W. Webster. Mechanical wall stress in abdominal aortic aneurysm: influence of diameter and asymmetry. *Journal of Vascular Surgery*, 27(4):632–639, 1998.

[118] P.N. Watton, N.A. Hill, and M. Heil. A mathematical model for the growth of the abdominal aortic aneurysm. *Biomechanics and Modeling in Mechanobiology*, 3(2):98–113, 2004.

[119] P. Weale. syngo native – Non Contrast MR Angiography Techniques. 2011. `http://www.clinical-mri.com/pdf/IT/hardware/MRA_Native_final.pdf`.

[120] B.K. Wicker, H.P. Hutchens, Q. Wu, A.T. Yeh, and J.D. Humphrey. Normal basilar artery structure and biaxial mechanical behaviour. *Computer Methods in Biomechanics and Biomedical Engineering*, 11(5):539–551, 2008.

[121] K. Wilson, H. MacCallum, I.B. Wilkinson, P.R. Hoskins, A.J. Lee, and A.W. Bradbury. Comparison of brachial artery pressure and derived central pressure in the measurement of abdominal aortic aneurysm distensibility* 1. *European Journal of Vascular and Endovascular Surgery*, 22(4):355–360, 2001.

[122] B. Wolters, M.C.M. Rutten, G.W.H. Schurink, U. Kose, J. De Hart, and F.N. Van De Vosse. A patient-specific computational model of fluid-structure interaction in abdominal aortic aneurysms. *Medical Engineering & Physics*, 27(10):871–883, 2005.

[123] J.R. Womersley. Method for the calculation of velocity, rate of flow and viscous drag in arteries when the pressure gradient is known. *The Journal of Physiology*, 127(3):553–563, 1955.

[124] S. Zeinali-Davarani, L.G. Raguin, D.A. Vorp, and S. Baek. Identification of in vivo material and geometric parameters of a human aorta: toward patient-specific modeling of abdominal aortic aneurysm. *Biomechanics and Modeling in Mechanobiology*, pages 1–11, 2011.

[125] O.C. Zienkiewicz and R.L. Taylor. *The finite element method: solid and fluid mechanics dynamics and non-linearity*. McGraw-Hill, 1991.

[126] Y. Zou and Y. Zhang. An experimental and theoretical study on the anisotropy of elastin network. *Annals of Biomedical Engineering*, 37(8):1572–1583, 2009.

APPENDIX

A

MODEL SETTINGS IN COMSOL MULTIPHYSICS

Table A.1: Model settings for the fluid model in Paper IV. The example is the AA of a 28 years old female volunteer.

Parameter	Expression	Description
Material properties		
rho_blood	1,060 [kg/m^3]	Mass density of blood
eta_blood	0.0035 [Pa·s]	Blood viscosity
Pi	16 [kPa]	Inlet pressure
Po	15 [kPa]	Outlet pressure
Ui	1.02 [m/s]	Inlet velocity
Shape functions		
u	Lagrange	Velocity field, x component
v	Lagrange	Velocity field, y component
w	Lagrange	Velocity field, z component
p	Lagrange	Pressure
Boundary conditions		
Average velocity	Ui/2	Laminar inflow
Pressure	Po	Outlet pressure
No-slip	0	Velocity at boundary
Mesh		
Calibrate for	Fluid dynamics	Optimize the element size for fluid dynamics
Maximum element size	3 mm	–
Minimum element size	0.895 mm	–
Maximum element growth rate	1.15	–
Triangular elements	2197	–
Solver settings		
Use study step	Stationary	Steady-state solution for the fluid problem
Linear solver	Direct	Solution is found from using a finite number of arithmic operations
Initial damping factor	0.01	Damping factor for the first Newton iteration
Minimum damping factor	1.0×10^{-6}	Smallest allowed damping factor

Table A.2: Model settings for the fluid model in Paper VI. The example given is for the elderly AA group, and lists the geometrical and material properties.

Parameter	Expression	Description
Geometry		
Ri	1 [cm]	Inner radius
L	5 [cm]	Length of the tube
h_AAold	1.49 [mm]	Aortic wall thickness
Pi	0 [mmHg]	Inlet pressure, used for parametrization of in the solution
Material properties		
c	3.22 [kPa]	Isotropic elastic material parameter
c11	41.57[kPa]	Material parameter c11
c21	26.21	Material parameter c21
c12	11.43[kPa]	Material parameter c12
c22	61.15	Material parameter c22
c1d	44.61 [kPa]	Material parameter c1,34
c2d	60.29	Material parameter c2,34
alpha0	0.824[rad]	Angle between axial and diagonal collagen fibers
kappa	1e10 [Pa]	Bulk modulus
I4_z	solid.Cl33	4th invariant, axial collagen fibers
I4_phi	solid.Cl22	4th invariant, circumferential collagen fibers
I4_dia1	solid.Cl33*(cos(alpha0))^2 +solid.Cl22*(sin(alpha0))^2	4th invariant, diagonal family 1
I4_dia2	solid.Cl33*(cos(-alpha0))^2 +solid.Cl22*(sin(-alpha0))^2	4th invariant, diagonal family 2
W_elastin	c/2(solid.J^(2/3)*solid.I1CIel-3)	strain energy function, elastin
W_collagen1	c11/(4c21)(exp(c21*(I4_z-1)^2)-1)	strain energy function, axial collagen fiber family
W_collagen2	c12/(4*c22)*(exp(c22*(I4_phi-1)^2)-1)	strain energy function, circumferential collagen fiber family
W_collagen3	c1d/(4*c2d)*(exp(c2d*(I4_dia1-1)^2)-1)	strain energy function, first diagonal collagen fiber family
W_collagen4	c1d/(4*c2d)*(exp(c2d*(I4_dia2-1)^2)-1)	strain energy function, second diagonal collagen fiber family
W_vol	0.5*kappa*(solid.J-1)^2	volumetric strain energy function

Table A.3: Model settings for the fluid model in Paper VI. The example given is for the elderly AA group, and lists the shape function, the boundary conditions, the mesh settings, and the solver settings.

Parameter	Expression	Description
Shape functions		
u	Lagrange	Displacement field, R component
w	Lagrange	Displacement field, Z component
solid.pw	Lagrange	Pressure
Boundary conditions		
Roller	–	Zero displacement in the direction perpendicular to the boundary
Boundary load	Pi	Pressure load
Free	–	No constraints, no loads
Mesh		
Maximum element size	3.35 mm	–
Minimum element size	0.015 mm	–
Maximum element growth rate	1.3	–
Triangulation method	advancing front	–
Triangular elements	196	–
Solver settings		
Use study step	Stationary	Steady-state solution for the fluid problem
Linear solver	Direct	Solution is found from using a finite of number arithmic operations
Parametric, Pi	range(1000,10,20000)	Parametrization of the solution

Table A.4: Model settings for the FSI model in Paper II. The table lists the functions for the boundary conditions,

Parameter	Expression	Description
Function expressions		
Function name	data	Profile grid
Function type	Interpolation	–
Function name	ramp	Function for optimal temporal model convergence
Function type	Ramp	–
Location	0.005	Start of the ramp function
Slope	20	
Cutoff	on	
Size of transition zone	0.01	
Smooth at start	on	
Smooth at cutoff	on	
Geometry		
Position, lumen	0, 0	Position of the lower left corner
Width, lumen	7.82 mm	Lumen radius of the volunteer
Height, lumen	100 mm	Lumen length
Position, wall	7.82, 0	Position of the lower left corner
Width, wall	1.5 mm	Wall thickness
Height, wall	100 mm	Wall length
Boundary conditions		
Inlet	0, 0, data(r*100,t*200)*ramp(t)	Velocity field
Outlet	10.7 kPa	Pressure
No-slip	0	Velocity at FSI boundary
Fixed	–	Fixed constraint
Boundary load 1	-spf.T_stressr, 0, -spf.T_stressz	Pressure load from fluid
Boundary load 2	0.867 kPa	External pressure

Table A.5: Model settings for the FSI model in Paper II. The table lists the functions for the boundary conditions,

Parameter	Expression	Description
Shape functions		
u	Lagrange	Velocity field, r component
v	Lagrange	Velocity field, z component
p1	Lagrange	Pressure
u2	Lagrange	Displacement field, R component
w2	Lagrange	Displacement field, Z component
solid.pw	Lagrange	Pressure
Mesh		
Calibrate for	Fluid dynamics	Optimize the element size for fluid dynamics
Maximum element size, fluid	1.21 mm	–
Minimum element size, fluid	0.466 mm	–
Maximum element growth rate, fluid	1.3	–
Triangular elements, fluid	1647	–
Maximum element size, solid	0.8 mm	–
Minimum element size, solid	–	–
Quadrilateral elements	1000	–
Solver settings		
Use study step, fluid	Time dependent	Time dependent solution for the fluid problem
Linear solver, fluid	Direct	Solution is found from using a finite of number arithmic operations
Use study step, solid	Stationary	Stationary solution for the solid problem
Linear solver	Direct	Solution is found from using a finite of number arithmic operations
Parametric, t	range(0.001,0.001,0.85)	Parametrization of the solution

PAPER I

TITLE New Interpretation of Arterial Stiffening due to Cigarette Smoking Using a Structurally Motivated Constitutive Model

AUTHORS Marie Sand Enevoldsen, Kaj-Åge Henneberg, Jørgen Arendt Jensen, Lars Lönn, and Jay D. Humphrey

JOURNAL Journal of Biomechanics

PUBLICATION HISTORY Submission date: 27-09-2010, Publication date: 18-02-2011

Journal of Biomechanics 44 (2011) 1209–1211

Contents lists available at ScienceDirect

Journal of Biomechanics

journal homepage: www.elsevier.com/locate/jbiomech
www.JBiomech.com

Short communication

New interpretation of arterial stiffening due to cigarette smoking using a structurally motivated constitutive model

M.S. Enevoldsen [a,*], K.-A. Henneberg [a], J.A. Jensen [a], L. Lönn [b], J.D. Humphrey [c]

[a] Department of Electrical Engineering, Technical University of Denmark, Oersteds Plads, Building 349, DK-2800 Kongens Lyngby, Denmark
[b] Department of Radiology, Rigshospitalet, University of Copenhagen, Copenhagen, Denmark
[c] Department of Biomedical Engineering, Yale University, New Haven, CT, USA

ARTICLE INFO

Article history:
Accepted 27 January 2011

Keywords:
Elastin
Collagen
Anisotropy
Stress
Biomechanics

ABSTRACT

Cigarette smoking is the leading self-inflicted risk factor for cardiovascular diseases; it causes arterial stiffening with serious sequelea including atherosclerosis and abdominal aortic aneurysms. This work presents a new interpretation of arterial stiffening caused by smoking based on data published for rat pulmonary arteries. A structurally motivated "four fiber family" constitutive relation was used to fit the available biaxial data and associated best-fit values of material parameters were estimated using multivariate nonlinear regression. Results suggested that arterial stiffening caused by smoking was reflected by consistent increase in an elastin-associated parameter and moreover by marked increase in the collagen-associated parameters. That is, we suggest that arterial stiffening due to cigarette smoking appears to be isotropic, which may allow simpler phenomenological models to capture these effects using a single stiffening parameter similar to the approach in isotropic continuum damage mechanics. There is a pressing need, however, for more detailed histological information coupled with more complete biaxial mechanical data for a broader range of systemic arteries.

1. Introduction

Cardiovascular disease is a leading cause of death worldwide and cigarette smoking is one of six major associated modifiable risk factors (Doll et al., 2004). For example, production of nitric oxide by the endothelium, which mediates vasodilatation in response to altered hemodynamics, is reduced in both active and passive smokers (Barua et al., 2001). Hence, endothelial dysfunction caused by smoking can diminish the dilatory capacity of arteries, which yields a stiffer wall, as well as promote thrombus formation and inflammation within the wall. Although these and similarly detrimental consequences of smoking have long been recognized, detailed experimental data on associated histo-mechanical changes to arteries are sparse. There is, therefore, a pressing need for more experimental data, a better understanding of effects on extracellular matrix (ECM) constituents, and associated constitutive modeling of bulk changes in mechanical behavior. The goal of this paper is to gain a better understanding of consequences of smoking on arterial properties and ECM constituents based on changes in material parameters in a proven structurally motivated constitutive relation for arteries. This goal was achieved by re-interpreting experimental data from main pulmonary arteries in rats (Liu and Fung, 1993b) using a new "four fiber family" constitutive relation for stress (cf. Ferruzzi et al., 2010).

2. Methods

2.1. Experimental data

Inflation-extension data were inferred from Liu and Fung (1993b); see the original paper for details. Briefly, 28 initially three-month old Sprague–Dawley rats were exposed to either room air or cigarette smoke for two or three months, thus yielding four groups of seven rats each: Group 1 represented two-month controls, Group 2 the two-month smokers, Group 3 the three-month controls, and Group 4 the three-month smokers. The main pulmonary artery was excised for inflation-extension testing and data were analyzed in terms of the second Piola–Kirchhoff stress ($\mathbf{S}$) and Green strain ($\mathbf{E}$). To facilitate use of the four fiber family constitutive relation, the biaxial data from their constitutive relation $\mathbf{S}=\hat{\mathbf{S}}(\mathbf{E})$ was regenerated in terms of components of the Cauchy stress $\mathbf{t}=(\mathbf{F}\cdot\mathbf{S}\cdot\mathbf{F}^T)/J$, where $\mathbf{F}$ is the deformation gradient and J its determinant (accomplished assuming no rotations, that is, $\mathbf{R}=\mathbf{I}$ and $\mathbf{V}\equiv\mathbf{U}$ using the polar decomposition theorem $\mathbf{F}=\mathbf{R}\cdot\mathbf{U}=\mathbf{V}\cdot\mathbf{R}$ where $\mathbf{U}$ and $\mathbf{V}$ are the right and left stretch tensors, respectively) and recalling that $\mathbf{E}=(\mathbf{F}^T\cdot\mathbf{F}-\mathbf{I})/2$. Note, too, that the constitutive relation in Liu and Fung (1993b) contained reference Green strains, values of which were not given. These reference strains were assumed to be $E^*_{\theta\theta}=0.182$ and $E^*_{zz}=0.274$ based on similar data by Debes and Fung (1995).

2.2. Constitutive framework

The primary load bearing constituents of the ECM in passive pulmonary arteries were assumed to be an amorphous matrix dominated by elastin and four

* Corresponding author. Tel.: +45 45253705; fax: +45 45880117.
E-mail address: mse@elektro.dtu.dk (M.S. Enevoldsen).

0021-9290/$ - see front matter © 2011 Elsevier Ltd. All rights reserved.
doi:10.1016/j.jbiomech.2011.01.032

families of locally parallel collagen fibers (axial, circumferential, and symmetric diagonal). The strain energy density function was thus assumed to have the form Ferruzzi et al. (2010),

$$W(\mathbf{C},\mathbf{M}^{(k)}) = \frac{c}{2}(I_C-3) + \sum_{k=1}^{4} \frac{c_1^{(k)}}{4c_2^{(k)}}\{\exp[c_2^{(k)}(IV_C^{(k)}-1)^2]-1\},$$

where c, $c_1^{(k)}$, $c_2^{(k)}$ are material parameters, I_C is the first invariant of the right Cauchy–Green tensor $\mathbf{C}=\mathbf{F}^T\cdot\mathbf{F}$, and $IV_C^{(k)}=\mathbf{M}^{(k)}\cdot\mathbf{C}\mathbf{M}^{(k)}$ is the fourth invariant of $\mathbf{C}$. Assuming incompressibility and plane stress ($t_{rr}=0$), the theoretically predicted non-zero stress components of stress are

$$t_{\theta\theta} = c\left(\lambda_\theta^2 - \frac{1}{\lambda_\theta^2\lambda_z^2}\right) + c_1^{(2)}(\lambda_\theta^2-1)\exp[c_2^{(2)}(\lambda_\theta^2-1)^2]\lambda_\theta^2 + 2c_1^{(3,4)}(IV_C^{(3,4)}-1)\exp[c_2^{(3,4)}(IV_C^{(3,4)}-1)^2]\lambda_\theta^2\sin^2(\alpha_0)$$

$$t_{zz} = c\left(\lambda_z^2 - \frac{1}{\lambda_\theta^2\lambda_z^2}\right) + c_1^{(1)}(\lambda_z^2-1)\exp[c_2^{(1)}(\lambda_z^2-1)^2]\lambda_z^2 + 2c_1^{(3,4)}(IV_C^{(3,4)}-1)\exp[c_2^{(3,4)}(IV_C^{(3,4)}-1)^2]\lambda_z^2\cos^2(\alpha_0)$$

where superscripts 1, 2, and 3,4 denote axial, circumferential, and symmetric diagonal fibers, respectively, and α_0 denotes the orientation of the diagonal fibers relative to the axial direction in the reference configuration. This constitutive relation was selected because it has faithfully captured differential changes in the contribution of elastic fibers and fibrillar collagens to load bearing by the arterial wall in two cases of genetic mutations to elastin-associated proteins as well as in both aging of and the development of aneurysms in the human abdominal aorta (Eberth et al., 2009; Ferruzzi et al., 2010; Wan et al., 2010).

2.3. Parameter estimation

Best-fit values of the eight material parameters were determined via nonlinear regression by minimizing differences between the theoretically predicted and experimentally measured Cauchy stresses in circumferential and axial directions (using the Optimization Toolbox in MATLAB™ 7.8.0 (R2009a) with the build-in function *lsqnonlin*; see Ferruzzi et al., 2010 for details). Specifically, the objective function to be minimized was

$$e(\boldsymbol{\beta}) = \sum_{i=1}^{n}\{[t_{zz}^{\mathrm{th}}(\lambda_z,\lambda_\theta;\boldsymbol{\beta})_i-(t_{zz}^{\mathrm{exp}})_i]^2 + [t_{\theta\theta}^{\mathrm{th}}(\lambda_z,\lambda_\theta;\boldsymbol{\beta})_i-(t_{\theta\theta}^{\mathrm{exp}})_i]^2\},$$

where $\boldsymbol{\beta}$ is the vector containing the eight material/structural parameters and n is the number of data points ($n \gg 8$). The most representative set of best-fit parameters was chosen as the mean of each parameter based on 100 successive estimations using randomly generated initial guesses that respected the physical constraint that all parameters remain non-negative. Note that Ferruzzi and colleagues have shown via an extensive non-parametric statistical analysis that results from such estimations tend to be robust, yielding unique fixed point estimates.

3. Results

An illustrative fit to data shows that the model captured well the biaxial data (Fig. 1). In general, the Cauchy stress was higher in the circumferential direction compared to the axial direction, and slightly higher in the older rats. More importantly, smoking caused significant stiffening in both age groups – stresses were generally three times greater in smokers compared to controls when evaluated at a common, upper-level deformation. The effect of smoking on the best-fit values of material parameters in the four fiber family constitutive relation was a marked increase in the value of all parameters, but particularly those associated with collagen ($c_1^{(k)}$,$c_2^{(k)}$), see Table 1.

4. Discussion

This re-interpretation of existing data on effects of smoking on arterial stiffness confirms that smoking accelerates stiffening of pulmonary arteries (cf. Doonan et al., 2010), but provides increased

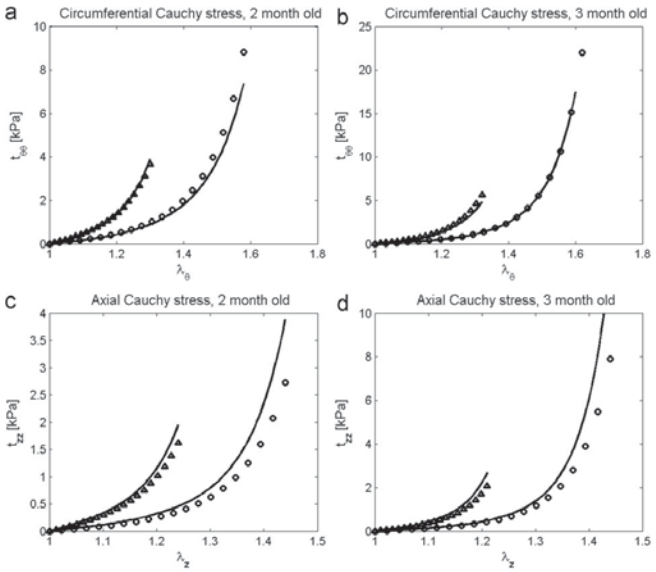

Fig. 1. Illustrative fit (solid lines) of experimental data (symbols) using the four fiber family constitutive model. Data from control groups are indicated by open circles and data from smokers are indicated by open triangles. Panel (a) shows circumferential stress $t_{\theta\theta}$ for Groups 1 (controls) and 2 (smokers); panel (b) shows similar results for Groups 3 (longer term controls) and 4 (longer term smokers). Panel (c) shows associated results for axial stress t_{zz} for Groups 1 and 2; panel (d) shows similar results for Groups 3 and 4.

Table 1
Mean values of the best-fit model parameters based on data from all 28 animals. Note the increased values for smokers relative to the paired controls for both periods of exposure to smoke. Group 1 is the two-month controls, Group 2 denotes rats exposed to smoke for two months, Group 3 is the three-month controls, and Group 4 denotes rats exposed to smoke for three months. Values in the parentheses show percent increases for smokers relative to controls. Albeit not shown, median values of the parameters represented much better the pooled data for each group than did mean values.

Group	c (kPa)	c_1^1 (kPa)	c_2^1	c_1^2 (kPa)	c_2^2	$c_1^{3,4}$ (kPa)	$c_2^{3,4}$	ϖ_0 (deg.)
1	0.072	0.13	1.72	0.411	0.564	0.131	0.932	43.5
2	0.142 (+97%)	0.424 (+226%)	3.39 (+97.1%)	0.915 (+123%)	1.77 (+214%)	0.44 (+236%)	2.16 (+132%)	48.8 (+12.2%)
3	0.079	0.143	2.81	0.545	0.814	0.13	1.57	26.5
4	0.139 (+75.9%)	0.454 (+217%)	6.28 (+123%)	1.16 (+113%)	1.62 (+99.0%)	0.408 (+214%)	3.56 (+127%)	38.1 (+43.8%)

insight into this process. Liu and Fung (1993a) showed that cigarette smoking stimulates an increase in the volume fractions of both elastin and collagen, together with a decrease in smooth muscle cells in pulmonary rat arteries. The present structurally motivated constitutive relation similarly suggested an increased stiffness due to increases in both the elastin related (through the parameter c) and collagen related (through the parameters $c_1^{(k)}$ and $c_2^{(k)}$) terms, but the effect due to the latter appeared more marked. That is, the elastin related parameter increased by ~85% whereas parameters associated with collagen in general increased at least two fold, thus suggesting overall nearly isotropic stiffening dominated by collagen.

The material symmetry associated with stiffening due to smoking has not received prior attention in the literature, but increased research on this aspect of stiffening may help increase our understanding of associations between smoking and cardiovascular disease and could simplify the phenomenological modeling that continues to dominate vascular mechanics. For example, one may be able to use a concept similar to that in isotropic damage mechanics to model progressive changes in arterial stiffening due to the duration or intensity of smoking. Toward this end, however, there is a pressing need for more data, particularly on the time course of long-term effects of smoking. We also focused on pulmonary arteries simply because the associated data were the most complete. Consequently, there is also a need for similar data on systemic arteries, especially carotids, cerebrals, coronaries, and aorta which are susceptible to smoking related diseases. Note, therefore, that we attempted a similar analysis of data from Cox et al. (1984), who reported findings on longer term effects of smoking on carotids and femorals from dogs. The associated parameter estimation was deemed unreliable, however, due to their focus on pressure-diameter data alone and too few data points within the systemic pressure range. There is, therefore, a critical need for more complete biaxial data, which in turn will permit more extensive evaluations of the associated constitutive behaviors. Consistent with other modeling studies (cf. Baek et al., 2007), note that we assumed an additive decomposition of the energy stored in the elastin-dominated and collagen-dominated portions of the ECM and further that the elastin responds isotropically (i.e., a neo-Hookean model). Clearly, interactions among the many different proteins that constitute the arterial wall should be expected, and models will need to account for these interactions once they are understood better. Although isotropy of the stress response of elastin has been questioned recently (e.g., Zou and Zhang, 2009; Lillie et al., 2010; Sokolis, 2010), most think that this possible anisotropy manifests primarily at low strains. Because of our ultimate interest in behaviors at physiological levels of strain, and consistent with findings by Gundiah et al. (2009) that neo-Hookean behavior dominates the stress response of elastin, we retained this assumption herein. Although such an assumption has allowed altered contributions of elastin to wall mechanics to be captured previously (Eberth et al., 2009; Ferruzzi et al., 2010; Wan et al., 2010), this as well as each aspect of the constitutive modeling needs to be considered more carefully as more detailed histological and mechanical data on the effect of smoking become available.

In summary, the increased stiffening of arteries due to smoking appears to result from concomitant changes to elastin and collagen, though effects on collagen are more pronounced perhaps because of its intrinsically higher stiffness. These effects appeared to occur nearly isotropically, which could simplify future analysis of the more complete data that are needed.

Conflict of interest statement

There is no conflict of interest.

Acknowledgments

We thank Mr. Jacopo Ferruzzi for providing custom software for the parameter estimation. This work was conducted in the Continuum Biomechanics Laboratory at Texas A&M University and supported, in part, by project 55562 at Technical University of Denmark, Radiometer Medical ApS., Danish Ministry of Science Technology and Innovation, and NIH R01 HL086418.

References

Baek, S., Gleason, R.L., Rajagopal, K.R., Humphrey, J.D., 2007. Theory of small on large large: potential utility in computations of fluid–solid interactions in arteries. Computer Methods in Applied Mechanics and Engineering 196, 3070–3078.
Barua, R.S., Ambrose, J.A., Eales-Reynolds, L.J., DeVoe, M.C., Zervas, J.G., Saha, D.C., 2001. Dysfunctional endothelial nitric oxide biosynthesis in healthy smokers with impaired endothelium-dependent vasodilatation. Circulation 104, 1905–1910.
Cox, R.H., Tulenko, T., Santamore, W.P., 1984. Effects of chronic cigarette smoking on canine arteries. American Journal of Physiology 246, H97–H103.
Debes, J.C., Fung, Y.C., 1995. Biaxial mechanics of excised canine pulmonary arteries. Heart and Circular Physiology 38, H433–H442.
Doll, R., Peto, R., Boreham, J., Sutherland, I., 2004. Mortality in relation to smoking: 50 years' observations on male British doctors. British Medical Journal 328, 1519.
Doonan, R.J., Hausvater, A., Scallan, C., Mikhailidis, D.P., Pilote, L., Daskalopoulou, S.S., 2010. The effect of smoking on arterial stiffness. Hypertension Research, 1–13.
Eberth, J.F., Taucer, A.I., Wilson, K., Humphrey, J.D., 2009. Mechanics of carotid arteries in a mouse model of Marfans syndrome. Annals of Biomedical Engineering 37, 1093–1104.
Ferruzzi, J., Vorp, D.A., Humphrey, J.D., 2010. On constitutive descriptors of the biaxial mechanical behaviour of human abdominal aorta and aneurysms. Journal of the Royal Society, Interface (Pub ahead of print).
Gundiah, N., Ratcliffe, M.B., Pruitt, L.A., 2009. The biomechanics of arterial elastin. Journal of the Mechanical Behavior of Biomedical Materials 2, 288–296.
Lillie, M.A., Shadwick, R.E., Gosline, J.M., 2010. Mechanical anisotropy of inflated elastic tissue from the pig aorta. Journal of Biomechanics 43, 2070–2078.
Liu, S.Q., Fung, Y.C., 1993a. Changes in the structure and mechanical properties of pulmonary arteries in rats exposed to cigarette smoke. The American review of respiratory disease 148, 768–777.
Liu, S.Q., Fung, Y.C., 1993b. Material coefficients of the strain energy function of pulmonary arteries in normal and cigarette-exposed rats. Journal of Biomechanics 26, 1261–1269.
Sokolis, D., 2010. A passive strain energy function for elastic and muscular arteries: correlation of material parameters with histological data. Medical and Biological Engineering and Computing 48, 507–518.
Wan, W., Yanagisawa, H., Gleason, R.L., 2010. Biomechanical and microstructural properties of common carotid arteries from fibulin-5 null mice. Annals of Biomedical Engineering 38, 3605–3617.
Zou, Y., Zhang, Y., 2009. An experimental and theoretical study on the anisotropy of elastin network. Annals of Biomedical Engineering 37, 1572–1583.

PAPER II

Title Comparison of In Vivo and Simulated Abdominal Aortic Deformation

Authors Marie Sand Enevoldsen, Mads Møller Pedersen, Martin Christian Hemmsen, Lars Lönn, Jørgen Arendt Jensen, Kaj-Åge Henneberg

Journal Journal of Biomechanics

Publication History Submission date: 06-12-2011, In review

Comparison of in vivo and simulated abdominal aortic deformation

Marie Sand Enevoldsen[a], Mads Møller Pedersen[b], Martin Christian Hemmsen[a], Lars Lönn[b], Jørgen Arendt Jensen[a], Kaj-Åge Henneberg[a]

[a] *Department of Electrical Engineering, Technical University of Denmark, DK-2800 Lyngby, Denmark*
[b] *Department of Radiology and Vascular surgery, Copenhagen University Hospital, University of Copenhagen, DK-2100 Copenhagen, Denmark*

Abstract

This work presents the initial evaluation of the predictability of the four fiber family (4FF) model in a fluid-structure interaction (FSI) model of the abdominal aorta (AA) using published material parameters. This was achieved by comparing the wall dynamics predicted by the 4FF model implemented with averaged material parameters based on large population studies to *in vivo* wall dynamics obtained with ultrasound. Simulations reveal that the 4FF model apparently overestimates the displacement of the AA wall. For example, for one healthy volunteer the simulation predicts the displacement to be four times higher compared to the *in vivo* measurement, i.e 1.9. mm (average) in simulation versus 0.44 mm *in vivo*. The volunteers in a middle-aged (30-60 years) group experience approximately the identical stretch of the wall tissue during the cardiac cycle, i.e. $\lambda = 1.22$ on average. In contrast, a volunteer from the elderly (>60 years) group show less stretch, $\lambda = 1.09$. Comparing the stretch ratios obtained by simulation and the stretch ratio obtained from the experimental data, the 4FF model appears to underestimate the stiffness of the aortic wall using the published material parameters. The volunteers included in this study cover differences in age, gender, and smoking habits, which capture the three most common risk factors in AAA development.

Keywords: Abdominal aorta, In vivo, Anisotropy, Constitutive relation, Finite element model

1. Introduction

Numerous studies on the mechanical behavior of the human abdominal aorta (AA) have been used for formulation of constitutive relations (Humphrey and Taylor, 2008; Holzapfel and Ogden, 2010; Vande Geest et al., 2004). The stress-state in the AA wall influence the mechanobiology which control the overall vascular homeostasis Humphrey (2008). Imbalance in the vascular adaptation to diverse biological stimuli can lead to vascular pathologies such as atherosclerosis and aneurysm formation (Nichols and O'Rourke, 1990; Humphrey, 2002; Valentín et al., 2011). Thus, it is interesting to study the AA wall in a computational simulation environment to gain knowledge about the onset of mechanical events which lead to pathologies. To do this, both the constitutive relation and the associated material parameters should be chosen carefully. Several structurally motivated constitutive relations have been proposed for description of the mechanical behavior of the AA wall (Holzapfel et al., 2000; Gasser et al., 2006; Ferruzzi et al., 2011b; Achille et al., 2011). These models capture the anisotropic nonlinear hyperelastic behavior of the AA. To obtain realistic mechanical behavior the four fiber family (4FF) model proposed by Baek et al. (2007) was applied in this work. The 4FF model is motivated by the histological findings by Wicker et al. (2008). This model has shown to capture the differential changes in the mechanical behavior due to altered contributions from elastin and collagen fibers influencing the load-bearing capability of the arterial wall (Cardamone et al., 2009; Eberth et al., 2009; Enevoldsen et al., 2011a; Ferruzzi et al., 2011b). It also describes the growth and remodeling of the AA because of aging and alterations in the hemodynamic load (Valentín and Humphrey, 2009; Valentín et al., 2011). A major part of the published experimental data used for estimation of material parameters have been obtained from *ex vivo* uniaxial tests (He and Roach, 1994; Vorp et al., 1996), *ex vivo* biaxial tests Vande Geest et al. (2004, 2006), and *ex vivo* inflation-extension test methods (Humphrey et al., 1993; Deng et al., 1994). These tests are valuable for development of a general constitutive relation. Ferruzzi et al. (2011b) applied the experimental biaxial data from Vande Geest et al. (2004, 2006) to produce mean values for the material parameters in the 4FF model. They showed that the 4FF model is capable of discriminating the mechanical behavior from ages less than 30 years to over 60 years. Hence, the proposed material parameters capture the structural changes induced by aging, i.e. decrease in elastin content as well as changes in collagen turn-over and organization (Valentín et al., 2011).

Still, however, it remains to be investigated how well these averaged material parameters fit the general population in a 3D model. The aim of this paper is to compare the wall dynamics predicted by the 4FF model and *in vivo* wall dynamics obtained non-invasively with ultrasound. The predictability of the 4FF model is evaluated in a group of healthy volunteers. The simulation model proposed for this purpose is a fluid-structure interaction (FSI) model incorporated in a straight axis-symmetric circular cylinder with adjustment of the luminal radius for each volunteer. The solid wall is modeled as a thick-walled cylinder allowing for inspection of the mechanical behavior inside the wall. The blood constituting the fluid domain is modeled as a Newtonian fluid with subject-specific space and time dependent inlet profiles.

2. In vivo data

Ultrasound is a versatile medical imaging technique with the advantage of being dynamic and real-time. In cardiovascular disease ultrasound is a valuable tool in screening studies, the diagnostic process, and the follow-up, (Lindholt et al., 2005). Here, the ultrasound data serve two important purposes. Measurements of the blood flow in the AA are used for estimation of the time and space dependent flow profile applied in the fluid domain inlet of the FSI model. Second, tracking of the wall dynamics provides direct comparison between *in vivo* and simulation results.

With the recent introduction of a versatile research interface implemented on a commercial ultrasound scanner, the extraction of raw ultrasound data for off-line processing has become available (Hemmsen et al., 2011). This provides full access to the raw data used in estimation of blood flow and wall displacement.

2.1. Volunteers

Ultrasound data were obtained from 14 healthy volunteers using a duplex ultrasound scanning setup. The demographic details on the volunteers are listed in Table 1. This study was approved by the Danish National Committee on Biomedical Research Ethics (H-3-2009-102, 2009/09/01). The volunteers signed an informed consent.

2.2. Blood flow velocity estimation

The received spectral data from the AA are complex, hence both the positional and the directional information of the flow along the scan line

were obtained. The subject-specific blood flow profiles were determined by reformulating Poiseuilles law for pulsatile flow in rigid tubes.

Assuming that the blood is Newtonian, the average spatial velocity over time can be found by superimposing the sinusoidal component for each harmonic frequency using the principles proposed by Womersley (1955) and Evans (1982), see B. The temporal evolution of the spatial velocity profile was calculated as (Jensen, 1996),

$$v_{\text{blood}}(t,r) = 2v_0\left(1-\left(\frac{r}{R}\right)^2\right) + \sum_{m=1}^{10} |V_m|\,|\psi_m(r,\tau_m)|\cos(m\omega t - \phi_m + \chi_m)\ , \tag{1}$$

where the first term is steady flow, and the last term is the superposition of the sinusoidal components of the average spatial velocity multiplied by the function ψ_m. In (1) ϕ_m is the phase of the sinusoid resulting from the Fourier decomposition of $\bar{v}(t)$ (see (8)), and χ_m is the angle of ψ_m. The first ten harmonics were applied for the velocity estimation. This approach to introduce subject-specific velocity profiles in FSI models has also been applied by Papaharilaou et al. (2007).

2.3. Estimation of wall displacement

To evaluate the predictability of the 4FF model in the AA the *in vivo* wall motion during the cardiac cycle was estimated from the raw ultrasound data. A sample volume covering the AA wall was chosen. Estimation of the radial velocity component within this volume was performed using the autocorrelation technique implemented with averaging of the radio frequency signals (Jensen, 1996; Kasai et al., 1985; Loupas et al., 1995),

$$v_{\text{wall}} = -\frac{c_{\text{speed}} f_{\text{prf}} \sin(\theta)}{4\pi f_0} \arctan\left(\frac{\mathcal{I}\{R(1)\}}{\mathcal{R}\{R(1)\}}\right)\ , \tag{2}$$

where f_{prf} is the pulse repetition time, $\mathcal{I}\{R(1)\}$ is the imaginary part of the autocorrelation function, $R(\tau)$ at lag one, and $\mathcal{R}\{R(1)\}$ is the real part of $R(\tau)$. Only the radial displacement could be determined from the present data sets. The displacement, $\vec{\mathrm{u}}(\vec{\mathrm{r}},t)$, was determined by integration of the velocity field over time,

$$\vec{\mathrm{u}}(\vec{\mathrm{r}},t) = \int_0^{T_{\text{pulse}}} \vec{\mathrm{v}}(\vec{\mathrm{r}},t)dt\ , \tag{3}$$

where T_{pulse} is the length of the cardiac cycle in seconds. A complete cardiac cycle was defined as the time between two consecutive peak velocities in forward flow.

3. Constitutive framework

The AA wall material is assumed to be a constrained mixture of an amorphous isotropic elastin dominated matrix reinforced by collagen fibers. The collagen fibers are grouped in four directions of orientation. The AA wall was assumed to be nearly incompressible, thus the strain energy function is divided into a purely volumetric elastic response, $W_{\text{vol}}(J)$, and a purely isochoric elastic response $W_{\text{iso}}\left(\bar{\mathbf{C}}, \mathrm{M}^{(\mathrm{k})}\right)$ (Holzapfel et al., 2000; Achille et al., 2011),

$$W\left(\bar{\mathbf{C}}, \mathrm{M}^{(\mathrm{k})}\right) = W_{\text{vol}}(J) + W_{\text{iso}}\left(\bar{\mathbf{C}}, \mathrm{M}^{(\mathrm{k})}\right) \ , \tag{4}$$

where $J = \det \mathbf{F}$ is the deformed-to-undeformed volume ratio with $\mathbf{F}$ as the deformation gradient tensor, $\bar{\mathbf{C}} = J^{-2/3}\mathbf{F}^{\mathrm{T}}\mathbf{F}$ is the modified right Cauchy-Green tensor, and $\mathrm{M}^{(\mathrm{k})}$ is a unit vector describing the direction of orientation for each collagen fiber family. For the purely volumetric response it was assumed (Holzapfel et al., 2000; Achille et al., 2011),

$$W_{\text{vol}}(J) = \frac{\kappa}{2}\left(J-1\right)^2 \tag{5}$$

where $\kappa = 10^9$ Pa is the bulk modulus of the tissue. The isochoric response was represented by the 4FF model (Baek et al., 2007),

$$W_{\text{iso}}\left(\bar{\mathbf{C}}, \mathrm{M}^{(\mathrm{k})}\right) = \frac{c}{2}\left(\bar{I}_{\mathrm{C}} - 3\right) + \sum_{k=1}^{4} \frac{c_1^{(\mathrm{k})}}{4c_2^{(\mathrm{k})}} \left\{ \exp\left(c_2^{(\mathrm{k})} \left(I\bar{V}_{\mathrm{C}}^{(\mathrm{k})} - 1 \right)^2 \right) - 1 \right\} \tag{6}$$

where c, $c_1^{(\mathrm{k})}$, $c_2^{(\mathrm{k})}$ are material parameters and the pseudo-invariants are given as

$$\bar{I}_{\mathrm{C}} = \operatorname{tr} \bar{\mathrm{C}} \ , \quad I\bar{V}_{\mathrm{C}}^{(\mathrm{k})} = \mathrm{M}^{(\mathrm{k})} \bar{\mathbf{C}} \mathrm{M}^{(\mathrm{k})} \ . \tag{7}$$

The material parameters used in this work were adopted from Ferruzzi et al. (2011b) using the median value of each material parameter within each age group. The choice of material parameters was based on the fact

that application of median parameters more accurately reflect the average mechanical behavior within each age group, see Fig. 1. The mean represents a more conservative reflection of the average mechanical behavior.

4. Finite element model

The 4FF model was implemented in the commercial finite element (FE) code COMSOL Multiphysics v4.2 (COMSOL AB, Stockholm, Sweden). The 4FF model implementation was validated in a simulation mimicking the biaxial tests performed by Vande Geest et al. (2004, 2006), see Enevoldsen et al. (2011b) for detailes. The geometry of the AA was simplified as a 10 cm long cylindrical vessel having a lumen radius (R_i) corresponding to the measured lumen radius for each volunteer. The wall thickness (h) was assumed to be uniform, i.e. 1.5 mm in the reference configuration before application of luminal flow. The wall was fixed at the upper and lower boundary to simulate the tethering of the AA. The luminal wall boundary motion was determined from the stress induced by the pulsating blood in the fluid domain. At the external lateral wall boundary a pressure of 0.87 kPa was applied to simulate the abdominal pressure under normal conditions. In this work the reference configuration was assumed to be the geometry at the end-diastole pressurized to 80 mmHg (10.7 kPa) resulting in a radial residual displacement.

Mesh

The model is axis-symmetric, hence it is only necessary to model a rectangular model consisting of a fluid domain and a solid domain. The fluid model was meshed with triangular elements by application of a user-controlled mesh algorithm in COMSOL Multiphysics calibrated for fluid dynamics. The solution was considered stable when further refinement of the mesh resulted in changes less than 1% in the peak velocity in the center of the vessel. A stable solution was achieved with 1680 tetrahedral elements. The solid model was meshed with a fixed number of rectangular elements in the axial direction. The number of elements in the radial direction was determined from a mesh convergence test comparing the magnitude of the circumferential stress ($\sigma_{\theta\theta}$) at a position inside the AA wall in two consecutive refinement steps. The solution was considered stable when further refinement of the mesh resulted in changes less than 10 Pa in the magnitude of the circumferential Cauchy stress component. A stable solution was achieved with eight rectangular elements in the radial direction.

5. Results

5.1. Blood flow

Due to aliasing in the acquired ultrasound data only data sequences from three of the 14 healthy volunteers were suitable for blood flow estimation. Fig. 2a illustrate the temporal velocity evolution averaged over the radial position in the AA of a 57 years old female. For comparison the same temporal velocity evolution for a 76 years old male, and a 53 years old male are displayed in Fig. 2b and Fig. 2c. The blood flow profiles are illustrated for each of the three volunteers in Fig. 3. As it can be seen, a parabolic flow profile is never obtained. This was also expected, as the flow in the AA is affected by curves and bends, as well as flow dividers such as the renal arteries and the iliac bifurcation. In the AA secondary flow has been observed (Frazin et al., 1990; Thomas, 1990; Pedersen et al., 1993). These observations are partly reflected in the complex flow profile seen in Fig. 3. The flow profile shifts from a blunt forward flow profile at peak systole (PS) through a complex profile with both forward and backward flow, and recurrence to the blunt profile at the end diastole (ED). To apply the *in vivo* velocity profiles as inlet boundary condition in the FSI model, the blood flow data are defined on a grid of time points and radial positions, see Fig. 4.

5.2. Wall behavior

The displacement of the AA wall was calculated using (3). The estimation of the wall displacement was performed by locating either the lower or upper boundary of the AA using the information from the ultrasound scanning. To obtain a good measure of the displacement, the motion detection was performed by averaging over a sample volume of 2.5 wavelengths of the transmitted ultrasound pulse ($\lambda_{\text{wavelength}}$) centered around the chosen wall boundary. The displacements of the AA wall for each of the three volunteers are depicted in Fig. 5. The displacement was tracked during the first complete cardiac cycle in the data sequence. Table 2 summarize the measured diameter at ED, the estimated total displacement from the ultrasound data, and the calculated stretch ratio for each of the three volunteers. The wall dynamics through a cardiac cycle is depicted in Fig. 5 for each of the three volunteers.

5.3. FSI model results

The simulation of wall motion was conducted in a circular axis-symmetric cylinder. The FSI model runs over an entire cardiac cycle for each of the three

volunteers. To compare the results, the circumferential stretch ratio and the radial displacement are presented in Fig. 6. The radial displacement and the circumferential stretch ratio is calculated at four positions in the AA wall (0% at the luminal wall boundary and 100% at the external wall boundary), see Fig. 6. The simulation model predict a significantly higher displacement of the AA wall compared to the experimentally measured, see Table 2. The implementation of subject-specific blood flow profiles do affect the displacement. A smaller displacement is observed for the female volunteer compared to the male volunteer, even though the same set of material parameters were applied in the solid domain as the two volunteers fall within the same age group (30-60 years). The displacement with in the subjects in this age group is significantly higher compared to volunteer no. 11, as the displacement is 0.7 mm on average, contrasted by 1.8 mm on average within the two middle-aged volunteers. Comparing the stretch ratios obtained by simulation and the *in vivo* stretch ratio, the 4FF model appears to underestimate the stiffness of the AA wall using the material parameters from Ferruzzi et al. (2011b), see Fig. 6 and Table 2. The implementation of the 4FF model in three dimensions allows inspection of the intramural stress components, and hence, provides a detailed reflection of the mechanical behavior. In Fig. 7 the stress distribution inside the AA wall of the three volunteers are displayed. The general pattern of stress distribution for each of the principal Cauchy stress components has been observed in several studies (Enevoldsen et al., 2011b; Achille et al., 2011; Holzapfel et al., 2000). Residual stress was not included in this study.

6. Discussion

In this paper a FSI simulation model was proposed to evaluate the predictability of the 4FF model applied to the AA. The *in vivo* data were obtained using a research interface implemented on an ultrasound scanner. The raw data for blood flow and wall motion were processed off-line. The group of subjects consist of 14 volunteers, however, due to aliasing of the flow data, only results from three volunteers are presented. The blood flow profiles and wall displacements were estimated using well-known techniques from signal processing. The applied constitutive framework captures the nonlinear hyperelastic anisotropic properties of the AA tissue. Based on the simulations the 4FF model overestimates the displacement, and hence the stretch of the AA tissue. The application of subject-specific blood flow profiles introduce

a difference in displacement even though the same material parameters are applied, see Fig. 6. Determination of material parameters is a vital part of predicting the wall stress. The biaxial data published by Vande Geest et al. (2004, 2006) is widely used for determination of material parameters, as it comprise data on both normal AA and AAA. Ferruzzi et al. (2011b) fitted these data to the 4FF model. However, the use of mean material properties might not reflect the overall mechanical behavior of the AA within a broad population group (Ferruzzi et al., 2011a). Fit of a model should preferably be based on individual data. But this is difficult to obtain, as it is not possible to do tension tests *in vivo*. Instead ultrasound techniques has been applied in several studies to obtain model fits based on *in vivo* data. Stålhand (2009) used pressure-radius measurements from the AA (Sonesson et al., 1994) to obtain material parameters for the two fiber family model proposed by Holzapfel et al. (2000). The fit of *in vivo* data was applied in three male volunteers. The AA was modeled as a hyperelastic incompressible thin-walled cylinder. Masson et al. (2008) demonstrated the viability of material parameter estimation for the 4FF model applied on human carotid arteries. They modeled the carotid artery as a thick-walled cylinder and included the effect from residual stress in the estimation of material parameters. In this work the predictability of the 4FF model was evaluated using the material parameters given in Ferruzzi et al. (2011b) as these were considered the most complete for this purpose. It has not been possible to find similar studies in the literature for comparison. Several FSI models for simulation of the wall stress in AAAs have been proposed (Rissland et al., 2009; Scotti et al., 2008; Wolters et al., 2005; Di Martino et al., 2001). Scotti et al. (2008) compared FSI modeling and finite element analysis in an idealized three dimensional geometry in order to investigate the effect of assuming a uniform arbitrary determined pressure inside the AAA sac compared to application of a non-uniform pressure resulting from FSI modeling in the same geometry. They found that the coupled FSI analysis produced a higher wall stress in the AAA compared to application of a stationary luminal pressure. The fluid domain inlet was modeled as a time-dependent parabolic profile. The material model for the solid domain was the isotropic hyperelastic model proposed by Raghavan and Vorp (2000). Rissland et al. (2009) and Di Martino et al. (2001) applied FSI models to realistic AAA geometries. Di Martino et al. (2001) used average blood flow velocities from the AA obtained with ultrasound. The inlet profile was assumed to be parabolic at the inlet of the aneurysm. Rissland et al. (2009) produced inlet and outlet conditions using the data

provided by Olufsen et al. (2000), and applied the two fiber family model in the aneurysmal tissue. As the analysis of the FSI models were performed in realistic AAA models, it is not possible to perform a direct comparison to the predicted stress levels. There are limitations to the presented work. The application of the principles of Womersley (1955) and Evans (1982) for reconstruction of blood flow profiles assumes that the flow is Newtonian and the pulsation is steady. In addition, the inlet geometry is assumed to be rotational symmetric and the walls of the tube are stiff. The predictability could only be evaluated in three of the volunteers as the FSI model setup requires subject-specific blood flow conditions in the inlet. Note, however, that the three volunteers cover differences in age, gender, and smoking habits which capture the three most common risk factors in AAA development, i.e. increasing age, male gender, and smoking (Enevoldsen et al., 2011a; Humphrey and Taylor, 2008).

Conflict of interest statement

There is no conflict of interest.

Acknowledgement

This work was supported by project 55562 at Technical University of Denmark, Radiometer Medical ApS., and the Danish Ministry of Science, Technology, and Innovation.

Appendices

A. Scanning procedure

The 14 volunteers were allowed to rest before the ultrasound scan in order to obtain identical setups for all volunteers. The echo signals (spectral data) from the blood were acquired using a convex array transducer connected to a 2202 ProFocus scanner (B-K Medical, Herlev, Denmark), and several data sequences of five seconds each were acquired for each volunteer. The spectral data were extracted using a UA2227 research interface implemented on the ultrasound scanner Hemmsen et al. (2011).

A data sequence was obtained by holding the transducer at a fixed position and then transmitting a series of ultrasound pulses (pulsed wave system). The backscattered echo signals were received by the same transducer and sampled with a time delay to assign the received signals to specific positions in the AA

B. Blood flow velocity estimation

The mean blood velocity was estimated from the frequency spectra of the received backscattered signals. The velocity along the scan line is in the longitudinal direction in the AA and a function of radius. The mean blood flow velocity, $\bar{v}$, is proportional to the mean frequency shift Jensen (1996),

$$\bar{v}(t) = -\frac{c_{\text{speed}}}{2f_0 \cos(\theta)} \bar{f} \quad , \tag{8}$$

where $c_{\text{speed}} = 1540$ m/s is the speed of sound in blood, $f_0 = 3$ MHz is the center frequency of the transducer, and θ is the angle between the ultrasound beam and flow direction. The mean frequency shift $\bar{f}$ was calculated using the power spectrum, $P(f)$, Angelsen (1981),

$$\bar{f} = \frac{\int_{-\infty}^{\infty} fP(f)df}{\int_{-\infty}^{\infty} P(f)df} \quad . \tag{9}$$

Mathematically, periodic velocity waveforms can be decomposed into Fourier series when linearity is assumed (Truskey et al., 2004), and then added to obtain the velocity profile as a function of space and time. The relationship between the pressure and volume flow rate for a single sinusoidal has been derived by Womersley (1955). Evans (1982) showed that the velocity profile of a steady-state pulsating flow can be determined when the

volume flow rate is known. Here the estimated velocity in (8) is decomposed into Fourier series, i.e.

$$V_m = \frac{1}{T}\int_0^T \bar{v}(t)\exp(-jm\omega t)dt \quad , \tag{10}$$

where T is the duration of one cardiac cycle, $\omega = 2\pi f$ is angular frequency, and m is an index for the harmonics. Assuming that the blood is a Newtonian fluid, the average spatial velocity over time of the pulsatile flow can be found by superimposing the sinusoidal components for each harmonic frequency, see (1).

The function ψ_m describes how the velocity changes with time and position over one period for each of the sinusoidal components. This function depends on radial position in the AA, the angular frequency ω, and the properties of the blood (Jensen, 1996),

$$\psi_m(r,\tau_m) = \frac{j^{2/3}\alpha J_0(j^{2/3}\alpha) - j^{2/3}\alpha J_0(j^{2/3}\alpha\frac{r}{R})}{j^{2/3}\alpha J_0(j^{2/3}\alpha) - 2J_1(j^{2/3}\alpha)} \ , \tag{11}$$

where J_n are n'th order Bessel functions of first kind, and α is the Womersley number,

$$\alpha = R\sqrt{\frac{\rho_{\text{blood}}}{\mu_{\text{blood}}}\omega_m} \ , \tag{12}$$

in which $\rho_{\text{blood}} = 1{,}060$ kg/m^3 is the mass density of the blood, and $\mu_{\text{blood}} = 3.5$ mPa·s is the dynamic viscosity of blood. This approach to introduce subject-specific velocity profiles in FSI models has also been used by Papaharilaou et al. (2007).

References

Achille, P. D., Celi, S., Puccio, F. D., Forte, P., 2011. Anisotropic AAA: Computational comparison between four and two fiber family material models. Journal of Biomechanics 44 (13), 2418 – 2426.

Angelsen, B. A. J., 1981. Instantaneous frequency, mean frequency, and variance of mean frequency estimators for ultrasonic blood velocity doppler signals. IEEE Transactions on Biomedical Engineering (11), 733–741.

Baek, S., Gleason, R. L., Rajagopal, K., Humphrey, J. D., 2007. Theory of small on large: Potential utility in computations of fluid-solid interactions in arteries. Computer methods in applied mechanics and engineering 196 (31-32), 3070–3078.

Cardamone, L., Valentín, A., Eberth, J., Humphrey, J. D., 2009. Origin of axial prestretch and residual stress in arteries. Biomechanics and Modeling in Mechanobiology 8 (6), 431–446.

Deng, S., Tomioka, J., Debes, J., Fung, Y., 1994. New experiments on shear modulus of elasticity of arteries. American Journal of Physiology-Heart and Circulatory Physiology 266 (1), H1–H10.

Di Martino, E. S., Guadagni, G., Fumero, A., Ballerini, G., Spirito, R., Biglioli, P., Redaelli, A., 2001. Fluid-structure interaction within realistic three-dimensional models of the aneurysmatic aorta as a guidance to assess the risk of rupture of the aneurysm. Medical engineering & physics 23 (9), 647–655.

Eberth, J., Taucer, A., Wilson, E., Humphrey, J. D., 2009. Mechanics of carotid arteries in a mouse model of marfan syndrome. Annals of biomedical engineering 37 (6), 1093–1104.

Enevoldsen, M. S., Henneberg, K.-A., Jensen, J. A., Lönn, L., Humphrey, J. D., 2011a. New interpretation of arterial stiffening due to cigarette smoking using a structurally motivated constitutive model. Journal of Biomechanics 44 (6), 1209–1211.

Enevoldsen, M. S., Henneberg, K.-A., Lönn, L., Jensen, J. A., 2011b. Finite element implementation of a structurally-motivated constitutive relation for the human abdominal aortic wall with and without aneurysms. In: 15th

Nordic-Baltic Conference on Biomedical Engineering and Medical Physics (NBC 2011). Springer, pp. 13–16.

Evans, D., 1982. Some aspects of the relationship between instantaneous volumetric blood flow and continuous wave Doppler ultrasound recordings. iii. the calculation of doppler power spectra from mean velocity waveforms, and the results of processing these spectra with maximum, mean, and rms frequency processors. Ultrasound in Medicine and Biology 8 (6), 617–623.

Ferruzzi, J., Enevoldsen, M. S., Humphrey, J. D., 2011a. On the mechanical behavior of healthy and aneurysmal abdominal aorta. In: Proceeding of the ASME 2011 Summer Bioengineering Conference. Farmington, Pennsylvania, USA.

Ferruzzi, J., Vorp, D. A., Humphrey, J. D., 2011b. On constitutive descriptors of the biaxial mechanical behaviour of human abdominal aorta and aneurysms. Journal of The Royal Society Interface 8 (56), 435–450.

Frazin, L., Lanza, G., Vonesh, M., Khasho, F., Spitzzeri, C., McGee, S., Mehlman, D., Chandran, K., Talano, J., McPherson, D., 1990. Functional chiral asymmetry in descending thoracic aorta. Circulation 82 (6), 1985–1994.

Gasser, T. C., Ogden, R. W., Holzapfel, G. A., 2006. Hyperelastic modelling of arterial layers with distributed collagen fibre orientations. Journal of the royal society interface 3 (6), 15–35.

He, C., Roach, M., 1994. The composition and mechanical properties of abdominal aortic aneurysms. Journal of vascular surgery 20 (1), 6–13.

Hemmsen, M. C., Nikolov, S. I., Pedersen, M. M., Pihl, M. J., Enevoldsen, M. S., Hansen, J. M., Jensen, J. A., 2011. Implementation of a versatile research data acquisition system using a commercially available medical ultrasound scanner. IEEE transactions on ultrasonics, ferroelectrics, and frequency control, accepted.

Holzapfel, G. A., Gasser, T. C., Ogden, R. W., 2000. A new constitutive framework for arterial wall mechanics and a comparative study of material models. Journal of elasticity 61 (1), 1–48.

Holzapfel, G. A., Ogden, R. W., 2010. Constitutive modelling of arteries. Proceedings of the Royal Society A: Mathematical, Physical and Engineering Science 466 (2118), 1551–1597.

Humphrey, J. D., 2002. Cardiovascular solid mechanics: cells, tissues, and organs. Springer Verlag.

Humphrey, J. D., 2008. Vascular adaptation and mechanical homeostasis at tissue, cellular, and sub-cellular levels. Cell biochemistry and biophysics 50 (2), 53–78.

Humphrey, J. D., Kang, T., Sakarda, P., Anjanappa, M., 1993. Computer-aided vascular experimentation: a new electromechanical test system. Annals of biomedical engineering 21 (1), 33–43.

Humphrey, J. D., Taylor, C. A., 2008. Intracranial and abdominal aortic aneurysms: similarities, differences, and need for a new class of computational models. Annual review of biomedical engineering 10, 221–246.

Jensen, J. A., 1996. Estimation of blood velocities using ultrasound: A signal processing approach. Cambridge Univ Pr.

Kasai, C., Namekawa, K., Koyano, A., Omoto, R., 1985. Real-time two-dimensional blood flow imaging using an autocorrelation technique. IEEE Trans. Sonics Ultrason 32 (3), 458–464.

Lindholt, J. S., Juul, S., Fasting, H., Henneberg, E. W., 2005. Screening for abdominal aortic aneurysms: single centre randomised controlled trial. bmj 330 (7494), 750–755.

Loupas, T., Powers, J., Gill, R., july 1995. An axial velocity estimator for ultrasound blood flow imaging, based on a full evaluation of the doppler equation by means of a two-dimensional autocorrelation approach. Ultrasonics, Ferroelectrics and Frequency Control, IEEE Transactions on 42 (4), 672 –688.

Masson, I., Boutouyrie, P., Laurent, S., Humphrey, J. D., Zidi, M., 2008. Characterization of arterial wall mechanical behavior and stresses from human clinical data. Journal of biomechanics 41 (12), 2618–2627.

Nichols, W. W., O'Rourke, M. F., 1990. McDonald's blood flow in arteries: theoretic, experimental and clinical principles. Lea & Febiger Philadelphia.

Olufsen, M. S., Peskin, C., Kim, W., Pedersen, E. M., Nadim, A., Larsen, J., 2000. Numerical simulation and experimental validation of blood flow in arteries with structured-tree outflow conditions. Annals of biomedical engineering 28 (11), 1281–1299.

Papaharilaou, Y., Ekaterinaris, J., Manousaki, E., Katsamouris, A., 2007. A decoupled fluid structure approach for estimating wall stress in abdominal aortic aneurysms. Journal of biomechanics 40 (2), 367–377.

Pedersen, E. M., Sung, H., Burlson, A., Yoganathan, A., 1993. Two-dimensional velocity measurements in a pulsatile flow model of the normal abdominal aorta simulating different hemodynamic conditions. Journal of biomechanics 26 (10), 1237–1247.

Raghavan, M., Vorp, D. A., 2000. Toward a biomechanical tool to evaluate rupture potential of abdominal aortic aneurysm: identification of a finite strain constitutive model and evaluation of its applicability. Journal of Biomechanics 33 (4), 475–482.

Rissland, P., Alemu, Y., Einav, S., Ricotta, J., Bluestein, D., 2009. Abdominal aortic aneurysm risk of rupture: patient-specific fsi simulations using anisotropic model. Journal of biomechanical engineering 131, 031001–1–013001–10.

Scotti, C. M., Jimenez, J., Muluk, S., Finol, E. A., 2008. Wall stress and flow dynamics in abdominal aortic aneurysms: finite element analysis vs. fluid–structure interaction. Computer methods in biomechanics and biomedical engineering 11 (3), 301–322.

Sonesson, B., Länne, T., Vernersson, E., Hansen, F., 1994. Sex difference in the mechanical properties of the abdominal aorta in human beings. Journal of vascular surgery 20 (6), 959–969.

Stålhand, J., 2009. Determination of human arterial wall parameters from clinical data. Biomechanics and modeling in mechanobiology 8 (2), 141–148.

Thomas, J., 1990. Flow in the descending aorta. A turn of the screw or a sideways glance? Circulation 82 (6), 2263–2265.

Truskey, G. A., Yuan, F., Katz, D., 2004. Transport phenomena in biological systems. Pearson Prentice Hall Upper Saddle River, NJ.

Valentín, A., Humphrey, J. D., 2009. Parameter sensitivity study of a constrained mixture model of arterial growth and remodeling. Journal of biomechanical engineering 131, 101006–1–101006–11.

Valentín, A., Humphrey, J. D., Holzapfel, G. A., 2011. A multi-layered computational model of coupled elastin degradation, vasoactive dysfunction, and collagenous stiffening in aortic aging. Annals of Biomedical Engineering, 1–19.

Vande Geest, J. P., Sacks, M. S., Vorp, D. A., 2004. Age dependency of the biaxial biomechanical behavior of human abdominal aorta. Journal of biomechanical engineering 126, 815–822.

Vande Geest, J. P., Sacks, M. S., Vorp, D. A., 2006. The effects of aneurysm on the biaxial mechanical behavior of human abdominal aorta. Journal of biomechanics 39 (7), 1324–1334.

Vorp, D. A., Raghavan, M., Muluk, S., Makaroun, M., Steed, D., Shapiro, R., Webster, M. W., 1996. Wall strength and stiffness of aneurysmal and nonaneurysmal abdominal aorta. Annals of the New York Academy of Sciences 800 (1), 274–276.

Wicker, B., Hutchens, H. P., Wu, Q., Yeh, A., Humphrey, J. D., 2008. Normal basilar artery structure and biaxial mechanical behaviour. Computer Methods in Biomechanics and Biomedical Engineering 11 (5), 539–551.

Wolters, B., Rutten, M., Schurink, G., Kose, U., De Hart, J., Van De Vosse, F., 2005. A patient-specific computational model of fluid-structure interaction in abdominal aortic aneurysms. Medical engineering & physics 27 (10), 871–883.

Womersley, J., 1955. Method for the calculation of velocity, rate of flow and viscous drag in arteries when the pressure gradient is known. The Journal of physiology 127 (3), 553–563.

Figures and tables

Table 1: Demographic data for the 14 volunteers included in the research protocol. BMI is body mass index, BMI = [weight (kg)]/[(height (m))^2].

Volunteer	**Gender**	**Age (years)**	**BMI (kg/m^2)**	**Smoking**
1	Female	26	20.2	No
2	Female	28	23.8	No
3	Female	31	19.0	No
4	Female	28	20.3	No
5	Female	57	29.1	No
6	Female	50	24.0	No
7	Male	27	25.6	No
8	Male	25	21.2	No
9	Male	23	19.9	No
10	Male	34	21.3	No
11	Male	76	22.8	No
12	Male	51	24.2	No
13	Male	53	22.7	Yes
14	Male	57	26.8	No

Table 2: Experimentally acquired measures of end diastolic (ED) diameter, the total displacement u_{total}, and the resulting stretch ratio, λ, for each volunteer.

		Stretch		
volunteer	ED	*in vivo*	simulation	difference
5	13.2 mm	1.09	1.22	+ 12 %
11	15.6 mm	1.08	1.09	+ 0.92 %
13	13.9 mm	1.07	1.22	+ 14 %
		Displacement		
volunteer	ED	*in vivo*	simulation	difference
5	13.2 mm	0.59 mm	1.6 mm	+ 171 %
11	15.6 mm	0.42 mm	0.72 mm	+ 71 %
13	13.9 mm	0.44 mm	1.9 mm	+ 332 %

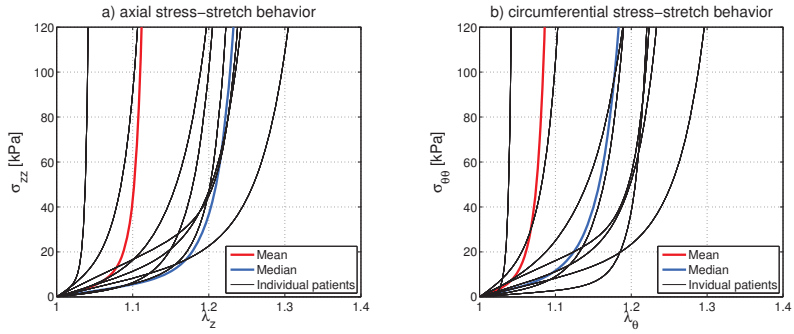

Figure 1: Illustration of the mechanical behavior of AA tissue within a group of subjects 30 to 60 years old where a) show the axial stress-stretch relation, and b) show the circumferential stress-stretch relation. The mechanical behavior predicted by the mean of material parameters is marked by the solid red line. The mechanical behavior predicted by the median of the the material parameters is marked by the blue solid line.

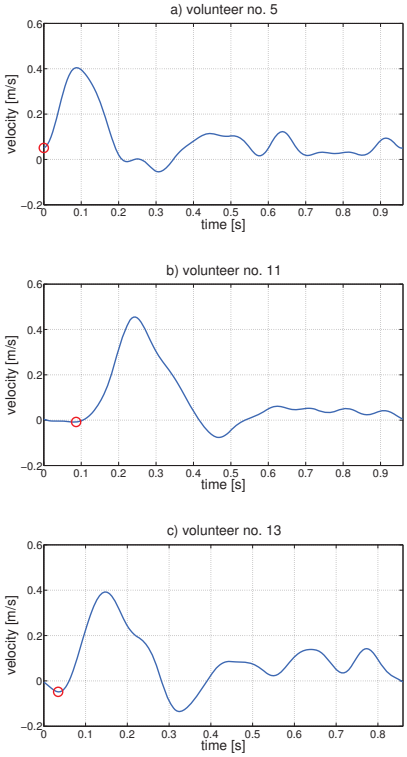

Figure 2: Plot of the velocity evolution during the cardiac cycle for three volunteers; a) a 57 years old healthy female (volunteer no. 5), b) a 76 years old healthy male (volunteer no. 11), and c) a 53 years old healthy male (volunteer no. 13). The velocity is averaged over the radial position. The red circle indicate the position of the end diastole during the cardiac cycle.

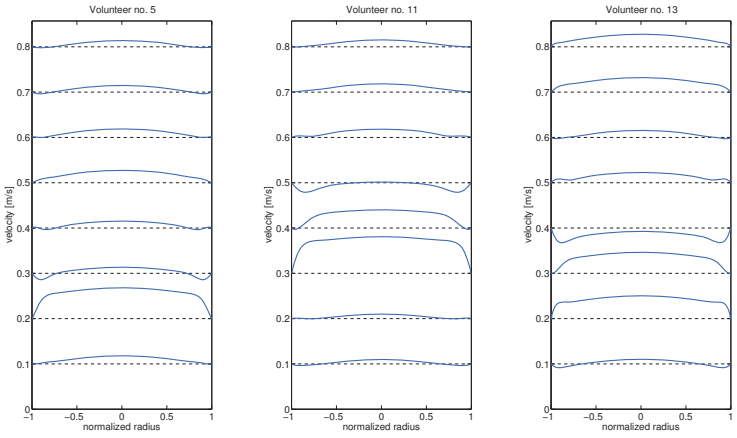

Figure 3: Plot of the blood flow profile for three volunteers; a) a 57 years old healthy female (volunteer no. 5), b) a 76 years old healthy male (volunteer no. 11), and c) a 53 years old healthy male (volunteer no. 13). The plot show the difference in evolution of the flow profile. The profiles are reconstructed from acquired *in vivo* data using (1).

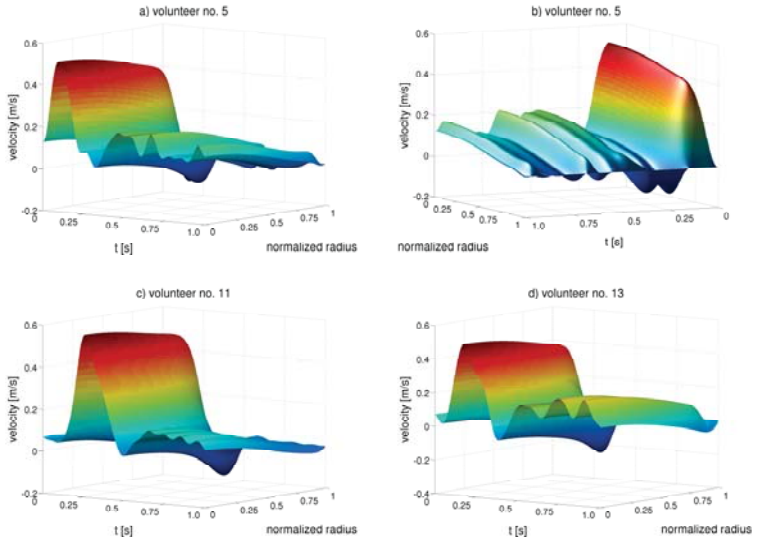

Figure 4: Three dimensional grid implemented as boundary condition in the FSI model for three volunteers; a) a 57 years old healthy female (volunteer no. 5), b) the velocity grid for volunteer no. 5 seen from the back, c) a 76 years old healthy male (volunteer no. 11), and d) a 53 years old healthy male (volunteer no. 13).

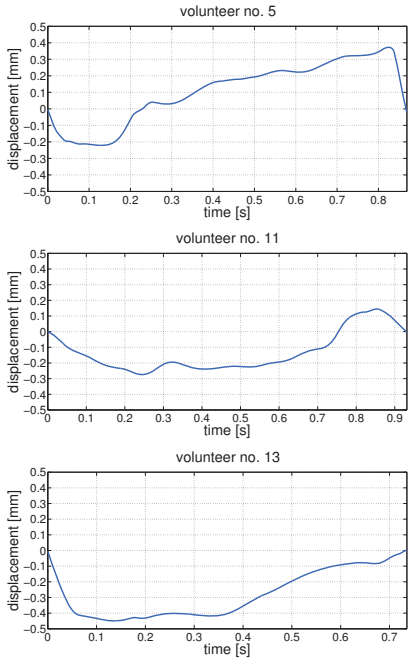

Figure 5: Movement and displacement experienced by the AA wall during one cardiac cycle from peak systole to peak systole. The top figure is the displacement for volunteer no. 5. The figure in the center is the wall displacement of volunteer no. 11. The lower figure is the displacement of the wall for volunteer no. 13.

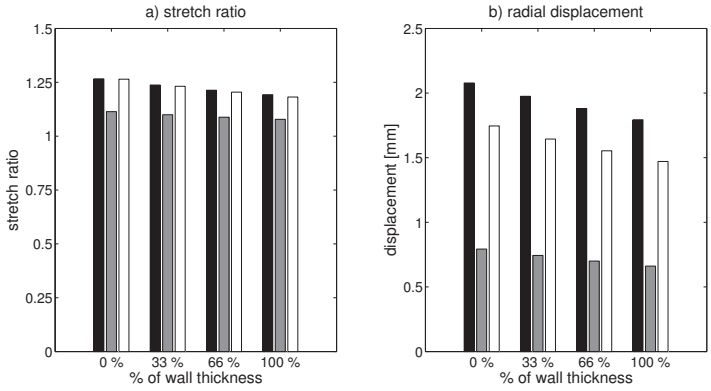

Figure 6: Bar graph of the simulation results using the 4FF model. a) show the stretch ratio obtained in the circumferential direction as a function of percentage of the wall thickness. b) show the displacement as a result of the applied fluid flow as a function of percentage of the wall thickness. The black bars are volunteer no. 13, the gray bars are volunteer no. 11, and the white bars are volunteer no. 5.

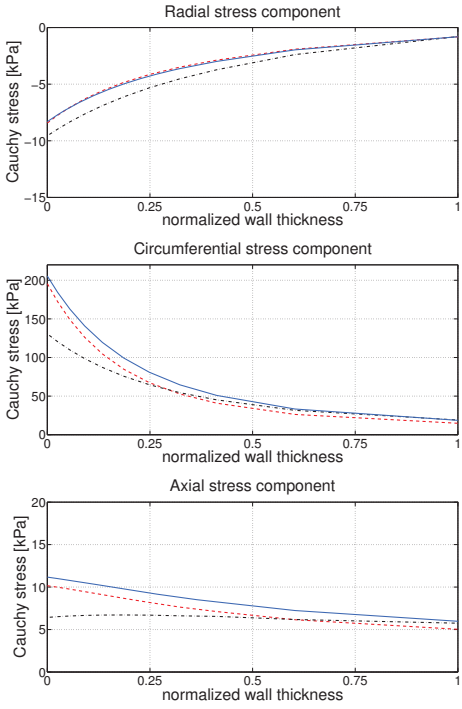

Figure 7: The three principal stress components within the AA wall as a function of the normalized wall thickness. The solid blue line ascribe to volunteer no. 13, the black dash-dot line ascribe to volunteer no. 11, and the red dashed line ascribe to volunteer no. 5. The top panel shows the radial stress components. The center panel shows the circumferential stress components, and the bottom panel displays the axial stress components for each volunteer. All stress components are deduces from the AA wall 50 % below the inlet of the FSI model.

PAPER III

Title Implementation of a Versatile Research Interface Data Acquisition Sysytem Using a Commercially Available Medical Ultrasound Scanner

Authors Martin Christian Hemmsen, Svetoslav Ivanov Nikolov, Mads Møller Pedersen, Michael Johannes Pihl, Marie Sand Enevoldsen, Jens Munk Hansen, Jørgen Arendt Jensen

Journal IEEE Transactions on Ultrasonics, Ferroelectrics, and Frequency Control

Publication History Submission date: 09-05-2011, Accepted for publication: 08-08-2011

Implementation of a versatile research data acquisition system using a commercially available medical ultrasound scanner

Martin Christian Hemmsen, Svetoslav Ivanov Nikolov, Mads Møller Pedersen, Michael Johannes Pihl, Marie Sand Enevoldsen, Jens Munk Hansen, and Jørgen Arendt Jensen

Abstract

This paper describes the design and implementation of a versatile and open architecture research data acquisition system using a commercially available medical ultrasound scanner. The open architecture will allow researchers and clinicians to rapidly develop applications and move them relatively easy to the clinic. The system consists of a standard PC equipped with a X64-CL Express camera link (Dalsa, Waterloo, Ontario, Canada) and a 2202 ProFocus equipped with a UA2227 research interface (BK-Medical, Herlev, Denmark). The 2202 ProFocus ultrasound scanner is an easy to use imaging device that is capable of generating high quality images. In addition to supporting the acquisition of multiple data types such as B-mode, M-mode, pulsed Doppler and color flow imaging, the machine provides users with full control over imaging parameters such as transmit level, excitation waveform, beam angle, and focal depth. Beamformed radio frequency data can be acquired from regions of interest throughout the image plane and stored to a file with a simple button press. For clinical trials and investigational purposes, where an identical image plane is wanted on both an experimental and a reference dataset, data can be captured interleaved. This form of data acquisition, allows switching between multiple setups, maintaining identical transducer, scanner, region of interest, and recording time. The data acquisition is controlled through a Graphical User Interface (GUI) running on the PC. This program implements an interface for third-party software, such as Matlab, to interact with the application. A software development toolkit (SDK) is developed to give researchers and clinicians the ability to utilize Matlab for data analysis and flexible manipulation of control parameters. Due to the advantages of speed of acquisition and clinical benefit, research projects have successfully used the system to test and implement their customized solutions for different applications. Three examples of system use are presented in this paper: Evaluation of Synthetic Aperture Sequential Beamformation (SASB), Transverse Oscillation (TO) for blood velocity estimation, and Acquisition of spectral velocity data for evaluating aortic aneurysms.

Martin Christian Hemmsen is with BK Medical, Denmark, and the Department of Electrical Engineering, Center for Fast Ultrasound, Technical University of Denmark. e-mail: mah@elektro.dtu.dk.

Svetoslav Ivanov Nikolov is with BK Medical, Denmark.

Mads Møller Pedersen is with the Department of Radiology, Rigshospitalet.

Michael Johannes Pihl is with the Department of Electrical Engineering, Center for Fast Ultrasound, Technical University of Denmark.

Marie Sand Enevoldsen is with the Department of Electrical Engineering, Center for Fast Ultrasound, Technical University of Denmark.

Jens Munk Hansen is with the Department of Electrical Engineering, Center for Fast Ultrasound, Technical University of Denmark.

Jørgen Arendt Jensen is with the Department of Electrical Engineering, Center for Fast Ultrasound, Technical University of Denmark.

I. Introduction

Difficulties accessing ultrasound data in the laboratory and clinic has not only limited the basic research, but also hindered the clinical testing of new ultrasound applications. In order to access raw ultrasound data, researchers have worked with ultrasound manufacturers to build custom ultrasound systems such as RASMUS [1], [2], and SARUS [3], but due to the size of these scanners they are inaccessible in the clinic. There also exist some commercial or partially commercial ultrasound systems that target the research or OEM market, i.e. OPEN [4], Verasonics [5], Samplify, FEMMINA [6], and DiPhAS [7]. Recently, a number of research interface platforms for clinical ultrasound scanners have been developed for systems such as Hitachi HiVision 5500 [8], Siemens Antares [9], Ultrasonix 500 [10], and Toshiba Aplio. With the introduction of research interface platforms on clinically available scanners it is now possible to acquire and store data. However, for a system to be suitable for acquisition of data for clinical evaluations, the system has to keep factors, such as identical transducer, region of interest, and recording time constant on both the reference and the experimental image. Another system requirement is the ability to acquire and store data fast enough for multiple acquisitions during a normal ultrasound examination, and under normal operating conditions. The objective of this work is to develop and implement a versatile research data acquisition system using a commercially available medical ultrasound scanner. This will allow researchers and clinicians to rapidly develop applications and ease the transition to the clinic for evaluation.

The ProFocus research package was developed by BK Medical ApS to ease experimental ultrasound data acquisition and control of scanner operation. The research package is an independent development product that complement the ProFocus scanner and is as such not a released product. The package includes a UA2227 research interface for real-time data acquisition and remote control of basic scanner operation, and a software toolbox for easy access of the complete control parameter set. The research package offers access to beamformed radio frequency data and provides flexible manipulation of control parameters such as filtering, compression, transmit level, excitation waveform, beam angle, and focal depth *etc*.

The developed research data acquisition system consists of a standard PC and a ProFocus ultrasound scanner. The system uses an open architecture that allows acquisition of data for experimental research, such as developing new image processing algorithms. With the system, users can tailor the data acquisition to fit their working environment, while still maintain the clinical integrity of using a robust medical device. This will allow researchers and clinicians to rapidly develop applications and move them relatively easy to the clinic for evaluation. A central part of developing new applications and methods is determination of both technical and diagnostic efficacy. With the system, users can acquire interleaved data sequences switching between multiple user defined imaging configurations. This, in combination with the ability to acquire and store multiple data sets during the same examination, makes the system adequate for clinical trials.

This paper describes the capabilities of the research data acquisition system, and demonstrates how it is used to test and implement customized solutions for different research applications. Three examples of system use are presented: Evaluation of Synthetic Aperture Sequential Beamformation (SASB), Transverse Oscillation (TO) for

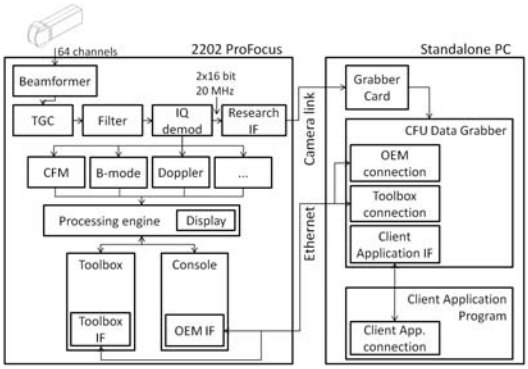

Fig. 1. Data flow and structure of the software and hardware of the system. Arrows indicate the direction of the data flow.

blood velocity estimation, and Acquisition of spectral velocity data for evaluating aortic aneurysms.

The remainder of this manuscript is organized as follows. Section II and III describes the system and developed Matlab Tools, and Section IV presents three examples of system use, followed by conclusions in Section V.

II. System Description

The developed ultrasound research system consists of a commercially available ultrasound scanner (2202 ProFocus equipped with a UA2227 Research Interface, BK-Medical, Herlev, Denmark) and a standard PC. The research interface implements a camera link protocol and allows the acquisition of digital beamformed radio frequency echo data. The acquired data can be received by any video grabber card that supports camera link. In our configuration a X64-CL Express camera link (Dalsa, Waterloo, Ontario, Canada) is used. The developed software running on the PC is based on libraries by Sapera, now a part of Dalsa. The PC is also connected to the scanner through an Ethernet link which provides access to system parameters. The research and OEM interfaces on the 2202 ProFocus architecture allows external devices to control and access data on the scanner. The OEM interface makes it possible to set and read system parameters and can be used to stream processed images. It is basically a substitute of the normal interface: keyboard, track ball, and screen, and enables embedding in 3th party products as a self-sufficient component. The research interface on the other hand, streams data prior to envelope detection. Unlike some other research interfaces all data is sent out of the scanner. It is however, possible to filter out undesired modes and e.g. only to receive CFM or B-mode data.

Fig. 1 illustrates the data flow and the structure of the software and hardware in the system. Raw channel data from the individual transducer elements are sampled and sent to the beamformer. The beamformed data is minimally processed because, aside from an optional time-variant band-pass filter, the only other processing is application of the time gain compensation (TGC) and transformation to baseband I/Q data and down sampling by a factor of 2.

The beamformed data stream is processed and sent to the research interface.

The I/Q data is further processed to generate B-mode, CFM, Doppler, and M-mode images. The results of this processing are transferred to the processing engine for subsequent post-processing and display. The user interface and the calculation of control parameters are handled by the main application called Console. The system architecture of the 2202 ProFocus makes it possible for several standalone applications to coexist and to interact with the control parameters. One such application is the Toolbox, and it is used for debugging of the system, for prototyping of new algorithms, and for image optimization. An example of image optimization is the design of pulses, definition of receive F-number, specification of center frequency and bandwidth for the sliding filter. One can view the Toolbox as a form of parameter control unit. Furthermore, it implements an interface that allows remote reading and writing of a complete control parameter set. The OEM interface is implemented by a module in the Console. As such it has access to the control parameters, and has knowledge of the user input. Using the OEM interface, one can, for example, query which transducer is used, get information about image geometry and imaging mode, set focus depth, manipulate settings, and start/freeze the scanner. One can view the OEM interface as a form of remote control. Furthermore, it can stream processed images as they were displayed on the scanner screen. The Research Interface is implemented as a separate hardware module. One can stream raw beamformed data to external devices using the Research Interface. Each scan line in the data stream is tagged with a header containing information to what kind of acquisition the line belongs - B-mode, CFM, Doppler. It also contains information about the length of a line, if the line is last-in-frame, and if the line is last-in-block, where block refers to the block of data needed to estimate flow. The remote control of acquisition and parameters is handled by the application called CFU Data Grabber. The application implements a communication module to the OEM interface and the Toolbox interface. Furthermore, it implements an interface that makes it possible for 3rd party programs, such as Matlab (Mathworks, Natick, MA, USA), to interact with the application.

A. Data Acquisition

The acquisition of data is controlled via the CFU Data Grabber software and can be performed with a single button click. Alternatively, the acquisition can be issued from a 3rd party program using messaging. In both cases, data are acquired and temporarily stored in memory for either review or download to a hard drive for storage. The maximum length of acquisition stored in memory varies depending on the depth of acquisition, the number of scan lines or ultrasound beams used to create a single frame, and the frame rate. A typical setup recording two B-mode frames interleaved each with 384 emissions, 15 cm penetration depth, and a frame rate of 7 Hz, allows acquisition of a 22 second sequence. Fig. 2 shows the CFU Data Grabber GUI that allows uploading a Usecase to the scanner, acquisition, review, and download of data to hard drive. The user can use the review function to display the acquired B-mode image of the first frame, and once the user is satisfied with their scan, he/she can save the data to hard drive. The data files stored to disk, can later be opened on any computer for analysis and processing. The data storage time is approximately 15.1 seconds for a 3 sec interleaved B-mode sequence including complete scanner settings and patient information.

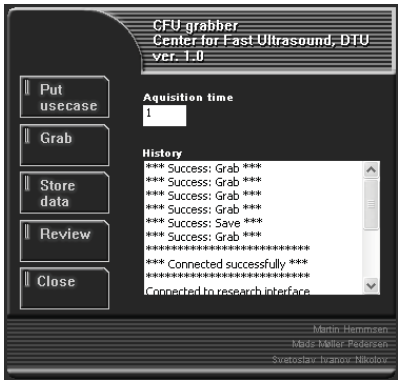

Fig. 2. CFU Data Grabber GUI that is available on the PC for uploading a Usecase to the scanner, acquisition of data, review, and download of data to hard drive.

The scan sequence of the ProFocus is defined as a set of one or multiple basic modes. The basic modes available on the ProFocus is B-mode, M-mode, CFM-mode, and spectral Doppler mode. The scan sequence can be split into two independent views; view A and view B. Each view can be a composition of one or more basic modes and both view A and B can be updated simultaneous. This feature allows data to be acquired interleaved, switching between multiple basic modes, maintaining identical transducer, scanner, region of interest, and recording time on both views. This allows for acquisition of an experimental and standardized data set for evaluation of new processing methods.

The available data for acquisition in all basic modes are beamformed complex baseband data. In the rest of this paper, this type of data will be referred to as I/Q data.

To complement the I/Q data, acquisition of the complete control parameter set including the individual basic mode setups and the scanner user interface setup is available. The control parameter set is called a Usecase and the scanner user interface setup is called OEM parameters.

B. Parameter Control

The system allows manipulation of the control parameters in two ways, either through the Console or using standalone applications such as the Toolbox. The Console is the standard user interface and the main application. Modifications made through the Console are limited to standard clinical use and a set of precalculated and safety validated control parameter setups. The Toolbox allows manipulation of the full control parameter set, and any changes made through the toolbox requires a safety verification to ensure the United States Food and Drug Administration (FDA) regulation is not compromised [11]. A subset of the parameters available, is described in Table I. These parameters are not available on the normal clinical interface or other typical scanners. The manipulation of the control parameters allows a wide degree of experimentation with the receive and transmit aperture control, color

TABLE I
DESCRIPTION OF A SUBSET OF THE PARAMETER CONTROLS.

Parameter	Description
Dynamic focusing and dynamic apodization	Receive aperture dynamic focusing and aperture growth can be disabled individually. When disabled, receive aperture size and focal position are fixed.
F#	Receive and transmit aperture size can be adjusted individually.
Receive apodization	Receive apodization can be chosen from a fixed list of standard curves such as Hamming, Gaussian, or rectangular apodization or optionally to upload a custom made apodization matrix. If defined as a matrix the apodization can vary between individual beam lines.
Receive time delay profile	Receive time delay profile can be specified individually for each image line when dynamic focusing is disabled.
Line density	The image line density can be chosen from a range of half an element pitch to two element pitch.
Speed of sound	Speed of sound can be specified to match the imaging application.
Excitation waveform	A bipolar excitation waveform can be specified with a time resolution of 8.3 nsec.
Region of interest	The region of interest can be adjusted in all imaging modes.
Ensemble size and Pulse repetition frequency	The ensemble size and pulse repetition frequency can be adjusted in both CFM imaging and Doppler imaging. A change in the ensemble size or pulse repetition frequency will trigger an automatically recalculation of the shot macro.

flow control, and Doppler control. We describe each below, and the examples included in Section IV demonstrate their use. Modifications made through the Toolbox can result in non-validated setups and measurements must be performed to ensure FDA regulation is not compromised.

1) Receive and Transmit Aperture Control: The Receive and transmit aperture control give the user the ability to control the fundamental parameters related to the formation of an echo line. The available parameters span from adjusting the size and growth of the aperture to controlling the weighting of the individual elements. A subset of the parameters are described in the following:

- Aperture growth and dynamic focusing. By default, the system dynamically moves the receive focal point outward and grows the aperture to optimize echoes received from increasing depths. With the Toolbox, the user is given the control to override this dynamic updating and define a static size and focal position of the receive aperture. Hereafter, the default state is referred to as a dynamic aperture, and the opposite, a static aperture. Of course, once the aperture is made static, the user has to choose a focal position and a size for the aperture.

- Aperture focal position. When the receive aperture is static, the user can adjust the focal depth and angular spacing between the scan lines. The transmit focal position is adjusted independently.
- Aperture size. The user can adjust the aperture size in dimensionless units of F-number.
- Aperture apodization. The user is given the ability to select between a set of predefined receive aperture weight functions, such as Hamming, Gaussian, or rectangular apodization or optionally to upload a custom made apodization matrix. If defined as a matrix, the apodization can vary between individual beam lines.

2) Color Flow Control: The Color flow Control gives the user the ability to control the fundamental parameters related to the formation of the echo lines for CFM. The available parameters span from adjusting the size of the color box to adjusting the time between individual beam lines. A subset of the parameters are described in the following:

- Region of interest. By default, the region of interest is selected as a square in the center of the imaging plane. The user is given the control to move and change the region of interest, either through the Console or the Toolbox.
- Ensemble size. The ensemble size is the number of color firings that are used in the velocity estimate along each beam line. The user is given the ability to experiment with the number of acquisitions to fit a specific application.
- Pulse repetition frequency. The pulse repetition frequency determines the time between to successive echo lines. The user is given the ability to change this frequency to fit a specific application. A change in the pulse repetition frequency, region of interest or ensemble size will trigger an automatically recalculation of the basic mode acquisition sequence.

3) Doppler Control: The Doppler control give the user the ability to control the fundamental parameters related to the formation of the echo lines for Doppler imaging. The available parameters span from adjusting the length of the echo lines to adjusting the time between each acquisition. A subset of the parameters are described in the following:

- Range gate. The parameters related to the range gate determines the angle of the beam line relative to the center of the aperture and the length of the echo line. The user is given the control to move and expand the range gate, either through the Console or the Toolbox.
- Pulse repetition frequency. As with the Color Flow Control, the pulse repetition frequency can be specified.

C. Data Management

Data management of the OEM parameters, Usecase, and I/Q data is split into three different file types and formats.

The file format used for handling I/Q data is a custom made file format. The file handling is developed in C++, and enables the user to load specified frames from a long data sequence, without loading the entire data set first. Data are stored as 16 bit signed integers.

For handling the OEM interface data characteristic, a C++ class called oemArray is implemented. The design of oemArray, resembles to a great extent the design of mexArray by Matlab. One of the design ideas was that oemArray can create its own queries to the OEM interface, as well as parse the data contained in a data string received by the OEM interface. The full parameter set describing the characteristic of the user interface on the scanner is saved in a XML format. The resulting OEM parameter file is a complete description of the scanner user interface setup and includes information such as zoom, overall gain, persistence, and various other visualization settings. The scanner parameters aid the user in redoing experiments by setting up the Console in the exact same mode as it was when the parameters were saved. A library is provided to read and write the parameters in Matlab.

The Usecase is a complete description of the control parameters used by the scanner and includes information such as excitation waveform, receive F-number, center frequency and bandwidth for the sliding filter. The control parameters aids the user to redo experiments, as well as create simulations using tools such as Field II [12], [13] with identical setup as used in measurements. The parameter set is saved in ASCII format. This allows the user to open the file with a normal text editor to read or write application specific initialization of control parameters.

III. MATLAB TOOLS

The CFU Data Grabber application implements an interface that makes it possible for 3rd party products, such as Matlab, to interact with the application via messaging. The interface provides the user to access the service interface layer in the application, giving access to system functions. Since many researchers utilize Matlab for data analysis, a SDK for Matlab is developed. The SDK implements a CFU_Data_Grabber class that allows a flexible manipulation of the control parameters and data acquisition. Further, the SDK implements a set of functions for basic file handling of the files collected with the system. A description of CFU_Data_Grabber member functions and functions available for file handling are listed in Table II.

IV. RESULTS

The developed ultrasound data acquisition system has extensively been used to acquire *in vivo* data from volunteers in the clinic as well as phantom measurements in the lab. Three research studies, that have benefited from the system, are presented here.

A. Preliminary evaluation of Synthetic Aperture Sequential Beamformation

1) Background: In multi-element Synthetic Aperture (SA) imaging the basic idea is to create a pressure wave from multiple elements with a focused transmission. The concept of using the transmit focal point as a virtual source was introduced by Passmann and Ermert [14]. Virtual sources in Synthetic Aperture Focusing (SAF) was further investigated by Frazier and O'Brien [15], Nikolov and Jensen [16], [17], and Bae and Jeong [18]. It was shown that the virtual source coincides with the focal point of the transducer, and that a depth independent resolution can be achieved. Kortbek et al. introduced in [19] the concept of Sequential Beamforming to SA imaging to reduce system requirements for real time implementation. It was shown that for a multi element linear array transducer

TABLE II
DESCRIPTION OF A SUBSET OF THE FUNCTIONS AVAILABLE IN THE SDK.

Function name	Description	Matlab call
Connect	Opens a connection to the CFU Data Grabber application. Optionaly an IP address can be specified as a char array.	`.Connect`
Disconnect	Disconnects any open connections to the CFU Data Grabber application.	`.Disconnect`
Grab	Grabs N seconds or N frames of data to application memory.	`.Grab('Nsec') or .Grab(N)`
Review	Displays the first B-mode data frame envelope detected and log-compressed to 60 dB dynamic range.	`.Review`

Save	The function allows storing of the usecase, OEM parameters and acquired I/Q data, to a specified filename. The procedure for saving the usecase and OEM parameters includes fetching the active parameters on the scanner and transfering to local hard drive. I/Q data must have been acquired to application memory prior to the function call.	`.Save('C:test','usecase')`
		`.Save('C:test','oem')`
		`.Save('C:test','frame')`
		`.Save('C:test','all')`

Load	The function allows uploading of a specified usecase or OEM parameter file to the scanner.	`.Load('C:test','usecase')` `.Load('C:test','oem')`
Send_msg	Transfers a message to the OEM interface (oem) or to the research interface (ri) on the scanner.	`.Send_msg('oem','msg')` `.Send_msg('ri','msg')`
Read_Usecase	Reads the specified file, parses the data and returns a Matlab structure.	`Read_Usecase('c:test.dat')`
cff_file_open	Opens a user specified cfu file type and returns a file identifier.	`cff_file_open('c:test.cfu')`
cff_file_close	Closes the file specified.	`cff_file_close(fid)`
cff_file_plane_read	Returns the data from the specified file and plane nr.	`cff_file_plane_read(fid,plane_nr)`

the lateral resolution could be made more range independent and improved significantly compared to conventional Dynamic Receive Focusing (DRF). Hemmsen et al. applied in [20] SASB to medical ultrasound imaging using convex array transducers. It was shown that the method is applicable for medical imaging and improves the lateral resolution compared to DRF.

The basic idea in Synthetic Aperture Sequential Beamforming (SASB) is to create a dual-stage procedure using

two separate beamformers. In the initial stage a beamformer using a single focal point in both transmit and receive, creates a set of focused image lines. A second stage beamformer creates a set of high resolution image points by combining information from multiple first stage focused image lines. The effect is a dynamically expanding array as the image depth increases and a more range independent lateral resolution is obtained.

In the following example, the developed system is used to acquire I/Q signals in order to create B-mode images using Dynamic Receive Focus (DRF) and Synthetic Aperture Sequential Beamformation (SASB). In this experiment the lateral resolution and signal-to-noise ratio of SASB will be calculated and compared to DRF. Furthermore, *in vivo* data are acquired, and B-mode images are generated for a visual comparison and evaluation of the image quality of the two image modalities.

2) Method: In the following experiment an abdominal 3.5 MHz probe with a room-temperature vulcanization (RTV) lens, 3ML35CLA192 (Sound Technology Inc., 1363 South Atherton St., State College, PA 16801, USA) transducer was used. In the first part of the experiment the transducer was clamped to immobilize the transducer over a speckle phantom, Model 571 (Danish Phantom Service, Frederikssund, Denmark). A water bath at the top of the phantom provided a coupling medium between the transducer and the phantom. The transmit frequency of the transducer was set to 5 MHz, and the transducer was fixed such that the transducer surface was parallel to the phantom. Using the Console application both view A and B was set to simultaneous B-mode imaging with a field of view of 14.6 cm and neutral TGC. Using the Toolbox, dynamic receive focusing and dynamic apodization were disabled on view A. Subsequently the F-number were fixed to 2 in both transmit and receive and the transmit and receive focus were set to 70 mm. The transmit focus point for view B was set to 105.5 mm with a transmit F-number of 5 and receive F-number of 0.8. Using the Matlab SDK, 20 frames of beamformed I/Q data from view A and B were acquired interleaved with identical excitation waveforms, TGC, and overall gain in both setups. The scan sequence was specified to a line density of 2 lines pr. element, resulting in 384 lines for each image. The acquired I/Q data from view A was subsequently processed using the Beamformation Toolbox III [21] to generate SASB second stage radio frequency data. The method used to compute the SNR of the second stage data and the acquired data from view B is described as

$$SNR(z) = \frac{1}{L}\sum_{l=1}^{L}\frac{S(z,l)^2}{N(z,l)}. \tag{1}$$

Where L is the number of acquired beam lines and $S(z,l)$ and $N(z,l)$ are the mean power of the signal and noise at depth z for the $l'th$ beam line and are expressed as

$$\begin{aligned} S(z,l) &= \frac{1}{N}\sum_{n=1}^{N} x(z,l,n). \\ N(z,l) &= \frac{1}{N}\sum_{n=1}^{N} (x(z,l,n) - S(z,l))^2. \end{aligned}$$

Where $x(z,n)$ is the sample at depth z for the $n'th$ frame and N is the total number of acquired frames.

In the second part of the experiment the transducer was clamped to immobilize the transducer over a wire and contrast phantom, Model 525 (Danish Phantom Service, Frederikssund, Denmark). A water bath at the top of the phantom provided a conducting medium between the transducer and the phantom. The transmit frequency was set to 5 MHz, and the transducer was fixed such that the vertical wires were placed along the vertical center of the field of view. The Usecase from the first experiment was uploaded to the scanner and 20 frames were acquired. The acquired I/Q data from view A was subsequently processed to generate SASB second stage data. The second stage data and the acquired data from view B was envelope detected, log-compressed, and scan converted to create B-mode images. Using the B-mode images the lateral resolutions at full-width-at-half-max (FWHM) and -20 dB were extracted.

In the final part of the experiment an *in vivo* scan of the Morison's Pouch from a 30 year old male volunteer was scanned. The scanner setup, control parameters, and scan sequence were identical to the one used in the first and second part of the experiment.

3) Results: Fig. 3a presents the SNR calculated as the ratio between the mean power of the signal divided by the power of the noise. The gray line represents the SNR using DRF and the black line using SASB. The SNR using SASB is on average 6.2 % or 1.18 dB better than the SNR using DRF.

Fig. 3b presents the lateral resolution calculated from the B-mode images of the measurement on the wire and contrast phantom. The lateral resolutions are calculated at FWHM (solid line) and -20 (dashed line) using DRF (gray line) and SASB (black line) in the range 10 to 140 mm. At FWHM and -20 dB the lateral resolutions are on average improved by 18.4% at FWHM and 17.4% at -20 dB using SASB. The standard deviation on the lateral resolution at FWHM were improved from 0.9 mm using DRF to 0.7 mm using SASB. At -20 dB the standard

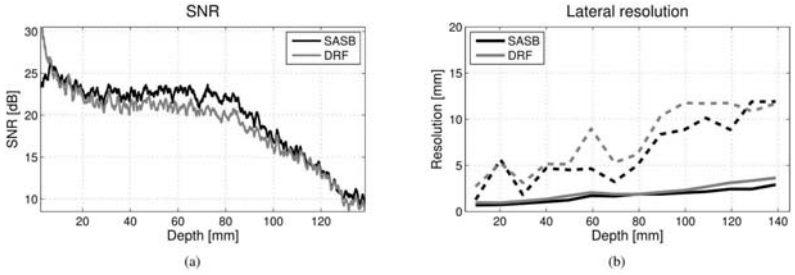

Fig. 3. (a) Visualization of the SNR using SASB (solid gray line) and DRF (solid black line) (b) Visualization of the lateral resolutions at FWHM (solid line) and -20 dB (dashed line) using DRF (gray line) and SASB (black line).

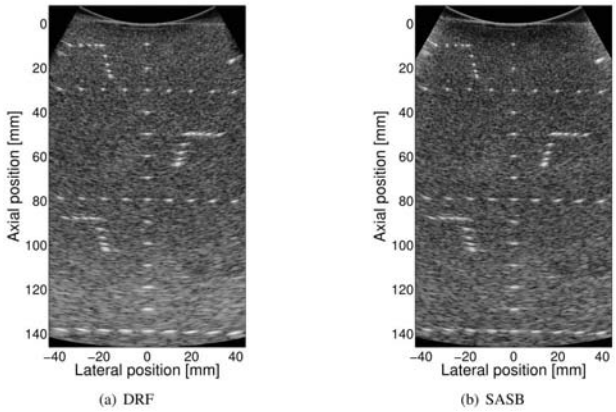

Fig. 4. Visualization of wire and contrast phantom measurement, using (a) DRF beamforming (b) SASB beamforming.

deviation were 3.5 for both modalities.

For visual inspection, Fig. IV-A2 displays the B-mode images created from the measurement on the wire and contrast phantom, using (a) DRF and (b) SASB. Note how SASB is able to maintain a more isotropic point spread function through depth and has a better lateral resolution. Fig. IV-A3 displays the B-mode images from the *in vivo*

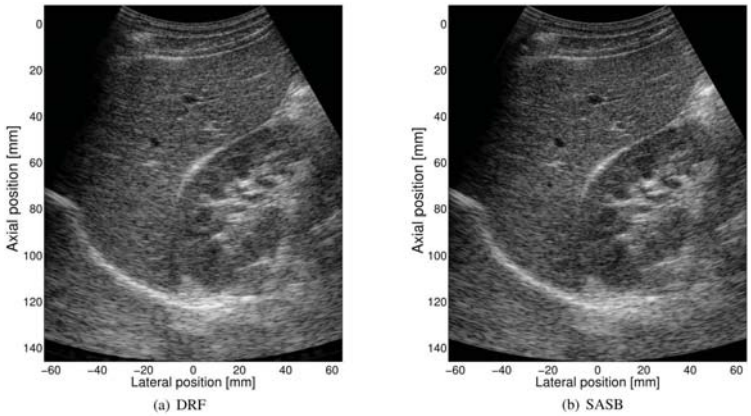

Fig. 5. Visualization of *in vivo* measurement of the liver (left side of the image) and right kidney (right side of the image) and Morison's pouch, not containing fluid, using (a) DRF and (b) SASB.

measurement of the Morison's Pouch, the right kidney, and the adjacent part of the liver from a 30 year old male, using (a) DRF and (b) SASB.

4) Summary: Three experiments were performed. The first two experiments were performed to measure the performance of SASB compared to DRF. The SNR and the lateral resolution were used as quantitative measures. The third experiment was performed as a preliminary *in-vivo* evaluation of the method. The evaluation using the quantitative measures showed the ability of SASB to decrease the standard deviation of the lateral resolutions at FWHM, the ability to obtain a more isotropic point spread function compared to DRF, and to improve the SNR. The performance gain using SASB compared to DRF was further supported by *in-vivo* scan of the right kidney and the adjacent liver. The results presented prove the viability of SASB for 2D ultrasound imaging using commercially available equipment.

B. Transverse Oscillation for blood velocity estimation

1) Background: Medical ultrasound is widely used to study blood flow dynamics in the human circulatory system. For instance, the estimation of blood flow velocities plays a key role in diagnosing major diseases in the carotid arteries [22]. However, blood velocity estimates using conventional color flow imaging or Doppler techniques are angle dependent. That is a major limitation, and poses a huge challenge for quantitatively estimating the magnitude of the blood velocity.

Several techniques [23]–[27] have been proposed to compensate for the inherent angle dependency problem. In this case, the Transverse Oscillation (TO) method suggested by Jensen and Munk [28] is used. Anderson [29] suggested a similar approach. The TO method has demonstrated promising *in vivo* results [30], [31]. However, the previously reported results have been obtained using the experimental scanner RASMUS [1], [2].

The basic idea in the TO method is to create a double oscillating field by using special apodization profiles in receive. Two lines with a lateral displacement of a quarter spatial wavelength, corresponding to a 90° phase shift, are beamformed simultaneously in receive. A center line is also beamformed for traditional axial velocity estimation. For a description and derivation of the estimator, the reader is referred to Jensen [32]. The lateral wavelength, λ_x, can be found by

$$\lambda_x = 2\lambda_z \frac{z}{D}, \tag{2}$$

where λ_z is the axial wavelength, z is the depth, and D is the distance between the two peaks in the receive apodization.

In the following example, the initial work on investigating the feasibility of a commercial implementation of the TO method for clinical use is presented. The developed research data acquisition system is used to acquire RF data from a flow rig for a statistical evaluation of the TO implementation.

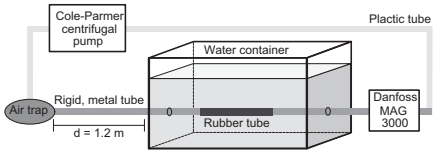

Fig. 6. The flow rig setup with a Cole-Parmer centrifugal pump, an air entrapment device, a water container with a rubber tube, and a Danfoss MAG 3000 magnetic flow meter. Notice that this figure is not to scale, and that the entrance length of the tube is more than 1.2 m, enough to ensure fully developed laminar flow. A fixture can be placed in the water container to keep the transducer fixed at a known beam-to-flow angle.

2) Method: In the following experiment a linear array transducer BK8812 (BK-Medical, Herlev, Denmark) was used. Velocity measurements were performed using a custom made circulating flow rig to evaluate the TO method. The setup consists of a long rigid metal tube replaced by a rubber tube (radius 5.7 mm) inside a water filled container as illustrated in Fig. 6. The tube is filled with a blood mimicking fluid [30]. A Cole-Parmer (Vernon Hills, IL) 75211-60 centrifugal pump controls the fluid flow, and a Danfoss (Sønderborg, Denmark) MAG 3000 magnetic volume flow meter is used to measure the actual volume flow. The centrifugal pump is only able to keep the flow constant at sufficiently low flow rates ($Q < 60$ L/h). Therefore, the peak velocity of the flow, v_0 was set to 0.215 m/s. The entrance length of the tube is more than 1.2 m, and, under the given settings, sufficient in length to ensure fully developed flow. The transducer was fixated with a distance of 16 mm to the center of the rubber tube and the beam-to-flow angle was set to $90°$.

Using the Console application view A was set to B-mode and CFM imaging. A number of parameters were set manually in either the Console or the Toolbox. They are listed in Table III. Multibeam of 3 means that three lines are beamformed simultaneously in receive: Two are TO lines, one is a center line for conventional axial velocity estimation.

Subsequently, the CFM receive delays and apodizations were downloaded from the scanner, modified according to the principles of the TO method, and then uploaded to the scanner again. With a focal point at 15 mm, a line density of 1 line per element, and beamforming the two TO lines next to each other ($i.e.$ $\lambda_x/4$ is equal to the pitch), the spacing between the two aperture peaks has to be 6.6 mm. The transmit and receive aperture functions are illustrated in Fig. 7.

Using the Matlab SDK, beamformed RF data from view A were acquired. Although data for whole CFM frames were acquired, only the central CFM line was extracted from each frame for further offline processing using Matlab. 75 flow profiles were generated for the purpose of investigating the performance of the TO estimator.

The performance of the method is investigated by comparing the true profile with the measured velocity profiles. The measured velocity is estimated from a number of emissions. The average, $\bar{v}(z_k)$, of N estimates and the

TABLE III
PARAMETERS FOR THE EXPERIMENTAL FLOW RIG MEASUREMENTS.

Scanner Parameters	Value
Pulse repetition frequency	1.3 kHz
Speed of sound	1480 m/s
Number of transmit cycles	6
Ensemble size	16
Transmit focus depth	15 mm
Center frequency of the CFM pulse	5 MHz
Transmit F-number	4
Line density	1 per element
Multibeam (parallel beamforming)	3

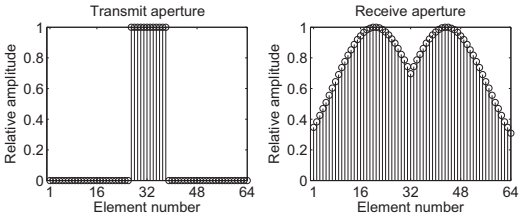

Fig. 7. The transmit and receive aperture for the TO estimator with a transmit focal depth at 15 mm. The transmit aperture is rectangular, and the F-number is 4. The receive aperture is the TO apodization.

estimated standard deviation, $\sigma(z_k)$, is calculated at each discrete depth as

$$\bar{v}(z_k) = \frac{1}{N}\sum_{i=1}^{N} v_i(z_k) \tag{3}$$

$$\sigma(z_k) = \sqrt{\frac{1}{N-1}\sum_{i=1}^{N}\left(v_i(z_k) - \bar{v}(z_k)\right)^2}, \tag{4}$$

where $v_i(z_k)$ is the ith velocity estimate at the discrete depth z_k.

3) Results: Fig. 8 shows the estimated lateral velocity component of the flow profiles for 75 measurements at a beam-to-flow angle of 90°. It also indicates the mean estimate $\pm$ one standard deviation and the expected true velocity. The TO method is clearly able to estimate the lateral velocity component, which is not possible with conventional estimators. As expected, the estimated lateral velocity profile has a parabolic shape.

There is a mismatch between the theoretical λ_x from Eq. 2 and the simulated mean $\bar{\lambda}_x$ in the generated TO field, because the assumptions for the Fraunhofer approximation are not fully met. The consequence of this is underestimated velocities. Using Field II, the mean lateral wavelength can be estimated based on the 2D spatio-temporal frequency domain of the combined pulse-echo TO field. At 15 mm, the theoretical λ_x is 1.35 mm and the

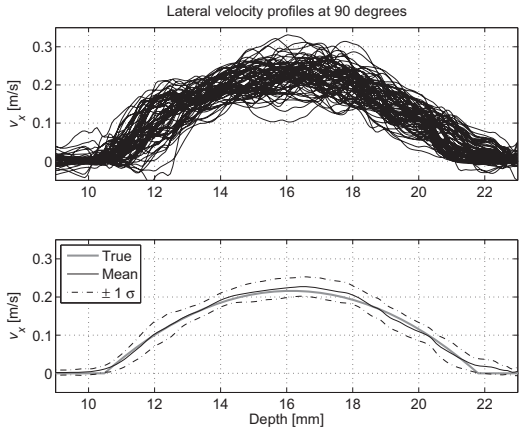

Fig. 8. TO estimated lateral velocities for 75 flow profiles with a beam-to-flow angle of 90° (top). Mean estimate ± one standard deviation and expected theoretical velocity profile (bottom).

simulated mean $\bar{\lambda}_x$ is 2.66 mm. Calculating the relative bias between the simulated mean value and the theoretical value one obtains (2.66-1.35)/2.66 = 0.494. The bias correction factor is therefore 1.494, and this value is multiplied to the estimated velocity. The mean $\bar{\lambda}_x$ is simulated for each 1/2 mm from 10 to 22 mm and interpolated before bias compensation is applied to the 75 velocity profiles. With this bias compensation, the mean of the estimated velocities closely follow the theoretical profile.

4) Summary: By using the research data acquisition system, beamformed data for the TO method were obtained. Based on these data the transverse (lateral) velocity component perpendicular to the ultrasound beam could be measured. The results demonstrate that the TO method is suitable for a commercial implementation.

C. Acquisition of spectral velocity data for evaluating aortic aneurysms

1) Background: Medical ultrasound is commonly used to study and diagnose cardiovascular disease because it provides a non-invasive, real time imaging technique to visualize pathology in both the solid arterial wall and abnormal flow patterns in the blood. One of the first attempts to quantify blood velocities was performed by Satomura [33] using a continuous wave Doppler system and estimating the flow pattern from the Doppler spectrum. This system was then further developed into a pulsed wave system able to probe at a certain depth and thereby the possibly to investigate individual blood vessels, mapping the velocity and time evolution of the velocity [34]. Blood consists of many scatterers, and it is the reflective scattering from these that constitutes the flow signal from the blood. The basic principle in spectral recordings using the pulsed wave system is that a number of pulses are emitted into the tissue from the same position. The received backscattered signal is then sampled at the time relative to the

emission, yielding a frequency that is proportional to the blood velocity [35].

In the following application, the developed system is used to acquire RF signals in order to obtain patient-specific spectral measurements to calculate velocity profiles in the human abdominal aorta. These velocity profiles are intended to be applied as inlet condition for the pulsating blood in a patient-specific fluid-structure interaction model which can be used as part of the diagnostic process of cardiovascular disease.

The finite element (FE) analysis of the combination of solid arteries (structure) and flowing blood (fluid) has developed over the years with different purposes and spectral measurements has been used as a tool to construct realistic numerical models of the fluid-structure interaction [36]. For example in the clinical quantification of coronary plaque progression, ultrasound simulation of velocity fields based on computational fluid dynamics [37], and rupture risk assessment of abdominal aortic aneurysms [38]. The spectral measurements are rarely used for other purposes than determination of inlet conditions in these simulation models. With the versatile data acquisition system the large amount of data can be used for further analysis of modeling results. For example the wall displacement during the heart cycle can be measured and compared to simulated results providing a method to evaluate the performance of different structural material models.

2) Method: Data for the presented application of the research interface origins from a study on the biomechanical properties of the human abdominal aorta. The total data set was collected from a group of 11 healthy volunteers and consists of a magnetic resonance angiography and an ultrasound scan using the Spectral Doppler method to obtain measurements of the blood flow in the abdominal aorta. To demonstrate the use of the research data acquisition system the collection and processing of Spectral Doppler measurements from a 53 year old healthy male is presented.

The data acquisition was performed using a convex array transducer, BK8803 (BK-Medical, Herlev, Denmark) with a center frequency of 5 MHz. Using the Console a scan sequence containing B-mode and Doppler mode was specified. The pulse repetition frequency of the Spectral Doppler mode was set to 2 kHz, interleaving the acquisition of the individual scan lines from the two basic modes.

The same clinician performed all ultrasound scans to avoid differences in scanning technique from subject to subject. During the scans the clinician was asked only to adjust the size of the range gate, angling of the flow direction relative to the beam direction without allowing beam steering, and the overall gain using the only the Console. The reason for this was to standardize the scanning sequence, and only allow changes in the scanner setup that would not affect the data acquisition method. This limitation of manipulation with control parameters was decided with the intention of providing clinicians with a simple method to collect flow data for investigation of pathological flow patterns. Fig. 9 illustrates the Console interface and the different control parameters available for the clinician to adjust are listed to right of the duplex image display. Four data sequences of Spectral Doppler spectrum data and B-mode image data were obtained from the volunteer, and using the Matlab SDK RF data for each sequence was acquired and stored subsequently.

The acquisition time for each blood flow measurement was set to five seconds in the CFU Data Grabber

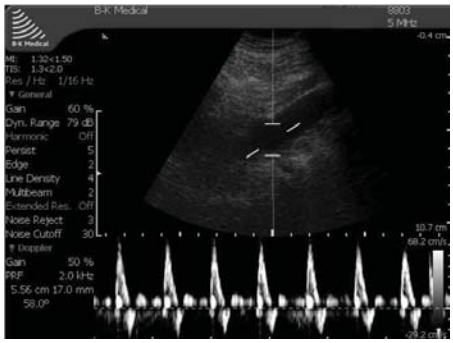

Fig. 9. Duplex interface on the Profocus scanner during the data acquisition. All parameters listed to the left are also registered in the usecase produced at each data acquisition sequence.

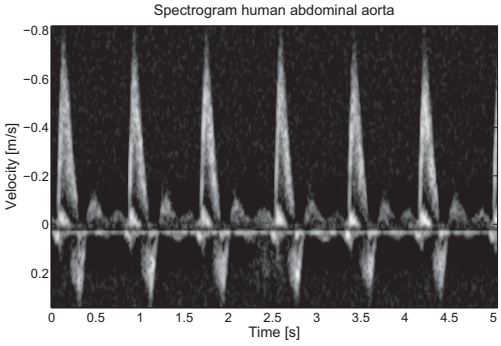

Fig. 10. Spectral density spectrum of the blood velocity in the abdominal aorta using the extracted research data set from the scanning sequence corresponding to the interface shown in Fig. 9.

corresponding to approximately five cardiac cycles. The volunteer was asked to stop breathing during each of the acquisitions to ensure as little artifacts from movement of the surrounding abdominal structures as possible. Each of the collected RF data sets for velocity estimation of the blood flow is a matrix with 10.240 lines and 1062 samples in each line. Subsequently, data was processed offline to inspect the quality of the RF data and to calculate the Spectral density spectrogram of the received flow signals. Each Spectral density spectrum was calculated from 16 emissions each having an overlap of 50%. Each Spectral density spectrum had a length of 128 samples and the time between spectra was five milliseconds resulting in 1011 spectra.

3) Results: Fig. 10 shows the computed Spectral density spectrum from the acquired RF data sequence corresponding to the setup displayed in Fig. 9. Comparing the two Spectral density spectra a high similarity is seen.

In both spectra the peak velocity is approximately 68 m/s in the forward flow direction (from proximal to distal relative to the heart) and a peak velocity in the backward flow direction of approximately 29 m/s. In general the peak forward velocity in the abdominal aorta is around 0.5-0.6 m/s with a mean velocity of 0.08-0.2 m/s [39]. So, this volunteer show a slightly increased velocity in the abdominal aorta compared to the general case.

The velocity change can be used to establish a patient-specific inlet condition for each patient-specific abdominal aortic geometry constructing a realistic simulation model for diagnostic purposes. This is done by assuming that the inlet cross-section is rotational symmetric, the flow is fully-developed, and that the blood is a Newtonian fluid in which case Womersleys theorem can be used to determine the flow pattern during the cardiac cycle.

4) Summary: The research data acquisition system facilitates access to raw flow data from Spectral Doppler spectral measurements which can be directly applied in a finite element model for simulation of patient-specific flow and biomechanical properties of the arterial wall. This is an important step towards a realistic patient-specific simulation model to support diagnosis of various cardiovascular diseases which can be introduced to and used directly in the clinic.

V. Conclusions

A versatile and open architecture research data acquisition system using a commercially available medical ultrasound scanner has been implemented. The system consists of standard PC and a BK Medical ProFocus ultrasound scanner. The system uses an open architecture that allows acquisition of data for experimental research, such as developing new imaging processing algorithms. With the system users can tailor the data acquisition to fit their working environment while still maintain the clinical integrity of using a robust medical device. This will allow researchers and clinicians to rapidly develop applications and move them relatively easy to the clinic.

The clinical usability of the scanner, including the frame rate, is unaffected by data acquisition. Furthermore the system allows remote control of basic scanner operation, and software for easy access of the complete control parameter set. The system allows access to beamformed radio frequency data and provides flexible manipulation of control parameters such as filtering, compression, transmit level, excitation waveform, beam angle, and focal depth etc. The system offers high speed data acquisition, beneficial for clinical scanning and system evaluation.

Data acquisition can be controlled through a GUI running on the PC or using third party products, such as Matlab. The developed software development toolkit (SDK) will give researchers and clinicians the ability to utilize Matlab for data analysis and flexible manipulation of control parameters. Due to these advantages, research projects have successfully used the system to test and implement their customized solutions for different applications. We believe that the system can contribute to accelerated advancements in ultrasound imaging by allowing more ultrasound researchers to test and clinically evaluate promising new applications.

Acknowledgment

This work is supported by grant 08-036099 from the Danish Science Foundation and by BK Medical Aps, Herlev, Denmark.

REFERENCES

[1] J. A. Jensen, O. Holm, L. J. Jensen, H. Bendsen, H. M. Pedersen, K. Salomonsen, J. Hansen, and S. Nikolov, "Experimental ultrasound system for real-time synthetic imaging," in *Proc. IEEE Ultrason. Symp.*, vol. 2, 1999, pp. 1595–1599.

[2] J. A. Jensen, O. Holm, L. J. Jensen, H. Bendsen, S. I. Nikolov, B. G. Tomov, P. Munk, M. Hansen, K. Salomonsen, J. Hansen, K. Gormsen, H. M. Pedersen, and K. L. Gammelmark, "Ultrasound Research Scanner for Real-time Synthetic Aperture Image Acquisition," *IEEE Trans. Ultrason., Ferroelec., Freq. Contr.*, vol. 52 (5), pp. 881–891, May 2005.

[3] J. A. Jensen, H. Holten-Lund, R. T. Nielson, B. G. Tomov, M. B. Stuart, S. I. Nikolov, M. Hansen, and U. D. Larsen, "Performance of SARUS: A Synthetic Aperture Real-time Ultrasound System," in *Proc. IEEE Ultrason. Symp.*, Oct. 2010, p. published.

[4] Lecoeur Electronique, "Users guide for OPEN system," Lecoeur-electronique.net, Tech. Rep., 2006.

[5] Verasonics, "The Verasonics Ultrasound Engine - A New Paradigm For Ultrasound System Architecture," Verasonics.com, Tech. Rep., 2007.

[6] L. Masotti, E. Biagi, M. Calzolai, L. Capineri, and S. Granchi, "Femmina: a fast echographic multiparametric multi-imaging novel apparatus," in *Proc. IEEE Ultrason. Symp.*, 1999, pp. 739 –748.

[7] H. J. Hewener, H. J. Welsch, C. Gnther, H. Fonfara, S. H. Tretbar, and R. M. Lemor, "A highly customizable ultrasound research platform for clinical use with a software architecture for 2d-/3d-reconstruction and processing including closed-loop control," *IFMBE*, vol. 25, no. 2, pp. 342–345, 2009.

[8] V. Shamdasani, U. Bae, S. Sikdar, Y. M. Yoo, K. Karadayi, R. Managuli, and Y. Kim, "Research interface on a programmable ultrasound scanner," *Ultrasonics*, vol. 48, no. 3, pp. 159–168, 2008.

[9] S. Brunke, M. Insana, J. Dahl, C. Hansen, M. Ashfaq, and H. Ermert, "Errata - an ultrasound research interface for a clinical system," *Ultrasonics, Ferroelectrics and Frequency Control, IEEE Transactions on*, vol. 54, no. 1, pp. 198–210, January 2007.

[10] T. Wilson, J. Zagzebski, T. Varghese, Q. Chen, and M. Rao, "The ultrasonix 500rp: A commercial ultrasound research interface," *Ultrasonics, Ferroelectrics and Frequency Control, IEEE Transactions on*, vol. 53, no. 10, pp. 1772–1782, October 2006.

[11] FDA, "Information for manufacturers seeking marketing clearance of diagnostic ultrasound systems and transducers," Center for Devices and Radiological Health, United States Food and Drug Administration, Tech. Rep., 1997.

[12] J. A. Jensen and N. B. Svendsen, "Calculation of Pressure Fields from Arbitrarily Shaped, Apodized, and Excited Ultrasound Transducers," *IEEE Trans. Ultrason., Ferroelec., Freq. Contr.*, vol. 39, pp. 262–267, 1992.

[13] J. A. Jensen, "Field: A Program for Simulating Ultrasound Systems," *Med. Biol. Eng. Comp.*, vol. 10th Nordic-Baltic Conference on Biomedical Imaging, Vol. 4, Supplement 1, Part 1, pp. 351–353, 1996.

[14] C. Passmann and H. Ermert, "A 100-MHz ultrasound imaging system for dermatologic and ophthalmologic diagnostics," *IEEE Trans. Ultrason., Ferroelec., Freq. Contr.*, vol. 43, pp. 545–552, 1996.

[15] C. H. Frazier and W. D. O'Brien, "Synthetic aperture techniques with a virtual source element," *IEEE Trans. Ultrason., Ferroelec., Freq. Contr.*, vol. 45, pp. 196–207, 1998.

[16] S. I. Nikolov and J. A. Jensen, "Virtual ultrasound sources in high-resolution ultrasound imaging," in *Proc. SPIE - Progress in biomedical optics and imaging*, vol. 3, 2002, pp. 395–405.

[17] ——, "3D synthetic aperture imaging using a virtual source element in the elevation plane," in *Proc. IEEE Ultrason. Symp.*, vol. 2, 2000, pp. 1743–1747.

[18] M. H. Bae and M. K. Jeong, "A study of synthetic-aperture imaging with virtual source elements in B-mode ultrasound imaging systems," in *IEEE Trans. Ultrason., Ferroelec., Freq. Contr.*, vol. 47, 2000, pp. 1510–1519.

[19] J. Kortbek, J. A. Jensen, and K. L. Gammelmark, "Synthetic aperture sequential beamforming," *Ultrasonics*, p. Submitted, 2009.

[20] M. C. Hemmsen, J. M. Hansen, and J. A. Jensen, "Synthetic aperture sequential beamformation applied to medical imaging using a multi element convex array transducer," "October" "2011", "Submitted to IEEE Ultrason. Symp, 16 - 18 October 2011, Kobe, Japan".

[21] J. M. Hansen and J. A. Jensen, "An object-oriented multi-threaded software beamformation toolbox," Feb. 2011, submitted to SPIE Medical Imaging, 12 -17 February 2011, Lake Buena Vista (Orlando), Florida, USA.

[22] E. G. Grant, C. B. Benson, G. L. Moneta, A. V. Alexandrov, J. D. Baker, E. I. Bluth, B. A. Carroll, M. Eliasziw, J. Gocke, B. S. Hertzberg, S. Katanick, L. Needleman, J. Pellerito, J. F. Polak, K. S. Rholl, D. L. Wooster, and R. E. Zierler, "Carotid Artery Stenosis: Gray-Scale and Doppler US Diagnosis - Society of Radiologists in Ultrasound Consensus Conference," *Radiology*, vol. 229, no. 2, pp. 340–346, 2003.

[23] M. D. Fox, "Multiple crossed-beam ultrasound Doppler velocimetry," *IEEE Trans. Son. Ultrason.*, vol. SU-25, pp. 281–286, 1978.

[24] G. E. Trahey, J. W. Allison, and O. T. von Ramm, "Angle independent ultrasonic detection of blood flow," *IEEE Trans. Biomed. Eng.*, vol. BME-34, pp. 965–967, 1987.

[25] V. L. Newhouse, D. Censor, T. Vontz, J. A. Cisneros, and B. B. Goldberg, "Ultrasound Doppler probing of flows transverse with respect to beam axis," *IEEE Trans. Biomed. Eng.*, vol. BME-34, pp. 779–788, 1987.

[26] O. Bonnefous, "Measurement of the complete (3D) velocity vector of blood flows," in *Proc. IEEE Ultrason. Symp.*, 1988, pp. 795–799.

[27] J. A. Jensen, "Directional velocity estimation using focusing along the flow direction: I: Theory and simulation," *IEEE Trans. Ultrason., Ferroelec., Freq. Contr.*, vol. 50, pp. 857–872, 2003.

[28] J. A. Jensen and P. Munk, "A New Method for Estimation of Velocity Vectors," *IEEE Trans. Ultrason., Ferroelec., Freq. Contr.*, vol. 45, pp. 837–851, 1998.

[29] M. E. Anderson, "Multi-dimensional velocity estimation with ultrasound using spatial quadrature," *IEEE Trans. Ultrason., Ferroelec., Freq. Contr.*, vol. 45, pp. 852–861, 1998.

[30] J. Udesen and J. A. Jensen, "Investigation of Transverse Oscillation Method," *IEEE Trans. Ultrason., Ferroelec., Freq. Contr.*, vol. 53, pp. 959–971, 2006.

[31] J. Udesen, M. B. Nielsen, K. R. Nielsen, and J. A. Jensen, "Examples of *In Vivo* blood vector velocity estimation," *Ultrasound in Med. & Biol.*, vol. 33, no. 4, pp. 541–548, 2007.

[32] J. A. Jensen, "A New Estimator for Vector Velocity Estimation," *IEEE Trans. Ultrason., Ferroelec., Freq. Contr.*, vol. 48, no. 4, pp. 886–894, 2001.

[33] S. Satomura, "Ultrasonic Doppler method for the inspection of cardiac functions," *J. Acoust. Soc. Am.*, vol. 29, pp. 1181–1185, 1957.

[34] D. W. Baker, "Pulsed ultrasonic Doppler blood-flow sensing," *IEEE Trans. Son. Ultrason.*, vol. SU-17, pp. 170–185, 1970.

[35] J. A. Jensen, *Estimation of Blood Velocities Using Ultrasound: A Signal Processing Approach*. New York: Cambridge University Press, 1996.

[36] M. S. Olufsen, C. S. Peskin, W. Y. Kim, E. M. Pedersen, A. Nadim, and J. Larsen, "Numerical simulation and experimental validation of blood flow in arteries with structured-tree outflow conditions." *Ann Biomed Eng*, vol. 28, no. 11, pp. 1281–1299, 2000.

[37] A. Swillens, L. Lovstakken, J. Kips, H. Torp, and P. Segers, "Ultrasound simulation of complex flow velocity fields based on computational fluid dynamics," *Ultrasonics, Ferroelectrics and Frequency Control, IEEE Transactions on*, vol. 56, no. 3, pp. 546–556, 2009.

[38] E. Di Martino, G. Guadagni, A. Fumero, G. Ballerini, R. Spirito, P. Biglioli, and A. Redaelli, "Fluid-structure interaction within realistic three-dimensional models of the aneurysmatic aorta as a guidance to assess the risk of rupture of the aneurysm," *Medical engineering & physics*, vol. 23, no. 9, pp. 647–655, 2001.

[39] C. G. Caro, T. J. Pedley, R. C. Schroter, and W. A. Seed, "Mechanics of the circulation," in *Cardiovascular Physiology*, A. Guyton, Ed. Medical and Technical Publishers, 1974.

PAPER IV

Title Age and Gender Related Differences in Aortic Blood Flow

Authors Marie Sand Enevoldsen, Mads Møller Pedersen, Martin Christian Hemmsen, Lars Lönn, Kaj-Åge Henneberg, Jørgen Arendt Jensen

Journal Proceedings of SPIE

Publication History Submission date: 25-07-2011, Accepted for presentation: 03-10-2011

Age and gender related differences in aortic blood flow

Marie Sand Enevoldsen[1], Mads Møller Pedersen[2], Martin Christian Hemmsen[1], Lars Lönn[2], Kaj-Åge Henneberg[1] and Jørgen Arendt Jensen[1]

[1]Department of Electrical Engineering, Technical University of Denmark, 2800 Lyngby, Denmark;
[2]Departments of Radiology and Vascular Surgery, Copenhagen University Hospital, 2100 Copenhagen, Denmark;

ABSTRACT

The abdominal aorta (AA) is predisposed to development of abdominal aneurysms (AAA), a focal dilatation with fatal consequences if left untreated. The blood flow patterns is thought to play an important role in the development of AAA. The purpose of this work is to investigate the blood flow patterns within a group of healthy volunteers (six females, eight males) aged 23 to 76 years to identify changes and differences related to age and gender. The healthy volunteers were categorized by gender (male/female) and age (below/above 35 years). Subject-specific flow and geometry data were acquired using the research interface on a Profocus ultrasound scanner (B-K Medical, Herlev, Denmark) and segmentation of 3D magnetic resonance angiography (Magnetom Trio, Siemens Healthcare, Erlangen, Germany). The largest average diameter was among the elderly males (19.7 ($\pm$ 1.33) mm) and smallest among the young females (12.4 ($\pm$ 0.605) mm). The highest peak systolic velocity was in the young female group (1.02 ($\pm$ 0.336) m/s) and lowest in the elderly male group (0.836 ($\pm$ 0.127) m/s). A geometrical change with age was observed as the AA becomes more bended with age. This also affects the blood flow velocity patterns, which are markedly different from young to elderly. Thus, changes in blood flow patterns in the AA related to age and gender are observed. Further investigations are needed to determine the relation between changes in blood flow patterns and AAA development.

Keywords: Blood flow estimation, abdominal aorta, aneurysms, spectral measurements, magnetic resonance angiography

1. INTRODUCTION

Cardiovascular diseases are a leading cause of death worldwide and accounted for 30% of all deaths in 2005 according to the World Health Organization (WHO).[1] Changes in the blood flow are suspected to play a role in the onset and progress of cardiovascular diseases.[2,3] The human abdominal aorta (AA) is liable for both atherosclerosis as well as development of abdominal aortic aneurysms (AAA). This work focus on the role of blood flow patterns in AAA development. The age-related changes in the AA configuration, the AA mechanical properties, and, as a consequence, the changes in the blood flow properties, is suspected to play an important role.[4] AAA is a focal pathological dilatation of the AA which may rupture if the lesion is left untreated. Even though AAA affect 6-9% of the elderly population above 65 years the details regarding the onset of the pathological process is still not known in detail.[3,5]

Computational fluid dynamics (CFD) is a valuable tool in the inspection and quantification of changes in blood flow properties in the human AA. The amount of studies on CFD simulations of blood flow in the AA are numerous. The simulations have evolved progressively over the years. Some simulations involve idealized geometries of the AAA with the purpose of investigating the influence of AAA shape on the blood flow patterns.[4,6]

Further author information: (Send correspondence to Marie Sand Enevoldsen)
Marie Sand Enevoldsen: E-mail: mse@elektro.dtu.dk, Phone: +45 45 25 37 05
Mads Møller Pedersen: E-mail: phd@medit.dk
Martin Christian Hemmsen: E-mail: mah@elektro.dtu.dk
Lars Lönn: E-mail: lars.loenn@rh.regionh.dk
Kaj-Åge Henneberg: E-mail: kah@elektro.dtu.dk
Jørgen Arendt Jensen: E-mail: jaj@elektro.dtu.dk

Others have evaluated the blood flow patterns in patient-specific aortas as well as patient-specific AAAs[7,8] in which the geometries were obtained using computer tomography (CT).

This study combines blood flow properties obtained with ultrasound and subject-specific geometries obtained using magnetic resonance imaging (MRI). Subject-specific blood flow profiles can be obtained with the implementation of research interfaces on commercial ultrasound scanners.[9,10] This enables extraction of raw spectral data from the flowing blood. These data are suitable for reconstruction of the subject-specific velocity profile in the AA as described in Sec. 2.2. These flow profiles are combined with subject-specific AA geometries obtained using a new imaging sequence for magnetic resonance imaging (MRI), which eliminates the use of intra-vascular contrast agents, see Sec. 2.4.

The purpose of this study is to investigate the influence of age and gender in blood flow properties in the AA using the tools described above. The differences in blood flow properties among the volunteers are quantified using four clinical parameters, and visual inspection of the velocity fields in the transverse plane together with visual inspection of the deviation from laminar flow using the velocity streamlines.

Section 2 presents the *in vivo* data which comprise the demographics of the volunteers, the acquisition and processing of ultrasound data and MRI data. Section 3 presents the computational fluid dynamics applied to obtain the results, which are presented in Section 4. The results are discussed in the final section of this paper.

2. IN VIVO DATA

2.1 Material

The material for this study consisted of 14 healthy volunteers aged 23 to 76 years of age. The group includes both males and females with the demographics listed in Table 1. Each volunteer was scanned with ultrasound to obtain subject-specific inlet profiles, see Section 2.2, as well as scanned using magnetic resonance imaging (MRI) to obtain the subject-specific AA lumen geometry, see Section 2.4. This study was approved by the Danish National Committee on Biomedical Research Ethics (H-3-2009-102, 2009/09/01). All volunteers signed an informed consent.

Table 1: Demographic data for the 14 volunteers included in the research protocol. BMI is body mass index, BMI = [weight (kg)]/[(height (m))^2].

Volunteer	**Gender**	**Age (years)**	**BMI (kg/m^2)**	**Smoking**
1	Female	26	20.2	No
2	Female	28	23.8	No
3	Female	31	19.0	No
4	Female	28	20.3	No
5	Female	57	29.1	No
6	Female	50	24.0	No
7	Male	27	25.6	No
8	Male	25	21.2	No
9	Male	23	19.9	No
10	Male	34	21.3	No
11	Male	76	22.8	No
12	Male	51	24.2	No
13	Male	53	22.7	Yes
14	Male	57	26.8	No

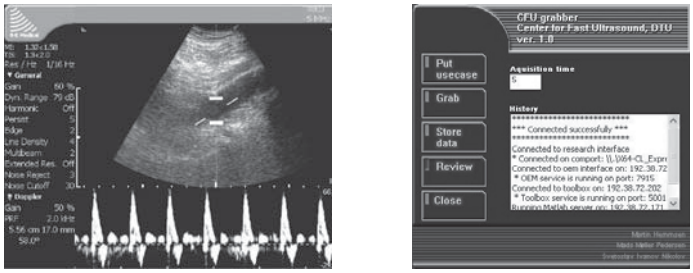

(a) **(b)**

Figure 1: Example of **(a)** the setup on the ProFocus scanner and **(b)** the CFU Grabber GUI during acquisition of the blood flow data. The range gate is marked by the white solid lines in the B-mode image in **(a)**. In the CFU Grabber GUI in **(b)** the functions are listed to the left and activated by point-and-click.

2.2 Ultrasound data acquisition

In this work, spectral data for each volunteer were acquired using a UA2227 research interface implemented on a 2202 ProFocus scanner (B-K Medical, Herlev, Denmark).[9] Several data sequences of five seconds each were acquired for each volunteer. The range gate was positioned in the center of the AA and adjusted by the operating physician to cover the entire diameter of the AA, see Fig. 1a. The volunteers were scanned using a convex transducer (BK8803, B-K Medical, Herlev, Denmark).

The scan sequence was controlled by the dedicated grabber program "CFU Data Grabber",[9] see Fig. 1b. The CFU Grabber GUI enables loading of specific setups on the scanner (usecases), acquisition of raw data directly from the scanner, fast preview of the recorded data, and download of the acquired data to a hard drive. To obtain usable data the pulsing strategy was designed such that the two types of data, i.e. the B-mode image lines and the spectral data were acquired interleaved. Each line of the data set is identified by a header.[9] After acquisition, the data was sorted and processed off-line using customized routines developed for MatLab (Mathworks, Natick, MA, USA).

2.3 Ultrasound data processing

The mean spatial velocity, $\bar{v}(t)$, in the AA was estimated using the power density spectrum of the received spectral data together with the relation between the mean frequency and the mean velocity. The mean spatial frequency, $\bar{f}$, was determined from the power density spectrum,

$$\bar{f} = \frac{\int_{-\infty}^{\infty} fP(f)\,\mathrm{d}f}{\int_{-\infty}^{\infty} P(f)\,\mathrm{d}f} \quad , \tag{1}$$

where $P(f)$ is the power density at a specific depth in the artery, and f is the frequency content of the received signals. The mean frequency is proportional to the mean velocity,

$$\bar{v}(t) = \frac{c}{2\cos(\theta) f_0}\bar{f} \quad , \tag{2}$$

where $c = 1540$ m/s is the speed of sound in blood, θ is the angle between the AA and the ultrasound beam, and f_0 is the center frequency of the transducer.

To perform subject-specific flow simulations a 3D profile, which is smooth and continuous in both time and space, is needed as inlet boundary condition. Such a profile was derived using the principles introduced by Womersley[11] and Evans.[12] Mathematically, under the assumption that the pulsation is periodic, the velocity

waveform can be decomposed into Fourier series[13] and then added to the parabolic profile characterizing the fully-developed flow in a stiff pipe. Womersley[11] found the relation between the flow rate and the pressure for each harmonic component of the velocity Fourier series. Evans[12] provided the method for determination of the velocity profile when the flow rate is known. In this work the first ten harmonics were included in the velocity estimation. Neglecting entrance effect, the temporal-spatial velocity profile was determined as,[14,15]

$$v(t,r) = 2v_0\left(1-\left(\frac{r}{R}\right)^2\right) + \sum_{m=1}^{10} |V_m|\,|\psi_m|\cos(m\omega t - \phi_m + \chi_m) \quad , \tag{3}$$

where the first term is the parabolic flow profile characterizing a Poiseuille flow, and the second term is the superposition of the sinusoidal components resulting from the Fourier decomposition, V_m, multiplied by the function ψ_m. In (3) ϕ_m is the phase of the sinusoids, and χ_m is the phase of ψ_m. The function ψ_m describes how the velocity changes with time and position in the AA over one period for each sinusoidal component such that,

$$\psi_m(\tau_m, r) = \frac{\tau_m J_0(\tau_m) - \tau_m J_0(\tau_m \frac{r}{R})}{\tau_m J_0(\tau_m) - 2J_1(\tau_m)} \quad , \tag{4}$$

where J_n are the n'th order Bessel functions of first kind, and $\tau_m = j^{3/2}\alpha_m$ where α_m is the Womersley number defined as,

$$\alpha_m = R\sqrt{\frac{\rho_{\text{blood}}}{\mu_{\text{blood}}}\omega_m}, \tag{5}$$

where $\rho_{\text{blood}} = 1,060$ kg/m^3 is the mass density of blood, and $\mu_{\text{blood}} = 3.5$ mPa·s is the constant viscosity of blood. Hence, the blood is assumed to be a Newtonian fluid. This assumption is applicable when the artery is large, as has been assumed in several studies of flow properties in the AA.[6–8]

2.4 Magnetic resonance imaging

The lumen geometry of each AA was obtained by segmentation of 3D magnetic resonance angiography (Magnetom Trio, Siemens Healthcare, Erlangen, Germany). The test person was place head first on the scan bed and the body coil was placed across the abdomen of the subject, see Fig. 2a.

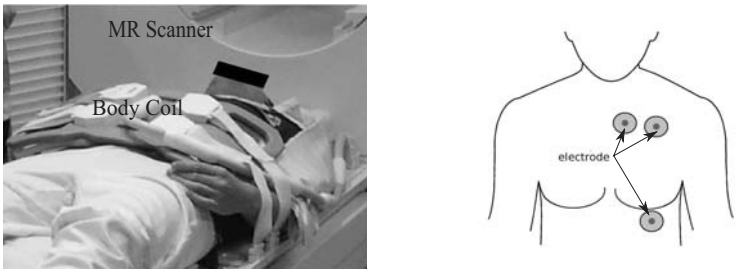

(a) **(b)**

Figure 2: Example of the preparation of the MRI scanning. In **(a)** the test person is placed head first on the scanner bed and the body coil necessary imaging is mounted over the abdomen of the volunteer. In **(b)** the position of the electrodes for registration of the ECG is shown.

The imaging sequence applied for the MRI procedure to obtain the highest possible contrast between the AA and the surrounding tissue is called Native True FISP (Fast Imaging with Steady-state Precession).[16] This sequence enables imaging of arteries using MRI without the use of intra-vascular contrast agents. It combines the True FISP sequence and synchronization of the electrocardiogram (ECG) of the subject in the scanner. Hence, electrodes for monitoring of ECG was placed on the left side of the chest of all volunteers. Hereby, the images are all acquired at the same instant during the cardiac cycle eliminating motion artifacts.

The AA varies in length from volunteer to volunteer depending on the height of the volunteer. The scan area defined by the MRI scanner software only covered part of the AA. Therefore, the scan area needed to be adjusted for each scan sequence, and depending on the volunteer two or three scan sequences were needed to cover the entire AA from the branching of the renal arteries to the iliac bifurcation. Unfortunately the renal arteries did not provide enough contrast for adequate segmentation in several volunteers.

2.5 Image segmentation

The AA lumen for each volunteer was obtained by segmentation of the 3D MRI angiography using ScanIP (Simpleware ltd., Exeter, United Kingdom). The geometry included the iliac bifurcation in all cases but one (volunteer no. 11) and was cut just below the branching of the renal arteries. The segmentation procedure was semi-automatic including three consecutive steps:

- Initial automatic coarse segmentation
- Manual editing of the coarse segmentation
- Smoothing of the segmented AA lumen

The initial automatic segmentation consisted of two segmentation algorithms. The first algorithm was a threshold algorithm which segmented the images according to gray scale values, where the lumen of the AA provide bright white color, see Fig. 3. Afterwards, a region-grow algorithm was applied to fill gaps in the initial segmented volume (mask).

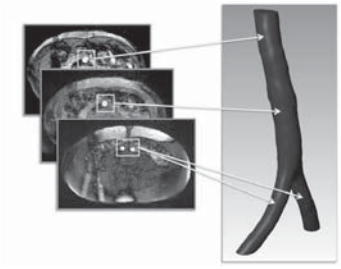

Figure 3: Example of the MRI images used for segmentation of the AA lumen. The example originates from a 28 years old female volunteer.

In the manual editing each image slice was inspected and the mask was adjusted to cover only the AA lumen using a "seed point" based algorithm and "pixel-by-pixel" editing. Lastly, the segmented AA lumen was smoothed to eliminate sharp edges. The final result of the segmentation is exemplified in Fig. 3.

3. COMPUTATIONAL FLUID DYNAMICS

3.1 Constitutive framework

The blood was considered as an incompressible Newtonian fluid. These assumptions simplifies the Navier-Stokes equation applied to describe the fluid dynamics,

$$\rho_{\text{blood}} \left(\frac{\partial \vec{v}}{\partial t} + (\vec{v} \cdot \nabla)\vec{v} \right) = -\nabla p + \nabla \cdot \vec{\tau} + \rho_{\text{blood}} \vec{g} \quad . \tag{6}$$

In (6) ∇p is the pressure gradient with ∇ being the del operator, $\vec{\tau}$ represents the shear forces of the flowing blood, and the last term on the right-hand-side is the body forces acting on the AA represented by gravity $\vec{g}$. The viscosity of an incompressible Newtonian fluid is constant at any shear rate, $\dot{\bar{\gamma}}$, hence, the constitutive relation for the blood is,

$$\eta \left(\dot{\bar{\gamma}} \right) = \mu_{\text{blood}} \quad . \tag{7}$$

The equation of motion, i.e. (6), to solve using CFD is then,

$$\rho_{\text{blood}} \left(\frac{\partial \vec{v}}{\partial t} + (\vec{v} \cdot \nabla)\vec{v} \right) = -\nabla p + \mu_{\text{blood}} \nabla^2 \vec{v} + \rho_{\text{blood}} \vec{g} \quad . \tag{8}$$

3.2 Finite element model generation

The AA geometries were loaded into the commercial FE software COMSOL Multiphysics (COMSOL AB, Stockholm, Sweden) using the CFD module. The geometries were meshed using a customized mesh algorithm in ScanIP. All elements in the geometries were tetrahedrons. For the three examples presented in Section 4, the mean aspect ratio varied between 0.73 and 0.751. The mean aspect ratio is the average ratio between side lengths in the tetrahedral elements and should be as close to unity as possible. To test the numerical accuracy of the a force coefficient was calculated after each mesh refinement as described by Papaharilaou et al.,[15]

$$C = \frac{|\vec{F}|}{\frac{1}{2}\rho \bar{v}^2 A} \quad , \tag{9}$$

where $|\vec{F}|$ is the magnitude of the total force integrated over the wall surface, $\bar{v}$ is the average velocity at peak systole, see Fig. 5, and A is the surface area of the AA wall. When the force coefficient deviated less than 1 % between to consecutive refinements the solution was considered stable. The final meshed geometries consisted of 100,000 to 150,000 tetrahedral elements.

Table 2: Blood flow velocity parameters for the 14 volunteers.

Parameter	**Males**		**Females**	
Age	< 35 years	≥ 35 years	< 35 years	≥ 35 years
Aortic diameter (mm)	17.5 (± 1.60)	19.7 (± 1.33)	12.4 (± 0.605)	17.0 (± 0.113)
PS velocity (m/s)	0.978 (± 0.145)	0.836 (± 0.127)	1.02 (± 0.336)	0.891 (± 0.027)
ED velocity (m/s)	-0.075 (± 0.016)	-0.059 (± 0.018)	-0.069 (± 0.004)	-0.072 (± 0.009)

4. RESULTS

In the investigation of the influence of age and gender on flow four clinical parameters were chosen for comparison; age, AA diameter, the velocity in the peak systole (PS), and the velocity at the end diastole (ED). Due to aliasing in the ultrasound flow measurements, it was not possible to reconstruct the spectrograms for all enrolled volunteers. Therefore, the velocities at PS and ED were adapted from the video sequences acquired for each ultrasound scan sequence in synchrony with the raw data acquisition. These results are summarized in Table 2. The diameter of the AA was measured on the MRI scans just below the branching of the renal arteries.

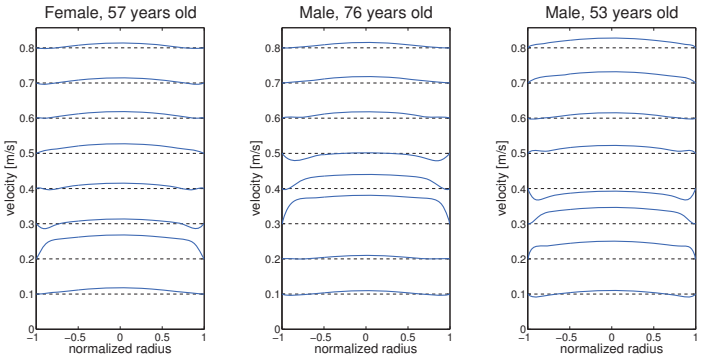

Figure 4: Examples of the temporal development of the velocity profile in the AA of three healthy volunteers. Panel (a) shows the characteristics of the profile for a 57 years old female, panel (b) shows the characteristics of the profile for a 76 years old male, and panel (c) shows the characteristics of the profile for a 51 years old male. The dashed line indicate the base line at zero blood velocity, and the solid black line is the velocity profile at the given time indicated on the ordinate axis.

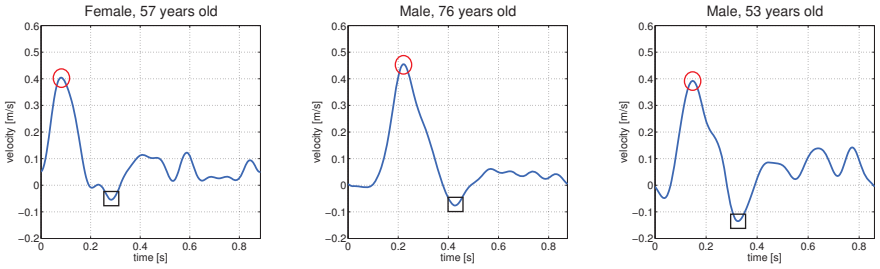

Figure 5: Examples of the mean velocity variation during the cardiac cycle calculated from superposition of the harmonic components. Panel (a) represents the variation for a 57 years old female, panel (b) represents the variation for a 76 years old male, and panel (c) represents the variation for a 53 years old male. The peak systole is marked by a red circle and the point of deceleration is marked by a black square.

4.1 Velocity profile reconstruction

Blood flow profiles were reconstructed for three volunteers; a 57 years old female, and two males aged 51 and 76 years. The profiles are shown in Fig. 4 with the time-dependent variation of the mean velocity shown in Fig. 5. The blood flow profile never obtain a parabolic shape, thus the simulated flow is never fully-developed. This was also expected as the flow in the human AA is never fully-developed due to curves, bends, and flow dividers.[17,18]

4.2 Computational fluid dynamics

In Fig. 6 the simulated velocity field and streamlines at peak systole is shown for three volunteers; a 57 years old female, and two males aged 53 and 76 years. The velocity field is influenced by the shape of the AA, however, the flow is approximately laminar in this phase of the cardiac cycle. With age the AA becomes more and more twisted as the elastic fibers degrade and the AA loose its recoil ability and extensibility. In Fig. 6 the AA for the 76 years old male is more twisted compared to the two younger volunteers.

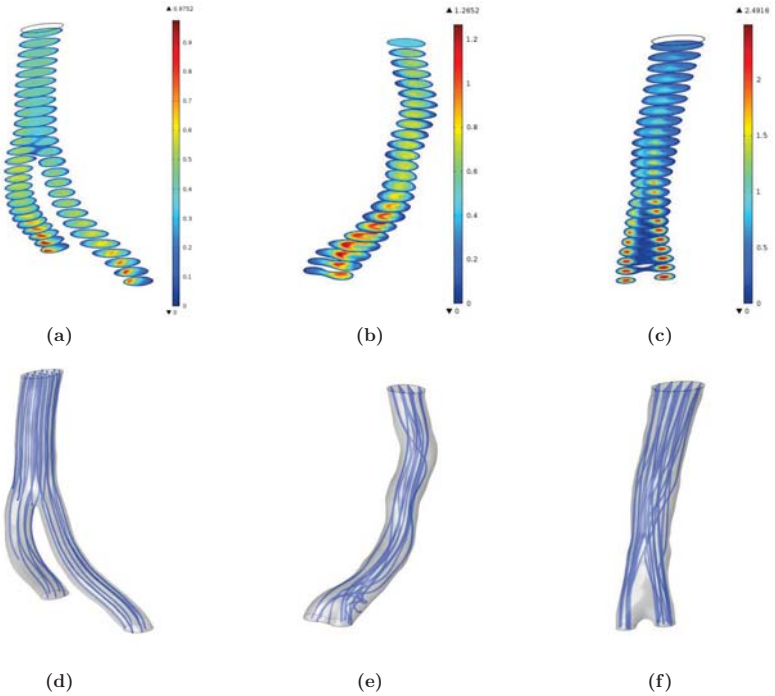

Figure 6: CFD simulation results of the velocity magnitude (top row) and velocity streamlines (bottom row) in the AA lumen of three volunteers. Panel (a) and (d) show the result from a 57 years old female, panel (b) and (e) show the result from a 76 years old male, and panel (c) and (f) show the velocity characteristics for a 53 years old male. All figures represent the time instant at peak systole during the cardiac cycle indicated by the red circles in Fig. 5. The color bar on in the top row indicate velocity magnitude in m/s.

During the deceleration after peak systole the flow deviates from the laminar flow observed up until peak systole as illustrated in Fig. 7. From Fig. 7 is it clearly seen that the flow becomes disturbed in the deceleration

phase after peak systole. Especially for the 76 years old male and the 57 years old female several vortexes in the AA are seen as these geometries are more curved compared to the AA of the 53 years old male.

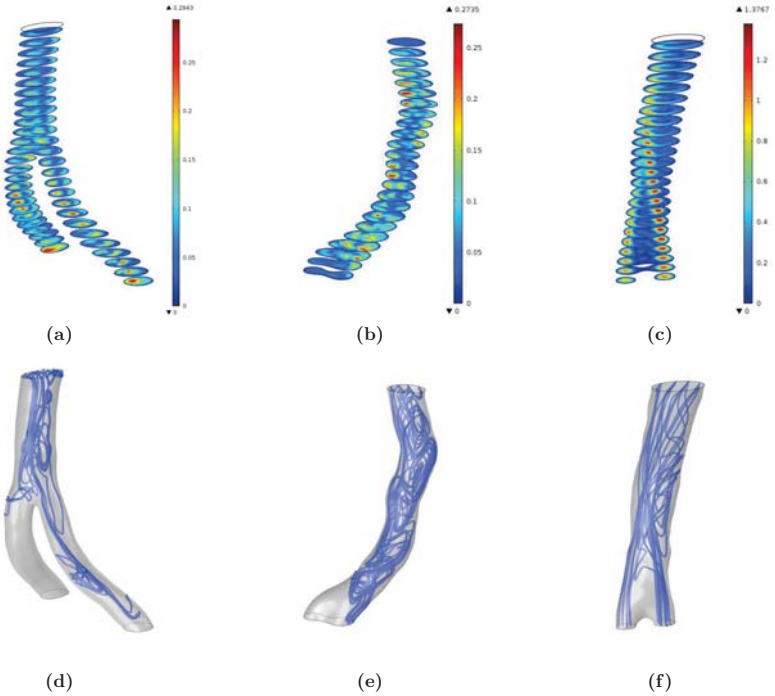

Figure 7: CFD simulation results of the velocity magnitude (top row) and velocity streamlines (bottom row) in the AA lumen of three volunteers. Panel (a) and (c) show the result from a 57 years old female, panel (b) and (e) show the result from a 76 years old male, and panel (c) and (f) show the velocity characteristics for a 53 years old male. All figures represent the time instant at deceleration after peak systole in the cardiac cycle indicated by the black squares in Fig. 5. The color bar on in the top row indicate velocity magnitude in m/s.

5. DISCUSSION

This work presents a new framework for investigation of blood flow patterns in the human abdominal aorta. The novelty emerges from the use of the native True FISP imaging sequence for the MRI scanning which provides high contrast between the artery and the surrounding tissue without the use of intra-vascular contrast agents. Non-contrast imaging with MRI using the native True FISP sequence has primarily been performed on patients with a kidney transplants.[19] Lanzman et al.[20] compared the image quality using the native True FISP sequence in a 1.5 Tesla and 3 Tesla MRI scanner and found that the 3 Tesla scanner results in higher image quality. The image quality was based on relative signal-to-noise ratio and relative contrast-to-noise ratio. Thus, using the 3 Tesla MRI scanner for visualization of the AA was used in this work to obtain high quality images which are easy to segment afterwards.

The use of subject-specific inlet profiles has been applied in CFD models before. Di Martino et al.[7] applied averaged blood flow velocity from the aorta obtained with Doppler ultrasound. The inlet profile in the aorta was assumed to be parabolic, i.e. the flow was fully-developed at the entrance. This is not the case *in vivo* as seen from the results of this work. Thus more accurate flow profiles should be applied as inlet boundary condition for the CFD model such as suggested in this work. Papaharilaou et al.[15] applied flow profiles obtained with ultrasound in the same manner as presented here. The geometry used in their study was, however, obtained with CT using intra-vascular contrast agents. Figueroa et al.[21] used geometries of the AA derived from MRI scans to simulate flow under the assumption that the wall was deformable. The inlet profile was a time-varying parabolic profile. The time-varying velocity was derived using the principles stated by Womersley.[11] The next step in this work will be to apply deformable walls to the CFD model.

The AA changes in geometrical configuration with age, which naturally affects the blood flow patterns. With aging the large conduit arteries dilate, stiffen, and loosely tethered arteries such as the AA increase in length and start to buckle.[22,23] These observations are confirmed in this study as the AA diameter increases with age for both genders, see Table 2. In general the AA diameter is larger in adult males compared to adult females,[24] which was also confirmed here as the average diameter among the males is larger compared to the female group. The diameter increase due to aging is speculated to be caused by the age-related degradation of elastin.[5] The results of the CFD simulations visually show a marked difference in flow properties related to age which is mainly due to large variations in the AA geometry. In addition, the easy access to both blood flow velocity data and geometrical information presented here provide a powerful tool for further research in the role of blood flow patterns in AAA development.

Acknowledgements

This work was supported by project 55562 at Technical University of Denmark, Radiometer Medical ApS., and the Danish Ministry of Science, Technology, and Innovation. Furthermore, the authors acknowledge the invaluable assistance from Professor, chief physician, dr. med. Carsten Thomsen in performing the MRI scans at the Department of Diagnostic Radiology at Copenhagen University Hospital.

REFERENCES

1. WHO, "Cardiovascular Diseases (CVDs)." `http://www.who.int/mediacentre/factsheets/fs317/en/index.html`, 2005. [Online; accessed 7-July-2011].
2. S. Oyre, E. Pedersen, S. Ringgaard, P. Boesiger, and W. Paaske, "In vivo wall shear stress measured by magnetic resonance velocity mapping in the normal human abdominal aorta," *European journal of vascular and endovascular surgery* **13**(3), pp. 263–271, 1997.
3. J. D. Humphrey and C. A. Taylor, "Intracranial and abdominal aortic aneurysms: similarities, differences, and need for a new class of computational models," *Annual review of biomedical engineering* **10**, p. 221, 2008.
4. Z. Li and C. Kleinstreuer, "Effects of blood flow and vessel geometry on wall stress and rupture risk of abdominal aortic aneurysms," *Journal of Medical Engineering and Technology* **30**(5), pp. 283–297, 2006.
5. A. Valentín, J. Humphrey, and G. Holzapfel, "A multi-layered computational model of coupled elastin degradation, vasoactive dysfunction, and collagenous stiffening in aortic aging," *Annals of biomedical engineering* **39**(7), pp. 2027–2045, 2011.
6. C. Scotti, J. Jimenez, S. Muluk, and E. Finol, "Wall stress and flow dynamics in abdominal aortic aneurysms: finite element analysis vs. fluid–structure interaction," *Computer Methods in Biomechanics and Biomedical Engineering* **11**(3), pp. 301–322, 2008.
7. E. Di Martino, G. Guadagni, A. Fumero, G. Ballerini, R. Spirito, P. Biglioli, and A. Redaelli, "Fluid-structure interaction within realistic three-dimensional models of the aneurysmatic aorta as a guidance to assess the risk of rupture of the aneurysm," *Medical engineering & physics* **23**(9), pp. 647–655, 2001.
8. P. Rissland, Y. Alemu, S. Einav, J. Ricotta, and D. Bluestein, "Abdominal aortic aneurysm risk of rupture: patient-specific fsi simulations using anisotropic model," *Journal of Biomechanical Engineering* **131**, pp. 031001–1–013001–10, 2009.

9. M. C. Hemmsen, S. I. Nikolov, M. M. Pedersen, M. J. Pihl, M. S. Enevoldsen, J. M. Hansen, and J. A. Jensen, "Implementation of a versatile research data acquisition system using a commercially available medical ultrasound scanner," *IEEE Transactions on Ultrasonics, Ferroelectrics, and Frequency Control* , p. Accepted, 2011.
10. V. Shamdasani, U. Bae, S. Sikdar, Y. M. Yoo, K. Karadayi, R. Managuli, and Y. Kim, "Research interface on a programmable ultrasound scanner," *Ultrasonics* **48**(3), pp. 159–168, 2008.
11. J. Womersley, "Method for the calculation of velocity, rate of flow and viscous drag in arteries when the pressure gradient is known.," *The Journal of physiology* **127**(3), pp. 553–563, 1955.
12. D. H. Evans, "Some aspects of the relationship between instantaneous volumetric blood flow and continuous wave Doppler ultrasound recordings III," *Ultrasound in Medicine and Biology* **8**, pp. 617–623, 1982b.
13. G. Truskey, F. Yuan, and D. Katz, *Transport phenomena in biological systems*, Pearson Prentice Hall Upper Saddle River, NJ, 2004.
14. J. A. Jensen, *Estimation of Blood Velocities Using Ultrasound: A Signal Processing Approach*, Cambridge University Press, New York, 1996.
15. Y. Papaharilaou, J. Ekaterinaris, E. Manousaki, and A. Katsamouris, "A decoupled fluid structure approach for estimating wall stress in abdominal aortic aneurysms," *Journal of Biomechanics* **40**(2), pp. 367–377, 2007.
16. P. Weale, "syngo Native - Non Contrast MR Angiography Techniques," 2011. `http://www.clinical-mri.com/pdf/IT/hardware/MRA_Native_final.pdf`.
17. L. Frazin, G. Lanza, M. Vonesh, F. Khasho, C. Spitzzeri, S. McGee, D. Mehlman, K. Chandran, J. Talano, and D. McPherson, "Functional chiral asymmetry in descending thoracic aorta," *Circulation* **82**(6), pp. 1985–1994, 1990.
18. J. Thomas, "Flow in the descending aorta. A turn of the screw or a sideways glance?," *Circulation* **82**(6), pp. 2263–2265, 1990.
19. X. Liu, N. Berg, J. Sheehan, X. Bi, P. Weale, R. Jerecic, and J. Carr, "Renal transplant: Nonenhanced renal mr angiography with magnetization-prepared steady-state free precession1," *Radiology* **251**(2), p. 535, 2009.
20. R. Lanzman, P. Kröpil, P. Schmitt, S. Freitag, A. Ringelstein, H. Wittsack, and D. Blondin, "Nonenhanced free-breathing ecg-gated steady-state free precession 3d mr angiography of the renal arteries: comparison between 1.5 t and 3 t," *American Journal of Roentgenology* **194**(3), pp. 794–798, 2010.
21. C. Figueroa, I. Vignon-Clementel, K. Jansen, T. Hughes, and C. Taylor, "A coupled momentum method for modeling blood flow in three-dimensional deformable arteries," *Computer Methods in Applied Mechanics and Engineering* **195**(41-43), pp. 5685–5706, 2006.
22. S. Greenwald, "Ageing of the conduit arteries," *The Journal of Pathology* **211**(2), pp. 157–172, 2007.
23. M. O'Rourke and J. Hashimoto, "Mechanical factors in arterial aging: a clinical perspective," *Journal of the American College of Cardiology* **50**, pp. 1–13, 2007.
24. W. Pearce, M. Slaughter, S. LeMaire, A. Salyapongse, J. Feinglass, W. McCarthy, and J. Yao, "Aortic diameter as a function of age, gender, and body surface area.," *Surgery* **114**(4), pp. 691–697, 1993.

PAPER V

Title On the Machanical Behavior of Healthy and Aneurysmal Aorta

Authors Jacopo Ferruzzi, Marie Sand Enevoldsen, Jay D. Humphrey

Journal Proceedings of the ASME Summer Bioengineering Conference 2011

Publication History Submission date: 23-01-2011, Accepted for presentation: 11-03-2011

Proceedings of the ASME 2011 Summer Bioengineering Conference
SBC2011
June 22-25, Nemacolin Woodlands Resort, Farmington, Pennsylvania, USA

SBC2011-53852

ON THE MECHANICAL BEHAVIOR OF HEALTHY AND ANEURYSMAL ABDOMINAL AORTA

J. Ferruzzi[1], M.S. Enevoldsen[2], J.D. Humphrey[1]

[1]Department of Biomedical Engineering
Yale University, New Haven, CT, USA

[2]Department of Electrical Engineering, Biomedical Engineering, Technical University of Denmark, Kgs. Lyngby, Denmark

INTRODUCTION

Abdominal aortic aneurysm (AAA) is a pathological condition of the infrarenal aorta characterized by a local dilatation of the arterial wall. The main histopathologic features of an AAA are smooth muscle cell death and loss of elastin. The biomechanical behavior of AAAs has been widely studied to determine the rupture potential according to the principles of material failure. However, most prior approaches are limited by the use of data from uniaxial tensile testing and by the assumption of material isotropy, leading to inaccurate characterization of the 3D multiaxial mechanical response of the aneurysmal tissue. To date, the best data available on the behavior of human abdominal aorta (AA) and AAA to planar biaxial testing are the ones reported by Vande Geest et al. [1,2]. In a recent work [3], we considered a structurally motivated four-fiber family strain energy function (SEF) [4] to capture the biaxial behavior of the human AA and AAA from Vande Geest et al. [1,2]. We showed that this constitutive relation fits human data better than prior models and most importantly it captures the stiffening of the arterial wall related to both aging and aneurysmal development. These changes in mechanical behavior are mirrored by changes in the best-fit values of the parameters, with a progressive decrease of the isotropic part attributed to elastin and a parallel increase in values associated with the families of collagen fibers.

In Ferruzzi et al. [3], we focused on different forms of the anisotropic contribution of collagen to the energy stored in the tissue, showing that a model that accounts for four families of locally parallel collagen fibers offers an overall better description of data from both AA and AAA. The contribution of elastin was accounted for by using a neo-Hookean (isotropic) term. Several works recently showed, however, that the mechanical response of purified elastic tissue is better described by anisotropic SEFs. In particular Zou and Zhang [5] observed that isolated elastin shows a stiffer behavior in the circumferential direction. Motivated by these findings, herein we seek to model human AA and AAA data from Vande Geest et al. [1,2] using two SEFs that account for elastin anisotropy.

MATERIAL AND METHODS

We employed a four-fiber family hyperelastic constitutive model [4] to quantify the measured passive biaxial behaviors of 26 AAA and 21 AA samples. According to our modeling approach, the SEF is divided into two terms, one associated with the elastin-dominated matrix (W^e) and one due to the embedded collagen fibers (W^c). Hence, we consider a SEF of the form $W = W^e + W^c$, where the second term is modeled using the four-fiber family model suggested by Baek et al. [4]. In order to account for elastin anisotropy, we considered the semi-empirical model proposed by Gundiah et al. [6] that incorporates specific contribution from orthogonal elastic fibers,

$$W^e = \frac{c_1}{2}\left(I_C - 3\right) + \frac{c_2}{4}\left(IV_C - 1\right)^2 + \frac{c_3}{4}\left(VI_C - 1\right)^2 \qquad (1)$$

where I_C = tr $\mathbf{C}$ is the first invariant of the right Cauchy-Green tensor while $IV_C = (\lambda_\vartheta)^2$ and $VI_C = (\lambda_z)^2$ represent the square of the stretches of the elastic fibers. We also considered a simplified version of the above model that accounts for a single preferential alignment of the fibers,

$$W^e = \frac{c_1}{2}\left(I_C - 3\right) + \frac{c_2}{4}\left(IV_C - 1\right)^2 \qquad (2)$$

where we used first $IV_C = (\lambda_\vartheta)^2$ according to the stiffer behavior of elastin in the circumferential direction reported in the literature, and then $IV_C = \mathbf{M}^e \cdot \mathbf{C}\mathbf{M}^e$, hence letting the direction of fiber reinforcement defined in the reference configuration by the unit vector $\mathbf{M}^e$ free to vary between axial (0°) and circumferential (90°). Best-fit values of the parameters were determined by minimization of the differences between theoretical and experimental Cauchy stresses. Similar to Ferruzzi et al. [3], we applied the nonparametric bootstrap to estimate the accuracy and the precision of the point estimates obtained via regression. We used the coefficient of determination R^2 as a measure of goodness-of-fit, and we employed the corrected Akaike information criterion (AIC_c) to compare models with a different number of parameters.

RESULTS

Similar to Vande Geest et al. [1], AA data were divided in three groups based on the age of donors (less than 30, between 30 and 60, and over 60 years of age). The results obtained using the constitutive models described by equations (1) and (2) were compared to the results obtained using the standard neo-Hookean model. Among the

selected anisotropic SEFs, the one that accounts for a single diagonal fiber direction is the only model that gives consistently better fits in terms of R^2 values across the four groups of data (AAA data and the three AA groups) than the neo-Hookean model, albeit these improvements are neither visually striking nor significant in terms of increased R^2 values. On average, we obtain lower AIC_c values only for AA specimens, whereas for AAA specimens we obtain higher AIC_c values. This means that the inclusion of additional parameters to account for preferential elastic fiber alignment does not improve the descriptive capability of the model when applied to AAA data. When accounting for elastin anisotropy, fits to AA data were improved in the high stretch regions (Figure 1). This result was unexpected since we usually tend to think that the stress in the high stretch regions is mainly due to collagen. Finally, the bootstrap replications used to approximate each parameter's probability distribution showed a very high variability in the orientation of the estimated elastin fiber angle, thus indicating a very high uncertainty associated with the estimation of the elastic fiber orientation. The above considerations suggested that a modeling approach that describes elastin as neo-Hookean captures reasonably well the mechanical response of human AA and AAA without the need to account for possible anisotropic behavior.

DISCUSSION

The results of the present study demonstrate that, although the complex structure of arterial elastin presumably gives rise to anisotropic behavior, the neo-Hookean model leads to an accurate description of the biaxial response of the AA and AAA data from Vande Geest et al. [1,2] without the need to further increase the number of parameters to be estimated. These results are consistent with those recently reported by Rezakhaniha et al. [7] where they analyzed inflation-extension data of rabbit common carotid arteries before and after treatment with elastase using two SEFs that regard elastin as isotropic and anisotropic. They found that before elastin degradation, the SEF that accounts for elastin anisotropy fits better the inflation-extension data, whereas after elastase treatment both SEFs result in similar prediction of the mechanical behavior of the arterial wall. Similarly, herein we showed that, albeit not significantly, fits to AA data were improved when the effect of elastin anisotropy was considered. On the other hand, consistent with the well known reduced elastin content in aneurysmal tissue, fits to AAA data did not improve when an anisotropic SEF was employed. We submit, therefore, that in order to improve the descriptive capability of the current model, we need to consider explicitly the interaction term between elastin and collagen within the SEF.

The utility of an approach that employs nonlinear regression and the bootstrap for a more accurate estimation of material parameters is motivated by the need for more reliable stress analyses and rupture potential predictions. Mean parameter values have been used in the past within finite-element models of AAA [8]. However, Figure 2 shows that mean parameter values provide conservative estimates of the mechanical behavior favoring stiffer specimens, while median parameter values are more representative of the average response of the specimens under investigation. This observation is important whenever dealing with human data, given the impossibility of knowing the natural history of each individual and the complex genetic and environmental factors that contribute to disease progression.

ACKNOWLEDGMENTS

This work was funded in part by NIH grant HL-86418. We acknowledge Professors J. Vande Geest, M. Sacks, and D.A. Vorp who collected and reported the original biaxial data.

REFERENCES

[1] Vande Geest, J.P., Sacks, M.S., and Vorp, D.A., 2004, "Age dependency of the biaxial biomechanical behavior of human abdominal aorta," *J Biomech Engr*, **126**(6), pp. 815-822.

[2] Vande Geest, J.P., Sacks, M.S., and Vorp, D.A., 2006, "The effects of aneurysm on the biaxial mechanical behavior of human abdominal aorta," *J Biomech*, **39**(7), pp. 1324-1334.

[3] Ferruzzi J., Vorp D.A., and Humphrey J.D., 2010, "On constitutive descriptors of the biaxial mechanical behavior of human abdominal aorta and aneurysms," *J Roy Soc Interface*, Epub ahead of print.

[4] Baek, S., Gleason, R.L., Rajagopal, K.R., and Humphrey, J.D., 2007, "Theory of small on large: Potential utility in computations of fluid-solid interactions in arteries," *Comp Meth Applied Mech Engr*, **196**(31-32), pp. 3070-3078.

[5] Zou, Y., and Zhang, Y., 2009, "An experimental and theoretical study on the anisotropy of elastin network,", *Ann Biomed Eng*, **37**(8), pp. 1572-1583.

[6] Gundiah, N., Ratcliffe, M.B., and Pruitt, L.A., 2009, "The biomechanics of arterial elastin," *J Mech Behav Mater*, **2**(3), pp. 288-296.

[7] Rezakhaniha, R., Fonk, E., Genoud, C., and Stergiopulos, N., 2010, "Role of elastin anisotropy in structural strain energy functions of arterial tissue," *Biomech Model Mechanobiol*, Epub ahead of print.

[8] Vorp, D.A., 2007, "Biomechanics of abdominal aortic aneurysms," *J Biomech*, **40**(9), pp. 1887-1902.

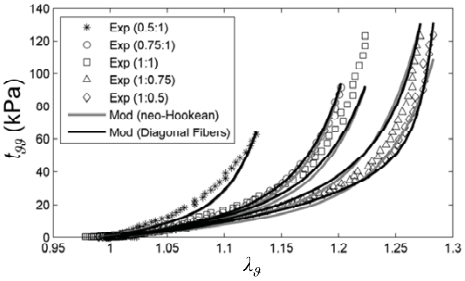

Figure 1. Fits to AA data (symbols) obtained modeling elastin as isotropic (gray lines) and accounting for anisotropy (black lines)

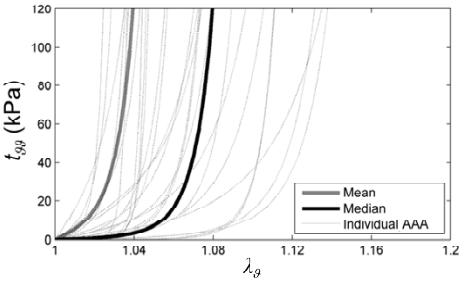

Figure 2. Comparison of the responses predicted using mean (gray line) and median (black line) values of AAA parameters

PAPER VI

Title Finite Element Implementation of a Structurally Motivated Constitutive Relation for Abdominal Aortas and Aneurysms

Authors Marie Sand Enevoldsen, Lars Lönn, Kaj-Åge Henneberg, Jørgen Arendt Jensen

Journal Springer Verlag IFMBE Proceedings Series

Publication History Submission date: 27-01-2011, Accepted for presentation: 27-03-2011

Finite Element Implementation of a Structurally-Motivated Constitutive Relation for Abdominal Aortas and Aneurysms

M.S. Enevoldsen[1], K.-A. Henneberg[1], L. Lönn[2] and J.A. Jensen[1]

[1] Biomedical Engineering, Department of Electrical Engineering, Technical University of Denmark, Kgs. Lyngby, Denmark
[2] Department of Radiology and Department Vascular Surgery, Rigshospitalet, University of Copenhagen, Copenhagen, Denmark

Abstract— **The structural integrity of the abdominal aorta is maintained by elastin, collagen, and vascular smooth muscle cells. Changes with age in the structure can lead to development of aneurysms. So it is interesting to construct a model to capture these changes. This paper presents an implementation of a structurally-motivated constitutive relation, the "four fiber family" model, in COMSOL Multiphysics. The constitutive relation is applied on data from a biaxial test of aortic tissue samples from four different groups; <30 years, 30-60 years, >60 years and abdominal aortic aneurysm (AAA) patients. The simulation shows good agreement with published experimental data and captures the anisotropy of the aortic tissue. The maximum axial and hoop stress in the group of AAA patients was 94.9 kPa (±0.283 kPa) and 94.3 kPa (±0.224 kPa) at maximum stretch ratios of 1.043 and 1.037, respectively. Secondly, the constitutive relation is applied to an axisymmetric circular cylinder imitating inflation-extension testing of arteries. The distribution of stress within the aortic wall resembles that of other similar simulations.**

Keywords— **Biomechanics, aorta, four fiber family model, finite element modeling.**

I. Introduction

Abdominal aortic aneurysm (AAA) is a focal dilation of the abdominal aorta affecting approximately 6-9 % of the population above 65 years in industrialized countries [1]. A common definition of an AAA is when the diameter is increased by more than 50% compared to the original diameter of the abdominal aorta. Most AAAs grow with time, 0.5 cm pr. year as a mean. The risk for rupture is exponentially related to aneurysmal diameter. Unfortunately, even small aneurysms can rupture, so it is generally acknowledged that a redefinition of the treatment criteria is necessary [2]. It is widely accepted that biomechanical measures such as wall stress and wall strength provide more detailed information of the rupture risk compared to the diameter and growth rate measures. The current challenge is to determine the arterial wall stress and strength accurately. This presents some difficulty, because arterial tissue is nonlinear in the stress-stretch relationship, displays pseudo-elastic behavior, and changes material properties with age due to structural change and remodeling. Many forms of a suitable strain energy density function (SEF) have been proposed [3,4]. This work applies the structurally motivated phenomenological "four fiber family" model introduced by Baek et al. [5]. The purpose is to provide an implementation of this particular constitutive relation in a finite element program (COMSOL Multiphysics v4.1). The model estimates a number of biomechanical properties, i.e. Cauchy stress, Green strain, deformation gradient etc. within the aortic wall. The constitutive relation is implemented in two and three dimensions and both the responses of normal and pathological tissue are analyzed using published material parameters.

II. Materials and Methods

A. Constitutive framework

It is assumed that the aortic wall is a constrained mixture of four locally parallel families of collagen fibers (axial, circumferential, symmetric diagonal) embedded in an amorphous isotropic matrix dominated by elastic fibers, see Fig. 1.

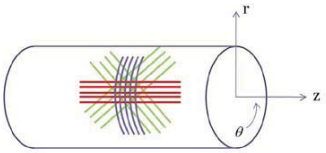

Fig. 1 Sketch of the collagen fiber families represented in the four fiber family model; axial alignment (red), circumferential alignment (blue) and symmetric diagonal alignment (green).

The biomechanical properties of a normal abdominal aorta and an aneurysm are described using the general formulation of the Cauchy stress (true stress) [6]

$$\boldsymbol{\sigma} = -p\mathbf{I} + 2\mathbf{F}\frac{\partial W}{\partial \mathbf{C}}\mathbf{F}^{T}, \qquad (1)$$

where $\boldsymbol{\sigma}$ [Pa] is the Cauchy stress tensor, p is a Lagrange multiplier, $\mathbf{I}$ is the identity tensor, $\mathbf{F}$ is the deformation gradient tensor, W [Pa] is the SEF and $\mathbf{C}=\mathbf{F}^{\mathrm{T}}\mathbf{F}$ is the right Cauchy-Green tensor. In order for the SEF to be as general

as possible the model accounts for compressibility by splitting the SEF in a purely volumetric elastic response, $W_{vol}(J)$, and a purely isochoric elastic response, $W_{iso}(\mathbf{C},\mathrm{M}^{(k)})$ [7],

$$W\left(\mathbf{C},\mathrm{M}^{(\mathrm{k})}\right)=W_{vol}(J)+W_{iso}\left(\mathbf{C},\mathrm{M}^{(\mathrm{k})}\right), \tag{2}$$

where J=det($\mathbf{F}$) is the deformed to undeformed volume ratio. Here the aortic tissue is assumed to be incompressible. To infer incompressibility the so-called penalty method is used in the finite element implementation. Here the tissue is modeled as slightly compressible by applying a very high bulk modulus in the volumetric elastic response, which has the simple form

$$W_{vol}(J)=\frac{\kappa}{2}(J-1)^2, \tag{3}$$

where κ [Pa] is the bulk modulus [7]. The isochoric response is modeled by the four fiber family constitutive relation [5]

$$W_{iso}\left(\mathbf{C},\mathrm{M}^{(\mathrm{k})}\right)=\frac{c}{2}(I_C-3)+\sum_{k=1}^{4}\frac{c_1^{(k)}}{4c_2^{(k)}}\left\{\exp\left(c_2^{(k)}\left(IV_C^{(k)}-1\right)^2\right)-1\right\} \tag{4}$$

where c, $c_1^{(k)}$, $c_2^{(k)}$ are material parameters, I_C is the first invariant of $\mathbf{C}$ and $IV_C^{(k)}=\mathrm{M}^{(k)}\mathbf{C}\mathrm{M}^{(k)}$ is the fourth invariant of $\mathbf{C}$ with $\mathrm{M}^{(k)}$ being a unit vector describing the direction of orientation of the collagen fiber family.

This model has proven useful by providing increased insight into differences in the mechanical behavior due to structural abnormalities in the arterial wall [8]. For detailed information on the material parameters used in this study we refer to [8].

In brief, the determination of material properties is based on biaxial testing of tissue slabs from four different age/patient groups; <30 years, 30-60 years, >60 years, and AAA patients. Within each group the mean value of each material parameter is used.

B. Simulation of biaxial and inflation-extension test of arteries

Biaxial tension test of arteries is a well-known method for deducing the biomechanical properties of arteries [9]. Here we have simulated the biaxial testing of both normal abdominal aorta and pathological AAA tissue described by Vande Geest et al. [10,11] using COMSOL Multiphysics v4.1 (COMSOL AB, Stockholm, Sweden) with the setup seen in Fig. 2a. In the simulation a tension of 120 N/m is applied in both directions, and the resulting stretch ratios and Cauchy stress components in the tissue sample are calculated.

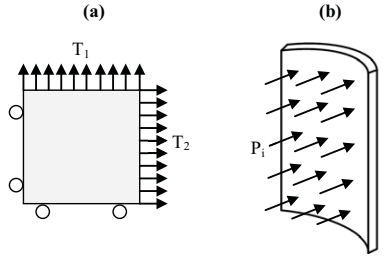

Fig. 2 Sketch of the simulated biaxial test (a) and the inflation-extension test (b). T_1 and T_2 are the applied tensions in the biaxial test and P_i is the applied internal pressure in the inflation-extension test. The arrows indicate the direction of the distributed load and the circles indicates a constrained frictionless boundary condition allowing only movement in the transverse direction.

The inflation-extension test is also a commonly used experiment for determination of arterial properties, since the geometrical configuration of the artery is conserved [6]. Here a uniform internal pressure, P_i [Pa] is applied, which results in a radial force on the interior wall of a circular axisymmetric cylinder (see Fig. 2b). The cylinder has a radius of 1 cm and a length of 5 cm.

C. Analysis of simulated experiments

The analytical solution to the stress components in the 2D situation is derived and compared to the simulated experimental result. In the 3D case no exact analytical solution exists, so the result of the simulation is compared to published numerical results by Holzapfel et al. [3].

III. Results

In this paper a negative Cauchy stress is interpreted as a compressive stress, and a positive stress is interpreted as a tensile stress. In addition, the unloaded configuration of the tissue is assumed to be stress free.

A. Biaxial test

Comparison of the numerical simulation of the biaxial test and the analytical solution for the Cauchy stress components is shown in Fig. 3. There is good agreement between the analytical and numerical solutions. The maximum stress values are seen in the circumferential direction (hoop

stress) ranging from 85-175 kPa (638-1313 mmHg) compared to 85-165 kPa (638-1238 mmHg) for the axial direction. The maximum standard deviation was under 0.5% for both the hoop and axial stress; ±0.224 kPa and 0.283 kPa respectively for the AAA patient group, which has the highest standard deviation compared to the other groups. In general the aortic tissue becomes less compliant with age, and AAA tissue is significantly stiffer than normal abdominal aortic tissue. However, using the mean values of the material parameters indicate that the biomechanical properties of the normal AA for the groups 30-60 years and >60 years are similar. The tissue from the group >60 years is

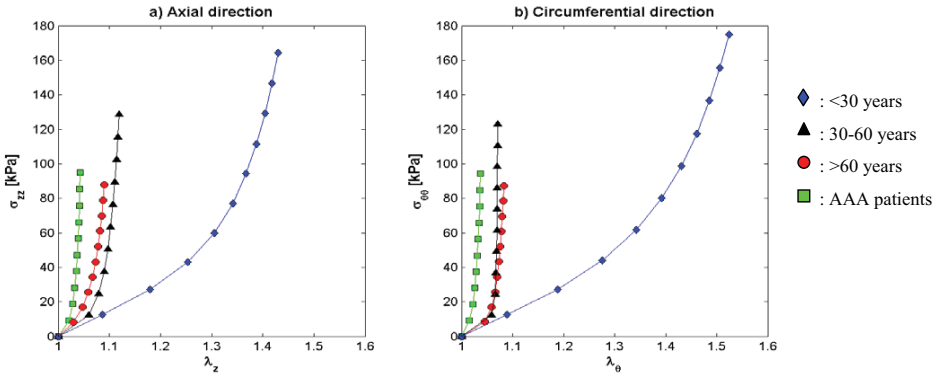

Fig 3 Stress-stretch plot comparing the known analytical solution for the 2D case with tension applied in the axial and circumferential directions. (a) shows the axial Cauchy stress (σ_{zz}) as a function of axial stretch ratio (λ_z) for all four patient groups. (b) shows the Cauchy hoop stress ($\sigma_{\theta\theta}$) as a function of circumferential stretch ratio (λ_θ) for all four patient groups. The solid lines are the analytical solutions, and the symbols indicate the numerical solution (blue diamond is the group under 30 years, black triangle is the group between 30 and 60 years, red circle is the age group over 60 years, and green square is the AAA patients).

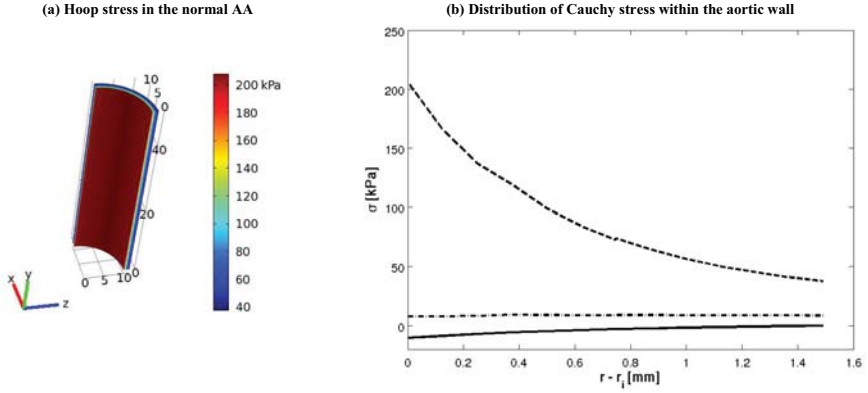

Fig 4 (a) simulated inflation-extension experiment showing the amount of hoop stress within the aortic wall for the patient group over 60 years. The dimension on the axes is millimeter. (b) shows the stress distribution within the aortic wall for the patient group over 60 years. The dashed line is the hoop stress, the dash-dot line is the axial stress, and the solid line is the radial stress.

less compliant in the axial direction compared to the group of 30-60 year-olds. But in the circumferential direction the difference is minimal. This clearly shows that the anisotropy of the aortic tissue is captured by the constitutive relation, since the stretch ratios in the two directions are different from each other for all four groups.

B. Inflation-extension test

The four fiber family constitutive relation was implemented in a circular, axisymmetric cylinder, and due to symmetry only one quarter of the cylinder is modeled. The simulation result for the hoop stress is shown in Fig 4a for the patient group over 60 years. A maximum hoop stress of 207 kPa is seen at the innermost part of the cylinder, and 40 kPa at the external part of the cylinder. With the 3D model it is possible to investigate the stress distribution within the aortic wall (see Fig 4b). The example shown is for the group of patients over 60 years. The highest stress is in the circumferential direction. The axial stress is almost constant varying from 7-9 kPa, and the radial stress is 10.7 kPa at the inner wall (corresponding to the applied internal pressure) and zero at the external part of the wall. The distribution of stress within the aortic wall resembles that of the rabbit carotid artery (cf. Holzapfel et al. [3]). It has not been possible to find comparable data for the aorta.

IV. Discussion and conclusion

In this paper the finite element implementation of the four fiber family constitutive relation in COMSOL Multiphysics is presented. The relation has been successfully implemented in both two and three dimensions using the mean values of material parameters for four different patient groups. The use of mean values of the material parameters in finite element models is common (see for example the review by Vorp [2]). But here the mean values indicate that there is not a significant difference between the groups of 30-60 years and >60 years in the biomechanical properties. This raises the question whether the division in the current age groups is suitable. An alternative could be to subdivide the group of 30-60 year-olds into smaller intervals of five or ten years, since it seems that the most significant change in arterial structure takes place in this period. This subdivision, together with extension of the mechanical tests to include inflation-extension tests of both normal abdominal aortic and aneurismal tissue, could improve the current model. In addition, with these improvements it might also be possible to obtain more complete knowledge about when the critical damage to the aortic tissue is most likely to occur.

Extending this finite element implementation to patient-specific model geometries with matching patient-specific blood flow will give the clinician a very powerful tool for detailed evaluation of AAAs. Moreover, such a model can be used to investigate the effect of the known pathological processes in AAAs.

Acknowledgment

We acknowledge the support of information on the tissue samples provided by Prof. David A. Vorp, and we thank Prof. Jay D. Humphrey and Mr. Jacopo Ferruzzi for providing the data on the material parameters.

This work is supported by project no. 55562 at the Technical University of Denmark and Radiometer Medical Aps.

References

1. Humphrey JD, Taylor CA (2008) Intracranical and abdominal aneurysms: similarities, differences, and need for a new class of computational models. Annu Rev Biomed Eng 10:221-46
2. Vorp DA (2007) Biomechanics of abdominal aortic aneurysm. J Biomech 40:1887-1902
3. Holzapfel GA, Gasser TC, Ogden RW (2000) A new constitutive framework for arterial wall mechanics and a comparative study of material models. J Elasticity 61:1-48
4. Vito PV, Dixon SA (2003) Blood vessel constitutive models 1995-2002. Annu Rev Biomed Eng 5:413-439
5. Baek S, Gleason RL, Rajagopal KR, Humphrey JD (2007) Theory of small on large: Potential utility in computations of fluid-solid interactions in arteries. Comput Method Appl M 196:3070-3078
6. Humphrey JD (2002) Cardiovascular solid mechanics: cells, tissues and organs. NY:Springer, New York
7. Holzapfel GA (2000) Nonlinear solid mechanics – a continuum approach for engineering. John Wiley& Sons, Chichester
8. Ferruzzi J, Vorp DA, Humphrey JD (2010) On constitutive descriptors the biaxial mechanical behavior of human abdominal aorta and aneurysms. J R Soc Interface DOI:10.1098/rsif.2010.0299
9. Sacks MS (2000) Biaxial mechanical evaluation of planar biological materials. J Elasticity 61:199-246
10. Vande Geest JP, Sacks MS, Vorp DA (2004) Age dependency of the biaxial biomechanical behavior of human abdominal aorta. J Biomech Eng – T Asme 126:815-822
11. Vande Geest JP, Sacks MS, Vorp DA (2006) The effect of aneurysm on the biaxial mechanical behavior of human abdominal aorta. J Biomech 39:1324-1334

Author: Marie Sand Enevoldsen
Institute: Biomedical Engineering, Department of Electrical Engineering, Technical University of Denmark
Street: Oersteds Plads, Building 349
City: Kgs. Lyngby
Country: Denmark
Email: mse@elektro.dtu.dk

www.elektro.dtu.dk
Department of Electrical Engineering
Section of Biomedical Engineering
Technical University of Denmark
Ørsteds Plads
Building 348
DK-2800 Kgs. Lyngby
Denmark
Tel: (+45) 45 25 38 00
Fax: (+45) 45 93 16 34
Email: info@elektro.dtu.dk

ISBN 978-87-92465-86-3